

**EFFECTS OF LIGHTWEIGHT AGGREGATES ON
AUTOGENOUS DEFORMATION AND
FRACTURE OF HIGH PERFORMANCE CONCRETE**

**Ph.D. Thesis by
Burcu AKÇAY, M.Sc.**

Department : Civil Engineering

Programme: Structural Engineering

JANUARY 2007

**EFFECTS OF LIGHTWEIGHT AGGREGATES ON
AUTOGENOUS DEFORMATION AND FRACTURE
OF HIGH PERFORMANCE CONCRETE**

**Ph.D. Thesis by
Burcu AKÇAY, M.Sc.
(501002114)**

Date of submission : 21 November 2006

Date of defence examination: 11 January 2007

Supervisor (Chairman): Prof. Dr. Mehmet Ali TAŞDEMİR

Members of the Examining Committee: Prof.Dr. Saim AKYÜZ

Prof.Dr. Turan ÖZTURAN (BÜ)

**Prof.Dr. Bhushan L. KARIHALOO
(Cardiff Univ)**

Prof.Dr. Abdurrahman GÜNER (NKÜ)

JANUARY 2007

**HAFİF AGREGALARIN YÜKSEK PERFORMANSLI
BETONLARIN OTOJEN DEFORMASYON VE
KIRILMASINA ETKİLERİ**

**DOKTORA TEZİ
Y. Müh. Burcu AKÇAY
(501002114)**

**Tezin Enstitüye Verildiği Tarih : 21 Kasım 2006
Tezin Savunulduğu Tarih : 11 Ocak 2007**

**Tez Danışmanı : Prof. Dr. Mehmet Ali TAŞDEMİR
Diğer Jüri Üyeleri Prof.Dr. Saim AKYÜZ
Prof.Dr. Turan ÖZTURAN (BÜ)
Prof.Dr. Bhushan L. KARIHALOO (Cardiff U.)
Prof. Dr. Abdurrahman GÜNER (NKÜ)**

OCAK 2007

to my brother

Dz. Kur. Kd. Yzb. Burak AKÇAY

ACKNOWLEDGEMENTS

First and foremost, I would like to express my deepest gratitude to my advisor, Prof. Dr. Mehmet Ali Taşdemir for his helpful comments, criticisms, generous guidance and many creative insights offered.

I express my thanks to Prof. Dr. Saim Akyüz and Prof. Dr. Turan Özturan for their valuable suggestions and comments throughout this study.

I also wish to express my thanks to Prof. Dr. Bhushan L. Karihaloo and Prof. Dr. Abdurrahman Güner for participation in my defense committee and for their useful suggestions.

I would like to thank Prof. Dr. Canan Taşdemir, Prof. Dr. Mehmet Uyan and Prof. Dr. Metin Aydoğan for their support and advice, and special thank must go to Prof. Dr. Süheyl Akman for his guidance and fruitful discussions. To accomplish the magnitude of this study, they were plenty of people helped willingly in the experiments. I would like to thank everyone in the Construction Materials Laboratory; Hüseyin Güler, Muhlis Polat, Murat Meydan and in particular, Dr. Fikret Bayromov and Cengiz Şengül.

I especially want to thank Ayda Şafak Ağar Özbek for all her friendship, encouragement, and helpful discussions.

I would also like to thank the Turkish State Planning Organization (DPT), Istanbul Technical University Research Foundation, Turkish Cement Manufacturers' Association (TÇMB), and the University of Kocaeli for financial support; Nuh Çimento A.Ş., Camiş Madencilik A.Ş., Soyak A.Ş., and YKS Yapkim A.Ş. for supplying product; the R&D Department of AKÇANSA A.Ş. for their help with cement analyses, and finally the researchers at Istanbul Technical University Biomaterials Research & Characterization Laboratory for conducting the MIP tests.

I would like to express my thanks to my family; Saime, Hüsametdin, Pınar, Burak and little cutie Çağla Akçay for their inspiration, unending support, and encouragement throughout my education and life.

Last but not least, I will always be grateful to my husband Dr. Ercan Aldanmaz for his encouragement, endless support and assistance, scientific insights and especially for his incredible love.

January, 2007

Burcu Akçay

CONTENTS

ACKNOWLEDGEMENTS	iv
ABBREVIATIONS	x
LIST OF TABLES	xii
LIST OF FIGURES	xiv
LIST OF SYMBOL	xxii
SUMMARY	xxvi
ÖZET	xxvii
1. INTRODUCTION	1
1.1. General	1
1.2. Research Objectives	2
1.3. Organization of Content	3
2. LITERATURE REVIEW	6
2.1. General	6
2.2. Cementitious Materials at Early Ages	6
2.2.1. Mechanism of the Hydration Process	7
2.2.2. Pore Structure	8
2.2.3. Water Held in Hydrated Cement Paste	10
2.2.4. Heat of Hydration of Cement	11
2.3. Literature on Autogenous Deformation	11
2.3.1. Types of Shrinkage	12
2.3.2. Terminology of Autogenous Deformation	14
2.3.3. Stages of Autogenous Deformation	15
2.3.4. Factors Affecting the Autogenous Deformation	17
2.3.4.1. Effect of water/cementing materials ratio	17
2.3.4.2. Effect of self-desiccation	18
2.3.4.3. Effect of cement type, fineness and composition	20
2.3.4.4. Effect of supplementary materials	22
<i>Silica fume</i>	23
<i>Fly ash</i>	24
<i>Slag</i>	25
<i>Metakaolin</i>	26
2.3.4.5. Effect of chemical admixtures	27
2.3.4.6. Effect of temperature	29
2.3.4.7. Effect of alkalis	30
2.3.4.8. Effect of sample size	32
2.3.5. Measurement of Autogenous Deformation	33

2.3.5.1. Volumetric measurement of autogenous deformation	33
2.3.5.2. Linear measurement of autogenous deformation	34
2.3.5.3. Inconsistencies between methods of volumetric and linear autogenous deformation	34
2.3.6. Definition of Early Age	36
2.4. Mitigation of Autogenous Deformation	37
2.4.1. General	37
2.4.2. Usage of Shrinkage Reducing Admixtures	37
2.4.3. Usage of Expansive Additives	38
2.4.4. The Use of a Slower Reacting (Coarser) Silica Fume	39
2.4.5. Internal Curing	40
2.4.5.1. Lightweight aggregates	41
2.4.5.2. Super-absorbent polymers	42
2.4.5.3. Recycled aggregates	42
2.4.5.4. Wood-derived powders and fibers	43
2.4.6. Effect of Fiber Addition	44
2.4.7. Internal Curing with LWAs	46
2.4.7.1. Properties of LWA	47
2.4.7.2. Amount of water for internal curing	48
2.4.7.3. Effects of LWAs on properties of concrete	51
2.5. Fracture Mechanics of Concrete	53
2.5.1. General	53
2.5.2. Linear Elastic Fracture Mechanics	54
2.5.2.1. Griffith theory of brittle fracture	55
2.5.2.2. Irwin theory of brittle fracture	56
2.5.2.3. Cohesive Crack Models	58
2.5.3. Application of LEFM to Concrete	59
2.5.4. Non-linear Fracture Mechanics	61
2.5.4.1. Fictitious crack model (FCM)	61
2.5.4.2. Crack band model (CBM)	63
2.5.4.3. Size effect law	64
2.5.4.4. Two parameter fracture model	64
2.5.4.5. Effective crack model	64
2.5.4.6. Boundary effect and local fracture energy distribution	65
2.5.5. Fracture Mechanics of Lightweight Concrete	65
3. EXPERIMENTAL PROGRAMME	72
3.1. General	72
3.2. Materials	72
3.2.1. Cement	72
3.2.2. Silica Fume	72
3.2.3. Aggregate	73
3.2.3.1. Normal weight aggregates	73
3.2.3.2. Lightweight aggregates	75
3.2.4. Superplasticizer	75

3.3. Material Composition and Specimen Preparation	76
3.3.1. Mixture Proportion	76
3.3.2. Mixing and Placing Procedures	77
3.4. Experimental Procedure	78
3.4.1. Autogenous Deformation	78
3.4.1.1. Linear autogenous deformation	79
3.4.1.2. Volumetric autogenous deformation	80
3.4.2. Temperature Development	80
3.4.3. Chemical Shrinkage	81
3.4.4. Heat of Hydration	81
3.4.5. Non-evaporable Water Content and Degree of Hydration	85
3.4.6. Mercury Intrusion Porosimetry (MIP)	86
3.4.7. Compression Test	87
3.4.8. Splitting Tension Test	88
3.4.9. Fracture Test	88
3.5. Summary of Programme	89
4. EXPERIMENTAL RESULTS AND DISCUSSION	91
4.1. General	91
4.2. Autogenous Deformation	91
4.2.1 Linear Autogenous Deformation	91
4.2.2. Volumetric Autogenous Deformation and Temperature Development	95
4.3 Chemical Shrinkage	98
4.4 Heat of Hydration	100
4.5. Non-evaporable water content and degree of hydration	101
4.6. Mercury intrusion porosimetry (MIP)	103
4.7. Pore Size Distribution	107
4.8. Mechanical Test Results	110
4.8.1. Compressive Strength and Modulus of Elasticity	111
4.8.2. Bending and splitting tensile strengths	113
4.8.3. Fracture Energy	114
4.8.4. Characteristic Length	119
5. EFFECT OF SIZE AND TYPE OF AGGREGATES ON AUTOGENOUS DEFORMATION AND FRACTURE PROPERTIES OF CEMENTITIOUS MATERIALS	121
5.1. General	121
5.2. Autogenous Deformation	122
5.2.1. Linear Autogenous Deformation	122
5.2.2. Volumetric Autogenous Deformation and Temperature Development	123
5.3. Heat of Hydration	126
5.4. Non-evaporable Water Content and Degree of Hydration	126
5.5. Mechanical Test Results	127

5.5.1. Compressive Strength and Modulus of Elasticity	128
5.5.2. Bending and Splitting Tensile Strengths	128
5.5.3. Fracture Energy	128
5.5.4. Characteristic Length	130
5.6. Modeling of Modulus of Elasticity	130
5.6.1. Meso-mechanical Modeling of the Modulus of Elasticity	132
5.6.1.1. Cement paste	132
5.6.1.2. Mortar	134
5.6.1.3. Concrete	135
5.7. Conclusions	136
6. MECHANISM AND MODELING OF AUTOGENOUS DEFORMATION	139
6.1. General	139
6.2. Mechanism of Shrinkage by Drying and Self-desiccation	140
6.2.1. Mechanisms of Variation of Capillary Depression	140
6.2.2. Mechanisms of Variation of Surface Tension of Colloidal Particles	142
6.2.3. Mechanisms of Variation of Disjoining Pressure	142
6.3. Modeling of Autogenous Deformation Based on its Mechanism	143
6.3.1. General Elastic Equations	144
6.3.2. Pressure applied internally	145
6.4. Estimation of Stress and Deformation due to Self-desiccation Shrinkage	147
6.5. Other Studies on Modeling of Autogenous Deformation	149
6.5.1. Modeling of Self-desiccation Shrinkage at Macroscopic Scale	149
6.5.1.1. Macroscopic stresses	150
6.5.1.2. Definition of Autogenous Deformation	150
6.5.2. A Model of Self-Desiccation in Concrete	152
6.5.3. Modeling Autogenous Deformation Based on Type of Cement	153
6.5.4. A Macro-Model for Self-desiccation in High Performance Concrete	155
6.6. Results of Modeling Self-desiccation Shrinkage of Cement Paste	158
6.7. Modeling of Autogenous Deformation of Concrete	159
6.8. Conclusion	162
7. DISTRIBUTION OF LWAS IN CEMENTITIOUS MATERIALS	163
7.1. General	163
7.2. Water Movement from LWA to the Cement Paste	163
7.3. Distribution of LWAs	165
7.3.1. Paste-Void Proximity	166
7.3.2. Void-Void Proximity	167
7.4. Application to the Internal Curing	168
7.5. Results of Image Analysis of	171
7.5.1. Concrete	171
7.5.2. Mortar	176
7.6. Comparison of Results of Image Analysis with Fracture Properties	179
7.7. Conclusion	181

8. OPTIMUM DESIGN OF CONCRETES	182
8.1. General	182
8.2. Response Surface Modeling	182
8.3. Regression Analysis	183
8.4. Optimization	189
8.5. Conclusions	195
9. CONCLUSIONS	199
REFERENCES	207
APPENDIX A	224
APPENDIX B	240
APPENDIX C	250
Curriculum Vitae	273

ABBREVIATIONS

ANOVA	:Analysis of variance
ASTM	:American Society for Testing and Materials
BFS	:Blast furnace slag
C₂S	:Dicalcium silicate
C₃A	:Calcium aluminate
C₃S	:Tricalcium silicate
C₄AF	:Ferrite
CBM	:Crack band model
CDF	:Cumulative Distribution Function
CH	:Calcium hydroxide
CMOD	:Crack Mouth Opening Displacement
CRC	:Compact reinforced composite
C-S-H	:Calcium silicate hydrate
CTOD_c	:Critical crack tip opening displacement
DIN	:Deutsches Institut für Normung
ECM	:Effective crack model
FCM	:Fictitious crack model
FLAIR	:Fine lightweight aggregates as internal reservoirs
FPZ	:Fracture process zone
GGBF	:Ground Granulated Blast Furnace
HPC	:High performance Concrete
HSC	:High strength concrete
HSC	:High strength Concrete
ITZ	:Interfacial transition zone
LEFM	:Linear elastic fracture mechanics
LVDT	:Linear Variable Displacement Transducer
LWA	:Lightweight aggregate
LWC	:Lightweight Concrete
MIP	:Mercury intrusion Porosimetry
NC	:Normal density concretes
NSC	:Normal strength concrete
OPC	:Ordinary Portland cement

PDF	:Probability Density Function
RH	:Relative humidity
RILEM	:Réunion Internationale des laboratoires d'Essais et de Recherche sur les Matériaux et les Constructions
RSM	:Response surface method
SAP	:Super absorbent polymers
SIF	:Stress intensity factor
SLWC	:Semi-lightweight concrete
SRA	:Shrinkage reducing admixtures
SSD	:Surface saturated dry
TPM	:Two parameter fracture model
UHPC	:Ultra high performance concrete

TABLES

	<u>Page No</u>
Table 2.1	Classification of pore sizes in hydrated cement paste (Jennings 1988, originally given by Mindess and Young, 1981)..... 9
Table 2.2	Applications benefited by internal curing (Roberts, 2005)..... 46
Table 3.1	Physical and chemical properties of cement..... 73
Table 3.2	Grading of aggregates used in the mixtures..... 74
Table 3.3	Densities and water absorptions of pumice LWAs..... 75
Table 3.4	Mixture codes and the change in size and volume fractions of LWAs in mixtures..... 76
Table 3.5	Compositional and some of the fresh properties of the mixtures..... 77
Table 3.6	The heat of solution (J/g) of cement paste and cement paste with 10% silica fume..... 85
Table 3.7	Summary of experimental programme..... 90
Table 4.1	Maximum temperatures and time to reach these values of paste and mortar phases..... 98
Table 4.2	The variations of non evaporable water content (water/cement + silica fume by weight) of samples with time..... 101
Table 4.3	Total intruded mercury volume and critical pore diameter of samples at different ages..... 106
Table 4.4	Total porosity of reference samples at different ages..... 106
Table 4.5	Pore size distributions of PREF, FMREF and MREF samples according to the porosity results (%)..... 108
Table 4.6	Fracture and strength properties of hardened cement paste and mortars..... 110
Table 4.7	Fracture and strength properties of concretes..... 110
Table 5.1	Mixture properties of composites..... 121
Table 5.2	The variations of non evaporable water content (water / cement + silica fume by weight) of samples with time..... 127
Table 5.3	Fracture and strength properties of hardened cement paste series with cement paste and aggregates at the age of 28 days..... 128
Table 5.4	Summary of models proposed to calculate modulus of elasticity of cementitious materials..... 131
Table 5.5	Comparison of experimental and calculated value of modulus of elasticity of composites..... 132
Table 5.6	The moduli of elasticity obtained from experiments and from meso-mechanical modeling..... 136
Table 6.1	Calculated and measured autogenous deformation for the age of 28 days, μD 161

Table 7.1	The results of Powers and Attiogbe mean spacings calculations and the image analysis of the distance of the nearest neighbor LWA-LWA proximities.....	173
Table 7.2	The results of Powers and Attiogbe mean spacings calculations and the image analysis of the distance of the nearest neighbor LWA-LWA proximities.....	177
Table 8.1	Model fitting results for each response.....	184
Table 8.2	The results of experimental and model fitting of each concrete.....	185
Table A1	Results of compressive strength and modulus of elasticity of produced cementitious materials.....	225
Table A2	Results of splitting tensile strength of produced cementitious materials.....	227
Table A3	Fracture properties of produced cementitious materials.....	228
Table B1	MIP test results of PREF (reference paste) sample at 1day, 2 and 7 days.....	241
Table B2	MIP test results of PREF sample at 28 and 100 days.....	242
Table B3	MIP test results of FMREF (reference fine mortar) sample at 1day, 28 and 100 days.....	243
Table B4	MIP test results of MREF (reference fine mortar) sample at 1day, 28 and 100 days.....	244
Table B5	MIP test results of MV10L24 (10% total aggregate content replaced by 2-4 mm LWA- mortar) sample at 1day, 28 and 100 days.....	245
Table B6	MIP test results of MV20L24 (20% total aggregate content replaced by 2-4 mm LWA- mortar) sample at 1day, 28 and 100 days.....	246
Table B7	MIP test results of MV30L24 (30% total aggregate content replaced by 2-4 mm LWA- mortar) sample at 1day, 28 and 100 days.....	247
Table C1	Image analysis results for CV10L24 series.....	252
Table C2	Image analysis results for CV20L24 series.....	254
Table C3	Image analysis results for CV30L24 series.....	257
Table C4	Image analysis results for CV10L48 series.....	260
Table C5	Image analysis results for CV20L48 series.....	262
Table C6	Image analysis results for CV30L48 series.....	264
Table C7	Image analysis results for MV10L24 series.....	266
Table C8	Image analysis results for MV20L24 series.....	268
Table C9	Image analysis results for MV30L24 series.....	270

FIGURES

	<u>Page No</u>
Figure 2.1 : View of the microstructure of a 100-day old cement paste (w/c 0.30) cured at room temperature (Diamond, 2004).....	8
Figure 2.2 : Typical BSE image of a Portland cement mortar (200 days old, water/cement=0.4), with the microstructural constituents distinguished (Scrivener, 2004).....	10
Figure 2.3 : Volumetric autogenous deformation and temperature versus time of cement paste with 10% silica fume.....	16
Figure 2.4 : One-dimensional autogenous deformations vs. age diagram of cement pastes with various w/c at T=20 °C (Baroghel-Bouny et al., 2006).....	18
Figure 2.5 : Correlation between the autogenous deformation and the internal RH of cement paste with the w/c=0.34 at the age of 28 days (Baroghel-Bouny, 1997).....	19
Figure 2.6 : Autogenous deformation of Portland cement paste as a function of internal relative humidity (Lura, 2003).....	19
Figure 2.7 : Influence of cement composition on autogenous deformation of cement paste (Miyazawa and Tazawa, 2005).....	20
Figure 2.8 : Effect of cement fineness on autogenous deformation of cement pastes (with w/c of 0.35) (Bentz et al., 2001b).....	21
Figure 2.9 : Effect of supplementary materials (SFsilica fume; FAfly ash; GGBground granulated blast furnace slag) on autogenous deformation (Pane and Hansen, 2002).....	22
Figure 2.10 : Autogenous deformation of two different cement paste containing 0%, 5% and 10% silica fume (Zhang et. al, 2003).....	23
Figure 2.11 : Autogenous deformation increased when the replacement of fly ash was 25%. However, when the replacement ratio reached 50%, the autogenous shrinkage had become remarkably small (Termkhajornkita, 2005).....	24
Figure 2.12 : Autogenous deformation of concrete with different BFS content (Lee et al., 2006).....	26
Figure 2.13 : Effect of metakaolin on the 200-day total autogenous deformation measured from the initial set ((Brooks and Megat Johari, 2001).....	27
Figure 2.14 : Effect of type and dosage of superplasticizer on autogenous deformation of cement paste (Tazawa and Miyazawa, 1995).....	28

Figure 2.15	: Autogenous deformation of Portland cement paste cured at different temperatures (Lura, 2003).....	29
Figure 2.16	: 6-months RH with low-alkali cement and RH with normal-alkali cement with 5% silica fume (Persson, 2005).....	31
Figure 2.17	: Effect of specimen size on autogenous deformation of concrete with the water to cementitious materials ratio of 0.30 (Han and Han, 2005).....	32
Figure 2.18	: Volumetric autogenous deformation vs. chemical shrinkage (Barcelo et al., 1999).....	36
Figure 2.19	: Effectiveness of SRA on reducing autogenous deformation of concrete. The last number of each series indicates the content of SRA (kg/m ³) in mixtures (Tanimura et al., 2005).....	38
Figure 2.20	: Effectiveness of expansive additives on reducing autogenous deformation of concrete. The first number of each series indicates the content of expansive additive (kg/m ³).....	39
Figure 2.21	: Schematic representation of the pore size distribution (Koenders and van Bruegel, 1997).....	40
Figure 2.22	: Autogenous deformation from setting of cement pastes (w/c=0.3) with different amounts of SAPs (Jensen and Hansen, 2002).....	42
Figure 2.23	: Autogenous deformation of VC (concrete with normal aggregate) and CFRC (concrete with recycled aggregate). Sealing is removed after 28 days (Maruyama and Sato, 2005).....	43
Figure 2.24	: Autogenous deformation of cement paste with wood powder (Mohr et al., 2005).....	44
Figure 2.25	: Autogenous deformation variation with time for mixes with (SF) and without fibers (SNF) at different times of the experimental study(a)0–24 h, (b)up to 75 days (Farhat et al., 2007).....	45
Figure 2.26	: Desorption isotherms of pumice fractions at 25 °C from vacuum-saturated conditions (Lura, 2003).....	47
Figure 2.27	: Volumetric phase composition of cement paste as function of the degree of hydration with w/c=0.30 (a) and with entraining water at w/c = 0.30 + 0.05 (b). Due to the low w/c ratio, full hydration of the cement cannot be obtained (Jensen and Hansen, 2001b)....	50
Figure 2.28	: Entrained w/c ratio necessary to avoid self-desiccation as a function of w/c ratio for different sf/c ratios (Lura, 2003).....	51
Figure 2.29	: Stress flow lines in thin sheet subjected to axial tensile loading, (a) an uncracked plate; (b) a cracked sheet (Karihaloo, 1995).....	55
Figure 2.30	: Fundamental crack modes (Karihaloo, 1995).....	56
Figure 2.31	: An infinite elastic body with a sharp crack length of 2a under mode I loading.....	57
Figure 2.32	: Barenblatt's cohesive crack model in mode I. Note $c \ll a$	59
Figure 2.33	: Typical load-deformation response of quasi-brittle materials in tension/flexure (a) and the fracture process zone ahead of the real traction-free crack (b) (Karihaloo, 1995).....	60

Figure 2.34	: Main differences between materials modeling with linear elastic fracture mechanics (a), non-linear plastic fracture mechanics ((Dugdale 1959)) (b) and non-linear quasi-brittle fracture mechanics (c). Linear elastic material is denoted with an L, non-linear material behavior with an N, while fracture behavior is denoted by F (Karihaloo 1995).....	61
Figure 2.35	: Fictitious crack behind the real traction-free crack (Karihaloo, 1995).....	62
Figure 2.36	: Crack band model for fracture of concrete (a) a microcrack band fracture and (b) stress-strain curve for the microcrack band proposed by Bazant and Oh, 1983 (from Shah, et al., 1995).....	63
Figure 2.37	: Compressive strength (a) and modulus of elasticity (b) in relation with the dry density (Wille and Dehn, 2003).....	66
Figure 2.38	: Typical results of stress-strain curves of concretes in compression (Tasdemir et al., 2002).....	67
Figure 2.39	: Stress-strain curve of an ALWA (all LWAs as defined by the author) concrete compares with NC-normal concrete of similar strength (Faust, 1997).....	67
Figure 2.40	: Some toughening mechanisms in fracture process zone(a) crack shielding; (b) crack deflection; (c) aggregate bridging; (d) crack surface roughness-induced closure; (e) crack tip blunted by void; (f) crack branching (Shah et al., 1995).....	69
Figure 2.41	: Characteristic length in relation to the type of LWA and to the fracture energy (Chang and Shieh, 1996).....	70
Figure 2.42	: Typical results of load-displacement curves obtained from for point bending test (Tasdemir et al., 2002).....	71
Figure 2.43	: Effect of compressive strength of concrete on the fracture energy. The series A and B have different aggregate grading curves (Tasdemir et al., 2002).....	71
Figure 3.1	: General appearance of used normal aggregates. From left to right; crushed stone, natural sand, siliceous powder and the binder of silica fume.....	73
Figure 3.2	: Grading curves of aggregate mixtures and standard curves.....	74
Figure 3.3	: General appearance of used lightweight aggregates. From left to right; 4-8 mm and 2-4 mm size fractions.....	75
Figure 3.4	: Linear autogenous deformation test set up for concrete specimens.....	79
Figure 3.5	: Test setups of volumetric autogenous deformation and temperature measurement in adiabatic condition.....	81
Figure 3.6	: Effect of silica fume content on heat of hydration (Sanchez de Rojas and Frias 1996).....	84
Figure 3.7	: Schematic representation of the three point bending test and the calculation of area under load versus displacement curve.....	89
Figure 4.1	: Linear autogenous deformation versus time diagrams of reference samples.....	92

Figure 4.2	: Effect of LWAs on linear autogenous deformation of mortar specimens.....	93
Figure 4.3	: Linear autogenous deformation of concrete samples.....	94
Figure 4.4	: Volumetric autogenous deformation of two reference paste samples.....	95
Figure 4.5	: Volumetric autogenous deformation and temperature development of paste and mortar phases.....	97
Figure 4.6	: Chemical shrinkage and volumetric autogenous deformation of PREF sample.....	99
Figure 4.7	: Chemical shrinkage and volumetric autogenous deformation of PREF sample.....	99
Figure 4.8	: The variations heat of hydration in time for reference cement paste, fine mortar, and coarse mortar samples.....	100
Figure 4.9	: Effect of LWAs on heat of hydration of mortars.....	101
Figure 4.10	: Effect of LWAs on degree of hydration of mortars.....	102
Figure 4.11	: Development of the degree of hydration in an adiabatical system (Mönnig, 2003).....	102
Figure 4.12	: The variations of cumulative introduced mercury volume (a) and critical pore diameter (b) of PREF sample at 1, 2, 7, 28 and 100 days of ages.....	103
Figure 4.13	: The variations of critical pore diameters of FMREF, MREF, MV10L24, MV20L24 and MV30L24 samples at 1, 28 and 100 days, respectively.....	104
Figure 4.14	: Partial porosity distributions of MV10L24, MV20L24, and MV30L24 series at the ages of 28 and 100 days.....	109
Figure 4.15	: The distribution of very fine, fine capillary, large capillary and large pores in total porosity of mortars with LWA.....	109
Figure 4.16	: Compressive strength (a) and modulus of elasticity (b) of reference cement paste (PREF), fine mortar (FMREF), coarse mortar (MREF) and concrete (CREF) without any LWAs.....	111
Figure 4.17	: Stress-strain curve of reference cement paste, fine mortar, coarse mortar and concrete for determining the modulus of elasticity ($\sigma < 0.33 f'_c$).....	112
Figure 4.18	: The model proposed for the strength of lightweight aggregate concrete.....	113
Figure 4.19	: The bending and splitting tensile strength of reference cement paste, fine mortar, coarse mortar, and concrete phases.....	114
Figure 4.20	: Typical load versus displacement curves for reference cement paste, fine mortar, coarse mortar, and concrete phases.....	115
Figure 4.21	: Typical load versus displacement curves for concretes contained (a) fine LWAs with the size fraction of 2-4 mm; (b) coarse LWAs with the size fraction of 4-8 mm. The results were obtained by three point bending test.....	116
Figure 4.22	: Effect of the size of used LWAs on load vs. disp. curves for concrete in which the normal aggregate was replaced by LWAs with volume replacement ratios of (a) 10% and (b) 30%.....	117

Figure 4.23	: Typical load displacement curves for reference mortar and mortars with LWAs obtained from three point bending test.....	118
Figure 4.24	: Final displacements at midspan for the concrete samples.....	119
Figure 4.25	: Effect of the size of LWA on both fracture energy and characteristic length (the values shown with arrow represent the linear autogenous deformation at the 28 days of age of concrete).	120
Figure 5.1	: Effect of size and type of aggregate on linear autogenous deformation of composites until the age of 28 days (a) and 360days (b).....	122
Figure 5.2	: Volumetric autogenous deformation (a) and temperature development (b) of paste and mortar phases.....	124
Figure 5.3	: Volumetric autogenous deformation versus time diagram for plain cement paste, cement paste with expanded clays samples and paste containing paraffin coated expanded clay.....	125
Figure 5.4	: Effect of size of LWAs on heat of hydration of composites.....	126
Figure 5.5	: Effect of size of LWAs on degree of hydration of paste.....	127
Figure 5.6	: Typical load displacement curves for reference cement paste and composites of paste and aggregates.....	129
Figure 6.1	: The model used for calculation (MacKenzie, 1950).....	143
Figure 6.2	: Measured and calculated autogenous deformation of Portland cement paste ($w/c=0.37+5\%sf$) vs. internal relative humidity (Lura, 2003).....	149
Figure 6.3	: Comparison of theoretical and experimental results autogenous deformation of cement paste with $w/c=0.42$ (adopted from Hua et al., 1995). Note that in this modeling, autogenous deformation is considered as self-desiccation shrinkage.....	152
Figure 6.4	: (a) Comparison of models of autogenous deformation of concrete, (b) Autogenous deformation vs. time diagram of concrete with the w/c of 0.3 where the observed value at the age of 91 days is taken to be 1.0 (Miyazawa and Tazawa, 2005).....	155
Figure 6.5	: The self-desiccation in high performance concrete, in principle (Nilsson and Mjörnell, 2005).....	156
Figure 6.6	: Comparison of theoretical and experimental results autogenous deformation of cement paste with $w/c=0.42$ (adopted from Hua et al., 1995). Note that in this modeling, autogenous deformation is considered as self-desiccation shrinkage.....	157
Figure 6.7	: Flow chart for calculation of self-desiccation shrinkage of cement paste and concrete.....	158
Figure 6.8	: Comparison of experimental and calculated autogenous deformations for cement paste.....	159
Figure 6.9	: Comparison of experimental and calculated results autogenous deformation of series of PN0-2, PN2-4, and PN4-8.....	161
Figure 6.10	: Comparison of experimental and calculated results	162
Figure 7.1	: (a) Expanded clays saturated with concrete colored pigment; (b) water flow from LWA to cement paste; (c) optical image of LWA including cement paste.....	164

Figure 7.2	: An idealized representation of a spacing cumulative distribution function (CDF) and the associated probability density function (PDF) for some distance s . The dashed lines demonstrate how to determine the 50th and the 95th percentiles from CDF data (Snyder, 1998).....	166
Figure 7.3	: (a) Real image of concrete, (b) LWAs in binary image of concrete, (c) fitting ellipses of LWAs. It is shown that there is only very small amount of particles with circle geometries.....	169
Figure 7.4	: Calculation steps of nearest distance of LWA-LWA surfaces.....	170
Figure 7.5	: (a) The cumulative distribution function (CDF) and (b) the probability distribution function (PDF) for the 838 nearest neighbor LWA-LWA proximities.....	172
Figure 7.6	: Comparison of the results of 95th percentile of the nearest neighbor LWA-LWA proximity distribution with the Attiogbe spacing factor s_2 for the mortars with fine and coarse LWAs.....	173
Figure 7.7	: Comparison of the results of 95th percentile of the nearest neighbor LWA-LWA proximity distribution with the autogenous deformation of concretes with LWAs at the age of 28 days.....	174
Figure 7.8	: Fraction of paste within distance from the LWA.....	175
Figure 7.9	: Comparison of the mitigation ratio of autogenous deformation according to the reference concrete with the protected paste volume calculated with the water travel distance of 1 mm.....	175
Figure 7.10	: (a) The cumulative distribution function (CDF) and (b) the probability distribution function (PDF) for the 623 nearest neighbor LWA-LWA proximities.....	176
Figure 7.11	: Comparison of the results of 95th percentile of the nearest neighbor LWA-LWA proximity distribution with the autogenous deformation of mortars with LWAs at the age of 28 days.....	178
Figure 7.12	: Fraction of paste within distance from the LWA.....	178
Figure 7.13	: Comparison of the mitigation ratio of autogenous deformation according to the reference mortar with the protected paste volume calculated with the water travel distance of 1 mm.....	179
Figure 7.14	: Comparison of the fracture energy and characteristic length of mortars with the 95th percentile of the nearest neighbor LWA-LWA proximity distribution.....	179
Figure 7.15	: Comparison of the fracture energy of mortars with the 95th percentile of the nearest neighbor LWA-LWA proximity distribution.....	180
Figure 7.16	: Comparison of the fracture energy and characteristic length of concretes with the 95th percentile of the nearest neighbor LWA-LWA proximity distribution.....	180
Figure 8.1	: The variation of compressive strength f_c with volume and size of LWAs.....	185

Figure 8.2	: The variation of modulus of elasticity E with volume and size of LWAs.....	186
Figure 8.3	: The variation of fracture energy G_F with volume and size of LWAs.....	186
Figure 8.4	: The variation of characteristic length l_{ch} with volume and size of LWAs.....	187
Figure 8.5	: The variation of splitting tensile strength f_{st} with volume and size of LWAs.....	187
Figure 8.6	: The variation of net bending strength f_{net} with volume and size of LWAs.....	188
Figure 8.7	: The variation of the value of the mitigation ratio of autogenous deformation according to the CREF series at 28 days of age with volume and size of LWAs.....	188
Figure 8.8	: Response surface plot of the composite desirability (D) when the mitigation ratio of autogenous deformation and f_c are maximized simultaneously.....	191
Figure 8.9	: Response surface plot of the composite desirability (D) when l_{ch} , f_{st} , and f_{net} are maximized simultaneously.....	192
Figure 8.10	: (a) Response surface and contour plot of the composite desirability (D) when the mitigation ratio of autogenous deformation, l_{ch} , f_{st} , and f_c are maximized simultaneously.....	193
Figure 8.11	: Response surface plot of the composite desirability (D) when mitigation of autogenous deformation (with $w_{tj} = 2$), l_{ch} , f_{st} , and f_c are maximized simultaneously.....	194
Figure 8.12	: Response surface plot of the composite desirability (D) when autogenous deformation is minimum (with $w_{tj} = 10$), l_{ch} , f_{st} , and f_c are maximized simultaneously.....	195
Figure A1	: Load displacement diagram for PREF samples.....	231
Figure A2	: Load displacement diagram for FMREF samples.....	231
Figure A3	: Load displacement diagram for MREF samples.....	232
Figure A4	: Load displacement diagram for MV10L24 samples.....	232
Figure A5	: Load displacement diagram for MV20L24 samples.....	233
Figure A6	: Load displacement diagram for MV30L24 samples.....	233
Figure A7	: Load displacement diagram for CREF samples.....	234
Figure A8	: Load displacement diagram for CV10L24 samples.....	234
Figure A9	: Load displacement diagram for CV20L24 samples.....	235
Figure A10	: Load displacement diagram for CV30L24 samples.....	235
Figure A11	: Load displacement diagram for CV10L48 samples.....	236
Figure A12	: Load displacement diagram for CV20L48 samples.....	236
Figure A13	: Load displacement diagram for CV30L48 samples.....	237
Figure A14	: Load displacement diagram for PN0-2 samples.....	237
Figure A15	: Load displacement diagram for PN2-4 samples.....	238
Figure A16	: Load displacement diagram for PN4-8 samples.....	238
Figure A17	: Load displacement diagram for PL2-4 samples.....	239

Figure A18	: Load displacement diagram for PL4-8 samples.....	239
Figure B1.	: The variations of cumulative introduced mercury volume of FMREF, MREF and MV10L24samples at 1, 28 and 100 days of ages, respectively.....	248
Figure B2.	: The variations of cumulative introduced mercury volume of MV20L24 and MV30L24 samples at 1, 28 and 100 days of ages, respectively.....	249
Figure C1.	: a) Image of CV10L24, b) selected pumices in binary image of CV10L24, c) ellipses mask, d) surface of pumices and (e) plot drawing of CV10L24	251
Figure C2.	: a) Image of CV20L24, b) selected pumices in binary image of CV20L24, c) ellipses mask, d) surface of pumices and (e) plot drawing of CV20L24.....	253
Figure C3.	: a) Image of CV30L24, b) selected pumices in binary image of CV30L24, c) ellipses mask, d) surface of pumices and (e) plot drawing of CV30L24.....	256
Figure C4.	: a) Image of CV10L48, b) selected pumices in binary image of CV10L48, c) ellipses mask, d) surface of pumices and (e) plot drawing of CV10L48.....	259
Figure C5.	: a) Image of CV20L48, b) selected pumices in binary image of CV20L48, c) ellipses mask, d) surface of pumices and (e) plot drawing of CV20L48.....	261
Figure C6.	: a) Image of CV130L48, b) selected pumices in binary image of CV30L48, c) ellipses mask, d) surface of pumices and (e) plot drawing of CV30L48.....	263
Figure C7.	: a) Image of MV10L24, b) selected pumices in binary image of MV10L24, c) ellipses mask, d) surface of pumices and (e) plot drawing of MV10L24.....	265
Figure C8.	: a) Image of MV20L24, b) selected pumices in binary image of MV20L24, c) ellipses mask, d) surface of pumices and (e) plot drawing of MV20L24.....	267
Figure C9.	: a) Image of MV30L24, b) selected pumices in binary image of MV30L24, c) ellipses mask, d) surface of pumices and (e) plot drawing of MV30L24.....	270

SYMBOLS

a	:crack length (mm)
A	:surface area (m ²)
a/W	:notch/depth ratio
a_{beam}	:notch depth of the beam (mm)
A_c	:aspect ratio of coarse aggregate
A_f	:aspect ratio of fine aggregate
a_h	:radius of pore (mm)
A_v	:lightweight aggregate volume fraction,
B	Width of the beam (mm)
C	:cement content (kg/m ³)
C_c	:heat capacity (kJ/ ⁰ C)
C_f	:cement content of mixture (kg/m ³)
CS	:chemical shrinkage (kg water/ kg cement hydrated)
D	:single composite response
d_{avr}	:average size fraction of lightweight aggregate
d_j	:desirability function
e_c	:shrinkage of concrete (μD)
e_p	:shrinkage of paste (μD)
e_r(t)	:linear autogenous shrinkage of the material (μD)
E	:modulus of elasticity (MPa)
E_{agg}	:modulus of elasticity of aggregate (GPa)
E_c	:modulus of elasticity of concrete (GPa)
E_{coarse}	:modules of elasticity of coarse aggregate (GPa)
E_m	:modulus of elasticity of matrix phases (GPa)
E_p	:modulus of elasticity of aggregate phases (GPa)
E_r	:modulus of elasticity of mortar (GPa)
E_t	:strain-softening modulus (GPa)
f'_c	:compressive strength (MPa)
f_{ck}	:characteristic compressive strength at 28 days (MPa)
f_j	:actual (experimental) values of j _{th} response
f_{net}	:net bending strength (MPa)
f_{st}	:splitting tensile strength (MPa)
f_t	:tensile strength (MPa)
f'_t	:direct tensile strength (MPa)
F_v	:fraction of the total paste volume within distance of
g	:gravitational acceleration (9.81 m/s ²)
G	:Gibbs energy (J/mol)

G_c	:critical Griffith surface energy density or critical energy release rate
G_F	:fracture energy (N/m)
G_f	:size-dependent fracture energy (N/m)
g_f	:local fracture energy (N/m)
h	:height of fluid pipe (mm)
H_1	:heat of solution of dry cement (kJ/kg)
H_2	:heat of solution of partially hydrated sample (kJ/kg)
h_b	:crack width (mm)
h_d	:height of disc specimen (mm)
$J^d(t,t')$:deviatoric component of creep function of cement paste
$J_{ijkl}(t,t')$:creep function of cement paste
$J^v(t,t')$:volumetric component of creep function of cement paste
k_1	:coefficient
K_I	:stress intensity factor ($MPa\sqrt{m}$)
K_{Ic}	:fracture toughness ($MPa\sqrt{m}$)
K_s	:bulk modulus of the solid material (MPa)
k_{wg}	:amount of water in the gel at saturation and complete hydration (m^3/m^3)
L	:length of the beam (mm)
l_{ch}	:characteristic length (mm)
m	:mass of the beam (mm)
n	:ratio of modulus of elasticity of the discrete phase to the continuous phase
n_p	:number of pores per unit volume
\emptyset	:diameter of disc specimen (mm)
P	:hydrostatic pressure (Pa)
p_p	:pressure in the pores (Pa)
p	:initial porosity
$p_c(t)$:capillary stress as a function of the time (MPa)
p_{hg}	:pressure caused by mercury penetration (MPa)
P_{max}	:peak load in three point bending test (kN)
P^0	:gas pressure of planar surface (Pa)
p_v	:paste volume fraction
q	:heat energy (joules)
Θ	:geometric function for discrete phase
θ_0	:calorimeter temperature when the sample was introduced ($^{\circ}C$)
θ_{20}	:calorimeter temperature at the end of the solution period ($^{\circ}C$)
θ_{40}	:calorimeter temperature at the end of the rating period ($^{\circ}C$)
r	:distance from the crack tip (mm)
r_{cap}	:radius of capillarity (mm)
R	:ideal gaseous constant (8.314 J/(mol.K))
r_0	:radius of spherical shell of real material (mm)
R_0	:observed temperature rise in calorimeter ($^{\circ}C$)
R_1	:corrected temperature rise in calorimeter ($^{\circ}C$)
ρ_{agg}	:particle density of aggregate (kg/m^3)
ρ_c	:density of cement (kg/m^3)
ρ_w	:density of water (kg/m^3)

RH_K	:relative humidity due to the menisci formation (%)
RH_s	:relative humidity due to dissolved salts (%)
S	:saturation of LWA or saturation factor (m ³ water/m ³ pore)
s	:coefficient of cement type
S_{beam}	:span of the beam (mm)
S_e	:enthalpy (joules/Kelvin)
sf	:silica fume
sf/c	:silica fume/cement ratio
\bar{s}_1 and \bar{s}_2	:Attiogbe spacing factors (mm)
T	:temperature (K)
t	:time
t₀	:initial setting time
t_d	:final calorimeter temperature (°C)
t_h	:final calorimeter temperature of partially hydrated cement (°C)
t_o	:time of mercury penetration
U	:internal energy (joules)
V	:volume fraction of the discrete phase (m ³ /m ³)
V_{agg}	:volume fraction of aggregates (m ³ /m ³)
V_{cs}(α)	:chemical shrinkage (m ³ /m ³)
V_{cw}(α)	:capillary water (m ³ /m ³)
V_{ew}	:evaporable water content (m ³ /m ³)
V_f	:volume fraction of lightweight aggregate (m ³ /m ³)
V_{gw}(α)	:gel water (m ³ /m ³)
V_lX_g	volume of the liquid part in V(X _g) (m ³)
V_m	:molar volume of fluid
V_p	:total pore volume (m ³ /m ³)
V_s	:volume fraction of fine aggregate (m ³ /m ³)
V_s(X_g)	volume of the solid part in V(X _g) (m ³)
V_{wat}	:volume of water entrained in the LWA (m ³)
w	:work to change the system (joules)
W_i	:initial water content (kg/m ³)
W	:depth of the beam (mm)
w/c	:water/cement ratio
w/cm	:water/cementitious materials ratio
(w/c)_e	:amount of entrained water (kg water/ kg cement)
w₀	:mixing water (kg/m ³)
W₀	:area under the load vs. displacement curve (Nm)
w_c	:critical crack opening (mm)
w_e(j)	:moisture content (%)
W_i	:mass of sample on ignited basis (g)
w_n	:nonevaporable moisture content (g water/ g cement)
wt_j	:weighting factor of the j _{th} response
X_l	:molar fraction of water in the pore fluid
X_g and y_l	:global and local variables (vectors)
x_k	:independent design variable

Y_j	:fitted value
α	:degree of hydration
α_c	:degree of reaction of the cement
α_{\max}	:maximum degree of hydration
α_s	:degree of reaction of the silica fume
α_v	:specific surface area of lightweight aggregates (mm^2)
β	:surface area of the debonded coarse aggregate
$\beta_a(t)$:coefficient for development of autogenous deformation with time
γ	:surface energy density (N/m)
γ_p	:energy used for plastic deformation (N/m)
δ_0	:specified deflection of the beam (mm)
$\Delta V(t_0)$:gaseous volume of an unsaturated porous material
$\varepsilon_{co}(w/c)$:ultimate autogenous deformation (μD)
$\varepsilon_p(t)$:autogenous deformation of cement paste at age t (μD)
η	:efficiency factor for water release of LWA
η_c	:shape factor of coarse aggregate
η_f	:shape factor of fine aggregate
η_k	:shape factor of capillary pore
η_u	:shape factor of an unhydrated cement particle
θ	:contact angle between water and solid
θ_{Hg}	:wetting angles for mercury
θ_w	:wetting angles for water
λ and μ	:Lame's constants
μ_c	:chemical potential (joules/molecule)
μ_{planar}	:chemical potential in planar surface (joules/molecule)
ν	:Poisson ratio
ν_{agg}	:Poisson's ratios of the aggregates
ν_c	:Poisson's ratios of the concrete
ρ	:relative density (kg/m^3)
ρ_l	:density of fluid (kg/m^3)
ρ_w	:density of water (kg/m^3)
σ	:stress (MPa)
σ_c	:critical stress (MPa)
σ_{cap}	:capillary stress in the pores (MPa)
ϕ_{LWA}	:porosity of LWA (m^3/m^3)
$\sum_{ij}^s (X_g)$:macroscopic stress of skeleton (MPa)
$\sigma_{ij}(y_l)$:real stress at microscopic level (MPa)
$V(X_g)$:representative elementary volume (m^3)
$\sum^s t'$:macroscopic compression of the solid skeleton (μD)
$\sum^s \delta_{ij}$:spherical internal stress due to the capillary depression (MPa)

EFFECTS OF LIGHTWEIGHT AGGREGATES ON AUTOGENOUS DEFORMATION AND FRACTURE OF HIGH PERFORMANCE CONCRETE

SUMMARY

Since high strength/high performance concretes (HS/HPCs) are produced using rich mixes with high cement content, low water/cement ratio, and silica fume, the material becomes very dense and more homogeneous than normal strength concrete. However, these properties cause significant increase in brittleness of hardened concrete and change of volume during the hardening of these materials. Early age autogenous deformations and self-desiccation are usually considered major problems in new generation HS/HPCs.

In order to mitigate the effects of early age autogenous deformation, dispersed saturated lightweight aggregates (LWAs) can be used as water reservoirs. In this study, experiments were conducted to determine the effects of volume fractions and the size of saturated pumice LWAs on fracture and mechanical properties of cementitious materials. For this purpose, in concretes with a constant low water/cement ratio, normal aggregates have been replaced by natural LWAs with size fractions of 2-4 mm or 4-8 mm at three different volume fractions such as 10%, 20% and 30% of the total aggregate volume of concrete. In addition, coarse mortar, fine mortar, and paste phases of concretes were produced. The effects of volume fraction and average particle size of LWAs on the load-displacement at mid-span curve were investigated by measuring the fracture energy, the characteristic length and final displacement. The nearest surface distribution of LWAs was also investigated using the image analysis, and its effects on the autogenous deformation and the fracture properties were determined.

The results imply that the inclusion of fine fraction of LWAs in concrete reduces the autogenous deformation significantly compared to that of the coarse fraction. It is also shown that the fracture energy, final displacement at the mid-span curve of the beam, splitting tensile strength and compressive strength of concrete with fine fraction are higher than those of the concrete with coarse fraction. It is demonstrated that the distance between LWAs is more effective than the mean particle size of LWAs on both the autogenous deformation and fracture properties of concretes. Increasing the replacement ratio of LWAs mitigates autogenous deformation, while having an unfavorable effect on fracture and mechanical properties of concrete for both fine and coarse fraction replacements. A multi-objective simultaneous optimization technique, in which Response Surface Method (RSM) was incorporated, was used to obtain a concrete with maximum fracture energy, characteristic length, compressive strength and minimum autogenous deformation.

HAFİF AGREGALARIN YÜKSEK PERFORMANSLI BETONLARIN OTOJEN DEFORMASYON VE KIRILMASINA ETKİLERİ

ÖZET

Yüksek dayanımlı/yüksek performanslı betonlar; yüksek çimento miktarı, düşük su/çimento oranı ve silis dumanı içeren zengin karışımlar kullanılarak üretildiklerinden, normal dayanımlı betona göre çok daha yoğun ve homojen malzemelerdir. Buna karşın, belirtilen özellikler malzemelerin gevrekliğinde ve sertleşmesi sırasında oluşan hacim değişikliklerinde önemli artışlara neden olmaktadır. Yeni kuşak yüksek dayanımlı/yüksek performanslı betonların en önemli sakıncaları ise erken yaş otojen deformasyon ve kendiliğinden kurumadır.

Erken yaşlardaki otojen deformasyonu önlemek için suya doygun hale getirilmiş hafif agregalar su rezervuarı olarak kullanılabilir. Bu çalışmada, suya doyurulmuş ponza taşlarının hacim ve tane boyutunun çimentolu malzemelerin kırılma ve mekanik özelliklerine etkisini belirleyen deneyler yapılmıştır. Bu amaçla, hazırlanan düşük su/çimento oranlı betonların normal agregalarının 2-4 veya 4-8 mm tane boyutlu bölümleri, %10, %20 ve %30 oranında doğal hafif agrega ile yer değiştirilmiştir. Bunun yanı sıra, betonların kaba harç, ince harç ve hamur fazları da üretilmiştir. Kullanılan hafif agreganın tane boyutunun ve hacim oranının, açıklık ortasında kaydedilen yük-şekil değiştirme eğrisine etkisi kırılma enerjisi, karakteristik boy ve en son deplasman ölçülerek incelenmiştir. Hafif agregaların en yakın yüzey komşulukları imaj analizi yapılarak incelenmiş ve bu büyüklüklerin otojen deformasyon ile kırılma parametrelerine etkileri belirlenmiştir.

Sonuçlar, ince hafif agrega kullanımının iri hafif agregaya göre belirgin şekilde otojen deformasyonu azalttığını göstermektedir. Aynı zamanda, ince hafif agregalı betonların kırılma enerjisi, kırışın açıklık ortasında ölçülen son deplasman değeri, yarılmada çekme dayanımı ve basınç dayanımının iri hafif agregalı betonlarınkine kıyasla daha yüksek olduğu görülmektedir. Hafif agregalar arasındaki mesafenin kırılma enerjisi ve otojen deformasyon üzerinde ortalama tane boyutundan daha etkili olduğu anlaşılmaktadır. Hafif agregaların normal agrega ile yer değişim oranı arttıkça otojen deformasyon azalırken, her iki hafif agrega bölümünün kullanımında betonların kırılma ve mekanik özelliklerinde azalmalar oluşmuştur. Kırılma enerjisi, karakteristik boy ve basınç dayanımı en büyük, otojen deformasyonu en düşük betonu elde etmek için Tepki Yüzey Yöntemi içeren çok amaçlı eşzamanlı optimizasyon tekniği kullanılmıştır.

1. INTRODUCTION

1.1 General

In recent decades, there has been increasing recognition of importance of examining the relationship between curing, shrinkage and cracking with the extensive usage of high performance concrete (HPC). Since high performance/ultra high performance concretes (HP/UHPCs) are produced using rich mixes with high cement content and low water/cement ratio, the material becomes very dense and more homogeneous than normal strength concrete. The most important properties of these concretes are low porosity and non-connected capillary pore structures. There will be insufficient amount of water in concrete to complete the hydration process, and also the water ingress will be prevented because of the impermeable character of concrete (Weber and Reinhardt, 1997 and Tasdemir et al., 2002). Thus, high strength concrete (HSC) may exhibit a substantial autogenous deformation at the early stages of hardening. With the formation of hydrates, after de-moulding (also before) time dependent volume changes of cement paste begin to take place (Sadouki and Wittmann, 2001). Development of the empty pores due to chemical shrinkage is the main reason for diminishing the radius of meniscus. Such a decrease causes the self-desiccation by increasing capillary stress in the pore water. Autogenous deformation occurs because of the self desiccation and water consumption by the cement hydration under closed system (i.e. no moisture loss) without temperature change. The absorption of free water in pores by the hydrates and formation of fine pores is driven by the chemical shrinkage. In later ages, however, self desiccation becomes the major drive mechanism. Development of empty pores continues concurrently with self-desiccation affecting also the hydration kinetics. This effect limits the ultimate degree of hydration and consequently the strength of cement paste. Conventional curing techniques are not effective in mitigating this decrease of relative humidity (RH) in cement paste (Tazawa, 1999; Lura et al., 2004; Akcay and Tasdemir, 2005). Using the pre-soaked fine lightweight aggregate (LWA) for preventing the

decrease of RH was first recommended by Philleo (1991). Later development of the technique was discussed by a number of authors (Bentur and Snyder, 1999; Bentur et al., 2001). Previous studies showed that lightweight aggregate and matrix are bonded stronger than normal aggregate (Sarkar et al., 1992; Swamy and Lixian, 1995). This enhanced interfacial zone prevents the length changes developed under RH and/or thermal conditions (Kayali et al., 1999).

In application, concrete is usually designed on the basis of compressive strength theory, in which the brittleness of concrete is ignored. For this reason, fracture parameters of concrete have to be defined along with its brittleness. In reality, concrete is always subject to crack development under the influence of shrinkage for instance. This makes the influence of crack size an important factor on concrete fracture (Hu and Wittmann, 2000). Since the tensile strain capacity of concrete at early ages is not sufficient enough to resist stresses caused by the external and internal restraints, autogenous deformation leads to the formation of cracks. These early age cracks may induce durability problems. Because the LWAs produce more microcracks, the concrete containing these aggregates behaves in a more ductile manner (i.e. less brittle) than normal cementitious materials (Tasdemir et al., 2002 and Akcay et al., 2005). On the other hand, the use of LWA instead of dense aggregate is expected to result in a lower strength. It is obvious that the amount of LWA for internal curing must be optimized according to the mechanical and fracture properties of cementitious materials.

1.2 Research Objectives

The main objectives of this thesis are:

- To investigate the autogenous deformations of cement paste, fine mortar, coarse mortar and concrete in detail.
- To determine the effect of size and volume of LWAs on autogenous deformation, heat of hydration, degree of hydration, and pore size distribution of cementitious materials.
- To investigate the fracture and mechanical characteristic of cementitious materials both with and without LWA.

- To evaluate the effect of size and type of aggregates on autogenous deformation and fracture properties of cement paste.
- To compare the results with the known mechanisms and modeling of the autogenous deformation.
- To investigate the effect of LWA-LWA proximity (obtained from image analysis) on the autogenous deformation and fracture properties of mortars and concretes.
- To optimize the size and volume of LWA for preventing autogenous deformation taking into consideration the fracture properties of concrete.

1.3 Organization of Content

The thesis comprises nine chapters

Chapter 1 gives an introduction to the subject matter of the investigation, research objectives, and organization of the thesis' content.

Chapter 2 presents a literature review related to the subject of the thesis. It gives brief information about the hydration and microstructure of cement paste and describes the autogenous deformation in terms of terminology, development stages, effecting factors, and methods of measurement. The chapter also gives a literature review on the mitigation methods of autogenous deformation. The last part of the chapter further deals with the fracture mechanics of cement based materials and discusses the fracture mechanics of concretes with LWAs.

Chapter 3 presents the experimental details used during the course of this study. The materials, mix proportion, mixing and placing procedure are explained in detail. Experimental procedures conducted to define the linear autogenous deformation, volumetric autogenous deformation, temperature development, chemical shrinkage, heat of hydration, non-evaporable water content, and degree of hydration are described along with the mercury intrusion porosimetry test, mechanical test, and fracture test (according to the RILEM recommendations). A summary of experimental programme is also appended at the end of this chapter.

Chapter 4 presents the results of experimental studies. Each result of experiments starts with presenting the results of test series without LWAs, and continues with the series with LWAs. Discussion and comparison of the results for the series with and without LWAs are also presented. The cement paste, fine and coarse mortars, and concrete are detailed and the relationships between these phases of cementitious materials are given.

Chapter 5 presents the results of experimental studies conducted for determining the restraining effect of both LWAs and normal weight aggregates (NWAs) on autogenous deformation and fracture properties of composites containing 70% paste and 30% aggregate by volume. At the end of the chapter, the meso-mechanical modeling of modulus of elasticity of cement based materials are explained and its application to the composites is demonstrated.

Chapter 6 reports the most recently used models of autogenous deformation and gives the background information on mechanism of autogenous deformation and on the calculation of self-desiccation shrinkage with the capillary tension approach. A comparison of the results of calculated self-desiccation shrinkage with that of experiments on cement paste and concrete is presented. This chapter also presents the use of the modulus of elasticity (obtained from the meso-mechanical modeling) for satisfactory predictions in calculating the autogenous deformation of cementitious materials.

Chapter 7 deals with the experimental studies on the travel distance of water from the cement paste. Dispersion characteristics of LWAs and their effects on both the internal curing and the fracture properties are examined.

In **Chapter 8**, the compressive strength, modulus of elasticity, fracture energy, characteristic length, splitting tensile strength, net bending strength, and autogenous deformation of concretes are defined in terms of the size and volume of substituted LWAs. A multi-objective simultaneous optimization technique, in which the Response Surface Method (RSM) is incorporated, is used. The experimental programs are designed to find the optimum solutions as combination of a number of factors estimated by fitting a polynomial model by using analysis of variance (ANOVA).

Chapter 9 summarizes the conclusions based on the data obtained during the course of the study. It describes the effect of the LWAs on autogenous deformation, degree of hydration, pore size and fracture properties of cement based materials. This section also gives a brief description of the effect of distribution characteristics obtained from image analysis and the results of the optimization analysis.

2. LITERATURE REVIEW

2.1 General

This chapter aims to provide the reader with the concepts used in this thesis. It should be noted that this thesis includes a number of topics (i.e. hydration, autogenous deformation, fracture mechanics, lightweight aggregate (LWA), image analysis, optimization) in which noteworthy publications are available in the literature. This chapter consists of three sections. First section presents brief information about the hydration and microstructure of cement paste and continues with a literature review on the autogenous deformation. The second section deals with a literature review on the mitigation methods of autogenous deformation with a particular interest in using pre-soaked LWAs. The third section, finally, gives the introduction to the fracture mechanics of cement based materials and discusses mainly the fracture mechanics of concretes with LWAs.

2.2 Cementitious Materials at Early Ages

Microstructure properties of cement paste, aggregate and bond between these two constituents affects the strength of cement-based materials. Although aggregate constitutes 60-70% by volume of concrete, the cement paste and its properties are the dominant factors affecting the chemical, physical, and mechanical properties of concrete. However, the mechanical properties of concrete are more influenced by the physical structures of hydration products than the chemical structure of hydrated cement (Atahan, 2002).

Fresh cement paste mainly consists of Portland cement and water in a plastic network. Portland cement is composed of four components: alite (tricalcium silicate, C_3S), belite (dicalcium silicate, C_2S), aluminate (calcium aluminate phase, C_3A), and ferrite (C_4AF). With the ongoing hydration, the hardened paste consists of (i) hydrated crystals which

are produced by different cement compounds defined as gel; (ii) crystals of calcium hydroxide; (iii) some minor components; (iv) unhydrated cement; and (v) the residue of water-filled spaces in the fresh paste (Neville, 1997). There are many publications available in literature about microstructure and development of hydration of cement (Powers, 1964; Jennings et al., 1981; Hansen, 1986; Neville, 1997; Scherer, 1999; Richardson, 2000; Scrivener, 2004).

2.2.1 Mechanism of the Hydration Process

The hydration is a physiochemical process and can be considered as three stages: the pre-dormant and the dormant period; the faster rate of hydration; and diminishing rate of hydration (Brunauer et al, 1973).

The pre-dormant period is defined as the stage when the water penetrates into cement particles, and the hydration is in a faster rate. After this fast start, the dormant period is observed. The hydration products cast a nearly impenetrable layer on the cement grains, and hence the hydration becomes slower. The beginning and the duration of the dormant period depends strongly on the temperature. This period starts at about 10 to 15% of hydration, and ends around 15 to 20% of hydration (Brunauer et al, 1973). During the hydration process, the degree of hydration (α) is defined as the ratio of the amount of hydrated cementitious material to the amount of original cementitious material. In this stage, C_3A reacts with gypsum and water to form ettringite within colloidal dimensions (10-1000 Å).

The second stage begins with collapsing the layer either as a result of the fact that the hydration products have larger volumes than unhydrated cement or by an osmotic mechanism (Neville, 1997). The hydration rate begins to increase after the water reaches the unhydrated cement particles. At this stage, C_3S and C_2S react with water and build amorphous calcium silicate hydrate (C-S-H) and crystalline calcium hydroxide (CH). During this period, aluminates also react to form ettringite which is in later stages converted into monosulphate. The early hydration products are mostly in the form of long fibers that grow into the pore space and connect the cement particles.

In the third stage, when the degree of hydration exceeds about 30%, diffusion through the hydration products becomes the controlling mechanism for the rate of hydration. This slow rate continues until the ultimate degree of hydration. The formation of the hydration products is accompanied by the formation of very small pores (i.e., the "gel pores" of Powers), and the term "diffusion through the hydration products" is used here to describe the diffusion through the pores rather than through the solid matter. As the hydration proceeds, the pores become narrower, and the path through which molecules or ions are likely to diffuse being longer. As a consequence, the diffusion becomes slower with increasing amount of hydration products (Brunauer et al, 1973).

2.2.2 Pore Structure

The production of hydrates consists of approximately 58% C-S-H (tobermorite), 37% CH (portlandite) and 15% other hydrate members (Postacıoğlu, 1986). The typical pore structure is given in Figure 2.1 (Diamond, 2004). Thus, the properties of C-S-H control the strength and durability of the hardened concrete (Atahan, 2002).

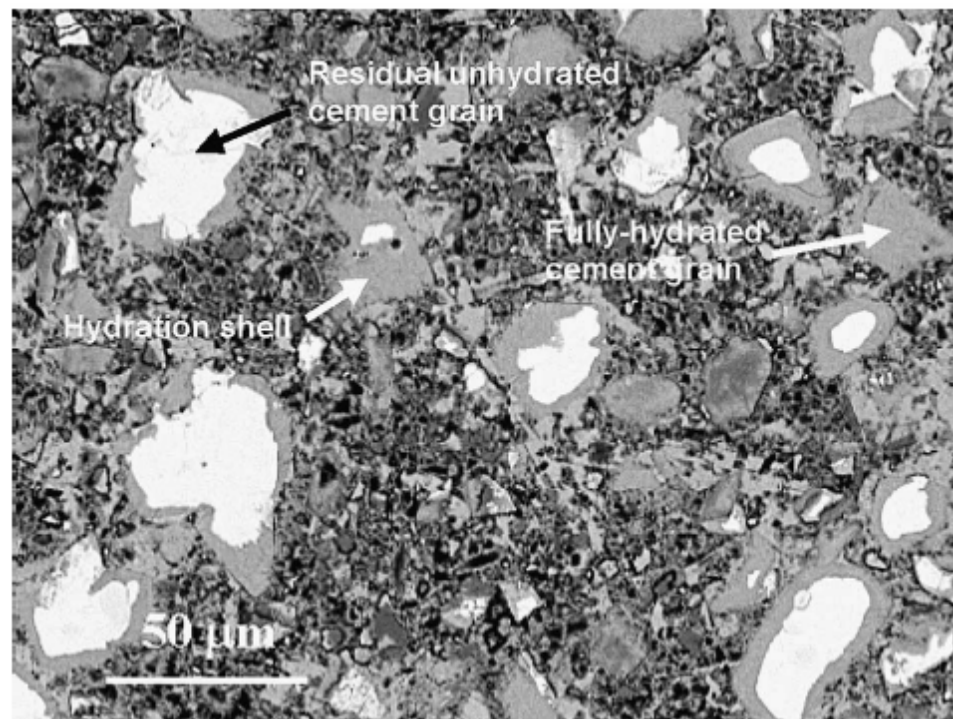


Figure 2.1: View of the microstructure of a 100-day old cement paste (w/c 0.30) cured at room temperature (Diamond, 2004).

The cement gel is defined by Hansen (1986) as “composition of solid particles having large internal surface area such as characteristic of colloidal gels.” It has been stated that there are variable morphologies of C-S-H phase at different degrees of hydration (Powers, 1964; Jennings et al., 1981; and Richardson, 2004). C-S-H has layered fibrous of tobermorite which contains water between the layers. Hydrated gel volume resulted from the hydration of 1 cm³ anhydride cement is approximately 2.1~2.2 cm³. The relative voids (water) to solid (cement) ratio controls the initial porosity, as water occupies void spaces at the outset (Nokken, 2004). Pores in hydrated cement paste can be defined as entrained air, capillary pores, and gel pores on the basis of their dimensions (Table 2.1).

Table 2.1: Classification of pore sizes in hydrated cement paste (Jennings, 1988; originally given by Mindess and Young, 1981).

Designation	Diameter	Description	Role of water	Paste properties affected
Entrained air	0.1-1.0 nm	Round cross-section	...	Strength
Capillary pores	10-0.05μm	Large capillaries	Behaves as bulk water	Strength, permeability
	50-10 nm	Medium capillaries	Moderate surface tension forces generated	Strength, permeability, shrinkage at high humidity
Gel pores	10-2.5 nm	Small (gel) capillaries	Strong surface tension forces generated	Shrinkage to 50% relative humidity
	2.5-0.5 nm	Micropores	Strongly absorbed water, no menisci form	Shrinkage, creep
	<0.5 nm	Micropores ‘interlayer’	Structural water involved in bonding	Shrinkage, creep

Capillary pores are water filled spaces which form the gaps between the products of hydration. In Figure 2.2, two types of products of hydrates in gel microstructure are shown as inner and outer (Scrivener, 2004). The inner products form throughout the boundaries of original solid anhydride cement. These products do not begin to form until some time after the reaction was initiated; therefore, a boundary coincides with the smaller, partly consumed, anhydrous particles (Jennings and Parrot, 1986). The outer products generally fill the water filled spaces. The outer products of hardened C₃S or

cement grain have microstructures of small needles with irregular shapes. The space between these needles forms capillary pores which affect the strength and durability of cement paste (Richardson, 2000). With ongoing hydration, the amount of the capillary pores decreases. Since the gel has a great proportion of evaporable water, it becomes porous microstructure. As the hydration proceeds, the amount of the gel increases. Thus, the volume of the gel pores increases with time, while those of the capillary pores decrease. A significant proportion of gel pores forms in the inner products. The gel pores occupy about 28% of the total volume of gel (Powers, 1964 and Hansen, 1986). This value is characteristic for a given cement, but it is largely independent of the water/cement ratio of the mix and of the progress of the hydration (Neville, 1997).

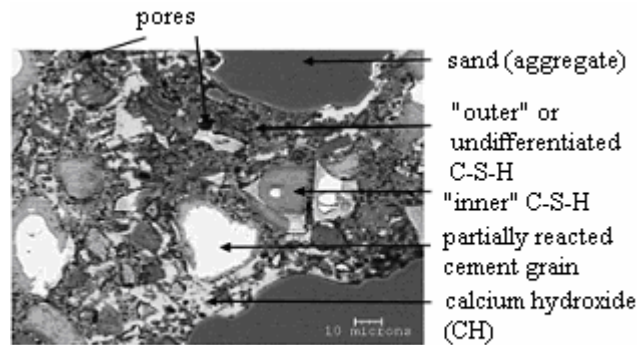


Figure 2.2: Typical BSE image of a Portland cement mortar (200 days old, water/cement=0.4), with the microstructural constituents distinguished (Scrivener, 2004).

2.2.3 Water Held in Hydrated Cement Paste

Water may present in three different forms in hardened cement paste. These are: chemically bound, physically bound, and free water. Chemically bound water is non-evaporable water and forms a complementary part of the gel. Thus, the amount of chemically bound water is used for determining the degree of hydration and the influence on properties (Jennings, 1988). On the other hand, physically bound water is held by the surfaces of cement gel with the van der Waals forces as it is largely immobile. The free water, also called capillary water, is the remaining water in structure, and is required for the hydration process to continue. The free water and also the

physically bound water are evaporable waters. Upon removal of water, menisci can form in capillary pores and large gel pores generate hydrostatic pressure on the solid (capillary effect) (Ai, 2000). This pressure collapses the C-S-H layers resulting in permanent change in microstructure as shrinkage and creep in hydrated cement paste.

2.2.4 Heat of Hydration of Cement

The heat of hydration is defined as the considerable amount of heat that is released during hydration because of its exothermic nature, and it is influenced by the compound composition of cement. This heat of hydration will lead to an increase in temperature of cement paste. The temperature rise and the gradients may lead to thermal cracking in early age concrete (Østergaard, 2003).

2.3 Literature on Autogenous Deformation

The definition of autogenous deformation was first mentioned as self-desiccation by Le Chatelier (1900). He observed the difference between the absolute and apparent volumes of cement paste in his experiments. It is well known that the volume of production of hydrates is less than the volume of components involving the reaction, and this situation is defined as chemical shrinkage (also called as Le Chatelier's contraction). On the other hand, hydrated structures absorb water in pores which has not been involved in reactions. The event independent of exterior surroundings is defined as self-desiccation. Self-desiccation is likely to form new pores in hydrating cement paste. The term 'autogenous shrinkage' was first used by Lynam in 1934 who postulated that the shrinkage was caused neither by thermal reasons nor by loss of relative humidity (RH) to air. Since the modulus of elasticity of aggregate is greater than that of hardening cement paste, autogenous deformation causes stresses in the concrete.

2.3.1 Types of Shrinkage

Crack induced volume changes in cementitious materials may be classified as (Weiss, 1999; Holt, 2001; Grasley et al. 2003):

- Thermal dilation
- Crystallization pressure
- Plastic shrinkage
- Carbonation shrinkage
- Drying shrinkage
- Internal moisture and moisture change
- Autogenous deformation

Thermal Dilation: The heat generated by the hydration reaction of cement dissipates quickly in thin structures, while it is very slow in massive structures. This additional heat accelerates development of material properties (i.e. hydration) and causes the concrete to set in expanded condition. As concrete or cement paste cools, it shrinks proportionally to the gradient of temperature and the resulting temperature gradient leads to cracking. Even seasonal or daily temperature change may cause thermal shrinkage.

Crystallization Pressure: During deposition of C-S-H, recrystallization is the principal process of grain growth and cementation processes (Curti et al., 2005). The maximum driving force for crystallization is related to the super saturation for the crystal growing in solution, and to the undercooling for the crystal growing from a melt (Scherer, 1999). While the formation of many small crystals is *kinetically* favored (i.e. they nucleate more easily), large crystals are *thermodynamically* favored. Thus, from a viewpoint of kinetics, it is easier to nucleate many small crystals. Many small crystals form in a system initially but slowly disappear except for a few that grow larger at the expense of the small crystals. The smaller crystals act as "nutrients" for the larger crystals. The expansion of larger crystals causes the area around them to be depleted in smaller crystals. This phenomenon is called ***Ostwald's ripening***, and occurs as a mean of big

CH clusters growing at the expense of small crystals (which have higher solubility than large particles).

The crystallization pressure of hydration products such as ettringite can lead to internal stresses. The crystallization pressure of the reaction products results in a bulk expansion of the solid (Tixier and Mobasher, 2003). The normal aging process of the cementitious systems involves dissolution of uniformly distributed fine ettringite crystals within the hardened cement paste and subsequent recrystallization as innocuous crystals in the largest accessible spaces.

Plastic Shrinkage: Plastic shrinkage continues during the evaporation from the surface of fresh cement. If the evaporated water content is greater than the bleeding water, plastic shrinkage occurs. It is known that the temperature of both air and fresh concrete, RH and the rate of wind all affect the amount of plastic shrinkage (Neville, 1997). Plastic shrinkage can be mitigated by the prevention of water loss of concrete in fresh state or increasing the cracking strength by fiber addition (Theodorakopoulus and Swamy, 1993).

Carbonation Shrinkage: This type of shrinkage occurs slowly on the surface of concrete as a consequence of the reaction between hydrated cement and carbondioxide in the atmosphere. Carbonation shrinkage can reach considerably high values in cases when the RH is about 50% and the concrete is exposed drying and wetting cycles. Carbonation is generally considered a durability issue that takes a long time, in an order of several years, to affect a concrete structure (Holt, 2001).

Drying Shrinkage: Drying shrinkage occurs as a result of water movement from the concrete to water unsaturated air. If the diameter of capillary pores is greater than 10 nm, the utilization of water allows the production of intergranular hydrates. On the other hand, a new hydration phase begins: the water is now consumed in the hydrates porosity in order to produce internal hydrates that expand by reaching the bulk of anhydrous cement particles (Morin et al., 2002). As the drying proceeds, the water in pores is absorbed by the disjoining forces and the cement paste shrinks as a result of the capillary stress occurring in meniscus. The most important factor effecting drying shrinkage is the water/cement ratio. Concretes with lower water/cement ratio exhibit small amount of

drying shrinkage, because they have smaller amount of pore water. On the other hand, it is well known that the self-desiccation increases with decreasing water/cement ratio, and this will cause an increase in the total shrinkage. With increasing degree of hydration, products of hydrates fill the pore spaces and the amount of movable water decreases; consequently, the amount of drying shrinkage will decrease. Bendoudjema et al. (2001) showed that there is a linear relationship between drying shrinkage and water loss. As the modulus of elasticity and volume of aggregate increase, dimensional stability and restraining of cement paste increase and amount of drying shrinkage decreases.

Internal moisture change: The drying process of concrete is affected by specimen size and moisture diffusion which can be modeled as a parabolic differential equation (Bendoudjema et al., 2001). In thin specimens, water can diffuse easily and hence the shrinkage may occur rapidly (Weiss, 1999). This moisture gradient causes both volume change and cracking.

Autogenous deformation: After the setting, the time dependent volume change of cement paste progresses. Continuous hydration causes expansion if there is water in the media. On the other hand, if the movement of the moisture between the cement and its environment is prevented, the cement paste will shrink. Autogenous shrinkage has been defined by the Japan Concrete Institute (JCI) committee as “the macroscopic volume reduction of cementitious materials when cement hydrates as a closed system after initial setting” (Tazawa, 1998). The following sections will discuss the autogenous deformation and its properties.

2.3.2 Terminology of Autogenous Deformation

Autogenous deformation may occur as shrinkage or expansion (Tazawa, 1998; Lura, 2003; Bjøntegaard, 2004). Although autogenous shrinkage has been widely used, the term “autogenous deformation” is preferentially used in this thesis. The term “autogenous deformation” has often been used instead of chemical shrinkage. In fact, chemical shrinkage, which is the internal volume reduction, causes the autogenous deformation. Before setting, this internal volume reduction may be completely transformed into a bulk deformation of the system, which is called the setting shrinkage. With the above definition, setting shrinkage has been described as an essential part of

autogenous deformation (Jensen and Hansen, 2001a). After setting, chemical shrinkage creates inner empty cavities if the cement paste is kept sealed. Due to the formation of menisci, chemical shrinkage leads to an RH-decrease and shrinkage of the cement paste, i.e., self-desiccation and self-desiccation shrinkage. A widely used definition of autogenous deformation and self-desiccation is reported by Jensen and Hansen (2001a). Autogenous deformation has been defined by these researchers as “the bulk deformation of cementitious material without any weight loss when cement hydrates in a closed, isothermal system not subject to external forces”. It does not, however, include the volume changes due to any exchange of material with the surroundings, temperature variations, or the application of external force and restraint. A similar RH reduction mechanism is also observed as self-desiccation. RILEM TC 196-ICC has defined the self-desiccation as “the reduction in internal relative humidity of a sealed system when empty pores are generated”. This occurs when the chemical shrinkage takes place at the stage where the paste matrix has developed a selfsupportive skeleton, and the chemical shrinkage is larger than the autogenous shrinkage (Bentz, 2005a). A phenomenon closely related to autogenous RH change is autogenous shrinkage (Lura, 2003). Autogenous RH change is defined as “the change of internal RH in a closed, isothermal, cementitious material system not subject to external forces” (Jensen and Hansen, 2001a).

2.3.3 Stages of Autogenous Deformation

It can be seen from both the temperature in adiabatic conditions vs. time, and volumetric autogenous deformation vs. time relationships for cement paste with 10% silica fume (Figure 2.3) that the autogenous deformation can be examined in four different stages (Termkhajornkit et al., 2005).

Stage 1 defines the beginning of sedimentation where the volume change in cement paste is very small. After the water addition, with the settlement, some of the water rises or bleeds to the surface. Corresponding to the pre-induction period of the hydration process several ions rapidly dissolve from cement particles. The reaction tends to slow down due to the deposition of a layer of hydration products on the surface of cement particles. It seems that the hydration process in this stage does not have much effect on

the shrinkage. In this stage, the chemical shrinkage is identical to the autogenous deformation.

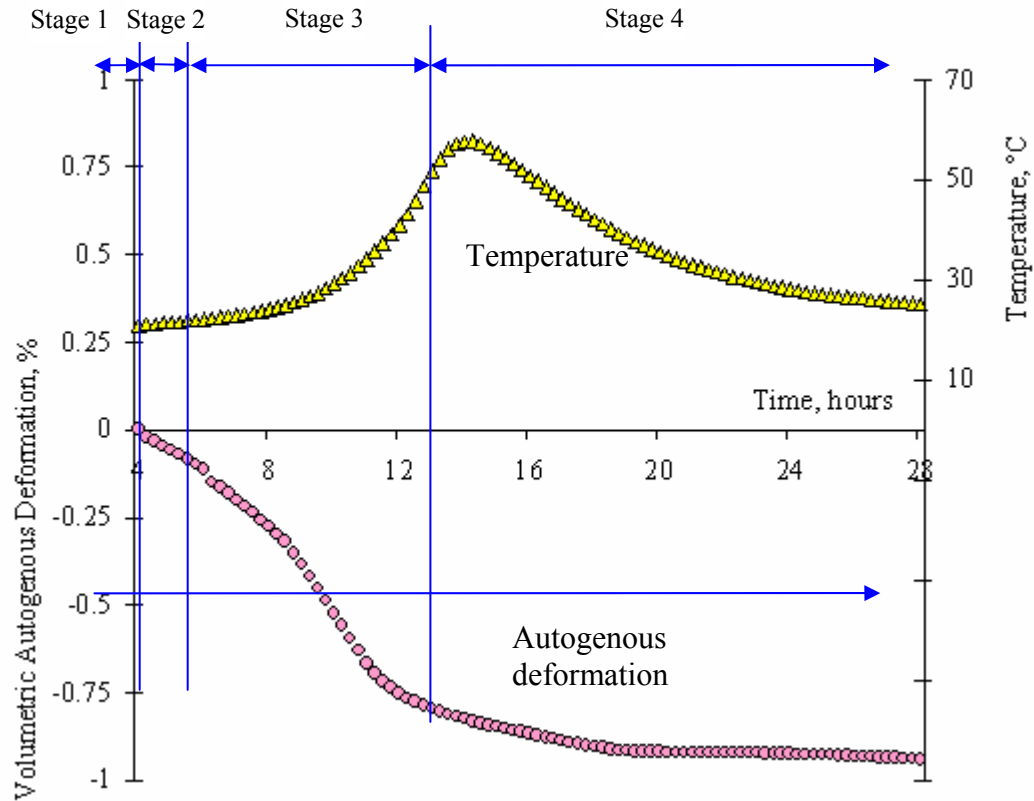


Figure 2.3: Volumetric autogenous deformation and temperature versus time of cement paste with 10% silica fume.

Stage 2 corresponds to the accelerated sedimentation. This stage occurs almost simultaneously with the setting, in which the hydration of all the clinker minerals progresses very slowly. The change of temperature shows that the temperature in this period is fairly constant. Thus, it seems that the large shrinkage does not result from hydration but from the rapid sedimentation of particles.

Stage 3 describes autogenous deformation which is generated from the hydration of ordinary Portland cement. Following the ions' reaching a critical concentration in the pore solution, the rate of hydration of the cement increases at this stage. Thus, the development of autogenous deformation is accelerated by the formation of hydration

products and consequently the menisci. When the hydration rate increases, the temperature of the cement paste sample also increases. Real autogenous deformation begins to develop after the initial setting. Sedimentation of particles still continues in this stage, but this effect tends to become less important as the rate of cement hydration increases. At the end of this stage, the temperatures of the samples reach to a maximum.

Stage 4 is defined as the post autogenous deformation. As the hydration proceeds, the reaction rate is reduced and becomes diffusion-controlled. The reason for this is that water must diffuse through the layer to reach the unhydrated cement and the ions must diffuse to reach the growing crystals. This stage begins when the temperature of the sample starts to decline, corresponding to the post acceleration period in the hydration process. In this stage temperature decreases gradually. The particles are fixed to one other by the hydrated product, thus, the effect of particle settlement is negligible.

2.3.4 Factors Affecting the Autogenous Deformation

2.3.4.1 Effect of water/cementing materials ratio

It is well known that the autogenous deformation is influenced by the water to cement ratio (w/c). As w/c decreases, magnitude of autogenous deformation increases (Hanehara et al. 1999; Feylessoufi et al., 2001; Persson, 1999a; Persson 1999b; Sato, 1999; Zhang et al., 2003; Baroghel-Bouny et al., 2006). There is almost a linear relationship between the w/c ratio and the autogenous deformation of cement paste as shown in Figure 2.4 (Baroghel-Bouny et al., 2006).

Lura, (2003) has shown that with lower w/c ratio, hydration stops due to lack of water and a considerable amount of anhydrous cement remains in the hardened cement paste. If the water is allowed to penetrate into the hardening cement paste (open system), the w/c ratio that is necessary to obtain full hydration is reduced to 0.36.

Autogenous deformation of concrete is less than that of cement paste at constant w/c , because of the diminishing cement paste content in unit volume and also the restraining effect of aggregates. This will be discussed later in Chapter 5.

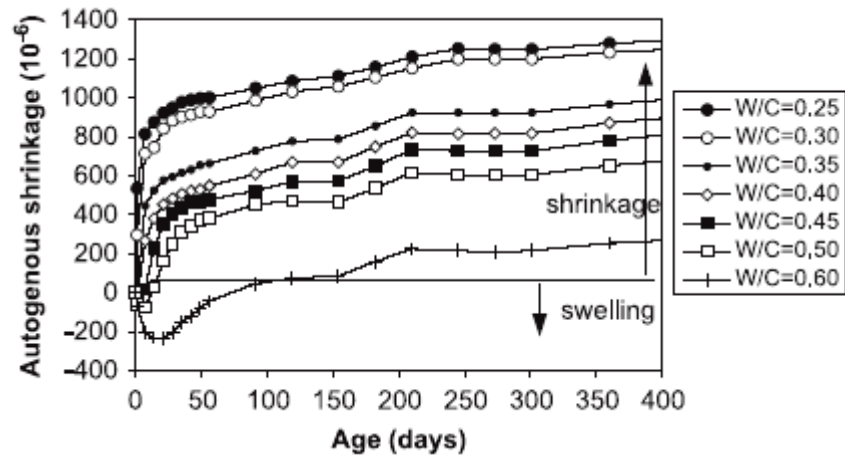


Figure 2.4: One-dimensional autogenous deformations vs. age diagram of cement pastes with various w/c at $T=20\text{ }^{\circ}\text{C}$ (Baroghel-Bouny et al., 2006).

2.3.4.2 Effect of self-desiccation

By the development of empty pores, chemical shrinkage becomes a triggering mechanism of autogenous deformation. The decrease of RH in the cement paste is followed by autogenous deformation. Thus, self-desiccation shrinkage becomes the main constituent of autogenous deformation after a certain time. Some other effects, such as chemical shrinkage, crystallization, and alkali effects, are operative at very early ages, particularly when the cement paste is fluid. The degree and amount of self-desiccation, as is also the case for autogenous deformation, are influenced by a number of factors, such as water/cementitious materials ratio, cement type, and curing condition. Baroghel-Bouny (1997) showed that there is almost a linear relationship between autogenous deformation and self-desiccation (Figure 2.5). The decrease of internal RH (self-desiccation), inducing for example capillary tension variations, is therefore in the range where the linear relationship exists, directly at the origin of the measured long-term autogenous strains. This gives the range where autogenous strains are only due to the transformation of the liquid pore water into chemically bound water and can be considered as self-desiccation shrinkage. This range occurs when RH is greater than 75% (pore size is nearly 50 nm) where capillary tension is operative owing to subtraction of pore water that resulted in the formation of menisci in the hardened

cement paste (Ai, 2000). Although capillary pores are empty when the value of RH is equal to 75%, the process of self-desiccation can continue due to the unreacted particles. On the other hand, Jensen (1995) proposed that the self-desiccation process cannot sufficiently reduce the RH beyond ~75% in cement paste.

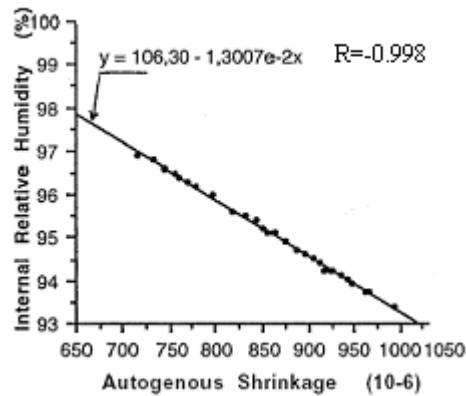


Figure 2.5: Correlation between the autogenous deformation and the internal RH of cement paste with the w/c=0.34 at the age of 28 days (Baroghel-Bouny, 1997).

In another research on self-desiccation, Lura (2003) has demonstrated that, in the first 24 hours, although the rate of decrease in the RH value is reasonably high, the slope of the curve decreases with increasing stiffness of the cement paste. Thus, self-desiccation begins to slow down as shown in Figure 2.6.

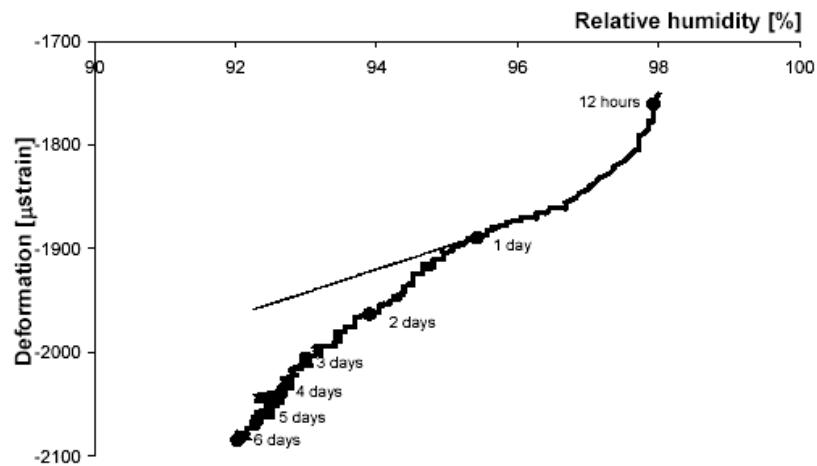


Figure 2.6: Autogenous deformation of Portland cement paste as a function of internal relative humidity (Lura, 2003).

Lura (2003) postulated that this fact could be due to the onset of the pozzolanic reaction of silica fume that consumed the CH crystals. Creep of the cement paste could be another additional reason. Increase in the slope of the deformation-RH curve after 1-day cannot be ascribed to temperature changes due to heat of hydration, because these occur only in the first hours after mixing with water.

2.3.4.3 Effect of cement type, fineness and composition

It is obvious that the type and composition of cement have major effects on autogenous deformation. In particular, the autogenous deformation depends largely on the contents and degree of hydration of C_3A and C_4AF (Tazawa and Miyazawa, 1995). It has been reported that the autogenous deformation of ordinary Portland cement (OPC) mixture is higher than that of high-belite Portland cement mixture (Park et al., 1999). One of the reasons for this is that high-belite Portland cement has lower C_3A or lower reactive Al_2O_3 . In addition, the solid fraction might shrink due to the reaction that produces ettringite at early ages. Miyazawa and Tazawa (2005) examined the variations in autogenous deformation of seven different type cements with different compositions as shown in Figure 2.7.

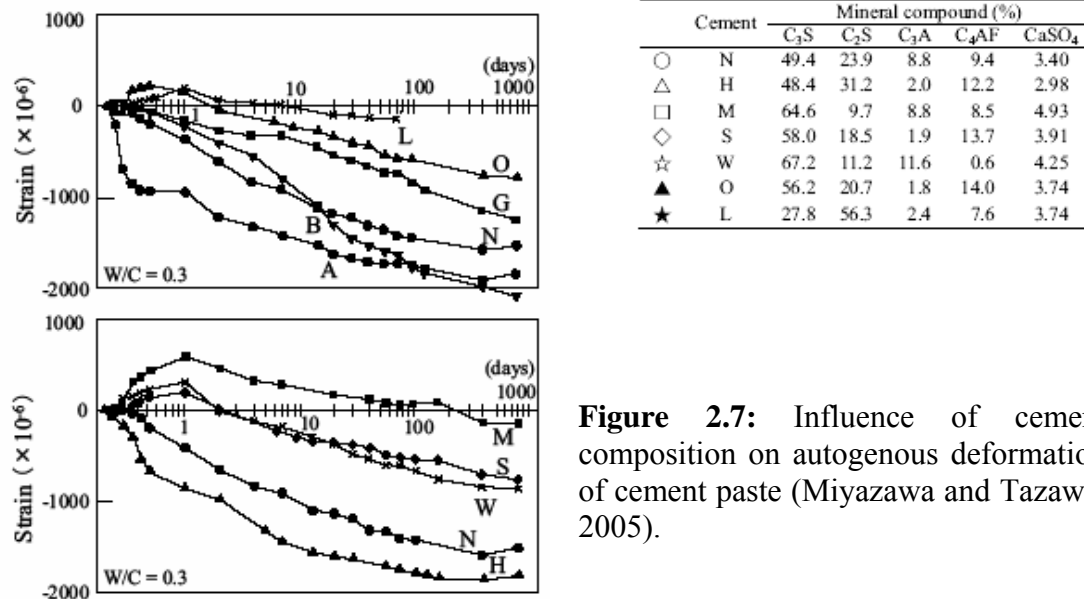


Figure 2.7: Influence of cement composition on autogenous deformation of cement paste (Miyazawa and Tazawa, 2005).

In Figure 2.7, the letters N, M, H, L, W, A, O, S, G and B indicate ordinary Portland cement, moderate-heat Portland cement, high-early-strength Portland cement, low-heat Portland cement, white Portland cement, calcium-aluminate cement, oil-well cement, sulphate-resistant cement, geothermalwell cement and Portland blast-furnace slag cement, respectively. Their results show that the autogenous deformation of moderate-heat Portland cement (M) and low-heat Portland cement (L) are much less than the ordinary Portland cement (N). High-early-strength Portland cement (H) resulted in a greater autogenous deformation than ordinary Portland cement. It was found that autogenous deformation increases with increasing C_3A and C_4AF contents of cement.

It is also shown experimentally that the cements with finer grain cause greater autogenous deformation than those with coarser one (Tazawa and Miyazawa, 1995; Bentz et al., 2001b; Bentz and Jensen, 2004). The developments of autogenous deformation of cements with different fineness are given in Figure 2.8 (Bentz et al., 2001b). After initial setting, the two coarsest cements in Figure 2.8 exhibit initial expansion (up to about 40 hours) rather than undergoing self-desiccation shrinkage because the effects of self-desiccation are initially overwhelmed by the effect of ettringite formation.

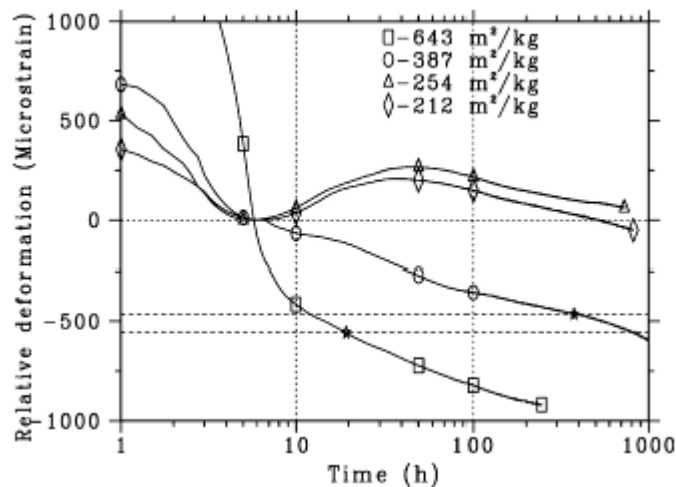


Figure 2.8: Effect of cement fineness on autogenous deformation of cement pastes (with w/c of 0.35) (Bentz et al., 2001b).

2.3.4.4 Effect of supplementary materials

The main purposes of using supplementary materials are to enhance durability and other properties of concrete, decrease the heat of hydration, and optimize the cost savings. This enhancement can be achieved by reaction with by-products or by increasing the particle packing efficiency (efficient filling of voids). It can be deduced that the pozzolanic reaction does not use evaporable water (Loukili et al., 1999). Thus, addition of mineral admixtures into the paste alters the hydration rate and microstructural characteristics, such as pore size distribution and amount of cement paste, which consequently results in high self-desiccation effect (Jiang et al., 2005). It is shown in Figure 2.9 that supplementary materials clearly change the autogenous deformation of concrete (Pane and Hansen, 2002). Thus, it is necessary to investigate the effect of these additives on autogenous deformation.

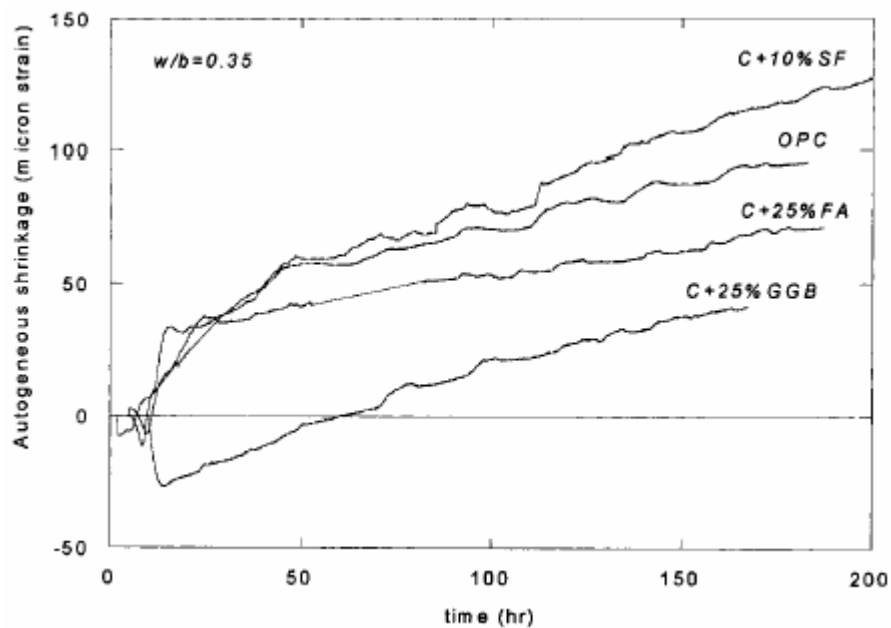


Figure 2.9: Effect of supplementary materials (SF: silica fume; FA: fly ash; GGB: ground granulated blast furnace slag) on autogenous deformation (Pane and Hansen, 2002).

Silica fume

The addition of silica fume has a major influence on autogenous deformation. The magnitude of autogenous deformation of cement paste increases drastically with increasing the volume of silica fume content (Dela and Stang, 1997; Brooks et al., 1999; Zhang et al., 2003). Zhang et al. (2003) have shown that for the concrete with silica fume, the autogenous deformation after 98 days was relatively high even at a w/c ratio of 0.35 ($>200 \mu\text{strain}$), but decreasing the w/c ratio to 0.26 only increased the autogenous deformation by $50 \mu\text{strain}$ for the concrete with 5% silica fume, and by $30 \mu\text{strain}$ for the concrete with 10% silica fume (Figure 2.10).

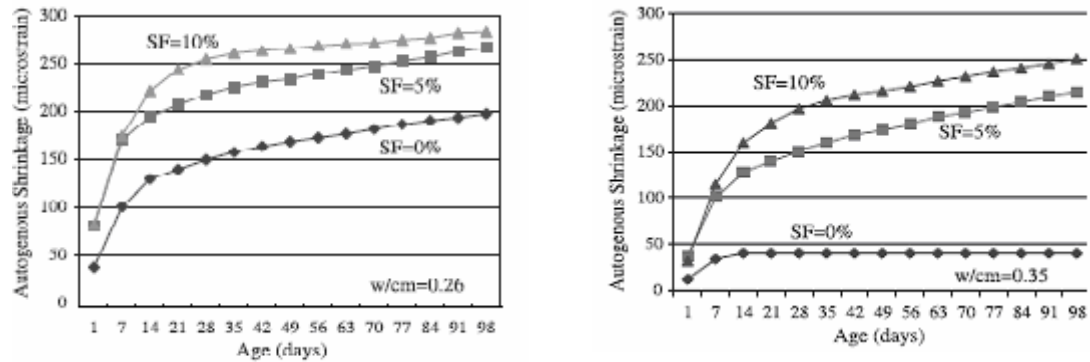


Figure 2.10: Autogenous deformation of two different cement paste containing 0%, 5% and 10% silica fume (Zhang et al., 2003).

In another research, Dela and Stang (1997) used cement paste with w/c of 0.30 and found that the differences in autogenous deformation of different types of paste result in different eigenstress levels. They show that the addition of silica fume causes further autogenous deformation in cement paste as the paste without silica fume exhibits autogenous deformation only in the first 50 hours after mixing, while the autogenous shrinkage of the paste with silica fume continues, though with a decreasing rate. The reason for this may be that the silica fume reacts with by-products at later ages. Silica fume also has an effect on self-desiccation. This effect, although can be very large in some cases, is usually much smaller than the effects of the type of the cement. The effect

of silica fume is also less reproducible, i.e. careful pre-testing is required if the silica fume is to be used to achieve a certain degree of self-desiccation.

Fly ash

Experiments have shown that using fly ash results in a substantial reduction in water migration in the pore structure (Tangtermsirikul, 1999; Chan et al. 1999; Lee et al., 2003; Kolluru et al., 2005; Termkhajornkita, 2005; Staquet et al, 2004). Composition and particle size of fly ash have strong influences on autogenous deformation. Fly ash with higher SO_3 content resulted in a lower autogenous deformation, and since the particle size of fly ash is greater than that of cement, the magnitude of autogenous deformation is smaller (Tangtermsirikul, 1999). Termkhajornkit et al. (2005) showed that both the type and volume of fly ash have a similar decreasing effect on autogenous deformation in two different cement pastes with w/c ratios of 0.22 and 0.30 (Figure 2.11).

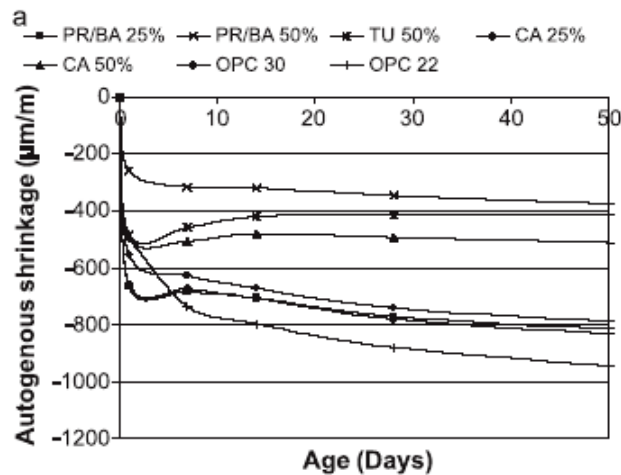


Figure 2.11: Autogenous deformation increase when the replacement of fly ash is 25%. However, when the replacement ratio reaches 50%, the autogenous deformation becomes remarkably small (Termkhajornkita, 2005).

On the other hand, the autogenous deformation increases at early ages when the replacement of fly ash was 25% relative to the OPC sample, although no substantial difference is observed at later ages, which means that 25% fly ash was not enough to mitigate the autogenous deformation. The difference observed at early ages is probably

due to the amount of ettringite in fly ash–cement mixes, which is higher than that in the OPC mixes during 2 to 5 hours after mixing (Berry et al. 1990). At the age of 5 days, the fly ash–OPC sample displays some kind of expansion behavior. Because of the smaller pores reasoned in bigger capillary pressure, concrete with silica fume exhibits a higher autogenous deformation than the concrete with fly ash.

Slag

While fly ash reduces the autogenous deformation, slag has an increasing effect on autogenous deformation. The reason for this alteration may be that the slag causes self-desiccation whereas the fly ash behaves relatively inert (Chan et al., 1999; Hanehara et al., 1999; Lim and Wee, 2000; Lura et al., 2001). Chan et al. (1999) showed in their research that autogenous deformation of concrete with 40% slag (out of total cementitious materials) is significantly higher than that of concrete without slag. When the slag content is further increased, the autogenous deformation decreases slightly, although it still remains much higher than that of concrete without slag. Recently, Lee et al. (2006) have investigated the autogenous deformation of concretes prepared using blast furnace slag (BFS) with replacement ratios of 0%, 30%, and 50%. The concrete made with BFS exhibited higher autogenous deformation than the ordinary concrete without BFS, e.g., the higher the BFS replacement level, the greater the autogenous deformation at constant water/cementitious materials (w/cm) ratio (Figure 2.12). They explained this in terms of the greater chemical shrinkage and finer pore structure of the concrete with BFS than pure Portland cement, and the particle shape of BFS.

Jiang et al. (2005) have also shown that while silica fume causes an increase in autogenous deformation of cement paste at early ages, its role is taken by slag at later ages. This can be explained as silica fume accelerates cement hydration for its active super-fine components taking part in hydration reaction rapidly at early ages and slag accelerates second hydration reaction at later ages.

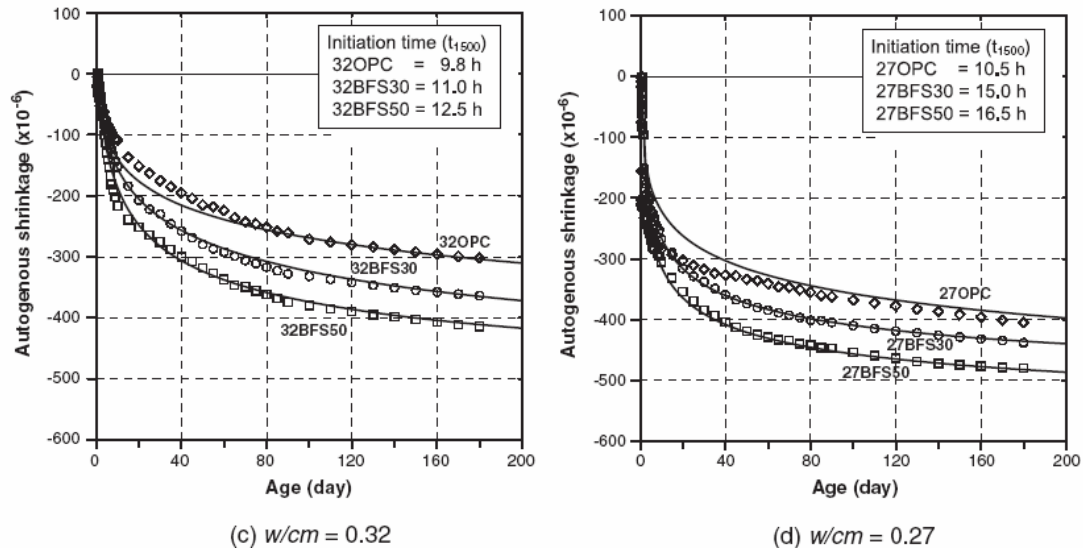


Figure 2.12: Autogenous deformation of concrete with different BFS content (Lee et al., 2006).

Metakaolin

The use of metakaolin increases autogenous deformation as the metakaolin concretes have lower porosity and finer pore structures which encourages loss of water by self-desiccation rather than by diffusion to the outside environment. The test results of Brooks and Megat Johari (2001) also indicated that the effect of metakaolin is to increase autogenous deformation (Figure 2.13). On the other hand, the replacement of metakaolin by cement with a replacement ratio of 15% resulted in 65% reduction in autogenous deformation at the age of 24 hours. This can be explained by the fact that in the concrete with metakaolin the amount of superplasticizer should be higher than the normal concrete, and this superplasticizer is known to retard hydration reaction at early ages.

Wild et al. (1998) studied autogenous and chemical shrinkage of metakaolin-Portland cement pastes for metakaolin contents in the range of 5% to 25%. Both autogenous deformation and chemical shrinkage were found to increase by up to 10-15% replacement, whereas at higher metakaolin contents both of them were found to decrease sharply when compared to the reference sample. The maximum value of autogenous

deformation is explained by the optimization of the combined effect of cement hydration and the removal of water from the system due to reaction of metakaolin.

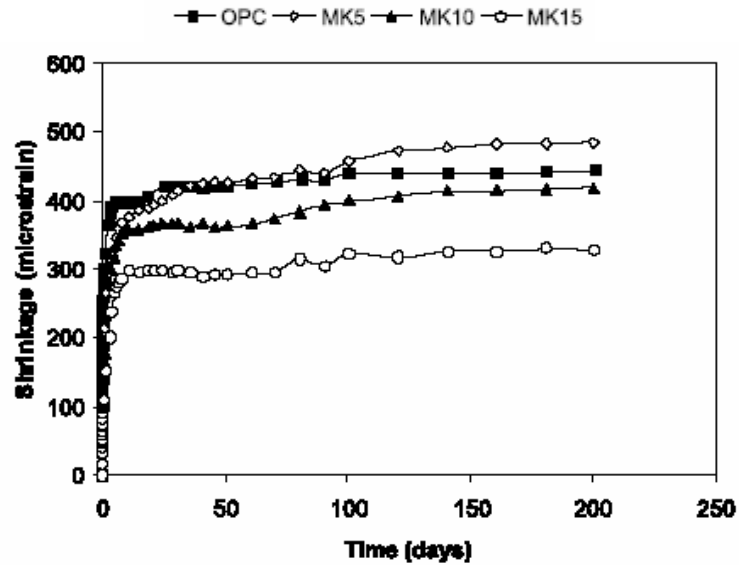


Figure 2.13: Effect of metakaolin on the 200-day total autogenous deformation measured from the initial set (Brooks and Megat Johari, 2001).

Another important factor affecting autogenous deformation of concrete with metakaolin is the particle fineness of metakaolin. Justice (2005) showed that the concrete with coarser metakaolin exhibits the greatest chemical shrinkage, while that with finer metakaolin shows the greatest autogenous deformation.

However, there are only a limited number of studies regarding the effects of metakaolin on autogenous deformation, and the possible effects of metakaolin should be investigated more comprehensively by further research.

2.3.4.5 Effect of chemical admixtures

High strength and high performance concretes have been widely used with benefits of new developing superplasticizer. It is well known that after superplasticizer is added, the main chain of polymer is adsorbed on the powder surface. However, the superplasticizer delays the hydration of OPC. When a large amount of superplasticizer is used, the hydration is significantly delayed, accordingly providing a delay in autogenous

shrinkage (Termkhajornkita, 2005). Tazawa and Miyazawa (1995) used 5 different types of superplasticizers (i.e. each with different dosage) to investigate the effects of type and amount of superplasticizers on the autogenous deformation of cement paste. They showed that autogenous shrinkage was slightly reduced by superplasticizers, whereas the differences due to the type of superplasticizer are small. The effects of the dosage were also found to be insignificant (Figure 2.14).

The effects of accelerators and retarders have also been investigated, and it has been stated that the use of these chemical admixtures will change the rate of reaction in cement. Thus, changing pore structure of cement paste is shown to influence the magnitude of autogenous deformation of cement paste (Nokken, 2004). With an accelerator, hydration begins earlier and results in a larger autogenous shrinkage at 24th hour. In contrast, with a retarder, the hydration reaction is delayed and smaller autogenous deformation developed at 24th hour (Aitcin, 1998). The effects of shrinkage reducing admixtures on autogenous deformation will be discussed further in Section 2.4.2.

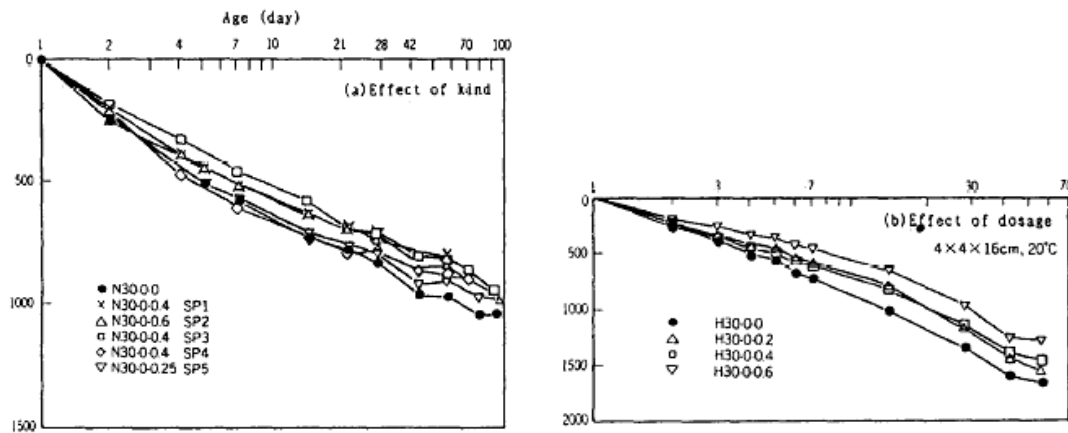


Figure 2.14: Effect of type and dosage of superplasticizer on autogenous deformation of cement paste (Tazawa and Miyazawa, 1995).

2.3.4.6 Effect of temperature

Effect of temperature on autogenous deformation has been studied in the temperature range of 15-40°C. The ultimate amount of autogenous deformation developed after setting as well as the rate of autogenous deformation depends on the temperature. As seen in Figure 2.15, it has been shown that higher curing temperature (40°C) accelerates the development of shrinkage, while the magnitude of the shrinkage after some days is similar for all tested curing temperatures (Lura et al., 2001; Jensen and Hansen, 1999). Jensen and Hansen (1999) pointed out that at 20°C, expansion in cement paste may be observed from setting until the age of one day after casting. This expansion is likely to have resulted from ettringite formation and overridden by counteracting shrinkage in early ages. On the other hand, Persson (2005) stated that self-desiccation was notably more pronounced after curing at 8°C than at 30°C. The pore structure with low temperature curing became finer, and thus more pronounced self-desiccations were observed.

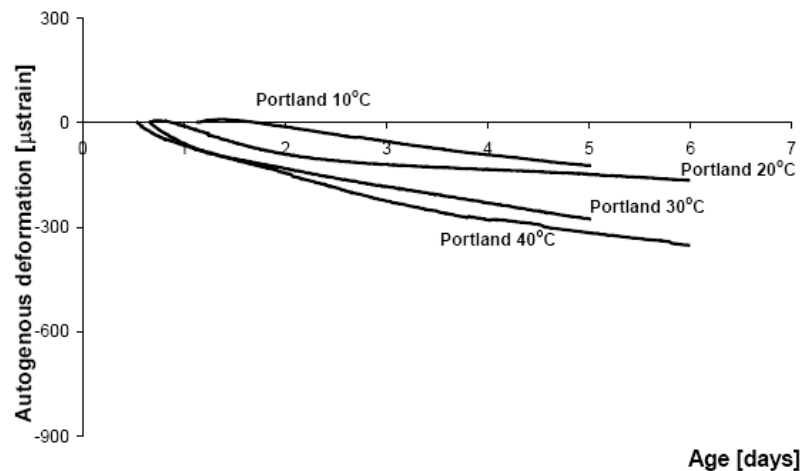


Figure 2.15: Autogenous deformation of Portland cement paste cured at different temperatures (Lura, 2003).

Type and composition of cement paste change the autogenous deformation behavior of cement paste at different temperatures. However, there is only a limited amount of literature information regarding the temperature effect. Lura (2003) showed that the BFS

cement paste displayed expansion at the beginning of the measurements, lasting for a couple of days at lower temperatures. A possible cause of this expansion is the crystallization pressure due to formation of ettringite, occurring before self-desiccation takes place.

2.3.4.7 Effect of alkalis

The effect of alkalis on the properties and performance of the products can be favorable or unfavorable. Although, the amount of sodium and potassium in cement are normally less than 1.5% ($\text{Na}_2\text{O} + \text{K}_2\text{O}$), their influences on properties are noticeable. It has previously been postulated that the chemical composition of the cement had a substantial influence on the autogenous deformation of cementitious materials (Persson, 1999b and 2001). Thus, the so-called alkali-effect should be taken into account when evaluating self-desiccation in cementitious materials. The alkali content of usual cement induces RH value of 97% instead of 100% at saturated state, and this is because of the dissolution of alkalis in the interstitial liquid phases. Depending on their concentration in the liquid phases, different ions can still induce even lower RH values in concrete (Baroghel-Bouny, 1997). On the other hand, Jensen and Hansen (1999) found that expansion due to salt crystallization and lowering of RH due to dissolution of salts in the pore water could generate autogenous deformation. These authors also stated that there is no possibility of distinguishing measured autogenous RH changes due to self-desiccation from RH changes due to dissolved salts. Alkali sulfates dissolve rapidly in the mixing water, whereas alkalis associated with aluminates and silicates are released gradually as dissolution and hydration of these phases proceed (Way and Shayan, 1989). However, Justnes et al. (1999a) showed that in addition to the soluble alkalis, C_3A and C_3S phases also have influences on autogenous deformation. They postulated that the dissolution of salts, such as clinker compound Aphthitalite (K_3NS_2), may lead to shrinkage. Persson (2005) also showed that there is a notable relationship between the cement constituents C_3A , C_4AF , K_2O and autogenous deformation. The influence of these components is in the order of ten times as large as that of C_2S and C_3S . Effects of alkali content on concrete with different w/c ratio are shown in Figure 2.16 (Persson, 2005).

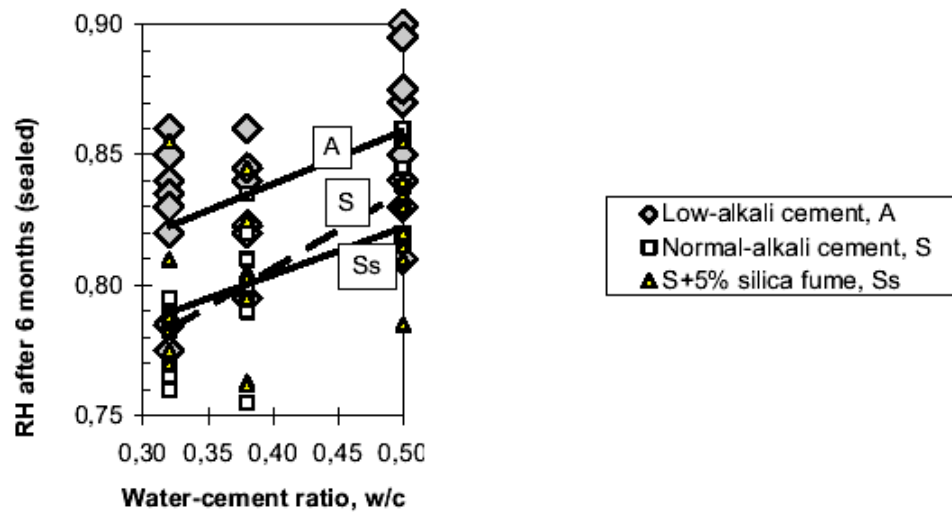


Figure 2.16: 6-months RH with low-alkali cement and RH with normal-alkali cement with 5% silica fume (Persson, 2005).

Figure 2.16 shows that concrete with normal-alkali cement yield lower RH values than concrete with low-alkali cement. RH in concrete with normal-alkali cement is not affected significantly by 5% silica fume. However, when silica fume is added to the concrete the pozzolanic reaction slightly reduce the alkali-effect. The variations in RH versus w/c are probably due to the available amount of pore solution for the probe to react properly.

It is naturally expected that the normal alkali cement gives rise to combined alkali concentration of pore solution to be higher than the low alkali cements. Because of this difference, the alkali concentration of the pore solution, according to the gypsum solubility, may be strongly dependent of the rate of ettringite formation. Aluminate is likely to play the major role at the very early ages as is assumed to dissolve more rapidly than ferroaluminate. Thus, the alkali and aluminate contents of the cement have major influences on the chemical shrinkage after 2 hours of hydration. It was shown that, for high dilutions, differences in alkali concentrations become negligible and autogenous deformation increases with increasing w/c (Beltzung and Wittmann, 2002).

It should also be noted that alkalis are likely to change the surface tension of the pore water, which affects the capillary stresses. Thus, differences in alkali content of pore

water can cause significant differences in autogenous deformation of cementitious materials. It is proposed that the main influencing factor is alkali content of pore water rather than the alkali content of cement.

2.3.4.8 Effect of sample size

The moisture distribution of sealed cement paste varies with the size of specimen. The RH reduction near the edges and surfaces of specimens with low w/c is higher and faster than that of the specimens with high w/c (Tazawa and Miyazawa, 1997). Self-desiccation and consequently autogenous deformation can occur even in moist curing conditions. As the specimen size increases, drying shrinkage becomes smaller because the larger volume of the specimen obstructs water to drive to the environment and self-desiccation takes place. However, autogenous deformation is not affected by the specimen size because it occurs without water movement between concrete and exterior environment (Han and Han, 2005). It was also found that there was a slight increase in autogenous deformation with increasing specimen size. This negligible increase can be attributed to the errors in measurements (Figure 2.17).

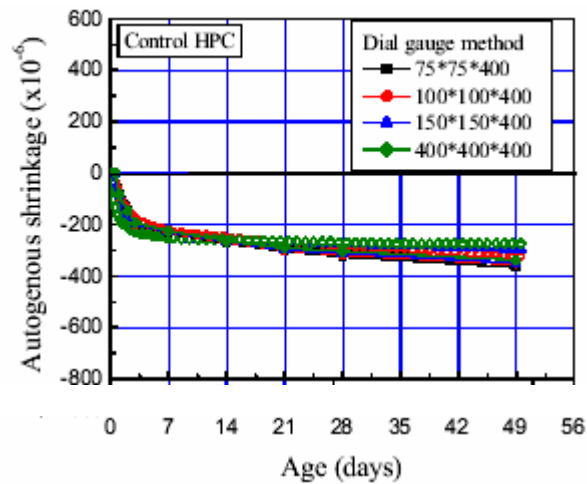


Figure 2.17: Effect of specimen size on autogenous deformation of concrete with the water to cementitious materials ratio of 0.30 (Han and Han, 2005).

2.3.5 Measurement of Autogenous Deformation

One of the attractive encountering subjects in the literature is that there are different methods of measurement of autogenous deformation and inconsistencies between them. It is commonly observed that each publication presents new results and discusses and interprets these, often with little regard to other sets of results (Bjøntegaard et al., 2004). Autogenous deformation of cementitious materials can be measured by either volumetric or linear methods.

2.3.5.1 Volumetric measurement of autogenous deformation

This method of measurement is performed by weighing the volume change in buoyancy of cementitious materials which is, according to the Archimedes principle, cast in a tight rubber bag (commercial condom) placed in temperature controlled water. Because the autogenous deformation is defined as a volume change without weight change, the change in the volume is measured by the change of the water content. Advantage of this method is that the measurements can be started just after casting. Before setting, the measurements have to be volume-based since the plastic state prevents an unambiguous definition of length (Lura, 2003). Disadvantages of this method are stated as (Barcelo et al., 1999): a non accurate temperature control; the pressure exerted on the sample by the membrane and the surrounding liquid may break the growing crystals; the presence of bleeding water may lead to an overestimation of autogenous shrinkage (the measure is then closer to a measure of chemical shrinkage than that of autogenous shrinkage) and may also induce the formation of ettringite. To reduce the misleading effect of bleeding, it has been proposed to rotate the rubber bag on rollers until the setting time of cement paste (Justnes et al., 1999b). Volume changes of cement paste before setting do not induce cracks. Thus, it is acceptable to take the setting time as the starting time of autogenous deformation although there is activation in this stage (Justnes et al., 1999a).

This method is usually performed on samples of cement paste and mortars. It is mentioned that there is a possibility of the aggregate particles scratching the elastic membrane during the volumetric measurements of concrete (Jensen and Hansen, 2001a).

2.3.5.2 Linear measurements of autogenous deformation

In the literature, there are number of tests for autogenous deformation which are mainly based on linear measurement. These are usually performed either by horizontal or vertical measurements on sealed specimens of cementitious materials cast in a rigid mould. Length change of specimens is measured by different techniques (Lura, 2003), such as; cast in nails through end plates (Bjøntegaard et al., 1999), moveable endplates with plugs (Morioka, 1999), cast in strain gauge (Hanehara et al., 1999), vertical cast in bars in a concrete slab (Holt and Leivo, 1999), metal plates placed on top of a vertical specimen (Hansen and Jensen, 1997), and horizontal transverse cast in bars (Lura, 2003). Displacements can be measured by strain gauge, linear variable differential transformers (LVDT), non-contact transducer (for example laser against metal chips) or SOFO sensor based on low-coherence interferometry in single-mode fibers (Glisic and Simon, 2000). Advantage of the linear method is being simple to handle. Conversely, it cannot be used to gain information before setting. The risk of restraining the cement paste in the linear method causes an additional problem. In the very first hours after setting the cement paste is too weak to overcome the friction against a rigid mould. However, this problem can be resolved by lubricating the mould. For this purpose, a special corrugated mould system which combines the advantages of linear and volumetric measurement has been suggested by Jensen and Hansen (1995). Before the setting time, the corrugated mould transforms the volumetric deformation into a linear deformation, and after the setting time a normal, well-defined linear deformation is measured. In this way the linear measurements can be made directly after casting.

2.3.5.3 Inconsistencies between methods of volumetric and linear autogenous deformation

Investigations have shown that there is an inconsistent relation between autogenous deformations measured volumetrically and linearly in the period after setting. For this purpose, hypothesis of isotropic behavior is used to allow comparison of the results between linear and volumetric data with the following equation (Barcelo et al., 1999).

$$\frac{\Delta V}{V} = 3 \cdot \frac{\Delta l}{l} \quad (2.1)$$

Assumptions regarding the effect of the difference of gas pressure in the volumetric experiments or the possibility of an anisotropic behavior have been made. Also inhomogeneous aggregate distribution has an effect on this anisotropic behavior. Further research is needed to confirm this hypothesis.

On the other hand, the measurements show that the volumetric deformation is much higher than the linear deformations. The reason for this may be that the rubber bags (condom) used are not waterproof, and thus allow water to penetrate. The difference in water activity (due to dissolved salts in the pore fluid) constitutes a driving force for osmosis through the membrane, causing a transport of water into the paste. Such an influence is insignificant in the initial phase and shortly after because there is no self-desiccation yet to drive the water through the rubber bag (Bjøntegaard et al., 2004). In the period beyond some days, however, the effect becomes significant (Lura and Jensen, 2005).

It is shown in Figure 2.18 that the volumetric measurement of autogenous shrinkage perfectly corresponds to chemical shrinkage from 0 to 2.5 hours. After that time, the autogenous shrinkage curve is displaced from the chemical shrinkage curve to form a knee point (at 3.5 hours) that is known as *stiffening threshold* (elastic modulus of the paste is about 2 GPa) (Barcelo et al., 1999). Volumetric method can be used for precisely defining the stiffening threshold that corresponds to the transition of mechanical behavior from a dense suspension of solid particles to a porous solid (Barcelo et al., 1999). In linear method, swelling is observed at approximately 6-11 hours that cannot be monitored in volumetric method (Justnes et al., 1999a). This potential early swelling mechanism is widely considered to be associated with ettringite formation (but not proven yet by experiments). Thus, there may be underlying swelling mechanism(s) related to chemical reactions (Bjøntegaard et al., 2004).

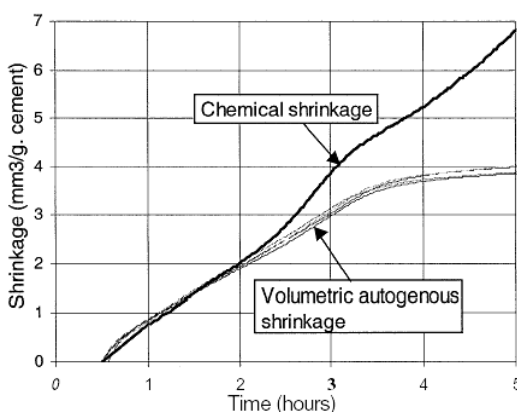


Figure 2.18: Volumetric autogenous deformation vs. chemical shrinkage (Barcelo et al., 1999).

In this thesis, volumetric autogenous deformation measurements have been performed for up to 48 hours on cement paste and mortar specimens, while vertical linear autogenous deformation measurements with cast in nails have been accomplished for a period of a year. However, only the linear autogenous deformation has been monitored on concrete specimens.

2.3.6 Definition of Early Age

There exist different definitions of early ages that are used in studies of shrinkage and autogenous deformation. A number of researchers have monitored autogenous deformation for the first 24 hours after mixing to investigate the early age (Hanehara et al., 1999; Morioka et al., 1999; Loukili et al., 2000; Holt, 2002; Moon et al., 2005; Baroghel-Bounya et al., 2006). On the other hand, some of the researchers preferred monitoring the first 48 hours (Barcelo et al., 1999; Park et al., 1999; Feylessoufi et al., 2001). Holt and Leivo (1999) postulated that the major part of autogenous deformation is to take place during the first 12 hours. Although the ratios of the autogenous deformation of cementitious materials within the first 24 hours to that at later ages are distributed in a wide range, it is known that approximately 80% of volumetric autogenous deformation is completed within the first 24 hours.

2.4 Mitigation of Autogenous Deformation

2.4.1 General

Because of the fact that the autogenous deformation has a tendency of cracking at early ages of cementitious materials, the matter of utilization of autogenous deformation draws attention nowadays. There are a number of methods proposed to mitigate autogenous deformation such as: shrinkage reducing admixtures (SRA), expansive additives, slower reacting (coarser) silica fume, internal curing with lightweight aggregates or superabsorbent polymers or recycled aggregates or wood derived powders and fibers. In addition, to prevent early age cracking due to the autogenous deformation, fibers can be used to enhance tensile strain capacity of cement paste. In another method, which will not be discussed in this section, specific cement composition, such as Portland cement containing higher C_2S content, can be used for minimizing the effects of autogenous deformation. In this section, the methods will be explained briefly and then the use of LWAs and its effects on autogenous deformation will be described.

2.4.2 Usage of Shrinkage Reducing Admixtures

Shrinkage reducing admixtures (SRAs), which are chemicals of lower-alcohol alkyleneoxide adduct or propylene glycol derivatives, are generally used for the purpose of controlling the drying shrinkage of cementitious materials. The addition of the SRA reduces the surface tension of the pore solution, and consequently, the magnitude of autogenous deformation. The advantage of SRA over competing products like shrinkage compensating concrete is that SRA does not undergo any early age expansion to compensate for the shrinkage (Lam and Hooton, 2005). Effect of SRA on autogenous deformation of ordinary Portland (N) and Belite-rich low heat Portland cement (L) are shown in Figure 2.19 (Tanimura et al., 2005). The figure shows that SRA is obviously effective in reducing autogenous deformation. At the age of 91 days, the reduction ratio of autogenous deformation is about 20-30% for NPC-based mixtures and about 40-70% for LPC-based mixtures.

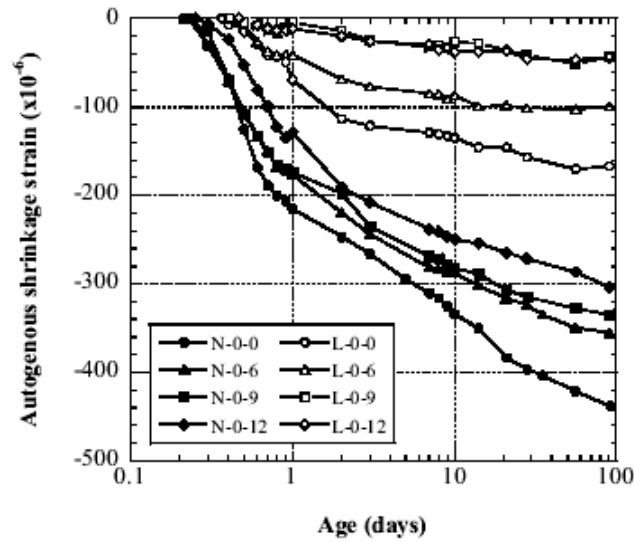


Figure 2.19: Effectiveness of SRA on reducing autogenous deformation of concrete. The last number of each series indicates the content of SRA (kg/m^3) in mixtures (Tanimura et al., 2005).

In addition, Bentz et al. (2001a) stated that if the paste containing SRA is placed on top and exposed directly to the drying environment, a very effective curing layer is created. This layer significantly reduces the bulk mass loss from the specimen and minimizes the water loss from the paste without the SRA that comprises the bottom layer of the system.

2.4.3 Usage of Expansive Additives

To mitigate autogenous deformation, expansive cement can be used to reduce shrinkage by ettringite formation. It is generally accepted that in these cements, expansion is due to forces generated during the growth of preferentially oriented ettringite crystals (Bentz and Jensen, 2004). Alternatively, expansion which is needed to compensate the autogenous deformation (mainly shrinkage) can be obtained by the expansive additives, usually calcareous type periclase (MgO). Hori et al. (1999) showed that the amount of expansion depends on not only the type of expansive additives, but also the type of cement and binders. They also found that free-lime rich calcium sulfoaluminate based expansive additive is more effective than the conventional calcium sulfoaluminate based one in reducing the autogenous deformation of high-fluidity mortar. Effect of expansive

additives on autogenous deformation of OPC is shown in Figure 2.20 as presented by Tanimura et al. (2005). They stated that at the time when expansive additive is added the cement paste shows expansion almost correspond to the time when the autogenous shrinkage strain of reference high strength concrete (HSC) develops significantly, indicating that expansive additives effectively compensate the autogenous deformation from early ages. It is also known that this type of expansion causes an irregular and unpredictable overall response which is difficult to control.

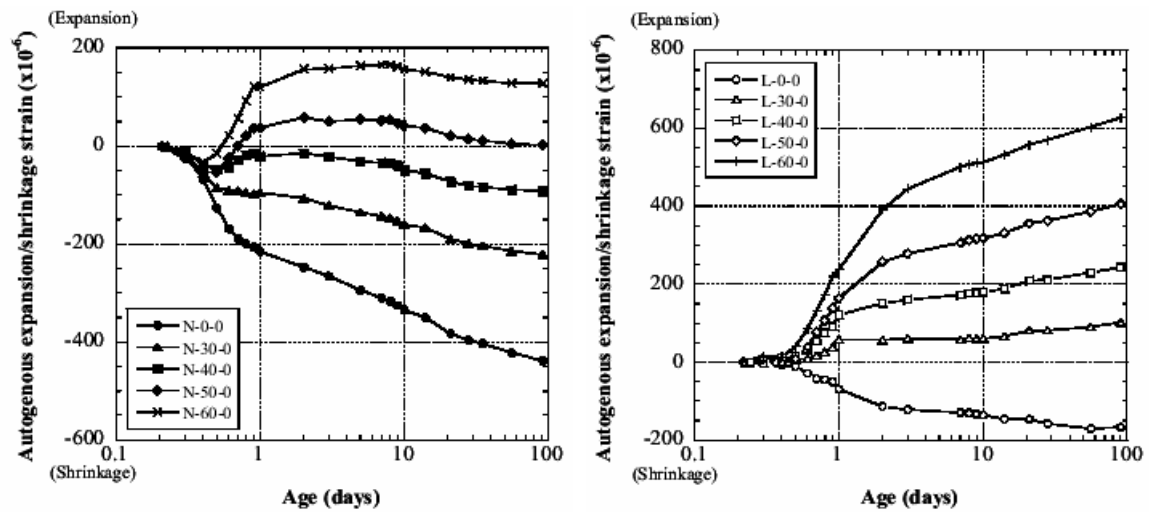


Figure 2.20: Effectiveness of expansive additives on reducing autogenous deformation of concrete. The first number of each series indicates the content of expansive additive (kg/m^3) in the mixtures (Tanimura et al., 2005).

It has also been suggested that in low w/c concretes, some cement could be saved by replacing the coarser cement particles with relatively inert fillers, such as ground sand or limestone powder (Bentz, 2005b). In this method, both the reduction in cement content and the expansive property of limestone will have beneficial effect on reducing the autogenous deformation.

2.4.4 The Use of a Slower Reacting (Coarser) Silica Fume

It was previously demonstrated (Section 2.3.4.4) that the addition of silica fume increases the autogenous deformation due to the fact that silica fume particles are much

finer than the cement and they lead to the formation of finer pore structure. On the other hand, Bentz et al. (2002) proposed the use of a slower reacting (coarser) silica fume to mitigate autogenous deformation. Although they did not find any significant reduction in a test period of approximately 20 days, they mentioned that an additional benefit of this method, that was successful in reducing autogenous deformation, may be that both degree of hydration and measured compressive strength increase at later ages due to the increased and persistent availability of moisture.

2.4.5 Internal Curing

It is well known that conventional curing techniques that can be used for drying shrinkage are not effective in mitigating autogenous deformation. In particular, in high strength concrete, because of its denser microstructure, it is difficult to cure the inner part of the member. One strategy to override the RH loss due to autogenous deformation is internal curing, which relies on providing a “sacrificial” set of larger water-filled pores within the concrete microstructures that will empty first while the smaller pores in the hydrating binder paste will remain saturated (Bentz and Stutzman, 2006). Moreover, in concrete the larger pores are the first to loose their internal water as demonstrated by Koenders and van Bruegel (1997) (Figure 2.21).

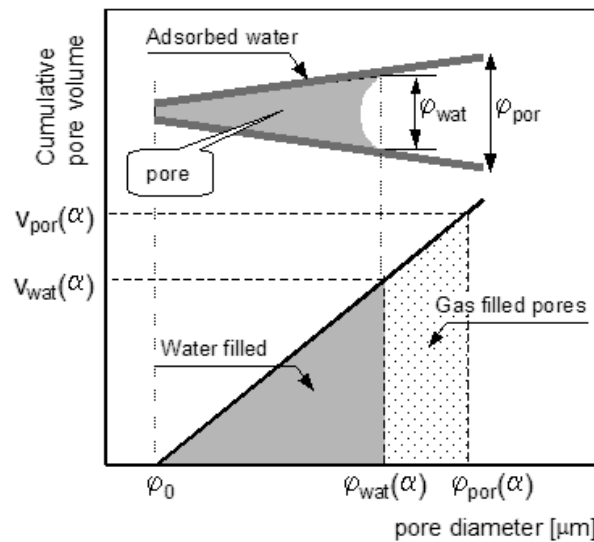


Figure 2.21: Schematic representation of the pore size distribution (Koenders and van Bruegel, 1997).

The shrinkage-reducing admixture operates by decreasing the surface tension of pore solution, while the internal curing changes the size of the pores that were emptied due to self-desiccation. RILEM TC 196 ICC defined the internal curing as “introduction of a component into concrete mixture that serves as a curing agent that performs as a water reservoir, which gradually releases water”. On the other hand, internal sealing by water soluble chemicals will reduce water evaporation under drying condition (Dhir et al., 1994) and is unable to prevent self-desiccation (Lura, 2003). Internal curing can be performed by lightweight aggregates, super-absorbent polymers, recycled aggregates and wood derived powders or fibers. The internal curing with lightweight aggregates will be detailed after giving brief information about other mitigation methods mentioned above.

2.4.5.1 Lightweight aggregates

Using the porous and absorbent lightweight aggregates as water reservoirs was first proposed by Philleo (1991). Weber and Reinhardt (1997) later introduced the new term *autogenous curing*. Water is transported from the LWA to the cement paste first by capillary suction and later by vapor diffusion and subsequent capillary condensation. This results in filling the pores with new hydration products, which might have caused self-desiccation to proceed. The partial replacement of normal weight aggregate with LWA is investigated and found to be effective in reducing the autogenous deformation of cementitious materials.

An effective method has recently been proposed by Bentz (2005c) which is termed as **FLAIR** (Fine Lightweight Aggregates as Internal Reservoirs). This method is based on autogenous distribution of the LWAs (or super-absorbent polymers (SAPs)) saturated with solutions of chemical admixtures such as shrinkage reducing admixtures or corrosion inhibitors. Advantages of the method are notified to be mitigation or avoidance of possible detrimental interactions between chemical admixtures or detrimental influences of the admixture on fresh concrete properties and a potentially more efficient delivery of admixtures that are partially absorbed by the cement during hydration and in the resulting hydration products. It is stated by Bentz (2005c) that further research is needed to determine the applicability of FLAIR to other admixtures

such as corrosion-inhibiting admixtures and admixtures for mitigating alkali-silica reaction, and the practicality of utilizing the technology at ready-mix plants and pre-casting facilities.

2.4.5.2 Super-absorbent polymers

Jensen and Hansen (2001b) have recently proposed a new method, which is based on the use of SAP particles as a water reservoir in the cement-based material. During mixing of the concrete, the SAP will absorb water and form macro inclusions, which essentially consist of only free water. Because of its resemblance to the air entrainment mechanism in frost protection of concrete, the proposed technique is called *water entrainment*. SAPs can be produced with water absorption of up to 5000 times their own weight. They have the ability to absorb a significant amount of liquid from the surroundings and to retain the liquid within their structure without dissolving. In Figure 2.22, beneficial effect of SAPs on autogenous deformation is shown clearly (Jensen and Hansen, 2002).

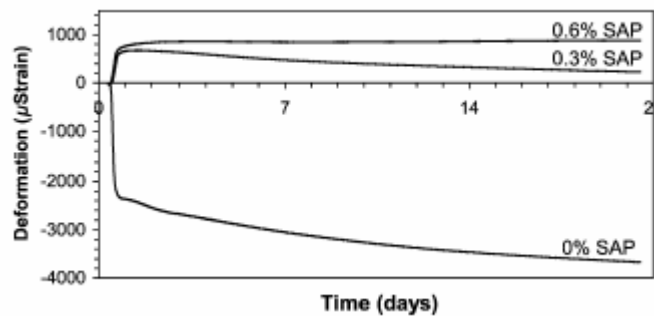


Figure 2.22: Autogenous deformation from setting of cement pastes ($w/c=0.3$) with different amounts of SAPs (Jensen and Hansen, 2002).

2.4.5.3 Recycled aggregates

It is proposed by Maruyama and Sato (2005) that recycled aggregate with the higher rate of absorption than normal weight aggregate can be used as water reservoir. They reported that this aggregate is effective in reducing autogenous deformation of concrete with w/c of 0.25 (Figure 2.23). It was found that autogenous deformation of concrete with recycled aggregate is about 40% smaller than that of concrete with normal weight

aggregate at 28 days. On the contrary, they showed that, under drying environment after removing the seal, the whole shrinkage deformation of concrete with recycled aggregate is developed rapidly and exceeds that of concrete with normal weight aggregate at 120 days after drying.

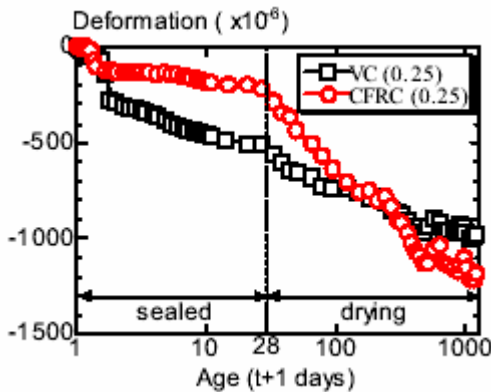


Figure 2.23: Autogenous deformation of VC (concrete with normal aggregate) and CFRC (concrete with recycled aggregate). Sealing is removed after 28 days (Maruyama and Sato, 2005).

2.4.5.4 Wood-derived powders and fibers

Mohr et al. (2005) has recently proposed another method of internal curing, which includes the usage of wood-derived powders and fibers, and is expected to have less unfavorable effects on strength and durability. The powders or fibers contain free water (i.e. water held in large pores and in the lumen) and weakly bound water, both of which may be released into the surrounding, providing relief from self-desiccation and subsequent autogenous deformation. The results of pastes with the w/c of 0.3 contain different amount of wood powder are shown in Figure 2.24.

In this method, the researchers used wood powder (average fiber length of approximately 0.5-1.0 mm), cellulose powder (average fiber lengths of 10 μm and 700 μm), thermo-mechanical cellulose fiber (average fiber length of 1-2 mm), and kraft fiber (average fiber length of 4-5 mm) at different dosages. The cement pore solution absorption capacity of thermo-mechanical cellulose fiber and wood powder are found to be 3.3, while kraft fiber and cellulose powders have a value of 1. The additional water

content for diminishing the autogenous deformation is chosen as approximately equal to 0.050 times of cementitious materials. It was concluded that thermo-mechanical cellulose fiber and wood powder reduced the autogenous deformation to a greater extent than the superabsorbent polymers when equivalent water entrainment rates are used. On the contrary, kraft pulp fibers and cellulose powders were ineffective for internal curing applications.

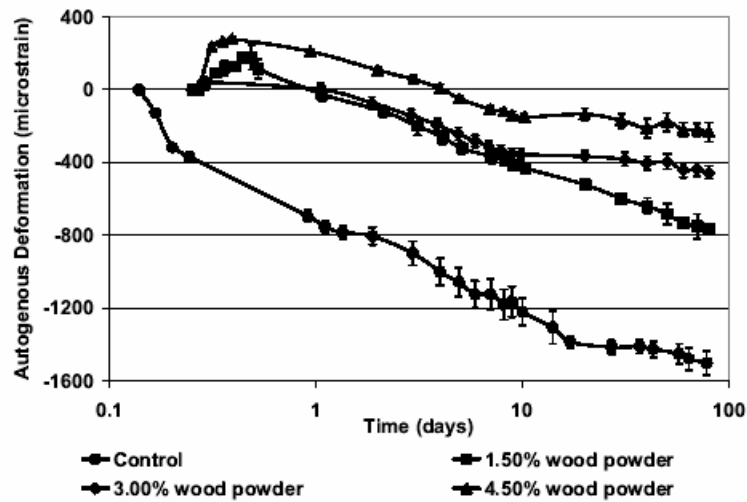


Figure 2.24: Autogenous deformation of cement paste with wood powder (Mohr et al., 2005).

2.4.6 Effect of Fiber Addition

It is well known that shrinkage cracking can be prevented by increasing the tensile strain deformation capacity by addition of fibers in matrices. It must be noted that the fibers cannot preclude the phenomena of autogenous deformation of cement paste while they are able to improve the cracking tendency of cement paste resulted from autogenous deformation, as well as other deformations. Loukili et al. (1999) examined the compact reinforced composite (CRC) with a w/c of 0.20, silica fume content of 24% weight of cement and 6% of added steel fiber. The autogenous deformation of CRC is shown to remain practically constant 10 days after water addition while shrinkage of the plain matrix developed very slowly. Interestingly, a sudden change is noted in shrinkage kinetics at the 10th day. The authors also stated that during the first week the high shrinkage strains lead to internal stresses in paste as well as in aggregates. In the CRC

these microcracks are bridged by steel fibers that allow retention of the tensile stresses. In the plain matrix the microcracking leads to relaxation of the specimen and the shrinkage will resume in the matrix.

Moreover, Mesbah et al. (2000) showed that the polypropylene fibers efficiently decrease and retard the shrinkage of mortars with high w/c at early ages. The 8-hours shrinkage decreased approximately 80% by using 0.25% volume content of polypropylene fibers, while metallic fibers only reduced the shrinkage 15% at the same volume content. The authors stated that the efficiency of polypropylene fibers on reducing shrinkage at early ages could be due to the bleeding effect of the fibers. Effect of polypropylene fibers on autogenous deformation of cementitious materials needs to be studied further as a future research.

Farhat et al. (2007) have recently studied the autogenous deformation of high performance fibre-reinforced cementitious composite CARDIFRC® developed in Cardiff University. They used 50×50×250 mm prisms for determining the autogenous deformation of specimens with and without fibers. The measurements started at 19 hours after casting. The effect of fibers in mitigating autogenous deformation is shown in Figure 2.25.

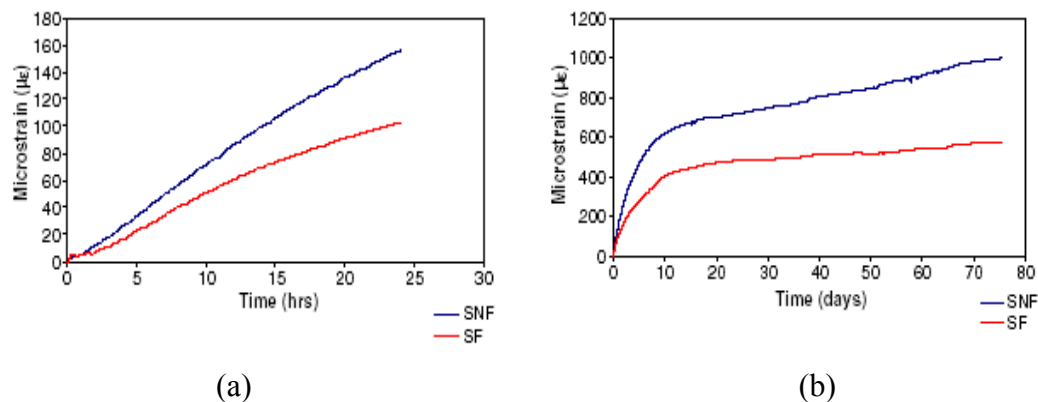


Figure 2.25: Autogenous deformation variation with time for mixes with (SF) and without fibers (SNF) at different times of the experimental study: (a) 0–24 h, (b) up to 75 days (Farhat et al., 2007).

The mixes without fibers (SNF) exhibit a rapid development of autogenous shrinkage strains. This increase in shrinkage strains takes place at a higher rate than for the mixes

containing fibers (SF). It has been noted that the inclusion of fibers in the matrix has a restraining effect on the development of the autogenous shrinkage strains. Their results show that the autogenous shrinkage strains of specimen without fibers are 74% larger comparing to those of specimens with fibers at 75 days.

Farhat et al. (2007) also monitored the autogenous deformation on 100×100×500 mm large beams. They showed that the autogenous deformation readings of specimens without fibers give very similar results, while the uneven distribution of fibers in the large specimens caused very large scatter in the autogenous deformation readings. Their image analysis results showed that the mitigation ratio of autogenous deformation of CARDIFRC has been affected by the distribution of fibers.

2.4.7 Internal Curing with LWAs

In Table 2.2 the application of internal curing is briefly summarized (Roberts, 2005).

Table 2.2: Applications (uses) benefited by internal curing (Roberts, 2005).

	Low autogenous shrinkage	Less cracking	Higher early age strength	Higher 3-day flexural strength	7-day compressive strength in 3 days	Lower turnaround time	Lower permeability	Improved rheology	Utilization of cement	Lower maintenance	Greater durability	Use of higher levels of fly ash	Higher modulus of elasticity	Sharper edges	Greater curing predictability	Higher performance
Architectural concrete		✓						✓		✓	✓			✓	✓	
Bridges	✓	✓	✓				✓	✓	✓	✓	✓				✓	✓
Concrete block		✓	✓					✓	✓					✓	✓	
Concrete pipe				✓		✓	✓									
High performance concrete	✓	✓	✓		✓		✓	✓	✓	✓	✓				✓	✓
High fly-ash concrete					✓				✓	✓	✓	✓			✓	
Mass concrete												✓				
Pavements		✓	✓	✓	✓				✓		✓	✓			✓	✓
Parking structures	✓	✓	✓				✓		✓	✓	✓				✓	✓
Precast		✓	✓	✓		✓			✓						✓	✓
Prestressed			✓				✓	✓	✓						✓	
Self-consolidating concrete								✓								
Tilt-up			✓		✓								✓			
Walls		✓	✓				✓	✓			✓					

All 14 uses receive all 16 benefits. (✓) indicates the most critical.

The use of pre-saturated lightweight aggregate for internal source of water to mitigate autogenous deformation and an investigation of its effect on fracture properties of high strength cementitious materials are the main objective of this thesis. Effectiveness of internal curing by LWAs has been studied by number of researchers (Weber and Reinhardt, 1997; Bentz and Snyder, 1999; Kohno et al., 1999; Takada et al., 1999; Bentur et al., 2001; Zhutovsky et al., 2002a; Lura, 2003; Geiker et al., 2004).

2.4.7.1 Properties of LWA

According to the Kelvin-Laplace equation, increasing the RH content of the pores in cement paste with LWAs minimizes the autogenous deformation considering that the shrinkage stress is governed by the size of the empty pores (Bentz and Snyder, 1999). In addition, Bentur et al. (2001) showed that the replacement of even air-dried fine artificial LWAs with normal weight aggregate significantly reduced the magnitude of autogenous shrinkage of high strength concrete, but the water retained in air-dried lightweight aggregate is not sufficient to totally eliminate autogenous deformation. Accordingly, it is important to know the saturation degree and also the amount of desorption of LWA. Moreover, it is evident that density, pore structure, and porosity of LWA are factors crucially effective on internal curing. It is shown in Figure 2.26 that the larger the aggregates, the higher the absorption (Lura, 2003).

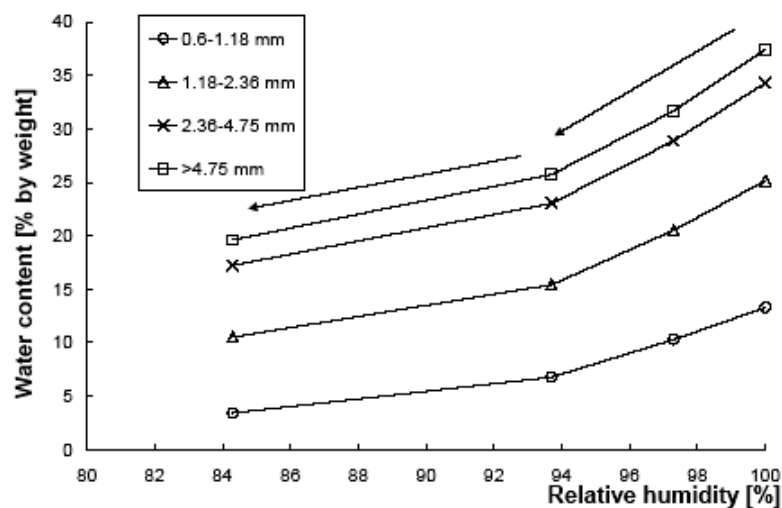


Figure 2.26: Desorption isotherms of pumice fractions at 25 °C from vacuum-saturated conditions (Lura, 2003).

It can be seen from Figure 2.26 that the smallest size fraction loses about 80% of the absorbed water at 84% RH, while the two coarsest pumices lose only about 50%. One would expect that the coarsest aggregates, having supposedly the largest pores, would lose proportionately more water than the smaller ones. The reason for this is that the emptying the larger pores will not occur until the RH drops beyond the equilibrium value for the smaller entryways. Since a significant amount of water is entrapped in the internal porosity of the coarser fractions, it seems viable to consider that only about half of it would be available for internal curing. When finer fractions are used the absorption is lower, but almost 80% of the water is lost by 85% RH (Lura, 2003).

2.4.7.2 Amount of water for internal curing

Recent studies have shown that LWA can release water into the cement paste from a surface layer approximately 1mm thick (Lura, 2003; Akcay et al., 2005). On the other hand, Bentz and Snyder (1999) have assumed that the thickness of water entrainment was about 100 μm from the outer surface of LWA. In this respect, it is crucial to determine the dispersion of these reservoirs within the matrix, and this issue will be discussed in more detail in Chapter 7.

Based on the above explanations, it can be said straightforwardly that the determination of the amount of water for mitigating the autogenous deformation is needed. Bentz and Snyder (1999) have previously proposed the following expressions for calculating the volume of water and LWA required for internal curing.

$$V_{wat} (m^3 \text{ water} / m^3 \text{ concrete}) = \frac{C_f \cdot CS \cdot \alpha_{max}}{\rho_w} \quad (2.2)$$

$$V_{LWA} = \frac{V_{wat}}{S \cdot \phi_{LWA}} \quad (2.3)$$

where, V_{wat} is the volume of water entrained in the LWA, C_f (kg/m^3) is the cement content of mixture, CS is the chemical shrinkage, α_{max} is the maximum degree of hydration (can be estimated as $(w/c)/0.40$), ρ_w is the density of water, S is the saturation of LWA and ϕ_{LWA} is the porosity of LWA. It should be noted that the authors proposed

these equations for fine size LWAs only. On the other hand, Zhutovsky et al. (2002b) suggest that the amount of water required to eliminate the autogenous deformation is considerably higher than that calculated from Eq. (2.2). This equation provides 18 to 23 kg/m³ entrained water to the mixture, while the required value is at least 30~40 kg/m.³ The reason for this difference is that the water in LWA cannot be totally released to the system, which can be explained by distinction between the absorption and desorption isotherms of LWA. Thus, Zhutovsky et al. (2002b) proposed the addition of η efficiency factor to the equation which is defined as the fraction of water absorbed in saturated aggregate that can counteract self-desiccation.

$$V_{LWA} = \frac{V_{wat}}{S \cdot \phi_{LWA} \cdot \eta} \quad (2.4)$$

If the LWAs are small in size and their pore structures are large and coarse, η is going to approach 1. Small size of particles would result in better dispersion of water reservoirs, making the paste volume to be more accessible for the water in the internal reservoirs. However, the coarser LWA has greater volumes of pores and also higher capacity of absorption than that of finer fraction, especially for natural LWAs.

Jensen and Hansen (2001b) proposed another approach to calculate the amount of water required for internal curing, which is based on the assumption that during the hardening the internal curing supplies the water to keep the cement paste in a saturated condition. They modified the volumetric calculation of Power's model as shown in Figure 2.27. It was shown that the self-desiccation of cement paste is prevented by this entrained water. When cement hydration is hindered due to the minimum porosity requirement of the precipitated cement gel, the RH is still 100%, and hence self-desiccation is prevented.

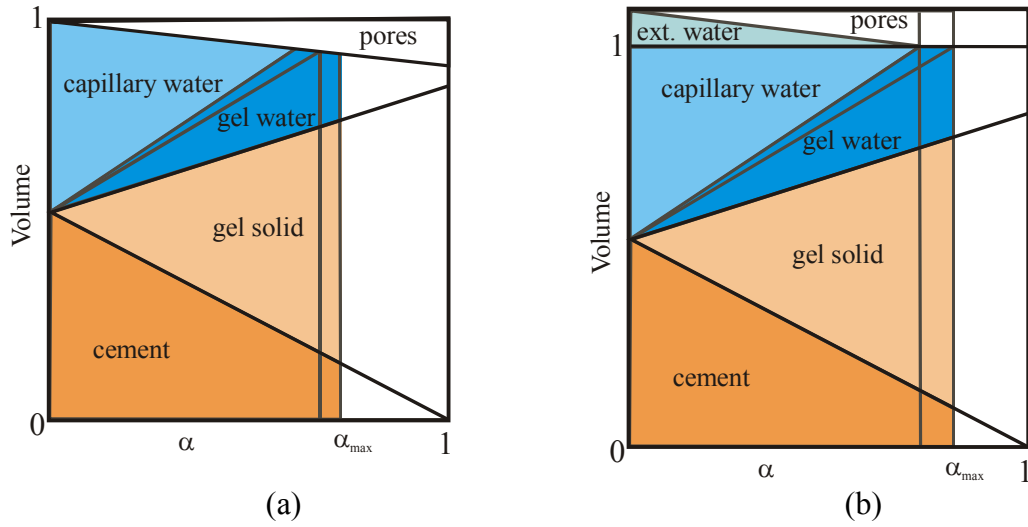


Figure 2.27: Volumetric phase composition of cement paste as function of the degree of hydration with $w/c=0.30$ (a) and with entraining water at $w/c = 0.30 + 0.05$ (b). Due to the low w/c ratio, full hydration of the cement cannot be obtained (Jensen and Hansen, 2001b).

At a low w/c ratio hydration stops when all the available space is taken up by gel water, gel solid and unhydrated cement. The relative volume of initially entrained water should equal to the chemical shrinkage developed at the maximum degree of hydration. The amount of entrained water can be calculated from the following equation (Jensen and Hansen, 2001b).

$$(w/c)_e = 0.18 \cdot (w/c) \quad \text{for} \quad (w/c) \leq 0.36 \quad (2.5)$$

$$(w/c)_e = 0.42 - (w/c) \quad \text{for} \quad 0.36 \leq (w/c) \leq 0.42$$

It is obvious that in addition to the type of cement, the presence of supplementary materials particularly silica fume alters the amount of entrained water required (Lura, 2003). It has been proposed that the quantity of entrained water can be calculated using the following equation in the case of silica fume usage where the (sf/c) is the ratio of silica fume to the cement by weight.

for $(w/c) \leq (0.36 + 0.28 \cdot (sf/c))$

$$(w/c)_e = \frac{0.2 + 0.69 \cdot (sf/c)}{1.12 + 0.88(sf/c)} \cdot (w/c) \quad (2.6)$$

for $(0.36 + 0.28 \cdot (sf/c)) \leq (w/c) \leq (0.42 + 0.73 \cdot (sf/c))$

$$(w/c)_e = (0.42 + 0.73 \cdot (sf/c)) - (w/c)$$

In Figure 2.28, it was shown that the amount of the entrained water to mitigate self-desiccation increased with increasing amount of silica fume (Lura, 2003).

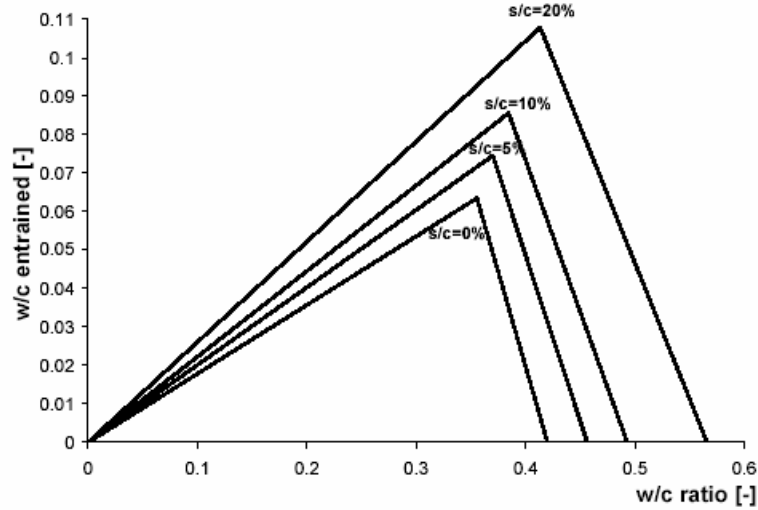


Figure 2.28: Entrained w/c ratio necessary to avoid self-desiccation as a function of w/c ratio for different sf/c ratios (Lura, 2003).

2.4.7.3 Effects of LWAs on properties of concrete

As is mentioned before, one of the most important parameters is probably the distribution of internal curing reservoirs in a cementitious materials system. The interfacial transition zone (ITZ) is the weakest component of mortar and concrete because of the higher porosity and presence of higher amount of $\text{Ca}(\text{OH})_2$. However, ITZ with LWA is enhanced by the presence of LWA. While the width of the ITZ for normal weight concrete is about 50-100 μm that for light weight concrete is found to be

approximately 5-10 μm (Lo and Cui, 2004). When the paste is in a plastic state, some of the paste infiltrates into the LWA. As the cement hydrates, the voids in the lightweight aggregate allow the C-S-H structure to form and grow with minimal hindrance (Lam and Hooton, 2005). The amount of paste penetration depends on the microstructure of the surface layer of the aggregate, the particle size distribution of the cement and silica fume, and the viscosity of the paste (Zhang and Gjorv, 1992). Ettringite crystals can form on the outer skin of the aggregate due to the roughness of the surface of LWA. The interface between the lightweight aggregate and cement paste is tight and characterized by a mechanical interlocking in combination with a chemical interaction in the form of pozzolanic reaction (Zhang and Gjorv, 1990). In addition, the absorption of mix water into the LWA may reduce the w/c ratio locally at the aggregate surfaces, and prevent bleeding water from accumulating at the aggregate surfaces (EuroLightCon/R2, 1998). The bleeding effect on aggregate surfaces is also reduced due to the decreased response of the LWA to vibration energy during compaction of the concrete. Due to the high amount of water in the paste-aggregate interfacial zone, the amount of cement converted into hydration product is higher than at some distance from the aggregate surface (Takada et al., 1999). Lo and Cui (2004) stated that the absence of the wall effect and the lack of a distinct boundary at the ITZ improved the integrity of lightweight concrete, leading to a higher initial strength (91%) in the first 7 days.

It is well known that the porosity and permeability of concrete is highly dependent on the ITZ and also microcracks in the matrix phases have influences on these properties of concrete. As explained before, ITZ enhanced using LWA will result in less permeable and lower porosity properties than normal weight concrete. Cement near the LWAs will be better hydrated than that away from the LWAs with the presence of LWAs and internal curing. Because of the effect of infiltration of cement paste by the LWA and well-hydrated cement grains, dense shell is formed around the LWA which has favorable effect on permeability of cementitious materials. In addition, the use of LWA reduces the thermal conductivity of concrete, thus the cementitious materials with LWAs are widely used as thermal insulation materials in construction industry.

2.5 Fracture Mechanics of Concrete

2.5.1 General

The lightweight concrete (LWC) is defined as concrete with density lower than 1850 kg/m^3 and with the minimum 28-day compressive strength of 17 MPa (ASTM C330; Neville, 1997). Since LWAs produce more microcracks, the concrete containing these aggregates behaves more ductile (i.e. less brittle) than normal cementitious materials (Akçay and Tasdemir, 2006a). On the other hand, the use of LWA instead of dense aggregate is expected to result in a lower strength. It is obvious that the amount of LWA for internal curing must be optimized according to the mechanical and fracture properties of cementitious materials which is detailed in Chapter 8.

LWCs are briefly classified as lightweight aggregate concrete and aerated concrete. LWC is produced using either natural or artificial lightweight aggregates. Natural LWAs are pumice, perlite, volcanic tuff and cinder or even unprocessed by-product of furnace clinker, furnace bottom ash and wood particles as a waste material. In addition, artificial LWAs are made from expanded or agglomerated clay, shale or pulverized fuel ash (Arisoy, 2002). On the other hand, aerated concrete is produced by formation of voids in the cement paste using gas or air entraining chemical agents or addition of foam. Gas producing chemical (i.e. hydrogen peroxide, aluminium or zinc powder) produce gas bubbles (0.1 to 1 mm in diameter) in mortar as a result of the reaction of powder with Ca(OH)_2 or alkalis. Hydrolysed protein or resin soaps are usually used as foaming agents, while performed stable foam (i.e. fire fighting foam) can also be used (Du and Folliard, 2005).

The use of structural LWC is of great practical importance owing mainly to their superiority over normal concretes because of thermal insulating properties in view of the current energy problem. Some other important benefits can be summarized as, i) Because of the reduction in density, formwork needs to stand a lower pressure for the same volume of the material. The total weight of the materials to be handled is reduced with a consequent increase in both production and transportation rates. ii) Dead load is reduced for the structure, which in turn reduces the dimensions of the foundations and other structural elements (Tasdemir et al., 2002). This is especially important where

there is a poor ground condition. iii) Less reinforcement is needed, since dead loads and thus the design moments are reduced, especially when lateral earthquake forces are considered, where the forces exerted on the buildings are proportional to the dead weight of the structure. Disadvantages of LWC in the use of construction, however, can be given as: i) Because of high porosity its strength is lower than that of normal concrete, ii) Insulation against moisture is necessary, iii) Resistance to abrasion is poor, iv) Shear strengths are lower than those of dense concretes, v) Deflections are larger, and creep is higher to a certain extent, because long-term behavior under sustained load is mainly related to the low modulus of elasticity of the aggregate, resulting in increase in both instantaneous deformation and creep (Tasdemir, 1982).

It is obvious that the mechanical behavior of structures is dominated by the properties and mechanical behavior of the materials used. In application, concrete is usually designed on the basis of compressive strength theory, in which the brittleness of concrete is ignored. For this reason, fracture parameters of concrete have to be defined along with its brittleness. In this section, first of all, the fracture mechanics of concrete will be explained briefly and then its application on LWC will be given in more detail.

2.5.2 Linear Elastic Fracture Mechanics

The introduction of Linear Elastic Fracture Mechanics (LEFM) by Griffith, for homogeneous and brittle materials such as glass, was a turning point for the theory of fracture mechanics. The fundamental contributions of Orowan and Irwin were based on developing this theory for the case of non-brittle materials (Irvin, 1957). While Kaplan (1964) was the first who accomplished to successfully adopt fracture mechanics theories to concrete, which is a quasi-brittle material, he also was the one who pointed out that fracture parameters of concrete cannot be extracted using LEFM due to the existence of the fracture process zone (FPZ), defined as the inelastic zone around the crack tip (Mindess and Diamond, 1982; Tasdemir and Karihaloo, 2001).

2.5.2.1 Griffith theory of brittle fracture

Griffith (1920) postulated that the large discrepancy between the theoretical and real tensile strengths of hard brittle materials is a result of the presence of small cracks and other crack-like defects in these materials. This theory can be demonstrated in glass sheet as shown in Figure 2.29. In the condition of constant remotely applied stress, with the presence of a sharp crack in a sheet of brittle material, it was demonstrated that the stresses near the crack tip tend to approach infinity (Karihaloo, 1995). Thus, the stress state in the vicinity of the crack tip proved to be crucial for the load capacity of the sheet.

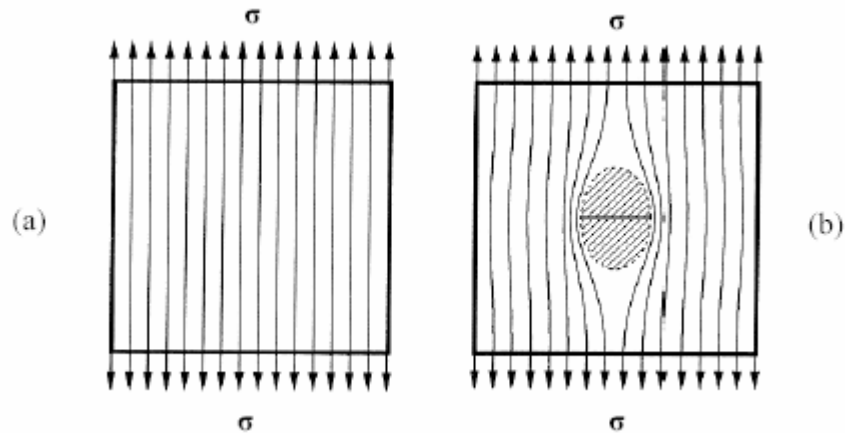


Figure 2.29: Stress flow lines in thin sheet subjected to axial tensile loading, (a) an uncracked plate; (b) a cracked sheet (Karihaloo, 1995).

Considering a large plate of unit thickness containing a sharp crack of length $2a$ subjected to a uniform tensile strength, for the crack initiation, a certain amount of potential energy must be accumulated in the system, available for release into the crack tips.

$$\sigma = \sqrt{\frac{2E\gamma}{\pi a}} \quad (2.7)$$

where E is the modulus of elasticity, γ is the surface energy density. If the stress σ reaches the value σ_c , the brittle material will fracture. It is shown that the strength of brittle material is dependent of physical parameters.

2.5.2.2 Irwin theory of brittle fracture

Irwin (1957) modified the Griffith Theory to the ductile materials. He introduced the new strain energy release rate by adding the energy used for plastic deformation (γ_p) to the strain energy determined by Griffith (1920) as follows

$$\sigma = \sqrt{\frac{2 E(\gamma + \gamma_p)}{\pi a}} \quad (2.8)$$

He also showed that the stresses near a sharp crack tip always demonstrate the similar deviation, called r -singularity, where r is the distance from the crack tip ($r \ll 2a$). This singularity is independent of the boundary conditions, geometry and loading. It is also independent of the opening mode of the crack. Generally, there are three possible modes of deformation at a crack tip as shown in Figure 2.30. These are:

- Mode I- opening or tensile mode, where the crack surfaces move directly apart which was examined originally by Griffith (1920).
- Mode II-sliding or in-plane shear mode, where the crack surfaces slide over one another in a direction perpendicular to the leading edge of the crack.
- Mode III- tearing or antiplane shear mode, where the crack surfaces move relative to one another and parallel to the leading edge of the crack.

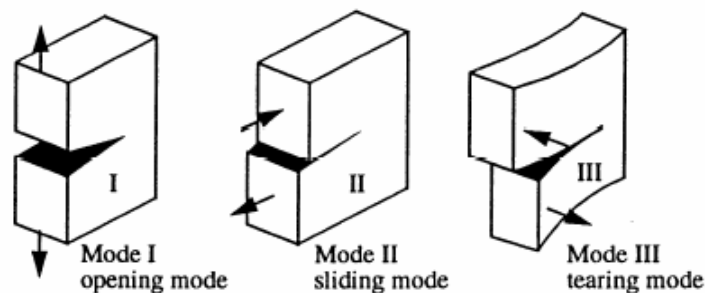


Figure 2.30: Fundamental crack modes (Karihaloo, 1995).

All these modes (particularly, Mode II) exhibit the same singularity near the crack. Considering opening mode of stress at the crack tip in a plane body of infinite extent subjected to a uniform stress as shown in Figure 2.31, the stress and deformation components of a point in the vicinity of the crack tip are calculated in polar coordinates (r and θ) as

$$\sigma_{ij} = \frac{K_I}{\sqrt{2\pi r}} f_{ij}(\theta) + \dots \quad i, j \in \{x, y\} \quad (2.9)$$

$$u_i = \frac{K_I(1+\nu)}{E} \sqrt{\frac{2r}{\pi}} g_i(\theta) + \dots \quad i \in \{x, y\} \quad (2.10)$$

where, E and ν are the Young modulus and the Poisson ratio of material, respectively.

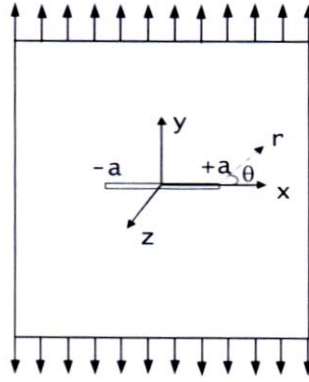


Figure 2.31: An infinite elastic body with a sharp crack length of $2a$ under mode I loading.

The factor K_I is the stress intensity factor and is dependent on the boundary conditions, geometry and loading mode of the system. Also, for these opening modes a square root r -singularity will be found, but the stress intensity factor will correspond to the loading of these situations, i.e. K_{II} and K_{III} . For the geometry shown in Figure 2.31, K_I is given by

$$K_I = \sigma \sqrt{\pi a} \quad (2.11)$$

According to the Irwin fracture criterion, if the stress intensity factor reaches a critical value, K_{Ic} , which is assumed to be a material constant and called the fracture toughness, propagation occur, and will be catastrophic, i.e. uncontrolled for a constant load. Thus, until the external stress reaches the value σ_c , no crack propagation will occur. If geometry and loading corresponding to the example investigated by Griffith (1920) is considered, the critical stress intensity factor at each tip of the crack will be equal to

$$K_{Ic} = \sigma_c \sqrt{\pi a} \quad (2.12)$$

This relation leads to a very important result. By inserting Eq(2.7) into Eq(2.12) it is seen that the two approaches essentially lead to the same result:

$$K_{Ic}^2 = EG_c \quad (2.13)$$

where, G_c is the critical Griffith surface energy density or the critical energy release rate, with $G_c=2\gamma$. Nonetheless, it is easier to determine the critical stress intensity factors using Irwin's fracture (Karihaloo, 1995).

2.5.2.3 Cohesive Crack Models

The Griffith and Irwin theories of brittle fracture have some problems as the stresses near the crack tips are assumed to approach infinity which causes an inconsistency between the linear elastic models and real situation where the materials have tensile strength. Also the theories disregard primary assumptions for elasticity regarding small strains. Barenblatt (1959) proposed a model to overcome these problems, assuming that certain distributions of large cohesive forces are acting in a small zone near the crack tip and that the crack faces close smoothly (Figure 2.32). This distribution is generally unknown and it is assumed that the stress intensity factor is zero at the crack faces.

Karihaloo (1995) stated that the model is essentially corresponding to Griffith and Irwin's crack models, but the important issue is that it presents a hypothesis of what physically happens close to the crack tips.

Dugdale (1960) proposed a model for explaining what happens in the fracture process zone by using similar cohesive zone model on elastic-plastic materials, assuming that the cohesive stress is constant and invariant with the crack opening. Furthermore, it was also assumed that the fracture process zone is infinite and in the same order of magnitude as the crack itself. In fact, a plastic zone will form at each crack tip and extends as far as the yield capacity is sufficient (Farhat, 2004). Consequently, the closing stress is known and will be constant and equal to the yield stress of material over the plastic zone.

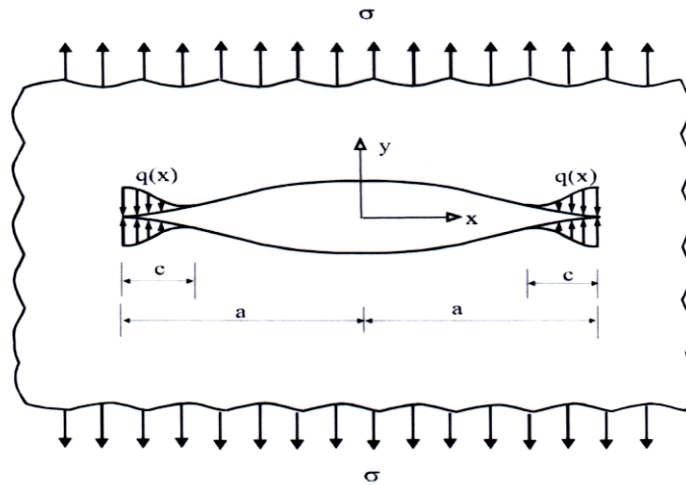
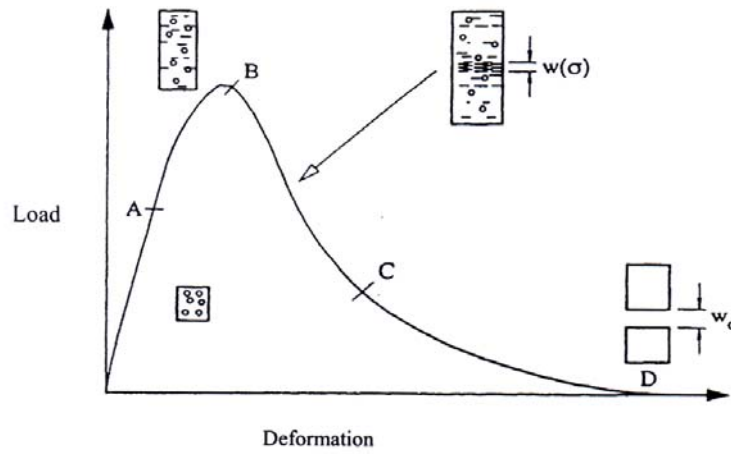


Figure 2.32: Barenblatt's cohesive crack model in mode I. Note $c \ll a$.

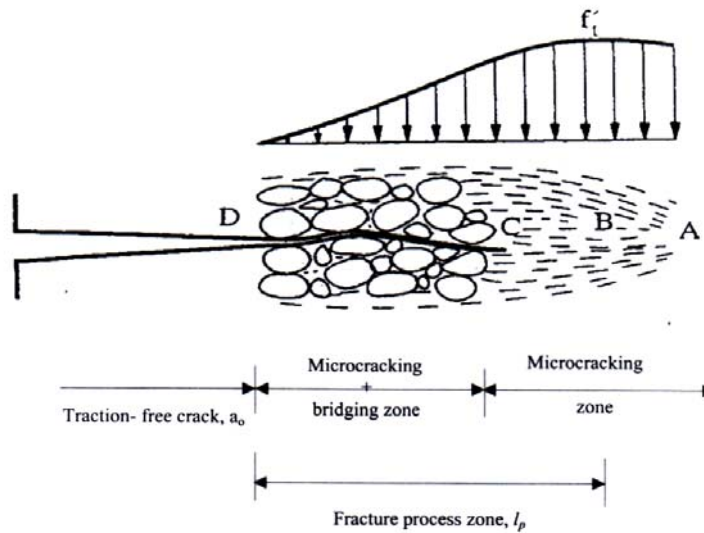
2.5.3 Application of LEFM to Concrete

As a result of the studies conducted on concrete, researchers arrived at the conviction that LEFM, which is based on the assumption that the stress approaches infinity at the crack tip, is not valid for concrete due to the existence of FPZ (Kaplan, 1961; Mindess and Diamond, 1982; Karihaloo, 1995). The detailed research concluded that the cement based materials behave different from the theories of linear elastic fracture mechanics (Alaee, 2002). The typical load-deformation response of concrete in tension is given in Figure 2.33. It can be seen that a substantial non-linearity exists before the maximum stress is reached (AB) and there is a region of tension softening after the attainment of the maximum load (BC). The tail region of tension softening (CD) is caused by the aggregate interlock and other frictional effects, meaning that the deformation increases

with decreasing tensile capacity (area of BCD). The material that exhibits this kind of behavior is called quasi-brittle material. Consequently, tension softening part of the load deformation curve leads to an increase in the fracture surface area, thus the application of LEFM to concrete is limited.



(a)



(b)

Figure 2.33: Typical load-deformation response of quasi-brittle materials in tension/flexure (a) and the fracture process zone ahead of the real traction-free crack (b) (Karihaloo, 1995).

2.5.4 Non-linear Fracture Mechanics

Extensive amount of research has been conducted over years to modify LEFM, to make it applicable to concrete and to establish the theories of nonlinear fracture mechanics. The differences between concepts are briefly shown in Figure 2.34.

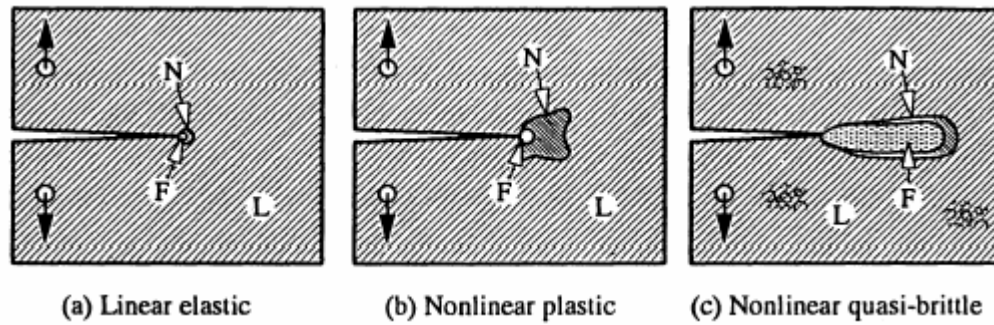


Figure 2.34: Main differences between materials modeling with linear elastic fracture mechanics (a), non-linear plastic fracture mechanics (Dugdale 1959) (b) and non-linear quasi-brittle fracture mechanics (c). Linear elastic material is denoted with an L, non-linear material behavior with an N, while fracture behavior is denoted by F (Karihaloo 1995).

The predominant fracture mechanics based approaches that have been proposed for the determination of the fracture parameters of concrete are; the fictitious crack model (Hillerborg, et al., 1976), the crack band model (Bažant and Oh, 1983), the size effect law (Bažant, 1984), the two parameter fracture model (Jenq and Shah, 1985), the effective crack model (Nallathambi and Karihaloo, 1990), and the recently proposed concepts of boundary effect and local fracture energy distribution (Hu and Wittmann, 2000, Duan et al., 2003). The fictitious crack model, the size effect law, and the two parameter models are among the RILEM recommendations (1985).

2.5.4.1 Fictitious crack model (FCM)

The first non-linear theory of fracture mechanics for concrete was proposed by Hillerborg et al. (1976). The model has similarities with cohesive crack models in that cohesive stresses result in a smooth closure of the crack tips. However, FCM accepts

that the closing stresses are inconstant and increase up to the tensile strength of the material, f_t at the tip of the fictitious crack, as shown in Figure 2.35.

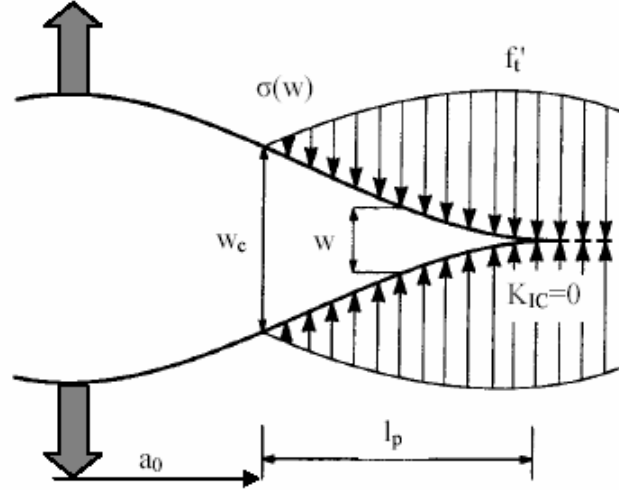


Figure 2.35: Fictitious crack behind the real traction-free crack (Karihaloo, 1995).

According to the fictitious crack model fracture energy (G_F) is determined using the area under the load versus displacement at mid-span curve as:

$$G_F = \int_0^{w_c} \sigma(w) dw \quad (2.14)$$

where, w_c is the critical crack opening at which the closing stress is equal to zero.

Characteristic length (l_{ch}), another material parameter, is defined in terms of modulus of elasticity (E), fracture energy (G_F), and direct tensile strength (f'_t), by the equation

$$l_{ch} = \frac{EG_f}{(f'_t)^2} \quad (2.15)$$

The characteristic length in the FCM is reliably used for evaluating the ductility properties in the design and analysis of cementitious composites and in the control of microcracking.

2.5.4.2 Crack band model (CBM)

Bažant and Oh (1983) modified the FCM of Hillerborg et al. (1976) by modeling the fracture process zone by a band of uniformly and continuously distributed microcracks with a fixed width of h_b as shown in Figure 2.36 instead of taking place discretely as in the FCM. Over this width, h_b , the inelastic deformation due to cracking takes place.

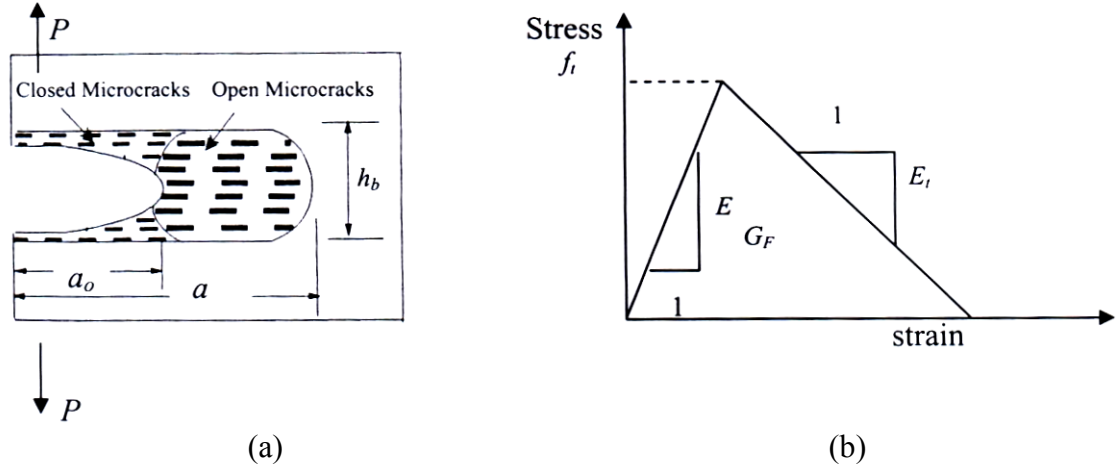


Figure 2.36: Crack band model for fracture of concrete (a) a microcrack band fracture and (b) stress-strain curve for the microcrack band proposed by Bažant and Oh, 1983 (from Shah, et al., 1995).

The energy consumed due to the crack advance per unit area of the crack band, G_F is the product of the area under the stress-strain curve given in figure, and the width of the crack band, h_b . This leads to

$$G_F = h_b \left(1 + \frac{E}{E_t} \right) \frac{f_t^2}{2E} \quad (2.16)$$

where E is the modulus of elasticity, E_t is the strain-softening modulus and f_t is the tensile strength of the material.

In the CBM, the cracking is assumed to be smeared over an entire element that is why it is also called smeared crack model. It is therefore necessary to choose the band width equal to the element size in order to avoid mesh dependency of the results. The CBM is generally used when the cracks are diffuse and numerous, while the FCM is used when the cracks are few and isolated.

2.5.4.3 Size effect law

Because of the widely accepted size effect, the fracture properties measured on laboratory size specimens need to be extrapolated to real-size engineering structures. In Bažant's size effect law (1984), geometrically similar three-point bending beam specimens of at least three different sizes are used to determine two fracture parameters using measured peak loads only. In this model, fracture of quasi-brittle material is simulated by an effective-elastic crack (Bažant and Kazemi, 1990). One of these fracture parameters is defined as the critical energy release rate, which is the unit fracture energy required for the crack initiation in an infinite specimen, while the other is the critical effective crack length that can be defined as the length of the FPZ between the notch tip and the crack tip at peak load of an infinitely large specimen.

2.5.4.4 Two parameter fracture model

In the two parameter fracture model (TPM), proposed by Jenq and Shah (1985), the specimen is loaded up to the maximum stress, and then exposed to an unloading and reloading cycle. Based on the initial and unloading compliances obtained, the two fracture parameters which are the critical stress intensity factor (K_{IC}^s) and the critical crack tip opening displacement (CTOD_C) are determined using only one size three-point bending specimens (Shah et al., 1995).

2.5.4.5 Effective crack model

The effective crack model (ECM), which is based on the effective-elastic crack approach, was proposed by Nallathambi and Karihaloo (1990). The basic concept of effective crack in this model is similar to the TPM. However, a secant compliance at the maximum load, rather than the elastic part of the unloading compliance as in the TPM, is used to determine the effective-elastic crack length in the ECM (Karihaloo and Nallathambi, 1989). Since the secant compliance at the maximum load includes effects of both elastic and inelastic deformations, the critical effective crack length obtained in such way is usually greater than that obtained from the TPM, where the latter only includes effect of elastic deformation (Shah et al., 1995).

2.5.4.6 Boundary effect and local fracture energy distribution

The size dependence of the fracture energy can be explained by the existence of nonuniform fracture energy dissipation along the crack growth path showing the influences of the specimen boundary and the variation of FPZ height (Hu and Wittmann, 2000; Duan et al., 2003). Previous studies conducted by Navalurkar et al (1999), Zhang and Wu (1999), and also the studies recently completed at ITU (Aldikacti et al., 2005; Mese et al., 2005) showed that the fracture energy curve decreases in a steepening trend as notch/depth ratio (a/W) increases, suggesting that G_f is highly dependent on a/W ratio. It has been pointed out that the size-independent specific fracture energy of concrete G_F can be determined using the size-dependent fracture energy G_f obtained by conducting three-point bending tests on single size specimens containing either very shallow or deep starter notches (Abdalla and Karihaloo, 2003). The fracture process zone characteristics in the middle of the specimens and those close to the back boundary are different i.e. the boundary effect exists (Duan et al., 2003). The boundary effect can be accounted for the nonuniform fracture energy dissipation along the crack growth path which is demonstrated by the non-constant behavior of the local fracture energy g_f . This varying behavior is modeled by a bilinear function which is used in determining the size-independent specific fracture energy (Akçay et al., submitted).

2.5.5 Fracture Mechanics of Lightweight Concrete

Basically, all lightweight aggregate-mixtures vary in only few parameters such as the type of aggregates, the cement content, the water/cement ratio, and the superplasticizer content. All these parameters have influence on the compressive strength and the brittleness of the LWC. It is well known that compressive strength and modulus of elasticity of LWC increase with the increasing dry density of LWA as seen in Figure 2.37 (Wille and Dehn, 2003).

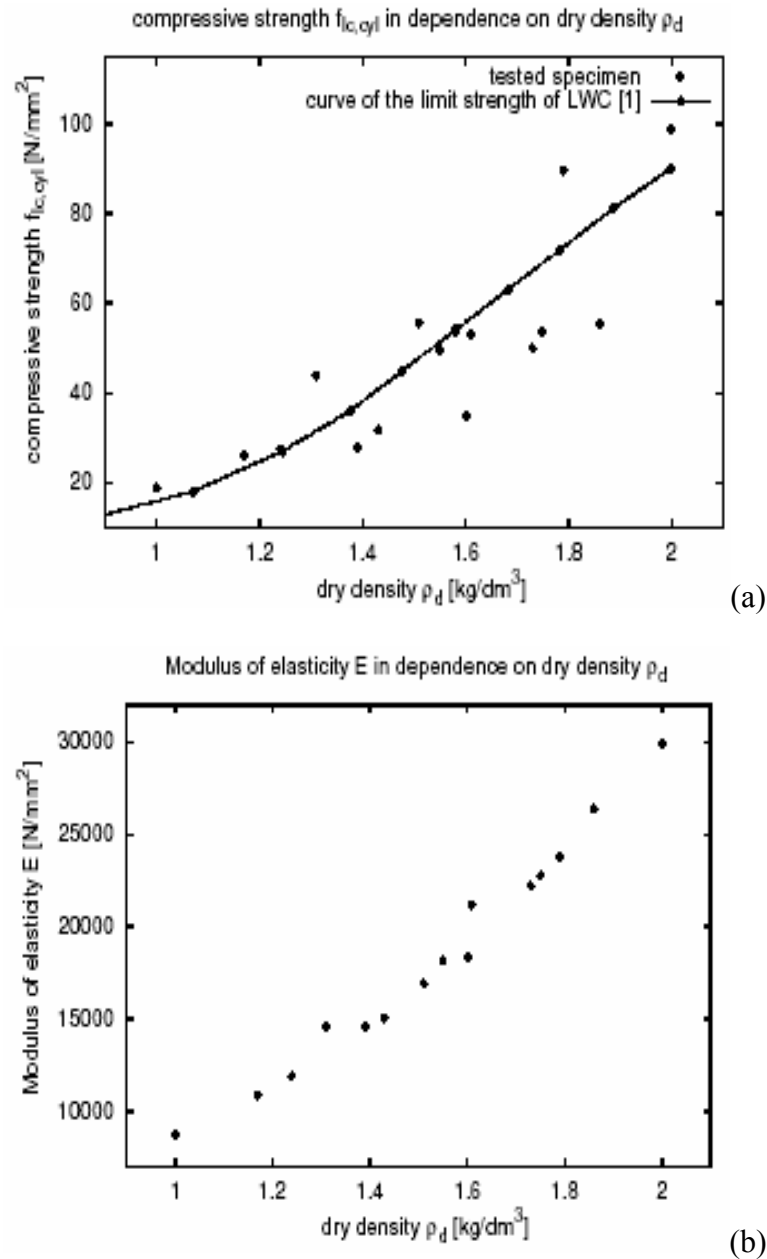


Figure 2.37: Compressive strength (a) and modulus of elasticity (b) in relation with the dry density (Wille and Dehn, 2003).

Also, Tasdemir et al., (2002) showed that particle size of LWA has influence on the stress-strain behavior of semi-lightweight concrete (SLWC) in compression as shown in Figure 2.38. It was concluded that concretes with coarser LWAs have smaller compressive strength values than those with finer LWAs, although both have similar moduli of elasticity.

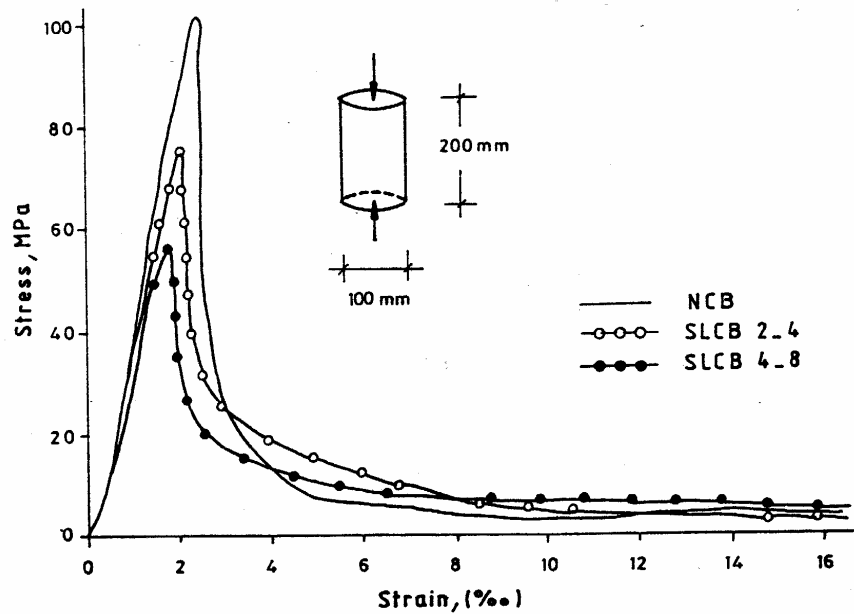


Figure 2.38: Typical results of stress-strain curves of concretes in compression (Tasdemir et al., 2002).

In addition, Faust (1997) showed that the stress/strain behavior of LWC in compression is, compared to normal density concretes (NC) of the same compressive strength, generally characterized by a linear ascending branch, a lower E-modulus and lower ductility in the post-failure region as shown in Figure 2.39. These characteristics are usually more pronounced with increasing compressive strength and decreasing oven dry density.

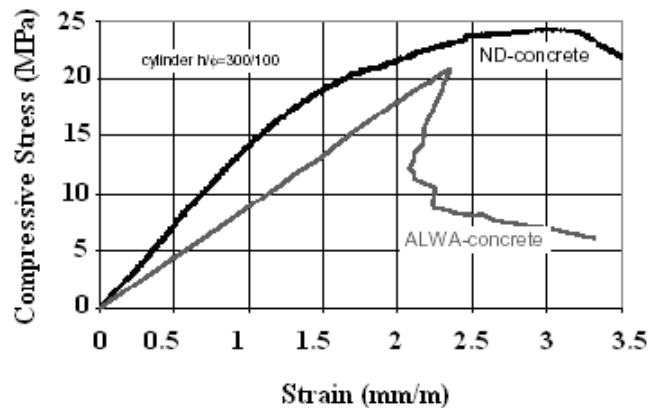


Figure 2.39: Stress-strain curve of an ALWA (all LWAs as defined by the author) concrete compared with NC-normal concrete of similar strength (Faust, 1997).

Wang and Li (2003) stated that multiple cracking and strain hardening can be achieved by one of the followings: air-entrainment admixture, polymeric micro-hollow-bubble, natural LWAs or glass micro-bubbles; however, tensile and compressive strengths and robustness of strain capacity vary significantly with the content and type of lightweight filler used.

The mechanical behavior of concrete can be modeled in three levels such as: micro, meso and macro (Wittmann, 1983). Because of the fact that the strain distribution of concrete composite is not uniform, for fracture modeling of extremely heterogeneous concrete at macro level it is necessary to know the fracture mechanics properties of concrete at meso level. In quasi-brittle materials such as concrete, fracture parameters cannot be determined accurately using LEFM due to the existence of the FPZ, where the toughening mechanisms are effective. The critical energy release rate is related to the stress intensity factor (SIF) of the material.

In meso-scale, internal structure of concrete consists of cement paste with voids, aggregates and the interface between the aggregate and the cement paste. FPZ contains inter-connected cracks along the aggregate and mortar interface, and branches are formed within this softening zone. The post peak tension softening behavior is related to the propagation of a crack and its interaction with other interfacial cracks and aggregates. There exist various toughening mechanisms that are effective in the FPZ and cause the energy dissipation in concrete which are; crack shielding, crack deflection, aggregate bridging, crack trapping, crack tip blunting by voids, distributed interfacial cracking, and crack branching mechanisms as shown in Figure 2.40 (Shah et al., 1995). During fracture, the high-stress state near the crack tip causes microcracking at flaws which is known as crack shielding and consumes a part of external energy caused by applied load (Shah et al., 1995). The crack deflection mechanism can be defined as the deflection of a crack along the matrix-aggregate interface, choosing the path of least resistance (Faber et al., 1983, Li and Maalej, 1996). In the bridging and trapping mechanism, aggregate particle acts as a bridge, anchoring the matrix on both sides of a crack so that crack face separation is inhibited; while trapping occurs as a matrix crack neither deflects nor goes through the aggregate in the vicinity of an aggregate, therefore a trap site is created against crack propagation (Li and Huang, 1996). Bridging and

trapping mechanisms combine and delay the propagation of the main crack. It has been reported that the crack tip is sometimes terminated by internal voids, which produces a blunt tip. This phenomenon is called “crack tip blunting by voids” and the additional energy is required to propagate the crack with a new blunt tip (Shah et al., 1995). The distributed interfacial cracking mechanism occurs as the highest tensile stress ahead of the dominant crack causes the interfacial cracks to open which results in a decrease in the modulus of elasticity of the material therefore, the SIF at the dominant crack tip is lowered, resulting in a toughening effect (Li and Maalej, 1996). Another mechanism is crack branching in which the crack may propagate into several branches due to heterogeneity of concrete.

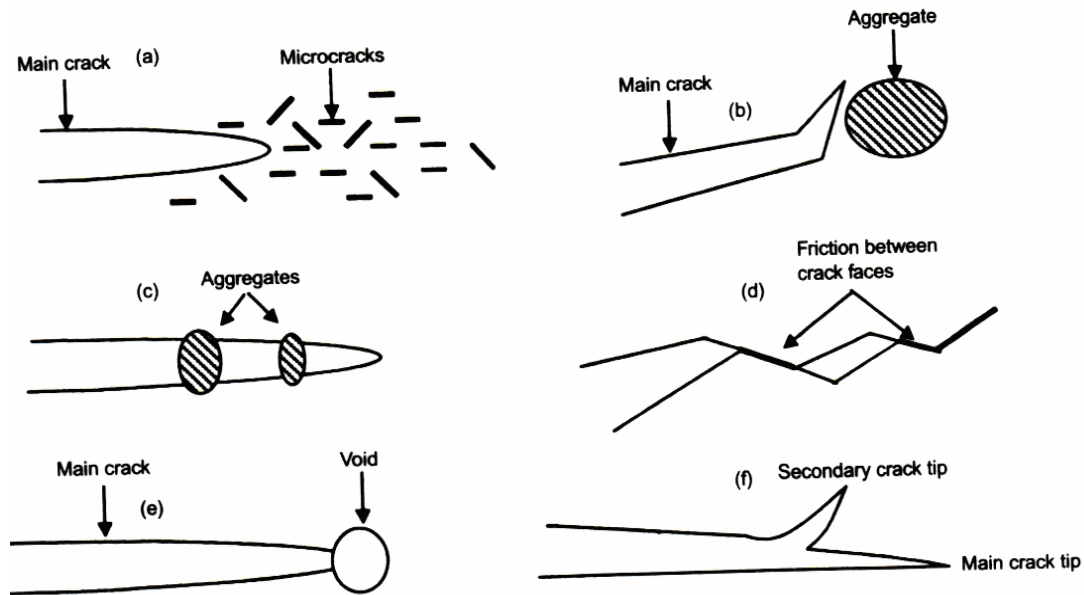


Figure 2.40: Some toughening mechanisms in fracture process zone: (a) crack shielding; (b) crack deflection; (c) aggregate bridging; (d) crack surface roughness-induced closure; (e) crack tip blunted by void; (f) crack branching (Shah et al., 1995).

When the aggregate is stronger than the matrix, crack propagates mainly through the matrix, around the stronger particles and the concrete strength is not very dependent on the aggregate strength. However, in LWC, fracture invariably passes through virtually all the relevant aggregate particles and their properties and volume concentration are of great significance (Lydon and Balendran, 1980). As a result, the mechanism of crack

deflection is not expected to be an important toughening mechanism in LWC. On the other hand, microcrack shielding is expected to remain an important toughening mechanism. Furthermore, the mechanism of aggregate/ligament bridging is expected to be present in LWC, except that its contribution to toughness will not be as large as in NSC (Li and Maalej, 1996).

The application of fracture mechanics to LWC is still in its early stage. Chang and Shieh (1996) stated that the measured values of G_F of LWC with artificial LWAs were in the range between 34.42 and 37.20 N/m, which is similar to the range for normal concrete with similar strength. As is shown in Figure 2.41 the maximal crack tensile load is increased with increasing the grain density of the coarse aggregate. In contrast, grain density of the fine aggregate has a great influence on the softening behavior (Wille and Dehn, 2003). In LWC, the brittleness increases by increasing the grain density of fine and coarse aggregate.

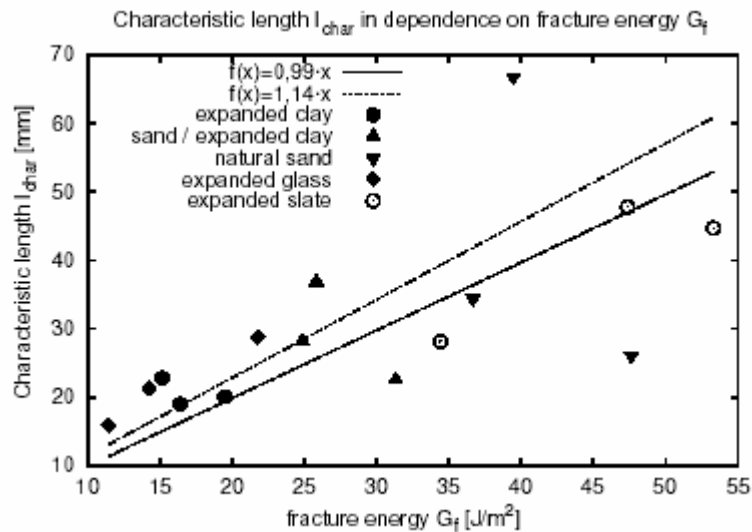


Figure 2.41: Characteristic length in relation to the type of LWA and to the fracture energy (Chang and Shieh, 1996).

Tasdemir et al. (2002) showed that HSC with a normal aggregate have greater peak load and steeper gradients of the softening branch than that of the SLWC, however, the tail of HSC concrete is close to those of SLWCs as shown in Figure 2.42.

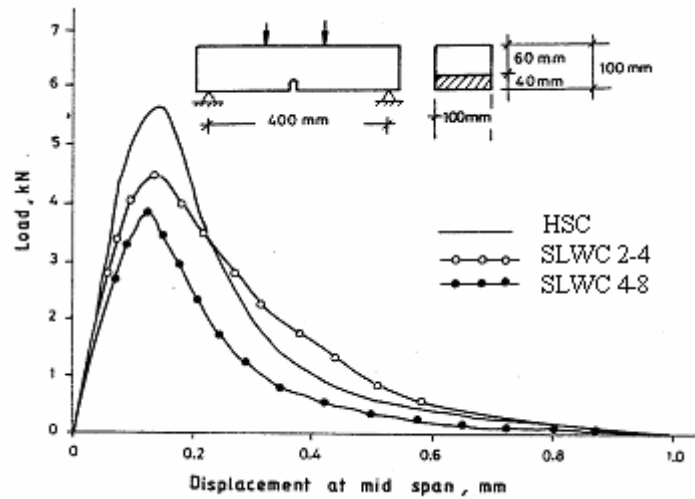


Figure 2.42: Typical results of load-displacement curves obtained from for point bending test (Tasdemir et al., 2002).

It was also shown that, for all concretes, there is a very good relation between compressive strength and their fracture energy. Since the flexural strength of HSCs is relatively high, their fracture energies are naturally greater than those of SLWCs. It is also seen that the fracture energy increases significantly, as the mean particle size of the LWA decreases as shown in Figure 2.43.

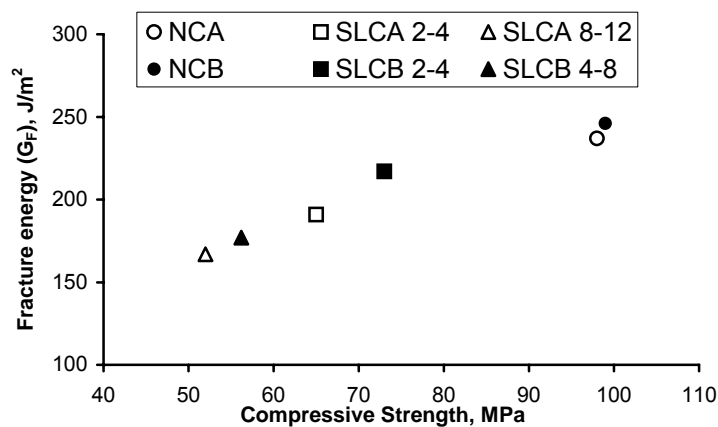


Figure 2.43: Effect of compressive strength of concrete on the fracture energy. The series A and B have different aggregate grading curves (Tasdemir et al., 2002).

3. EXPERIMENTAL PROGRAMME

3.1 General

In this study, experiments were conducted to determine the effect of the variations in both the volume fractions and the size of saturated LWAs, which alter the value of autogenous deformation and also fracture and mechanical properties of concrete. For this purpose, in concretes prepared using a constant low water to binder ratio of 0.28 with addition of 10% silica fume, normal aggregates were replaced by natural LWAs with size fractions of 2-4 mm or 4-8 mm at three different volume fractions such as 10%, 20% and 30% of the total aggregate volume of concrete. In order to understand the autogenous deformation behavior, phases of cement paste, fine mortar and coarse mortar of concretes were cast. In addition, individual type of composites including cement paste and aggregate with different type and particle size were prepared.

3.2 Materials

3.2.1 Cement

In all mixtures, an ordinary Portland cement (OPC 42.5) manufactured by Nuh Cement Company was used. Compressive strengths at the age of 7 and 28 days of the standard RILEM Cembureau cement mortars were 40 and 50.6 MPa, respectively. In addition, their flexural strengths at 7 and 28 days were found to be 6.4 and 8.5 MPa, respectively. Some of the physical and chemical properties of cement are given in Table. 3.1

3.2.2 Silica Fume

The silica fume (with 93.7% SiO₂; reported in producer's report) used in all mixtures was 10% by weight of cement. The maximum particle size of silica fume was 0.1 mm and its particle density was 2240 kg/m³. The silica fume was used in dry condition and mixed with cement before the water addition.

Table.3.1: Physical and chemical properties of cement.

Density	3110 kg/m ³	Time of setting (Vicat Test)	Initial set	203 minutes				
Blaine fineness	3280 cm ² /g		Final set	285 minutes				
Volume stability (Le Chatelier)		3 mm						
Compound composition (%)								
C ₃ S		C ₂ S	C ₃ A	C ₄ AF				
56.82		16.88	5.12	11.14				
Chemical Compound (%)								
SiO ₂	Al ₂ O ₃	Fe ₂ O ₃	CaO	MgO	SO ₃	Insoluble residue	Loss on Ignition	Free lime
20.84	4.27	3.66	63.92	1.12	2.63	0.67	1.90	0.89

3.2.3 Aggregate

3.2.3.1 Normal weight aggregates

All the aggregates were sieved using certain sieve sizes before adding into the mixtures. Crushed limestone was used as coarse aggregate, while natural quartz sand and siliceous powder were used as fine aggregates (Figure 3.1). Particle densities of crushed limestone, crushed sand, quartz sand, and siliceous powder were 2720, 2710, 2650 and 2620 kg/m³, respectively.



Figure 3.1: General appearance of normal aggregates used. From left to right; crushed stone, natural sand, siliceous powder and the binder of silica fume.

The maximum aggregate size was chosen as 8 mm. Effective water absorption of the coarse aggregates (ASTM C127, 1994) and fine aggregates (ASTM C128, 1994) were 1.1% and 2.1%, respectively. The grading of aggregates and percentage of used aggregates are given in Table 3.2. Grading curve of aggregate used in the mixtures is given with standard curves in Figure 3.2.

Table 3.2: Grading of aggregates used in the mixtures.

Sieve size (mm)	Percentage passing			
	Crushed stone No.I(4-8 mm)	Crushed sand (2-4 mm)	Natural sand (0-2 mm)	Siliceous powder (0-0.5 mm)
8	100	100	100	100
4	0	100	100	100
2	0	0	100	100
1	0	0	81	100
0.50	0	0	56	100
0.25	0	0	14,9	97,4
0.120	0	0	1,8	71,7

Volume concentration of aggregates in concrete				
Proportion to the total aggregate volume (%)	30	30	30	10

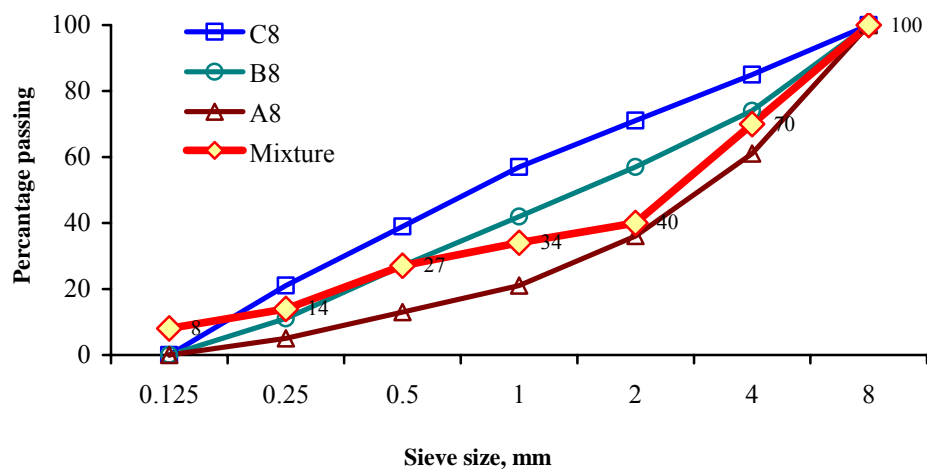


Figure 3.2: Grading curves of aggregate mixtures and standard curves.

3.2.3.2 Lightweight aggregates

Crushed pumice from Cappadocia area, Central Turkey, was used as lightweight aggregate in size fractions of 2-4 mm and 4-8 mm (Figure 3.3). The particle densities (both oven dried and 24 hours saturated surface dry (SSD) conditions) and water absorptions of the pumice LWAs (as shown in Table 3.3) were determined according to DIN 4226. In an attempt to obtain homogenous materials, pumices were sieved using certain sieve sizes and were heated over night to dryness. The pumices were then cooled and placed in a water tank for about 5 minutes, and only those floating on water were used in mixtures. Pre-soaked water content was determined using the 30 minutes water absorption.

Table 3.3: Densities and water absorptions of pumice LWAs.

Size fraction, mm	Particle density, kg/m ³		Bulk unit weight kg/m ³	Water absorption. % by dry weight			
	oven dry	24 hours SSD condition		10 min	30 min	60 min	24 hours
2/4	750	1070	410	28	35	38	45
4/8	730	1020	400	26	33	35	41



Figure 3.3: General appearance of lightweight aggregates used. From left to right; 4-8 mm and 2-4 mm size fractions.

3.2.4 Superplasticizer

A commercially available polycarboxylic ether based superplasticizer (Glenium 55 from YKS) was used to adjust the slump of fresh concrete in the range of 160 ± 20 mm. The

values of slump were chosen close to that of self-compacting concrete because the mixtures with LWAs were intended not to be exposed to any strong vibration for compaction.

3.3 Material Composition and Specimen Preparation

3.3.1 Mixture Proportion

All concretes were prepared using a constant aggregate volume of 65% and constant water to binder ratio of 0.28. Normal aggregates were replaced by natural LWAs with the size fractions of 2-4 mm or 4-8 mm at three different volume fractions of 10%, 20% and 30% of the total aggregate volume of concrete. Since autogenous deformation is an event occurring in cement paste, the coarse mortar (MREF, MV10L24, MV20L24, and MV30L24), fine mortar (FMREF) and paste phases (MREF) of concretes were cast. The designation and replacement ratios of LWAs are summarized in Table 3.4.

Table 3.4: Mixture codes and the size and volume fractions of LWAs.

Concentration of LWA	Replaced Size fraction	Concrete	Coarse Mortar
0	-	CREF	MREF
10	2-4	CV10L24	MV10L24
	4-8	CV10L48	
20	2-4	CV20L24	MV20L24
	4-8	CV20L48	
30	2-4	CV30L24	MV30L24
	4-8	CV30L48	

In order to understand the effect of LWAs and internal curing on both autogenous deformation and fracture mechanics, additional series were prepared with only 70% volume of paste and 30% volume of aggregate. In these series, five different composites were produced and their designation codes are given in Table 3.5 as PN0-2, PN2-4, PN4-8, PL2-4 and PL4-8. The second letter in each code stands for the type of aggregate (e.g. N-normal weight and L-lightweight aggregate), while the following numbers denote the size fraction of aggregates such as 2-4 and 4-8 mm. Details of all mix proportions and some of the fresh properties are given in Table 3.5.

Table 3.5: Compositional and some of the properties of the fresh mixtures.

Composition of concrete in 1 m ³												Fresh Concrete Properties	
	Binder		Liquid			Aggregate						Air, %	Unit weight, kg/m ³
Code	Cement, kg	Silica Fume, kg	Water, kg	Pre-soaked water, kg	Superplasticizer, kg	Siliceous powder, kg	Natural sand (0-2), kg	Crushed sand (2-4), kg	Crushed stone No.I (4-8), kg	LWA 2-4 mm, kg	LWA 4-8 mm, kg		
CREF	497	50	153	0	10	169	514	520	529	0	0	1.4	2441
CV10L24	496	50	153	17	10	169	513	344	529	48	0	1.5	2328
CV10L48	497	50	153	34	10	169	513	173	529	0	47	1.3	2224
CV20L24	496	50	153	51	10	169	513	0	529	97	0	1.2	2115
CV20L48	497	50	153	16	10	169	514	520	353	0	94	1.2	2328
CV30L24	496	50	153	31	10	169	513	519	177	145	0	1.3	2211
CV30L48	496	50	153	47	10	168	512	518	0	0	141	1.4	2095
MREF	610	61	188	0	12	207	630	638	0	0	0	2.5	2345
MV10L24	605	61	186	19	12	206	626	422	0	58	0	3.0	2196
MV20L24	610	61	188	39	12	207	631	213	0	118	0	2.5	2080
MV30L24	609	61	188	58	12	207	630	0	0	176	0	2.6	1941
FMREF	800	80	247	0	12	272	828	0	0	0	0	3.3	2239
PREF	1464	146	451	0	9	0	0	0	0	0	0	0.5	2070
PN0-2	1005	101	309	0	6.3	0	765	0	0	0	0	2.3	2186
PN2-4	1005	101	309	0	5.0	0	0	765	0	0	0	2.4	2185
PN4-8	1018	102	314	0	3.7	0	0	0	805	0	0	1.7	2239
PL2-4	1010	101	311	73	5	0	0	0	0	222	0	2.0	1717
PL4-8	1007	101	310	71	3.7	0	0	0	0	0	215	2.3	1704

3.3.2 Mixing and Placing Procedures

Before the production of concrete all LWAs were dried overnight. After cooling the LWAs at room temperature, presoak water is sprayed into the LWAs and the container of LWAs was kept closed for 30 minutes to obtain the water saturated surface dry condition. The LWAs were mixed three times for homogenization during this 30 minutes period. All mixtures were prepared using a 45 liters capacity pan mixer with vertical rotation axis. Typically coarse aggregates were mixed for two minutes, and then

siliceous sand and natural sand were added within the following two minutes, while the mixer was still spinning. Previously mixed cement and silica fume were added in aggregate and then they were mixed for another 4 minutes. Water was added slowly for about two minutes. LWAs were added immediately after the addition of water and mixing was continued for the next two minutes. In the following two minutes superplasticizer was added and the mixture was mixed for three minutes and then mixer was stopped and kept covered for three minutes before the final two minutes of mixing. Since the capacity of the mixer (45 liters) is smaller than the necessary volume of the mixtures, two 35-liter identical batches were produced using the same material. Mixtures were placed in the molds in two or three equal lifts with tamping between each lift. Before approximately 5 seconds of vibration, the stainless steel molds were hit gently with a rubber hammer to obtain smooth surfaces. Before the pouring, two layers of plastic sheets were placed in molds. The specimens were then covered with a plastic film. All specimens were kept in their molds for 24 hours except the specimens for autogenous deformation. After de-molding, each specimen was sealed using two layers of plastic sheets together with two layers of aluminum foil. Measurements were taken in the casting room at $20\pm 2^{\circ}\text{C}$ and 65% RH.

3.4 Experimental Procedure

This section describes the experimental details including the testing equipment and procedure, and the methods of evaluation of the data. The experimental work consisted of determining the autogenous deformation, temperature development, chemical shrinkage, compression strength, splitting tensile strength, fracture parameters, heat of hydration, and non-evaporable water content. In addition, the mercury intrusion porosimeter tests and image analysis (detailed in Chapter 7) were also conducted.

3.4.1 Autogenous Deformation

In cement paste and mortar specimens, both linear and volumetric autogenous deformation tests were performed, while only linear autogenous deformation tests were performed on concrete specimens.

3. 4.1.1 Linear autogenous deformation

The linear autogenous deformations were determined by measuring displacements on the sealed cement paste, mortar, or concrete specimens. In this study, autogenous deformations of concretes were measured on four prism specimens of $70 \times 70 \times 280$ mm. As mentioned above, two layers of plastics were inserted inside the moulds before casting. Stainless steel studs were settled on specimens using a thin layer of adhesive after setting time of approximately 4 hours and the side walls were de-molded. The measurements were taken over a 200 mm gage length (Figure 3.4).

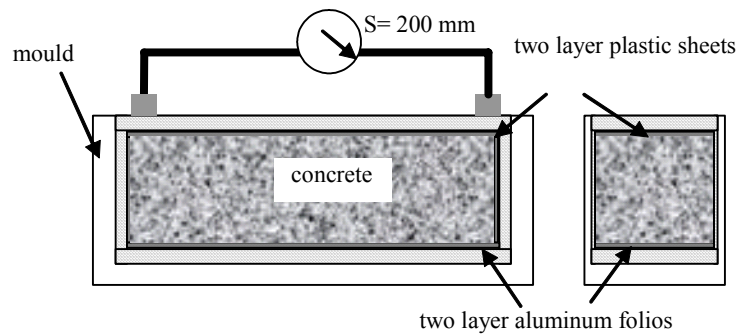


Figure 3.4: Linear autogenous deformation test set up for concrete specimens.

The extensometer used in the measurements was equipped with a comparator with an accuracy of 0.001 m/m (Figure 3.4). The specimens were stored in a room at $20 \pm 2^\circ\text{C}$ and 65% RH. Immediately after de-molding at 24 hours, each specimen was sealed using two layers of plastic sheets and with a layer of aluminum foil. Measurements were made according to the ASTM C 41 after 24 hours in the casting room. Specimens of

each series were weighed at one and 28 days to monitor whether the sealing layers preserved RH in the specimens. Weight changes for all specimens in each series were not greater than 0.08%.

3.4.1.2 Volumetric autogenous deformation

In the volumetric measuring method, approximately 100 g cement paste or mortar was cast in a rubber bag (condom) immediately after casting. The specimens were filled into the latex membrane taking care to remove entrapped air. Because of the lower water to cement ratio, bleeding was not expected to occur. The membrane was tied up by thin stainless steel wire and stored in a water bath at 20 ± 2 °C. Specimen was weighted by an electronic semi-micro balance (Sartorius) with a resolution of 0.0001g. Weight data were recorded every 15 minutes. The samples were not rotated. To ensure the impermeability of latex membrane, sand was filled in membrane and weighted in water bath. No significant weight change was observed. Deformation was calculated using the change in buoyancy as shown in Figure 3.5. The autogenous deformation was calculated 4 hours after casting. The tests were duplicated with practically identical specimens produced using small laboratory mixer of 5-liter capacity.

3.4.2 Temperature Development

As shown in Figure 3.5, while monitoring the weight change, the temperature development in a semi adiabatic condition was also recorded. The specimen from the same batch was poured in a polyurethane cup and Pt 100 temperature sensor was inserted into the specimen. The cup was located in the center of 30×30×50 cm polyurethane prisms. The variation of temperature was monitored for at least 24 hours starting from 30 minutes after the addition of water.

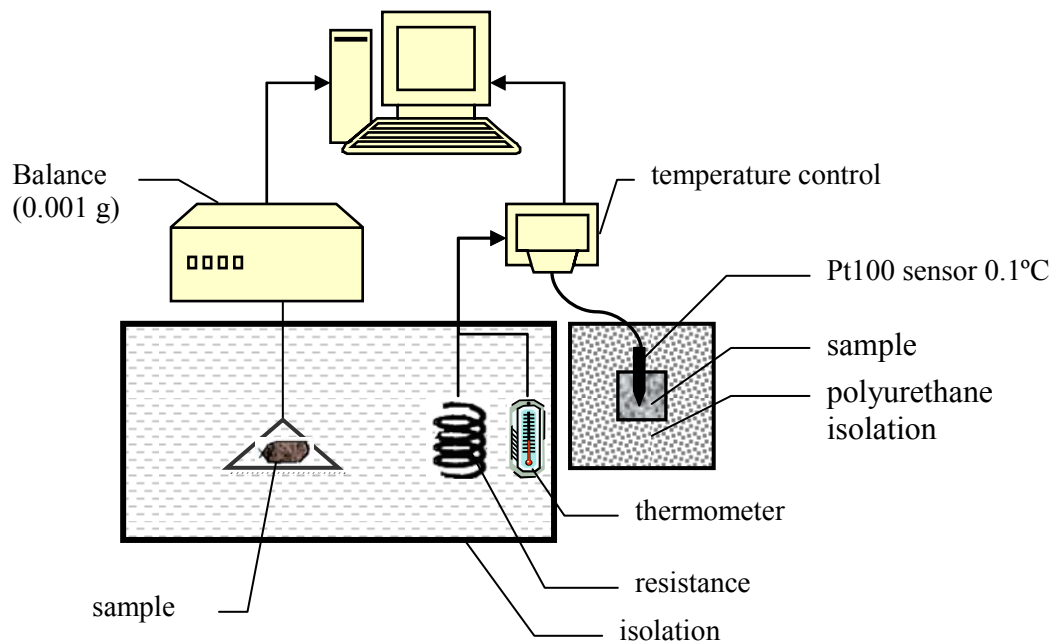


Figure 3.5: Test setups of volumetric autogenous deformation and temperature measurement in adiabatic condition.

3.4.3 Chemical Shrinkage

Chemical shrinkage tests were performed using weighing methods in volumetric autogenous deformation test setup. The specimens (about 30 g) were poured in a plastic vial with 50 mm diameter and 10 mm height. The top surfaces of specimens were not sealed and water penetration was allowed in contrast to the volumetric autogenous deformation test. The measurements were recorded from the initial setting time to 24 hours after the addition of water. The temperature development in a semi-adiabatic condition was also recorded in the chemical shrinkage test. The chemical shrinkage of the initial cement and silica fume was determined using two specimens.

3.4.4 Heat of Hydration

Several methods are used for determining the heat released during hydration. These include conduction calorimeter, heat of solution calorimeter, and adiabatic and semi-adiabatic calorimeter (Schindler, 2002). In this study, ASTM C186-98 was used. It is based on measuring the heat of solution of dry cement and the heat of solution of a

separate portion of the cement that has been partially hydrated, the difference between these values being the heat of hydration for the respective hydrating period. A representative part of each mixture was poured in a vial. The vial was closed by filling with molten paraffin wax and stored in an upright position in a climated room with other samples. For the tests, the samples were extruded by breaking the plastic vials. The samples were treated by prophanol to stop the hydration. The samples were rapidly crushed in a mortar to pass a 250 μm mesh sieve; then samples were quickly weighted in accuracy of 0.0001g. The half of the sample was used for determining the non-evaporable water content and the other half for determining the heat of solution. In each mixture, two samples were used. Then, similar mixtures were prepared using a 5-liter small laboratory mixer and the tests were duplicated. Consequently, the heat of solution of and the non-evaporable water content were taken as the average of the results of 4 samples.

In this experiment, calorimeter was filled with an acidic solution and the rise in the temperature was measured by Beckmann thermometer. The acidic solution was prepared using dilute HNO_3 (nitric acid) and concentrated HF (hydrofluoric acid). Dilute nitric acid used in the experiment contained 127ml of concentrated HNO_3 (sp g. 1.42) per liter of solution (with distilled water). To ensure the homogeneity of solution, large quantity of nitric acid solution was prepared. In the tests, the first 400 g of dilute HNO_3 solution (at room temperature) was weighted and 8ml of HF was added. Then, dilute HNO_3 solution was added to make up the total weight of acid solution 425 g. The acid solution was transferred into the coated vacuum jar and calorimeter was assembled. The stirring motor was operated for 20 minutes and then, the specimen was added in the acidic solution. The stirring motor was started for an additional 40 minutes again. The temperature change was read in every minute in an accuracy of 0.01°C. Temperature rise was calculated as:

$$R_0 = \theta_{20} - \theta_0 \quad (3.1)$$

$$R_1 = R_0 - (\theta_{40} - \theta_{20})$$

where, R_0 and R_1 are the observed and corrected temperature rise, respectively. θ_{20} is the calorimeter temperature at the end of the solution period, θ_0 is the calorimeter temperature when the sample was introduced and θ_{40} is the calorimeter temperature at the end of the testing period.

The heat capacity of the calorimeter was found to be 1641.2 J/°C according to the ASTM C186-98. Then, the heat of solution of approximately 3 g dry cement was determined by using the following equation.

$$H_1 = \frac{R_1 \cdot C_c}{W_i} - 0.80(T - t_d) \quad (3.2)$$

where H_1 is the heat of solution of dry cement (kJ/kg), R_1 is the corrected temperature rise (°C), C_c is the heat capacity (kJ/°C) of the calorimeter, W_i is the mass of sample on ignited basis (g), T is the room temperature (°C), and t_d is the final calorimeter temperature at the end of test on dry cement (°C). Determination of ignited mass will be explained in the following Section 3.4.5.

For calculating the heat of solution of partially hydrated sample the following equation was used:

$$H_2 = \frac{R_1 \cdot C}{W_i} - 1.7(T - t_h) - 1.3(t_d - t_h) \quad (3.3)$$

where H_2 is the heat of solution of partially hydrated sample (kJ/kg), t_d and t_h are the final calorimeter temperature at end of determination on dry cement and partially hydrated cement (°C), respectively. R_1 , C , W_i , and T are as defined in Eq. (3.2) for partially hydrated sample.

In order to refer the results to 25°C, the following equation was used for calculating the heat of hydration:

$$H = H_1 - H_2 - 0.4(t_h - 25.0) \quad (3.4)$$

This method is usually applied to cement paste samples only. In this study, pastes were carefully separated from the mortars. Parts of the samples used for measuring the heat of hydration were taken when they were produced. However, it should be noted that the samples obtained by separation always contained siliceous sand and natural sand. The effect of these sands on heat of solution was determined separately, and will be discussed later.

In the literature no substantial information has been found regarding the heat of solution of silica fume. Kishi and Maekawa (1995) proposed that heat of hydration values of fly ash and GGBF slag could be superposed to heat of cement. On the other hand, it is expected that the use of silica fume increases the heat of hydration because of strong lime pozzolanic reaction. Sanchez de Rojas and Frias (1996) showed that increasing the silica fume content (paste with $w/c=0.5$) to 30% caused a decrease in the heat of hydration at early ages as shown in Figure 3.6.

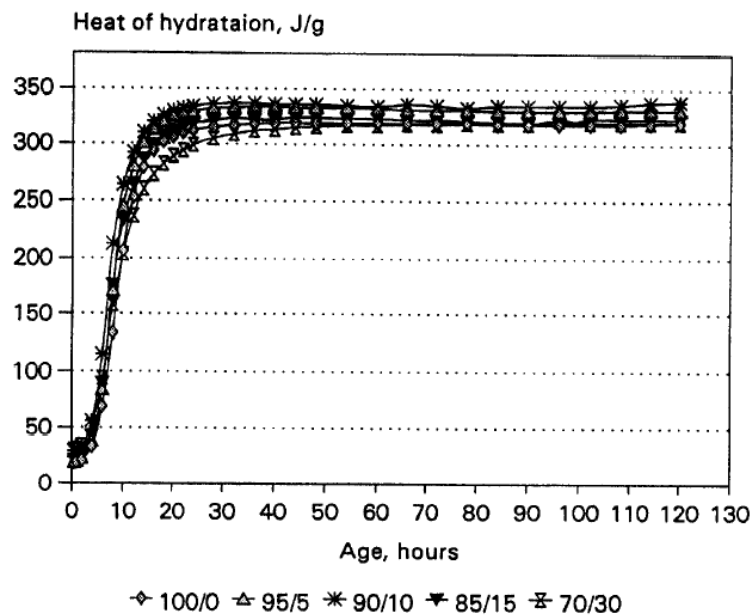


Figure 3.6: Effect of silica fume content on heat of hydration (Sanchez de Rojas and Frias 1996).

They proposed that the percentage of cement substitution counteracts the heat from the pozzolanic reaction, and the substitution effect predominates over the effect of the

pozzolanic activity. They also showed that the presence of silica fume in cement paste increases the heat of hydration as compared to the plain cement, since after 48 hours the temperature began to stabilize and the heat release was of little significance. They performed heat of hydration test in semi adiabatic Langavant calorimeter. It was also reported that 10% substitution of cement by silica fume was not sufficient to compensate for the heat release during the pozzolanic reaction. On the other hand, Yogenrdran et al. (1991) showed that reduction of the total heat of hydration per gram of cement and silica fume was significant for up to 25% silica fume content at low water/cement ratio.

In this study, the heat of solution of dry cement was found to be 2264.9 J/g, while that of dry silica fume was found to be 390.7 J/g. Unfortunately, no data has been found in the literature on heat of solution of cement paste with silica fume. To verify the reliability of the test setup, the cement paste investigated (with silica fume; PREF, w/b=0.28) was compared to the pure cement paste for up to 100 days as given in Table 3.6. It was found that the use of 10% silica fume did not affect the heat of solution of samples significantly, especially at early ages. It should also be noted that the silica fume may give different values of heat in different acid solutions.

Table 3.6: The heat of solution (J/g) of cement paste and cement paste with 10% silica fume.

	Heat of solution (J/g)					
	10 hours	1 day	2 days	7 days	28 days	100 days
Cement paste	240.3	251.6	325.6	416.5	458.3	433.5
Cement paste +10% silica fume	227.3	238.7	306.6	395.8	446.9	430.6

3.4.5 Non-evaporable Water Content and Degree of Hydration

The degree of hydration (α) is defined as the ratio of hydrated cement particles to the total weight of initial dry cement. The non-evaporable water content is generally used to determine the degree of hydration. As mentioned before, for non-evaporable water content test, the part of sample prepared for determining the heat of hydration was used. The two powdered samples were placed in crucibles and heated at 105 °C for 24 hours. The samples were weighted and then kept at 1000 °C for at least 4 hours. This duration is above the time given in the standard (ASTM C186-98). The non-evaporable water

content (w_n) was measured as the quantity of water released from dried specimen when it was exposed to ignition with compensation for the loss on ignition of the dry cement powder. The degree of hydration has been calculated as the ratio of non-evaporable water content of partially hydrated sample to that of fully hydrated sample (w_n^o). The non-evaporable water content of fully hydrated cement paste with 10% silica fume content was accepted as 0.244 (Lam, 2005). For the calculations of the non-evaporable water content of the mortars, the corrections were made for the normal and lightweight aggregates used.

3.4.6 Mercury Intrusion Porosimetry (MIP)

MIP have been used to evaluate meso and macro pore structure of cementitious materials. It is based on introducing the non-wetting fluid with a pressure P , into a pore of the diameter d . It is assumed that the structure consists of interconnected, entirely open cylindrical pores. Assuming that the pores are equally accessible to the mercury, Washburn equation is usually applied to estimate the diameter of the cylindrical pores as:

$$d = -4\gamma \cos \theta / P \quad (3.5)$$

Where, γ is the surface tension of mercury and θ is the contact angle of mercury on the solid. In fact, this hypothesis is not confirmed because the measured and the real pore size distributions were found to be significantly different (Frias and Cabrera, 2000; Diamond, 2000). This is probably due to the fact that the pores in cementitious materials are not really in cylindrical shape and also not open and connective type. Cook and Hover (1999) stated that the pore width corresponding to the highest rate of mercury intrusion per change in pressure is known as the “threshold,” “critical,” or “percolation” pore width. After this diameter, mercury reaches the interior of the sample. Diamond (2000) stated that because of the assumptions only the critical pore diameter and intrudable pore space measurements can be found, while the actual pore sizes and distribution of that cannot be obtained by MIP test. In this study MIP tests were conducted on paste and mortar specimens of different ages to show the variance of the

critical pore diameters. For this purpose, cylindrical samples with 8 mm diameter and 15 mm height were used. The plastic laboratory tubes were filled with paste or fine mortar specimens and then sealed with paraffin. At the test age vials were broken. On the other hand, coarser mortar was filled into 100 mm cubes and broken into pieces with hammer at the test age. The pieces of nearly cylindrical paste and finely crushed mortar samples were used. Methods of taking cores from sample or shaping with diamond were not preferred. In these methods drilling and shaping are applied using water and water may alter the pore structures of specimen, especially at early ages. In addition, in some recent studies the MIP results of cored and crushed concrete samples have been found nearly identical (Kumar and Bhattacharjee, 2003). All the specimens for MIP test were treated by prophanole and dried at 70°C for 4 hours before testing. The tests were done on a Quantachrome-33 in the Department of Metallurgical and Materials Engineering at the Istanbul Technical University. The maximum intrusion pressure used in the experiment was 220 MPa, the contact angle of mercury on the solid was 130° and the surface tension of mercury was 48.5 N/m².

3.4.7 Compression Test

Compression test was performed to obtain the elastic modulus and compressive strength according to the ASTM C469 and ASTM C39, respectively. At least five cylindrical samples with 100 mm diameter and 200 mm height for each series were tested. The tests were performed using an Amsler press with a capacity of 200 kN. The top and bottom surfaces of cylinder were capped with a mortar of cement and gypsum. In order to obtain the elastic modulus, the frame with a comparator was used. The accuracy of the comparator was 0.001 mm and gage length was 100 mm. The loading rate was tried to keep in 15×10^{-6} /sec. for all samples. The frame was moved before the load approach the peak load. The cylinder sample was then reloaded until the peak load was reached. All tests were conducted at the age of 28 days. Static modulus of elasticity was calculated from the ascending part of the stress-strain curve for stresses up to approximately 33% of the ultimate strength. Standard compression tests were conducted in accordance with the European Standards (EN 206 and EN 12390).

3.4.8 Splitting Tension Test

Splitting tension tests were performed on disc specimens of 150 mm diameter and 60 mm height. Six specimens tested at the age of 28 days and the splitting tensile strength was obtained from maximum load using following equation:

$$f_{st} = \frac{2P}{\pi h_d \phi} \quad (3.6)$$

where, P, h_d and ϕ are maximum load, height and diameter of disc specimen, respectively.

3.4.9 Fracture Test

The tests for determining the fracture energy G_F were performed in accordance with the recommendation of RILEM 50-FMC Technical Committee. As schematically shown in Figure 3.7, the deflection was measured by using a linear variable displacement transducer (LVDT). The load was applied by a closed-loop testing machine (Instron 5500R) with a maximum capacity of 100 kN. The beams prepared for the fracture energy tests were 500 mm in length and 100 mm \times 100mm in cross section. The notch to depth ratios (a/W) of specimens were 0.4 and the notches were formed using a diamond saw. The effective cross section was reduced to 60 mm \times 100 mm to accommodate large aggregates in more abundance, and the length of support span was 400 mm. The crack mouth opening displacement (CMOD) was used as a feedback control variable to obtain stable tests, and deflections were measured simultaneously by means of a LVDT at midspan. Thus, load versus CMOD and load versus displacement at the midspan (δ) curves were obtained for each specimen.

The fracture energy was determined using the following expression (RILEM, 1985):

$$G_F = \frac{W_0 + mg \frac{S_{beam}}{L} \delta_0}{B(W - a_{beam})} \quad (3.7)$$

where, B , W , S_{beam} , L , a_{beam} , m , δ_0 , and g are the width, depth, span, length, notch depth, mass, specified deflection of the beam and gravitational acceleration, respectively. At least five specimens of each mixture were tested. All the beams were loaded at a constant rate of 0.02 mm/minute.

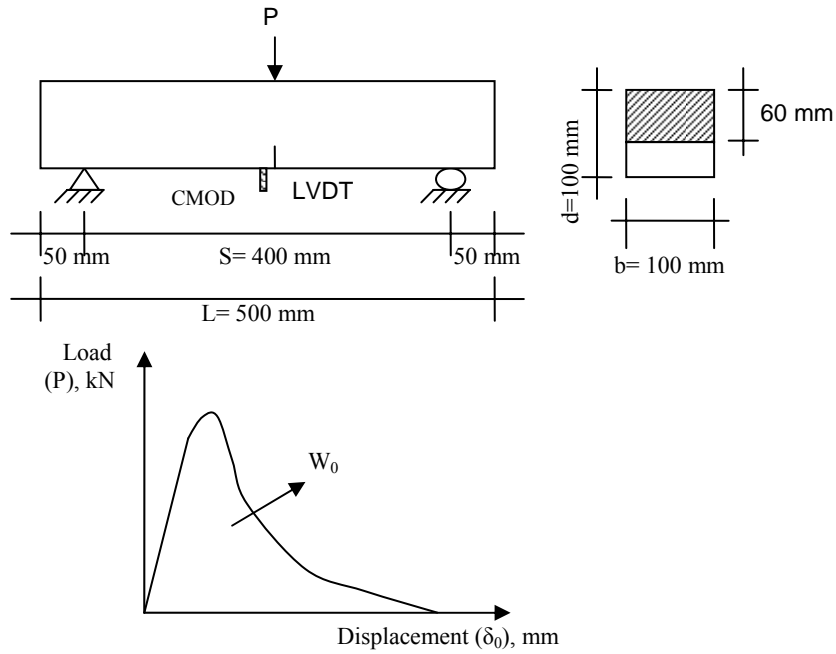


Figure 3.7. Schematic representation of the three point bending test and the calculation of area under load versus displacement curve.

3.5 Summary of Programme

The tests applied are given in Table 3.7.

Table 3.7: Summary of experimental programme.

Designation	Linear Autogenous Def.	Volumetric Autogenous Def.	Temperature Development	Chemical Shrinkage	Heat of Hydration	Non-evaporable water content	Mercury Intrusion Porosimetry	Compression Test	Splitting Tension Test	Fracture Test	Image Analysis
CREF	✓		✓					✓	✓	✓	✓
CV10L2-4	✓		✓					✓	✓	✓	✓
CV10L4-8	✓		✓					✓	✓	✓	✓
CV20L2-4	✓		✓					✓	✓	✓	✓
CV20L4-8	✓		✓					✓	✓	✓	✓
CV30L2-4	✓		✓					✓	✓	✓	✓
CV30L4-8	✓		✓					✓	✓	✓	✓
MREF	✓	✓	✓		✓	✓	✓	✓	✓	✓	✓
MV10L2-4	✓	✓	✓		✓	✓	✓	✓	✓	✓	✓
MV20L2-4	✓	✓	✓		✓	✓	✓	✓	✓	✓	✓
MV30L2-4	✓	✓	✓		✓	✓	✓	✓	✓	✓	✓
FMREF	✓	✓	✓		✓	✓	✓	✓	✓	✓	
PREF	✓	✓	✓	✓	✓	✓	✓	✓	✓	✓	
PN0-2	✓	✓	✓		✓	✓		✓	✓	✓	
PN2-4	✓	✓	✓		✓	✓		✓	✓	✓	
PN4-8	✓	✓	✓		✓	✓		✓	✓	✓	
PL2-4	✓	✓	✓		✓	✓		✓	✓	✓	
PL4-8	✓	✓	✓		✓	✓		✓	✓	✓	

4 EXPERIMENTAL RESULTS AND DISCUSSION

4.1 General

This chapter presents the results from the experimental work conducted during the course of the study. Throughout the chapter, the cement paste, fine and coarse mortars, and concrete are individually detailed and the relationships between these phases of cementitious materials are demonstrated.

4.2 Autogenous Deformation

4.2.1 Linear Autogenous Deformation

The measurements of linear autogenous deformation for the paste, fine mortar, coarse mortar and concrete phases for 28 and 360 days are shown in Figure 4.1. The first measurements were taken immediately after the initial setting time, while the second measurements were taken 24 hours after water addition to the cement paste. The results of linear autogenous deformation are average of 4 samples. The autogenous deformation of cement paste at 28 days was $-760 \mu\text{D}$ ($1\mu\text{D}=1\times 10^{-6}$), while the deformation in fine mortar, coarse mortar and concrete phases were measured as -600 , -543 and $-537 \mu\text{D}$, respectively. These results show that both the restrained effect of aggregates and diminishing the cement paste content in a unit volume by addition of aggregate reduce the autogenous deformation. It is also shown that the linear autogenous deformation of cementitious materials can reach significant values in a couple of days after production. Although the total aggregate contents of CREF and MREF phases were 65 and 56% respectively, the linear autogenous deformation values of MREF and CREF samples have been found to be similar. The effect of aggregate size and type will be discussed in Chapter 5.

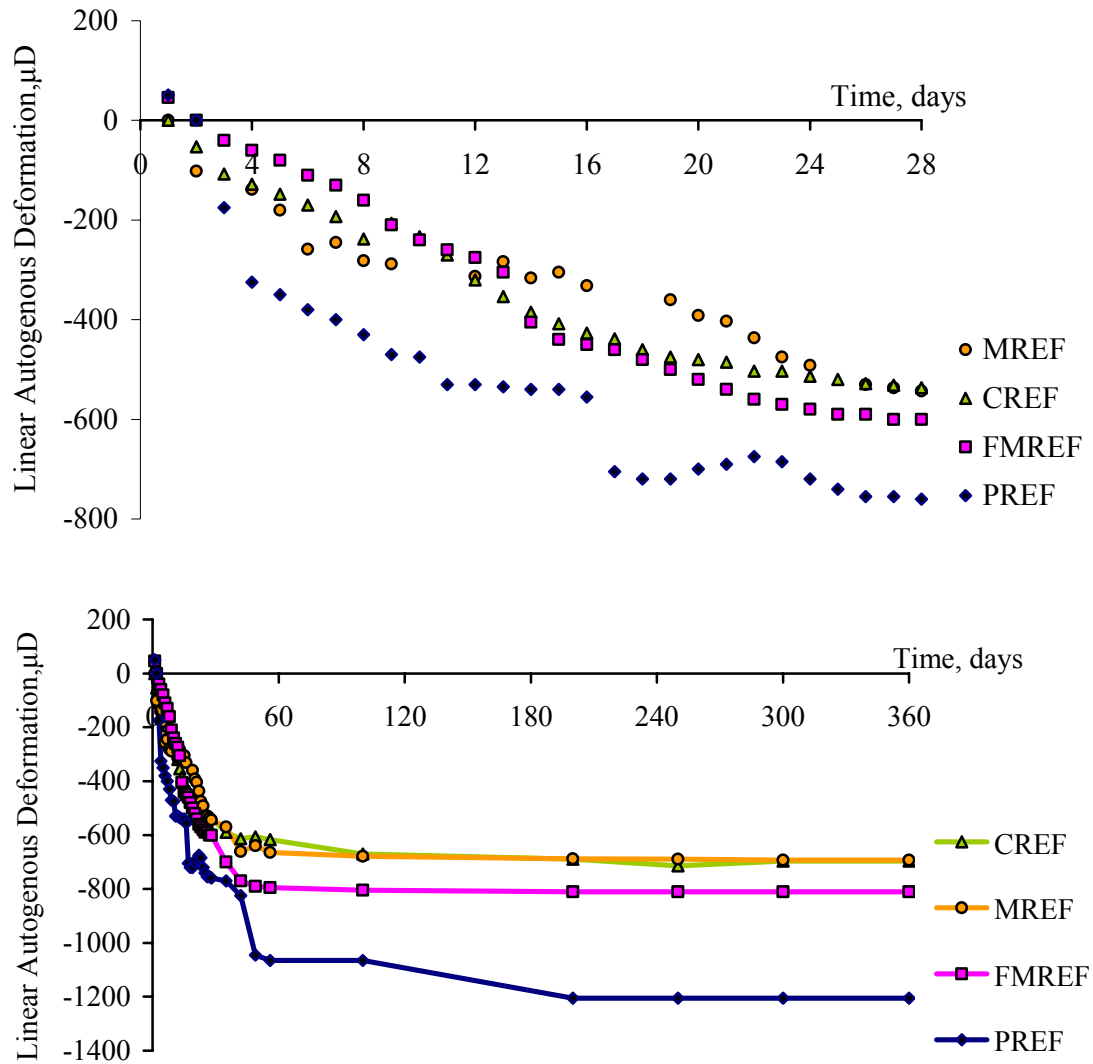


Figure 4.1: Linear autogenous deformation versus time diagrams of reference samples.

The effect of LWAs on linear autogenous deformation of mortars is shown in Figure 4.2. The results show that the use of fine LWAs (2-4 mm) decreased the linear autogenous deformation of mortars. Even 10% replacement of 2-4 mm normal aggregates by 2-4 mm LWAs is shown to have caused a subsequent decrease in autogenous deformation with respect to the MREF sample. On the other hand, when the replacement ratio was 20%, the swelling has been observed at the early ages. A possible reason for this is that the pore radius of cement paste at early ages is larger than at the later ages; and hence internal curing water can easily travel into the cement paste at early ages. With ongoing hydration the probable travel distance will be decreased and also the newly occurred

smaller pores will not find enough water to counteract their RH loss. Thus, the shrinkage has been observed again in mortars with LWAs. At higher amount of replacement (i.e. 30%) the swelling behavior of linear autogenous deformation has always been observed to occur (Figure 4.2). The autogenous swelling can also be harmful for cementitious materials, as is the case for autogenous shrinkage. Thus, the amount of replacement of LWAs to mitigate autogenous deformation should be determined with necessary optimization.

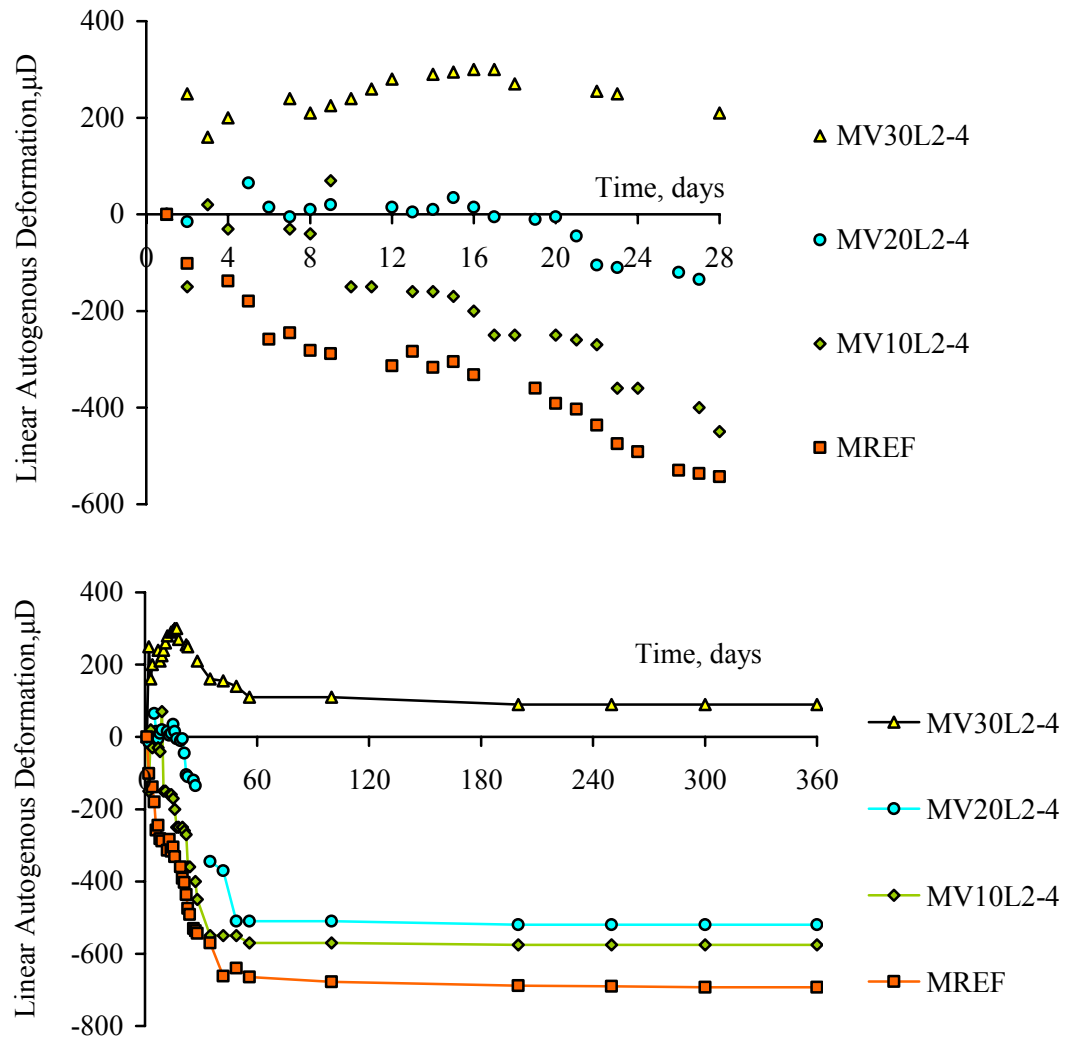


Figure 4.2: Effect of LWAs on linear autogenous deformation of mortar specimens.

The effect of both size and volume of LWAs on linear autogenous deformation of concretes are shown in Figure 4.3. The results obtained indicate that while the linear autogenous deformation of reference concrete (CREF) was $-537\mu\text{D}$ at 28 days, substituting the 2-4 mm size fraction of normal aggregate concentration by LWAs at a rate of 10% reduced the autogenous deformation to $-410\mu\text{D}$.

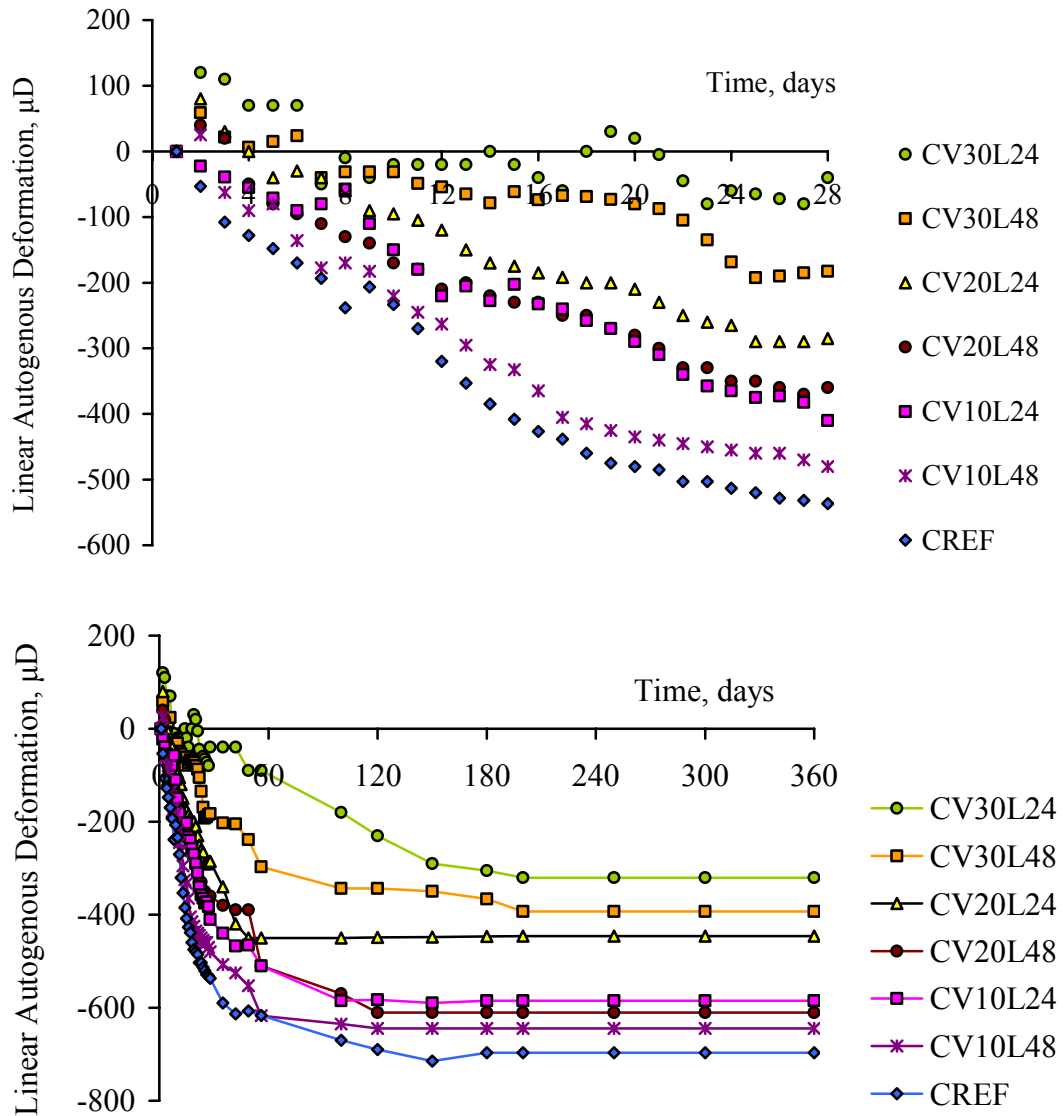


Figure 4.3: Linear autogenous deformation of concrete samples.

In concretes for which the substitution was applied using the same volume but larger size fractions such as 4-8 mm, the autogenous deformation was measured as $-480 \mu\text{D}$. When the normal aggregate is replaced by pumice LWAs with 2-4 mm size fractions, the linear autogenous deformation of concrete at 28 days was mitigated by 24%, 47% and 92%, for volume fractions of 10%, 20% and 30%, respectively. The use of coarse LWAs (4-8 mm size fractions), however, prevents autogenous deformation of concrete by 11%, 32% and 65% at the same volume fractions. Thus, the results have shown that the fine LWAs are more effective than the coarse LWAs in reducing the autogenous deformation of concrete. A similar behavior is also seen in 360-days autogenous deformation results (Figure 4.3).

4.2.2 Volumetric Autogenous Deformation and Temperature Development

Volumetric autogenous deformation diagrams of two cement paste samples are given in Figure 4.4. One of these samples was taken from the 35 liters original batch, whereas the other was taken from another batch produced using 5 liters small laboratory mixer. Although the samples were not from the same batch, both samples display similar behaviors of volumetric autogenous deformation, indicating that the method used is reliable.

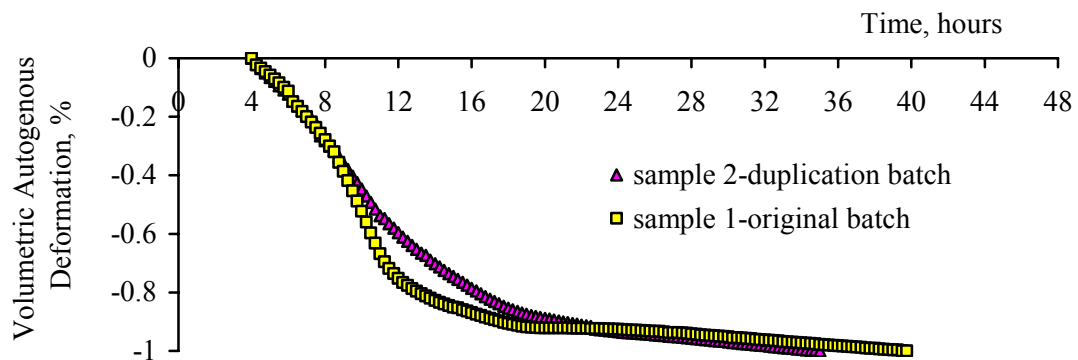


Figure 4.4: Volumetric autogenous deformation of two reference paste samples

For all the tests, the deformations were zeroed at the setting time of approximately 4 hours. Before setting, the volume changes occur due to the chemical shrinkage, while autogenous deformation begins to produce with the formation of solid skeleton of hydration products. Thus, it can be said from Figure 4.4 that the great proportion of volumetric autogenous deformation for PREF sample has been completed within the first 24 hours. As mentioned in Section 2.3.3, within the first few hours the volumetric autogenous deformation is increased with a gradually decreasing rate, and then the slope of deformation begins to increase (near the 9 hours). This is probably related to the rate of the increasing volume fraction of the connected solid phase changes at this transition point (Feylessoufi et al., 2001). Voigt et al. (2005) showed that the transition point of specific contact area of the hydrated cement particles (which is defined as the contact area per unit volume of cement paste void) is a parameter of describing the degree of the inner-particle bonding of the cement particles. After this point the hydration products form with lower specific volumes and the rate of autogenous deformation begin to decrease

Volumetric method is not a proper method for measurements of autogenous deformation of mortar because the aggregates in mortar can scratch the latex membrane. Thus, the tests were performed carefully on mortar samples. Also Figure 4.5 shows that there is no unusual expansion observed on each series, thus strengthening our confidence in the reliability of the data. The results shown in Figure 4.5 are average of two samples. As shown in Figure 4.5, volumetric autogenous deformations of mortars were naturally lower than that of the reference cement paste sample (PREF) because of the lower content of cement paste in samples. It is found that both fine mortar (FMREF) and coarse mortar (MREF) have the values of volumetric autogenous deformation similar to one another. The amount of cementitious materials used were 880 kg/m^3 and 671 kg/m^3 for FMREF and MREF samples respectively at the same water to binder ratio of 0.28. Because of its higher cement content, the FMREF sample would be expected to have higher autogenous deformation than the MREF sample. The reason for the similar values of volumetric autogenous deformation for the two samples may be the restraining effect of aggregates. In the MREF sample the total aggregate content was $0.560 \text{ m}^3/\text{m}^3$, while this value in the FMREF sample was $0.425 \text{ m}^3/\text{m}^3$. The volumetric autogenous

deformation increased with increasing the cement content, while increasing the aggregate content (especially larger ones) restrains the deformation of cement paste.

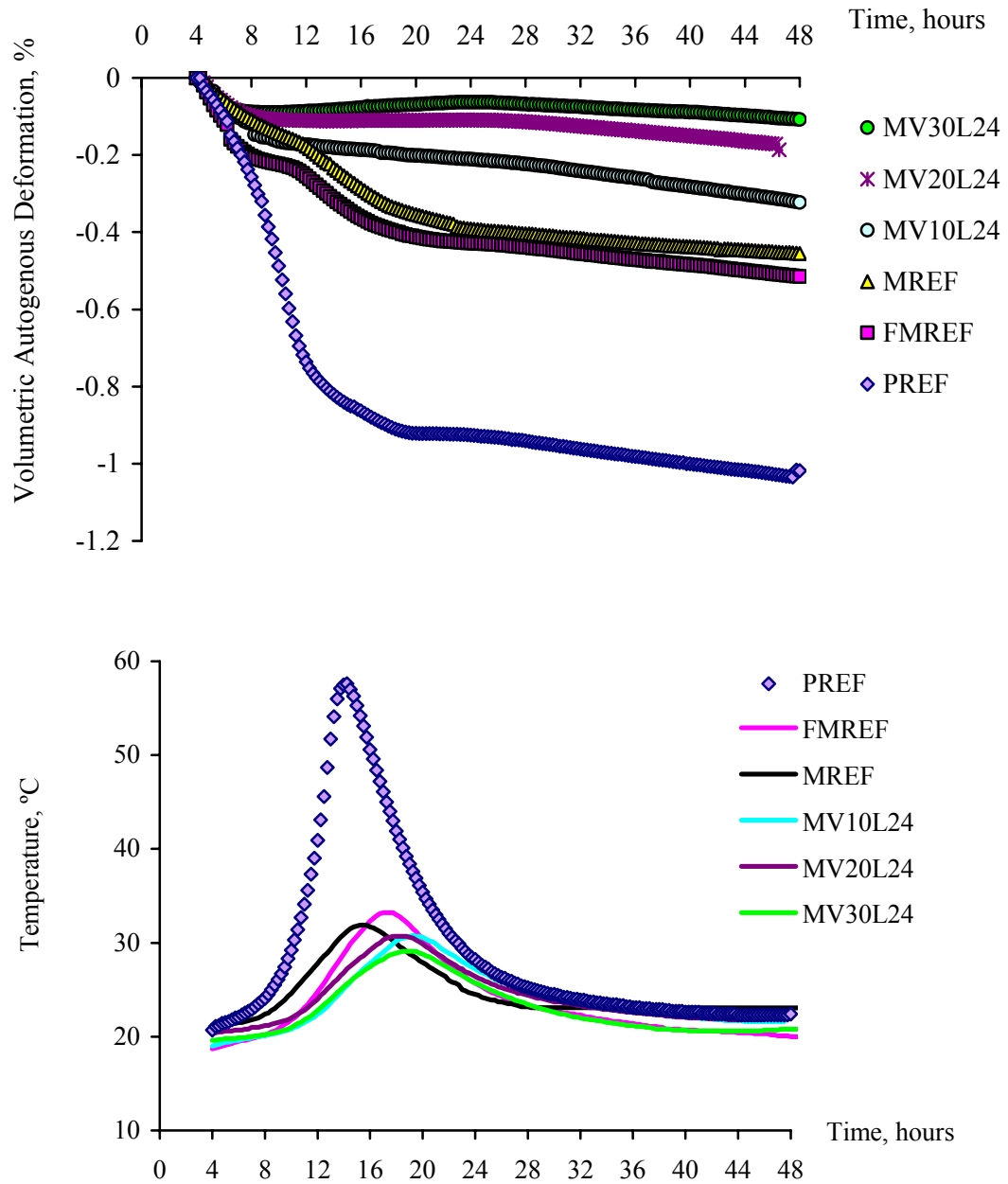


Figure 4.5: Volumetric autogenous deformation and temperature development of paste and mortar phases.

Figure 4.5 also shows the effect of volume of LWAs on autogenous deformation. It can be seen that the autogenous deformation decreases significantly with increasing the volume of LWAs. Even 10% replacement of aggregate by 2-4 mm LWAs resulted in 46% reduction in the value of autogenous deformation of MREF at 24 hours. For the replacement ratio of 20 and 30%, the reductions of mitigation of autogenous deformation were found to be 72% and 84%, respectively. On the other hand, for the replacement ratio of 10%, 20% and 30% of normal aggregates by LWAs, the reductions of mitigation for 48 hours autogenous deformation were found to be 29%, 61% and 76%, respectively. It can be concluded that the capability of LWAs in mitigating autogenous deformation decreases with time, because of the enhancing impermeable character of cement paste. The pores through which the LWAs transport water are getting smaller with the hydration products continue to form.

The temperature developments of paste and mortar phases in semi adiabatic condition are also shown in Figure 4.5. The test results shown are the average of two samples. It is found that the time to reach the maximum temperature was longer for the FMREF sample than for the MREF sample, which is unexpected (Table 4.1). The maximum temperatures of mortars were slightly decreased with the increasing volume content of LWAs. In addition, the time to reach the maximum temperature was getting longer with the increasing LWA content. Thus, it can be said that using LWAs has an effect in preventing the thermal deformation of cementitious materials.

Table 4.1: Maximum temperatures and time to reach these values for paste and mortar phases.

	PREF	FMREF	MREF	MV10L24	MV20L24	MV30L24
Maximum temperature, °C	57.6	33.2	31.9	30.8	30.7	29.1
Time to reach the maximum temperature, hours	14.25	17.25	15.5	17.5	18.5	19.25

4.3 Chemical Shrinkage

The variation in chemical shrinkage of PREF sample with time is shown in Figure 4.6. In the figure, the diagram of volumetric autogenous deformation of PREF sample is also shown. It should be noted that the PREF sample includes silica fume by 10%. As is shown, the most important part of chemical shrinkage has been completed in 24 hours after water addition. The results obtained in this work confirm the other available

findings (Hammer and Heese, 1999; Justness et al., 1999b; Holt, 2002). It is usually known that there is no significant correlation between autogenous deformation and chemical shrinkage (Barcelo et al., 1999). However, it is obvious from the figure that in early ages the main drive mechanism of autogenous deformation is chemical shrinkage.

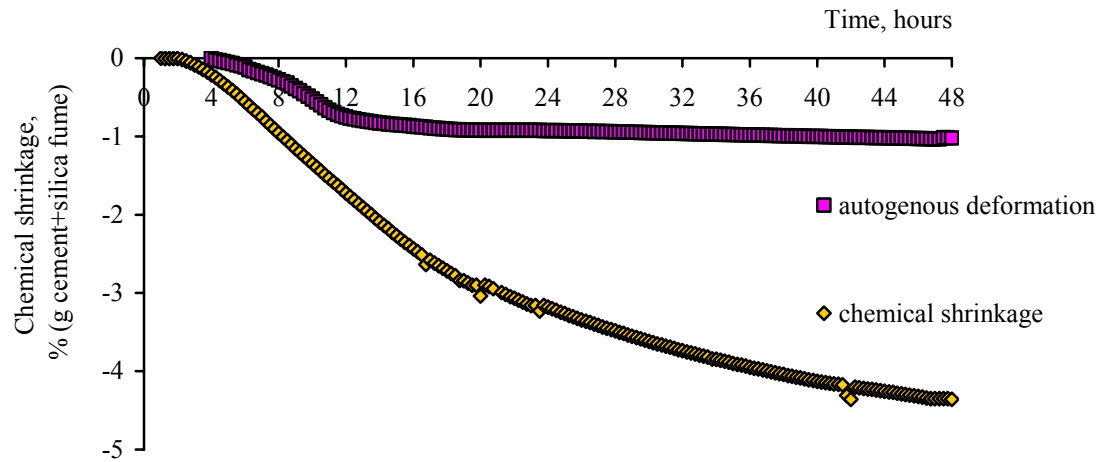


Figure 4.6: Chemical shrinkage and volumetric autogenous deformation of PREF sample.

The relationship between the autogenous deformation and chemical shrinkage of PREF sample is shown in Figure 4.7. The linear relationship between the two samples has been corrupted at about 11 hours of age. After this point no relationship between the autogenous deformation and chemical shrinkage has been observed.

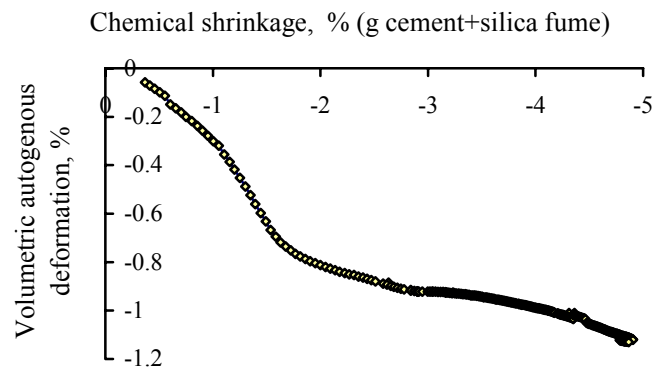


Figure 4.7: Chemical shrinkage and volumetric autogenous deformation of PREF sample.

4.4 Heat of Hydration

The heat of hydration tests were conducted on cement paste, fine mortar and coarse mortar samples as shown in Figure 4.8. As already mentioned in the experimental procedure, the cement paste pieces, which were divided from the coarse mortar samples, included fine aggregates. The minor corrections were made for the heats of solution of siliceous powder and natural sand which were previously determined. The heats of solution of siliceous powder and natural sand were found as 5.9 and 41.6 J/g, while that of dry cement was 2264.9 J/g. As shown in the figure, although three samples have similar paste phases, the results of their heat of hydration show slight differences. The heat of hydration of PREF samples were found smaller than those of FMREF and MREF samples at early ages, while the trends reversed at later ages. The effects of LWAs on heat of hydration of mortars are compared with the results of reference mortar.

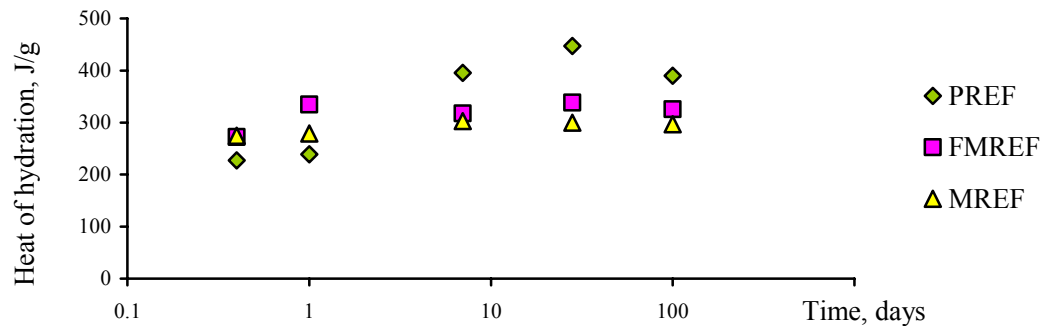


Figure 4.8: The variations heat of hydration in time for reference cement paste, fine mortar and coarse mortar samples.

The effect of replacement of normal aggregates by fine LWAs on heat of hydration is demonstrated in Figure 4.9. As the amount of LWAs increases, the heat of hydration also increases slightly. The cement particles can easily find water to hydrate with using LWAs, and consequently the amount of hydrated particles increases due to internal curing.

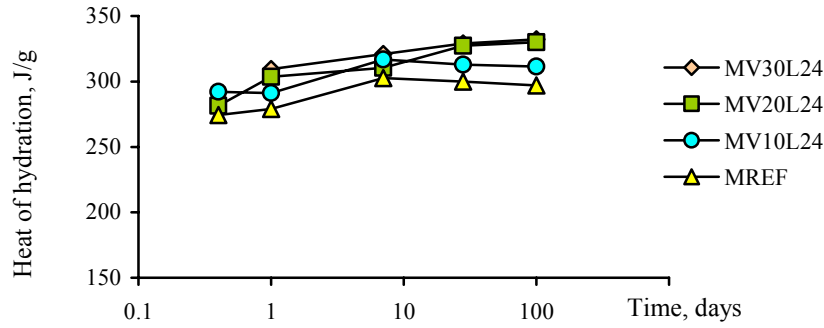


Figure 4.9: Effect of LWAs on heat of hydration of mortars.

4.5 Non-evaporable water content and degree of hydration

The non evaporable water contents (g water / g cement + silica fume) for the test specimens are given in Table 4.2. Similar to the results of heat of hydration, slight differences have been observed in the non evaporable water contents of the reference samples of paste, fine mortar and coarse mortar.

Table 4.2: The variations of non evaporable water content (water / g cement + silica fume by weight) of samples with time.

Non-evaporable water content (water/cement+silica fume by weight)					
	10 hours	1 day	7 days	28 days	100 days
PREF	0.031	0.068	0.104	0.097	0.126
FMREF	0.028	0.063	0.108	0.102	0.138
MREF	0.024	0.081	0.087	0.098	0.125
MV10L24	0.034	0.082	0.089	0.104	0.152
MV20L24	0.059		0.067	0.115	0.153
MV30L24	0.061	0.097	0.101	0.130	0.155

The results show that at early ages the rate of reaction for the MREF sample is greater than those of mortars with LWAs. The time to reach approximately the asymptotic value of the non evaporable water content is delayed with using LWAs. This is probably due to fact that with higher degree of hydration, the products will be larger in size and the diffusion of water through the CSH needles will take less time. The effect of LWAs on the degree of hydration of mortars, which was calculated from the non evaporable water

content, is shown in Figure 4.10. The amount of hydrated cement particles was increased by using LWAs.

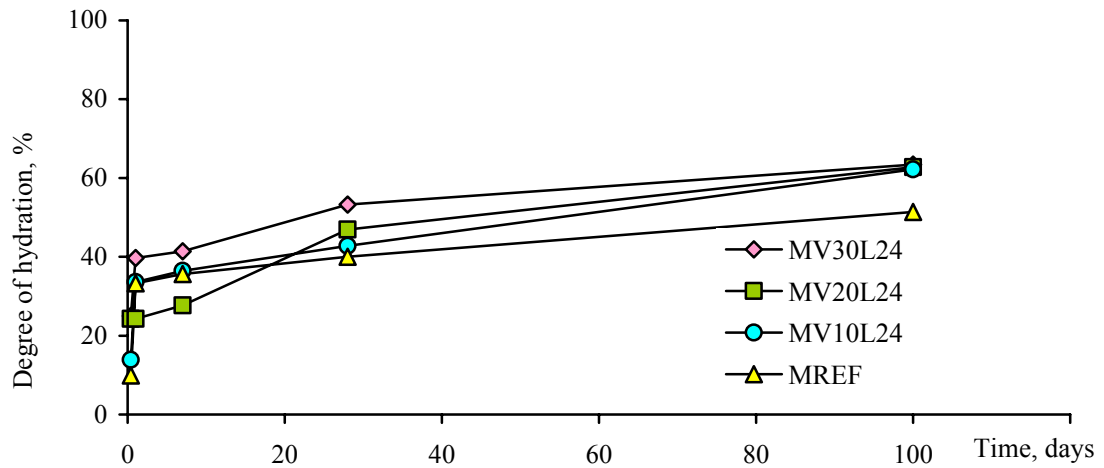


Figure 4.10: Effect of LWAs on degree of hydration of mortars.

The results are in agreement with the results of Mönnig (2003) who simulated the effect of LWAs on degree of hydration (Figure 4.11). It was also stated by the same author that LWAs has little effect on the degree of hydration, because the water transport mechanism is controlled by Darcy's law which connects local pressure differences with permeability. Hence, within an adiabtical system no transport of vapor and water exists.

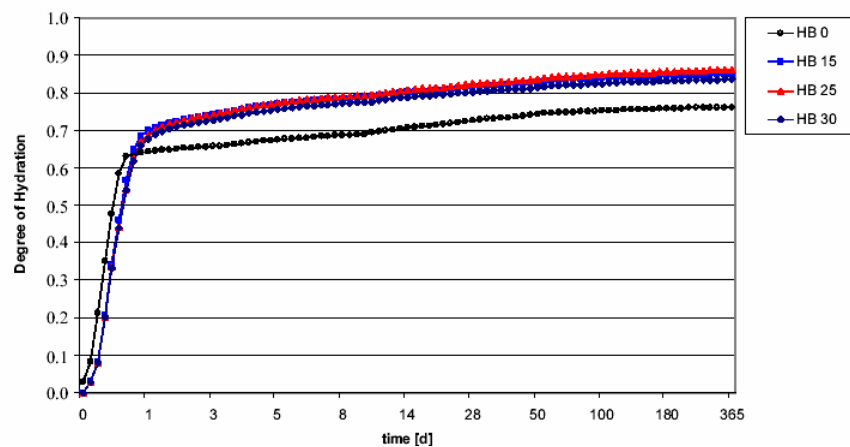


Figure 4.11: Development of the degree of hydration in an adiabtical system (Mönnig, 2003).

4.6 Mercury intrusion porosimetry (MIP)

The cumulative intruded volume and critical pore diameter of PREF samples from MIP test results are shown in Figure 4.12. The results show that the intruded volumes decrease with ongoing hydration. In addition, clear peaks in the figure imply that the critical pore diameter of reference paste with silica fume is decreased with time.

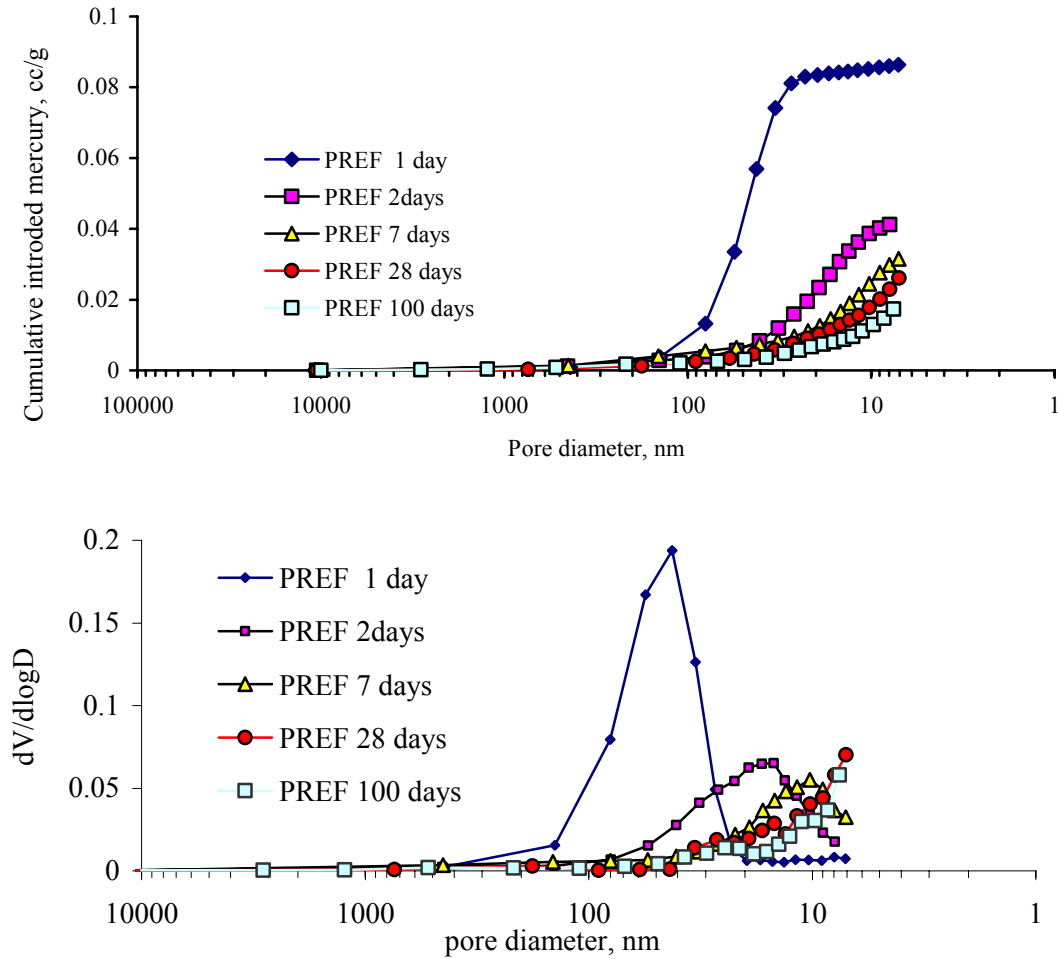


Figure 4.12: The variations of cumulative introduced mercury volume (a) and critical pore diameter (b) of PREF sample at 1, 2, 7, 28 and 100 days.

The critical diameters of the PREF sample have been found to be 42.29nm, 16.81nm, 10.26nm, <7.06nm and < 7.56nm at the ages of 1, 2, 7, 28 and 100 days respectively. The cumulative intruded pore diagrams at 7, 28 and 100 days did not reach the asymptotic value, meaning that the pressure capacity of MIP equipment was not sufficient. Therefore, the precise values of the critical pore diameters of some series have not been determined. The log differential pore volume as a function of pore diameter diagrams of FMREF, MREF, MV10L24, MV20L24, MV30L24 samples at different ages are shown in Figure 4.13. As seen in the figure, the critical pore diameters of PREF have been found different from those of the FMREF and MREF samples at all tested ages. The critical pore diameters (or maximum continuous pore radius) of PREF sample are larger than those of FMREF and MREF samples at the age of 1 day, but smaller at the later ages. The critical pore diameter of MREF sample has also been found larger than that of the FMREF sample.

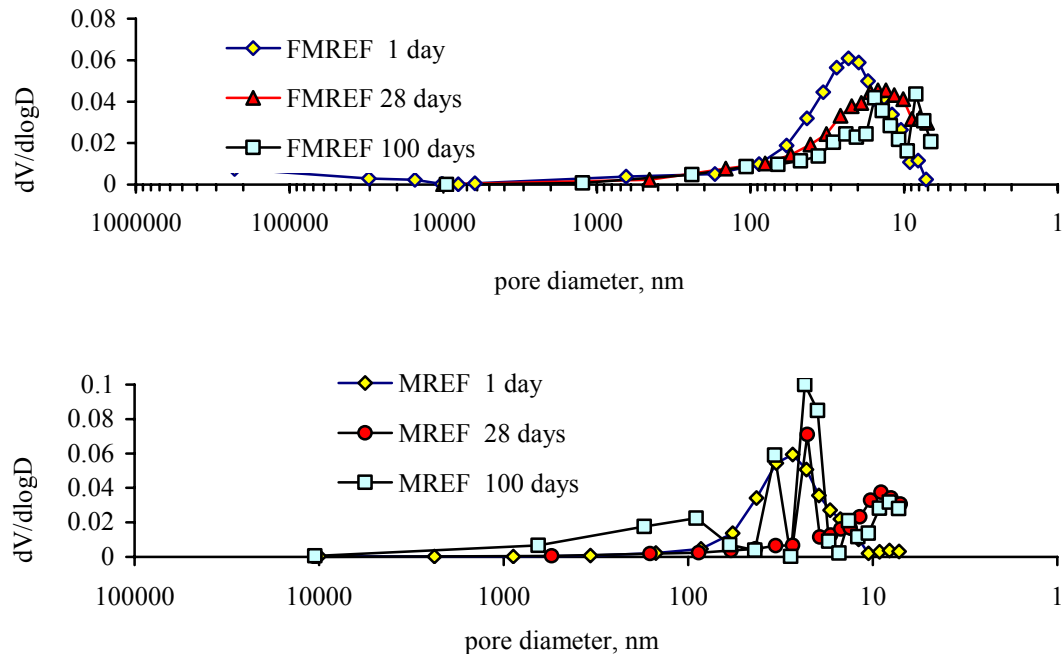


Figure 4.13: The variations of critical pore diameters of FMREF, MREF, MV10L24, MV20L24 and MV30L24 samples at 1, 28 and 100 days, respectively.

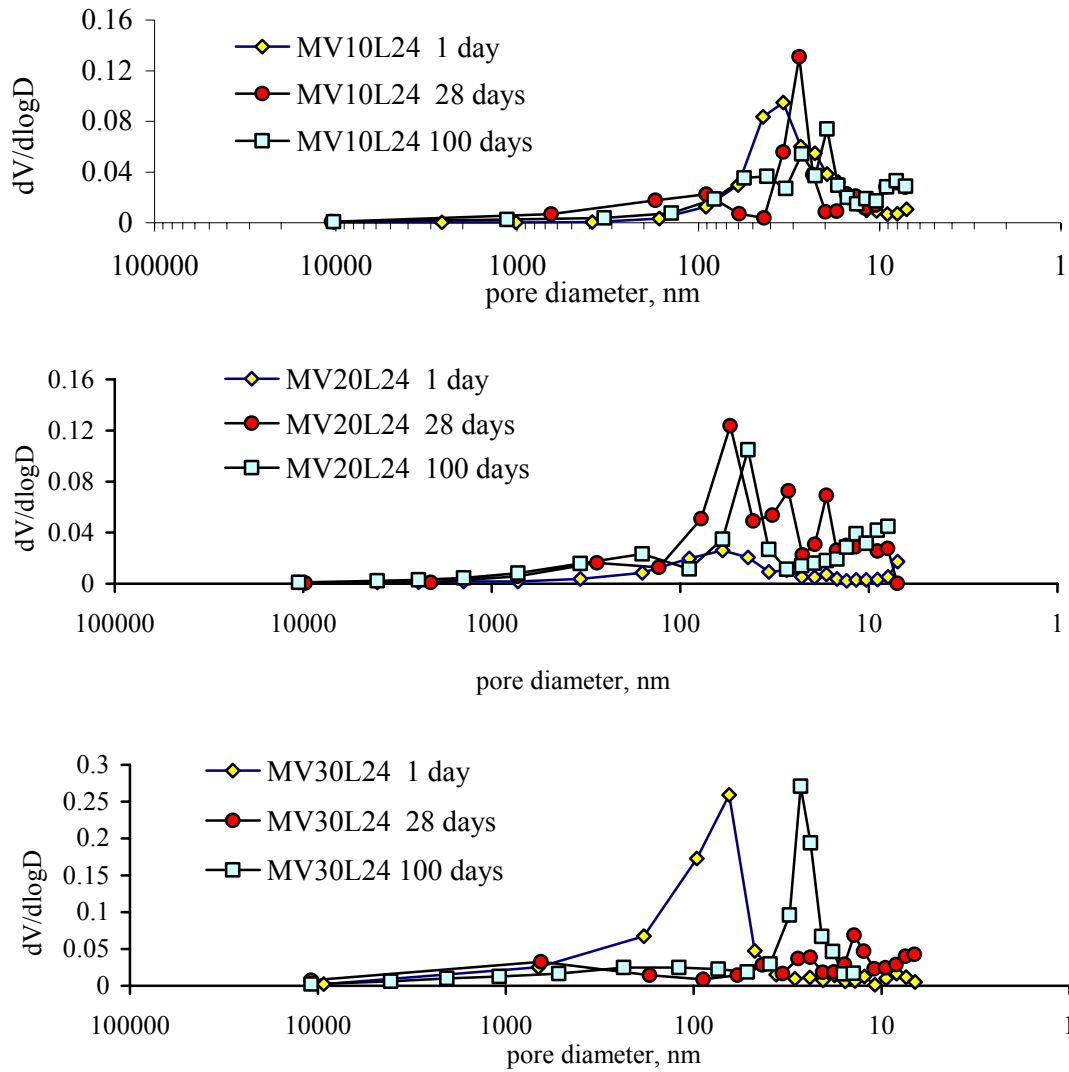


Figure 4.13 cont.: The variations of critical pore diameters of FMREF, MREF, MV10L24, MV20L24 and MV30L24 samples at 1, 28 and 100 days, respectively.

Total intruded mercury volume and critical pore diameter of the samples are summarized in Table 4.3. The results show that the addition of aggregate to the cement paste caused a decrease in the total intruded mercury volume because of the diminishing content of cement paste. On the other hand, substituting normal aggregate by LWAs increased the total intruded mercury volume. However, considering that some of the pores in LWAs may have been filled with mercury, it may not be reasonable to compare the results of mortars with normal aggregate to those with LWAs. Although, the total intruded mercury volume for the samples MV20L24 and MV30L24 have been found to

be similar, the critical pore diameter for the sample MV20L24 was inconsistently different from the other series. In addition, the results obtained show that LWAs causes decrease in the critical pore diameter significantly compared to the reference mortar, especially at 100 days, except the MV20L24 sample. It is also shown that by using LWAs the interfacial transition zones are enhanced by continuous internal curing which results in the development of more impermeable cementitious zone.

Table 4.3: Total intruded mercury volume and critical pore diameter of samples at different ages.

	Age, day	PREF	FMREF	MREF	MV10L24	MV20L24	MV30L24
Total intruded mercury volume, cc/g	1	0.0864	0.0493	0.0288	0.0463		
	2	0.0412					
	7	0.0315					
	28	0.0261	0.0368	0.018	0.0425	0.0729	0.0717
	100	0.0173	0.0305	0.0128	0.0474	0.0476	0.0461
Critical pore diameter, nm	1	42.29	23.05	27.14	34.07		
	2	16.81	-	-	-	-	-
	7	10.26	-	-	-	-	-
	28	< 7.06	14.79	22.57	27.8	54.38	26.93
	100	< 7.56	8.38	23.3	19.51	34.74	13.98

The total porosity was also calculated as the ratio of intruded volume of mercury to the bulk volume of the sample. Bulk volumes of the reference samples were arranged according to the volume of cement paste phase of the mixtures. It is found that the cement paste in fine mortar and coarse mortar were more porous than the PREF sample as given in Table 4.4.

Table 4.4: Total porosity of reference samples at different ages.

	Age, day	PREF	FMREF	MREF
Porosity, %	1	10.20	10.03	6.92
	2	4.36		
	7	3.54		
	28	3.04	5.91	4.28
	100	2.04	5.15	2.89

The same results have also been found by other researchers (Kumar and Bhattacharjee, 2003; Halimickova et al., 1995), and this is probably due to the fact that the interfacial transition zone between aggregates and paste is more porous than the paste phase. On the other hand, the sample FMREF was found more porous than the sample MREF, and this is probably due to the rough surface of the limestone crushed sand which can strongly adhere to the cement paste.

4.7 Pore Size Distribution

In order to determine the distribution of pores, the normalized porosity was calculated from the cumulative intruded mercury curves. The distribution results were investigated for four different pore widths such as >200 , $100-200$, $10-100$ and <10 nm. The pore width smaller than 10 nm has been chosen for representing the very fine gel pores. The second range of 10-100 nm has been used to find out the capillary porosity, while the range of 100-200 nm represents the large capillaries. The capillary pores govern the transport process if the pores are connected (Yang et al., 2006). The pore which has a width greater than 200 nm is mainly related to the strength and permeability of the cementitious materials. The results of pore size distribution for the samples PREF, FMREF and MREF are given in Table 4.5. It has been found that the amount of very fine pores (<10 nm) in PREF sample increased with time, while the amount of capillary pores decreased. The partial 10-100 nm porosity of PREF sample at the age of 1 day has been found much greater than that at later ages and in other pore width ranges. This is probably due to the breakdown of newly produced weak pores by intruded mercury. In all specimens, the amounts of very fine pores at the age of 100 days were smaller than that at the age of 28 days. This can be explained by the pozzolanic effect of silica fume which reacts with the lime to form secondary products that fill the pores.

It has been shown that the addition of aggregates had no significant effect on the amount of pores greater than 200 nm. The major effect of aggregate addition on pore size distribution has been observed at the pore width range of 100-200 nm. At this capillary pore width range the porosity of the MREF sample has been found smaller than that of finer mortar. As mentioned above, the bond of interfacial transition zone between cement paste and quartz sand is weaker than that of with the limestone which results in

more porous microstructure. Thus, the amount of partial porosity of MREF sample has been found smaller than that of FMREF sample.

Table 4.5: Pore size distributions of PREF, FMREF and MREF samples according to the porosity results (%).

	Age, day	>200 nm	100-200 nm	10-100 nm	<10 nm
PREF	1	0.18	1.38	8.51	0.13
	2	0.34	3.68	0.07	0.26
	7	0.28	0.33	2.15	0.79
	28	0.15	0.14	1.78	0.97
	100	0.20	0.05	1.27	0.52
FMREF	1	0.18	2.42	7.04	0.39
	28	0.53	0.34	4.23	0.82
	100	0.30	0.42	3.87	0.56
MREF	1	0.19	0.17	6.44	0.12
	28	0.19	0.14	2.02	1.93
	100	0.60	0.38	1.64	0.27

It is obvious that the porosity of samples with LWAs cannot be determined reasonably with the mercury intrusion because of the possible corruption of the pores of LWA by the applied pressure. In addition, it is expected that some of the mercury intrudes not only the pores of cement paste but also the pores of LWAs, meaning that an adequate determination of the porosity of samples with LWAs using the MIP results is extremely difficult. On the other hand, Lura et al (2004) have recently presented some MIP results for cement specimens with pumice grains, and no breaking point is observed in their results. The pore size distributions of MV10L24, MV20L24 and MV30L24 are given in Figure 4.14. As shown in the figure the amount of larger pores (>200 nm) increases with increasing the volume of LWAs, but decreases with time. This is reasonable because the pumices used in this study mostly have pores with the width range of 100-1000 nm. The major contribution of using LWAs was observed at the large capillaries. The amount of large capillaries decrease with the LWA content, while very fine pore volume increase at the age of 28 days. It is indicated that the hydrated cement ratio and the amount of gel pores increased by means of internal curing. This affirmative effect was also observed at the age of 100 days. On the other hand, at the age of 100 days, the amount of larger capillaries increases with the increasing amount of LWA.

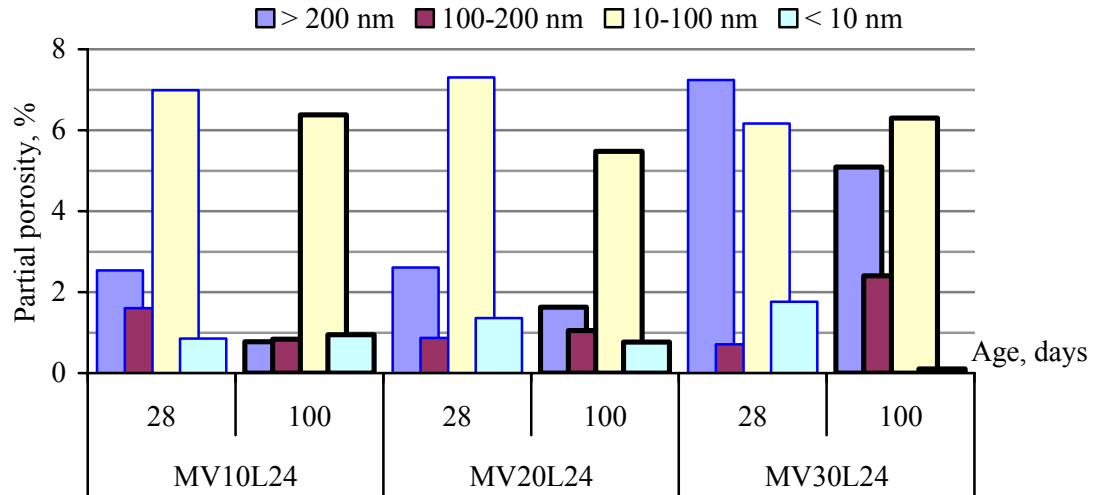


Figure 4.14: Partial porosity distributions of MV10L24, MV20L24 and MV30L24 series at 28 and 100 days.

The ratios of the porosity at certain pore ranges to the total porosity of mortars are given in Figure 4.15. As shown in Figure 4.15, with the decreasing LWA content the volume ratio of fine (10-100 nm) capillaries increases due to the self desiccation. It has been demonstrated that the use of 10% LWA was not sufficient to mitigate the autogenous deformation. As seen in the figure the pore structure of mortars smaller than 200 nm became even finer with the increasing amount of LWA content, which means that the internal curing provided the enhancement in the hydration kinetics.

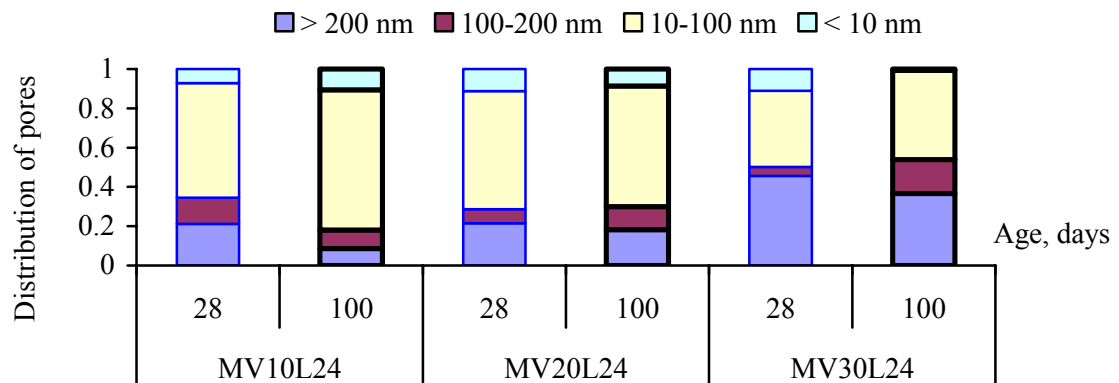


Figure 4.15: The distribution of very fine, fine capillary, large capillary and large pores in total porosity of mortars with LWA.

4.8 Mechanical Test Results

The mechanical test results and fracture parameters of produced cement pastes, mortars and concretes are summarized in Table 4.6 and 4.7 respectively.

Table 4.6: Fracture and strength properties of hardened cement paste and mortars.

	PREF	FMREF	MREF	MV10L24	MV20L24	MV30L24
Compressive strength, MPa	68	75	88	59	46	41
Modulus of elasticity, GPa	18	31	40	32	28	24
Area under the curve (W_0), Nmm	128	327	413	442	380	271
Fracture energy, N/m	27	62	77	82	71	52
Final disp. at midspan, mm	0.137	0.546	0.512	0.662	0.640	0.640
P_{max} , kN	1.6	2.88	4.21	2.96	2.73	2.29
Net bending strength, MPa	2.7	4.7	7.1	4.9	4.5	3.7
Splitting tensile strength, MPa	2.9	5.1	6.1	4.5	4.1	3.4
Characteristic length, l_{ch} , mm	55	75	82	132	122	108

Table 4.7: Fracture and strength properties of concretes.

	CREF	CV10L24	CV20L24	CV30L24	CV10L48	CV20L48	CV30L48
Compressive strength, MPa	93	79	62	50	68	61	48
Modulus of elasticity, GPa	46	40	37	32	40	37	27
Area under load-disp. curve, Nmm	508	563	551	432	451	422	322
Fracture energy, N/m	85	101	95	77	84	77	59
Final disp. at midspan, mm	0.313	0.609	0.687	0.618	0.699	0.671	0.475
P_{max} , kN	5.28	4.34	3.67	2.94	3.81	3.03	3.01
Net bending strength, MPa	8.6	7.1	6.0	4.4	6.1	5.0	4.8
Splitting tensile strength, MPa	6.7	6.4	4.8	4.6	5.6	5.0	4.1
Characteristic length, mm	86	98	155	118	107	115	95

4.8.1 Compressive Strength and Modulus of Elasticity

As shown in Figure 4.16 while the compressive strength of reference paste, fine mortar and coarse mortar did not vary considerably, the modulus of elasticity increased with increasing aggregate content. The addition of aggregate to the cement paste had an initial effect of decreasing the compressive strength. Under compression, there may be some three dimensional fracture surfaces which are parallel to the load direction. In addition, stress concentration at the interface between cement paste and aggregate increases with increasing the aggregate content, which causes a reduction in the compressive strength. A satisfactory value for the number of aggregates at the vertical cross section was attained when the aggregate concentration reached approximately the value of $0.50 \text{ m}^3/\text{m}^3$. As a consequence, the vertical cracks begun to incline into the aggregate. Because of the fact that the tensile strength of aggregate is greater than that of cement paste, the compressive strength of composites increased little more with increasing aggregate content.

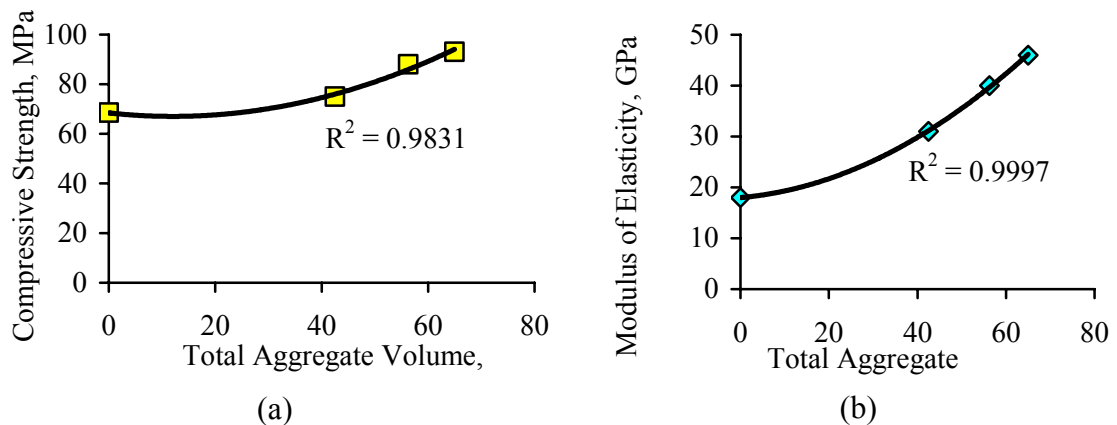


Figure 4.16: Compressive strength (a) and modulus of elasticity (b) of reference cement paste (PREF), fine mortar (FMREF), coarse mortar (MREF) and concrete (CREF) without any LWAs.

The effect of aggregate concentration on modulus of elasticity is shown in Figure 4.16. The modulus of elasticity increased with increasing aggregate content; the variation between the two parameters is marked by a second order curve with high correlation

coefficient. Figure 4.17 shows the typical stress-strain diagram for determining the modulus of elasticity of the reference samples.

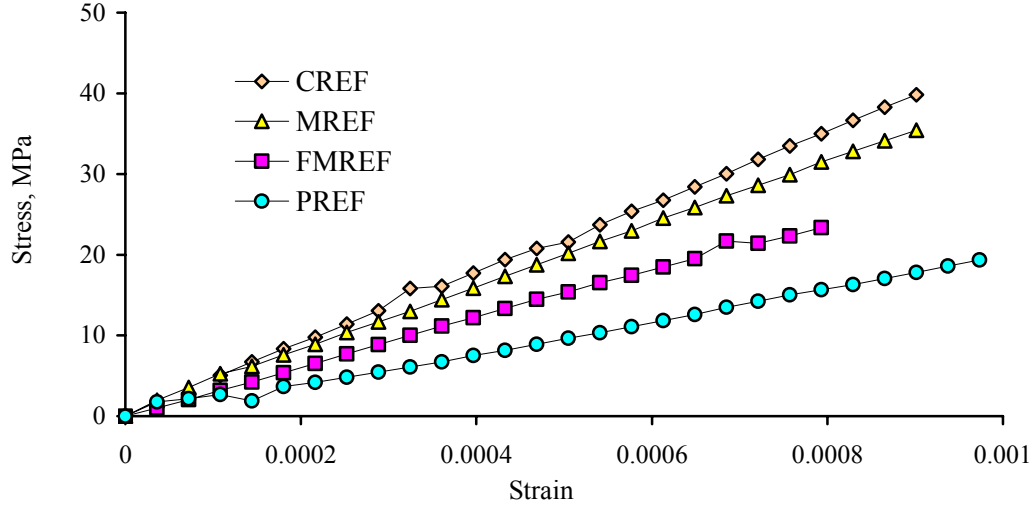


Figure 4.17: Stress-strain curve of reference cement paste, fine mortar, coarse mortar and concrete for determining the modulus of elasticity ($\sigma < 0.33 f'_c$).

Since the modulus of elasticity of LWA is lower than that of normal aggregate, a significant reduction in compressive strength for mortars with LWAs was observed with respect to the reference mortar (Table 4.6). The compressive strength also decreased with increasing volume of the substituted LWA. A decrease in the modulus of elasticity was also recorded with increasing the replacement volume of the LWAs. In addition, the compressive strength of concretes with LWAs decreased with increasing the particle size and volume of the substituted LWA. A slight decrease in the modulus of elasticity was recorded with increasing the replacement volume of the LWAs, although the change in the size of LWA had no significant effect on the modulus of elasticity of concrete.

The effect of the size of LWA on bending and compression can be modeled in that LWA behave in concrete phase as a defect (Tasdemir, 1982; Tasdemir et al., 2002; Akcay et al., 2005). The strength of the continuous phase is greater than that of lightweight aggregate, which is embedded in this phase. Therefore, it is possible to consider the weak lightweight aggregate as defects in the matrix phase. In all three sections given in Figure 4.18, the total volumes of lightweight aggregate are identical. As seen in the

figure, the probability of coarse LWA weakening the matrix phase for the cross section (a) is taken as one (i.e. $P(a)=1$). In the cross section (b), in order for the weakening to be in a similar degree as in (a), the two LWA particles must coincide on the same cross section and this means a lower probability than 1. For the cross section (c), the four LWA particles must be on the same line, and thus they will have a lower probability than the one at (b). Among these three cases the probability for (a) is the highest, while (c) is the lowest, as a result, the inequality $P(a)>P(b)>P(c)$ can be written. Thus, the model considered is in a good agreement with the experimental results.

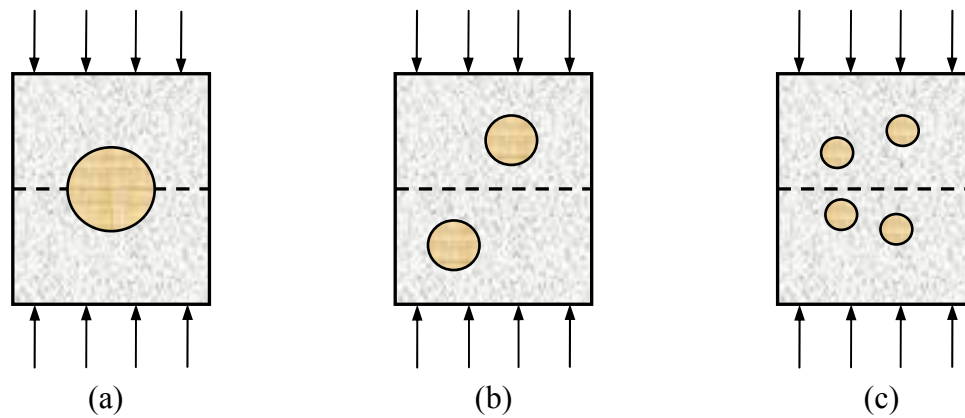


Figure 4.18: The model proposed for the strength of lightweight aggregate concrete.

4.8.2. Bending and splitting tensile strengths

The bending and splitting tensile strengths have been increased with addition of aggregate to the cement paste phase as shown in Figure 4.19.

As presented in Table 4.6 and 4.7, the size and volume concentration of LWAs had effects on bending and splitting tensile strengths in a way similar to that observed on the compressive strength results. The use of fine LWA to prevent autogenous deformation of concrete seems more effective in terms of the mechanical properties of concrete comparing the use of coarse LWA.

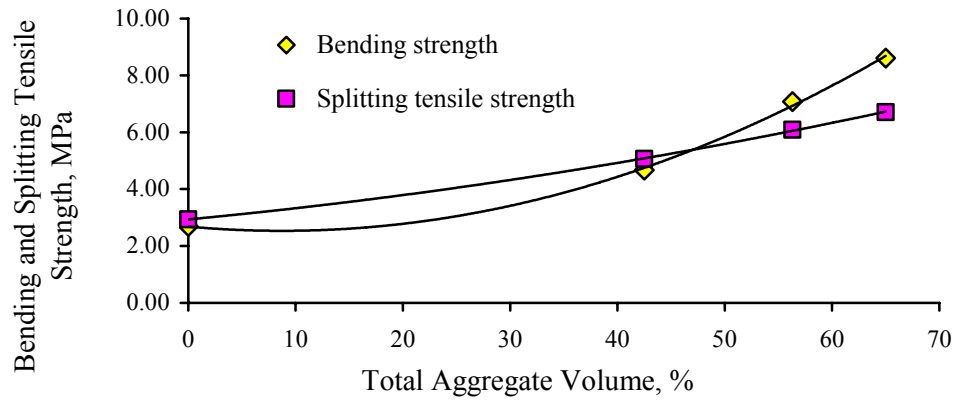


Figure 4.19: The bending and splitting tensile strength of reference cement paste, fine mortar, coarse mortar, and concrete phases.

4.8.3 Fracture Energy

The typical load- displacement at midspan curves of reference samples are shown in Figure 4.20. It can be said that the addition of aggregate in cement paste phase increased the area under the load-displacement curve. It has been found that the area under the curve increased about 3.5 times with respect to the PREF sample when the aggregate concentration is $0.65 \text{ m}^3/\text{m}^3$. The main reason for this substantial increase in the fracture energy of concrete with the increasing aggregate volume concentration is that the microcracks at the fracture process zone decrease the stress concentration. As a result, cracks are forced to incline into the aggregate, or near the aggregate, and to excess the aggregate obstacle, and hence the amount of consumed energy increases. It is also seen in Figure 4.20 that the value of final displacement at midspan increased up to 0.56 (MREF), and then decreased for the CREF sample. The reason for this decrease is that the amount of cement paste phases was lower in the high strength concrete with high aggregate concentration. Thus, matrix cracks passed through the aggregate rather than turning around the aggregate which resulted in the fracture of aggregate, and the final displacement of CREF will be lower than that of MREF. Thus, it can be concluded that transgranular type of fracture occurs. When testing the cement paste sample the loading rate was reduced after peak load because of the brittle character of cement paste. If the loading rate was kept constant the carried load decreased rapidly and such a decrease

caused the work-out of data logger. As a result, some ductile behavior after the peak load (which is unusual) was observed on cement paste sample as seen in Figure 4.20.

The test results have shown that the most significant effect of LWAs was observed on the fracture energy of concrete. The results given in this study were obtained using the area under the load-displacements curve. As seen in Figure 4.21 and Table 4.7, in cases of using both fine and coarse fractions, the area under the load displacement curve increased with increasing the replacement volume of LWA, although the peak load decreased with especially the use of fine LWA. Because the LWAs produce more microcracks, the concrete containing these aggregates behaves more ductile (i.e. less brittle) than the reference concrete. Although the slope of the ascending branch of the curves remained almost constant, the measured final displacement at midspan increased significantly with using the LWAs.

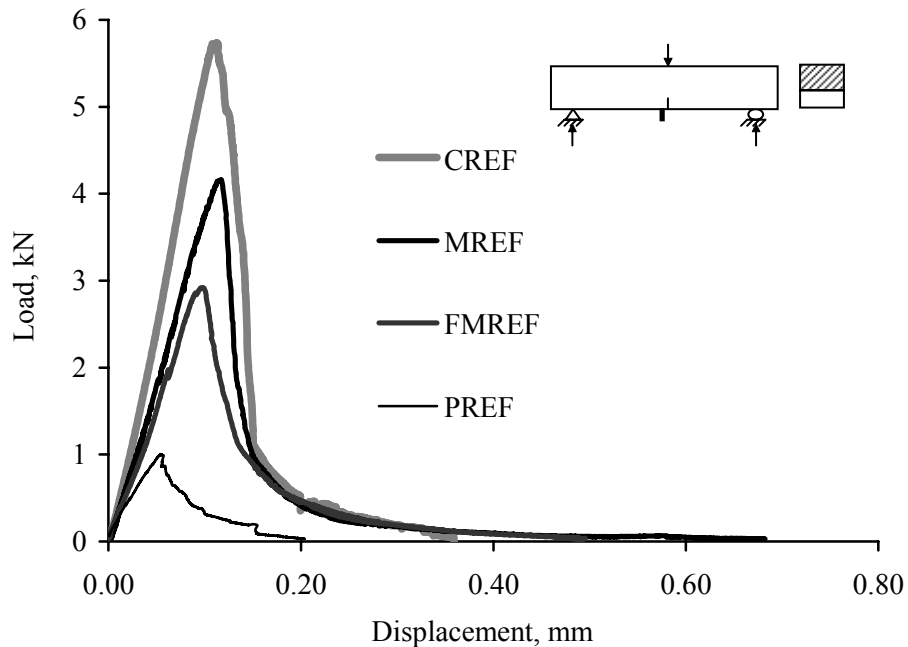


Figure 4.20: Typical load versus displacement curves for reference cement paste, fine mortar, coarse mortar, and concrete phases.

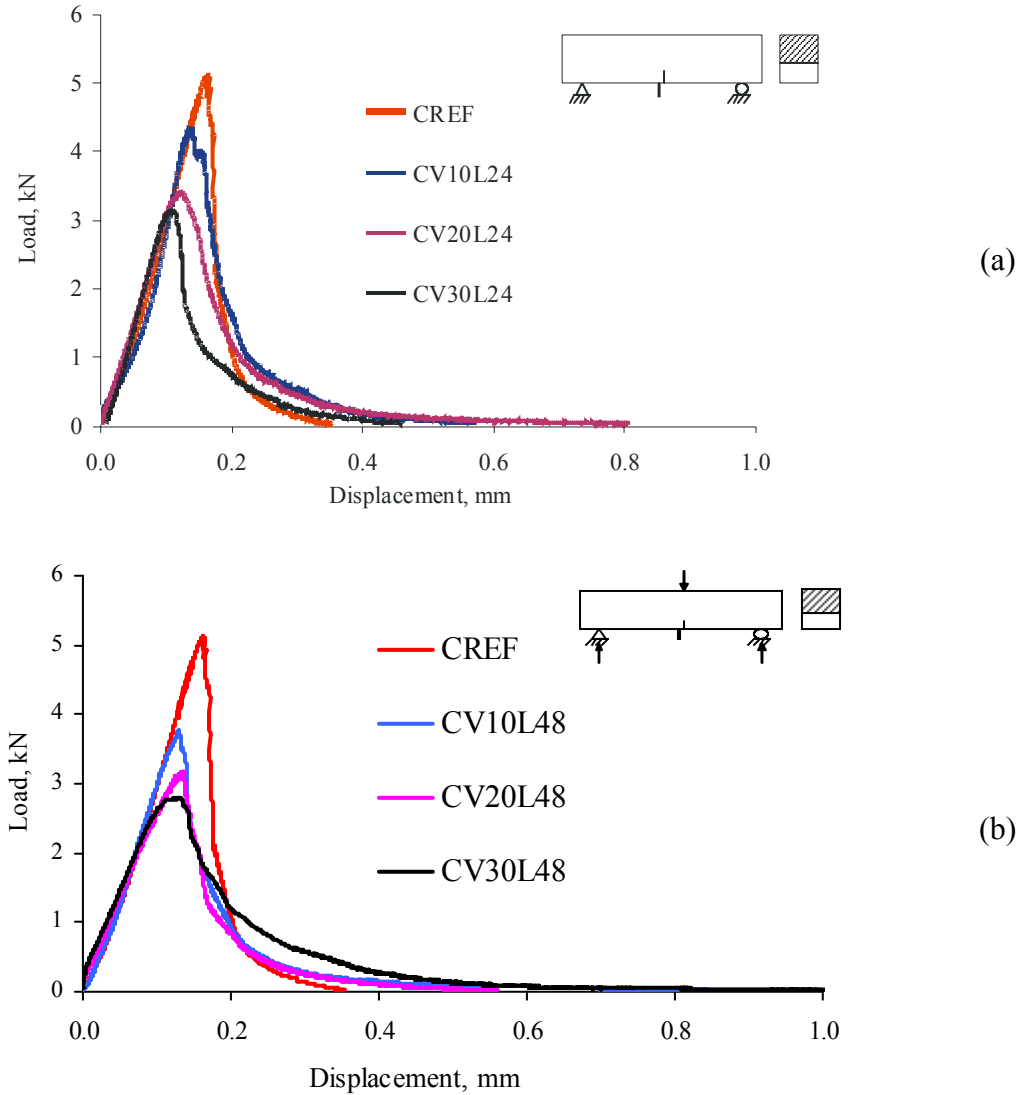


Figure 4.21: Typical load versus displacement curves for concretes contained (a) fine LWAs with the size fraction of 2-4 mm; (b) coarse LWAs with the size fraction of 4-8 mm. The results were obtained by three point bending test.

In particular, replacement of normal aggregate by fine LWAs by volume of 10% caused the fracture energy to have increased by 19% with respect to the reference concrete. However, using the coarse fraction of the same volume, although caused a decrease in the peak load, did not change the fracture energy significantly when compared to the reference concrete. The fracture energy also decreased with increasing the volume of the LWAs. For substitution of normal aggregates with LWAs by 10, 20 and 30 volume percent, concretes with fine fraction of LWAs had greater peak load and also the area

under the curve increased with respect to that of the coarser fractions (Figure 4.22). Although the ultimate load did not vary significantly, longer tail was an indication of mean particle size of LWA.

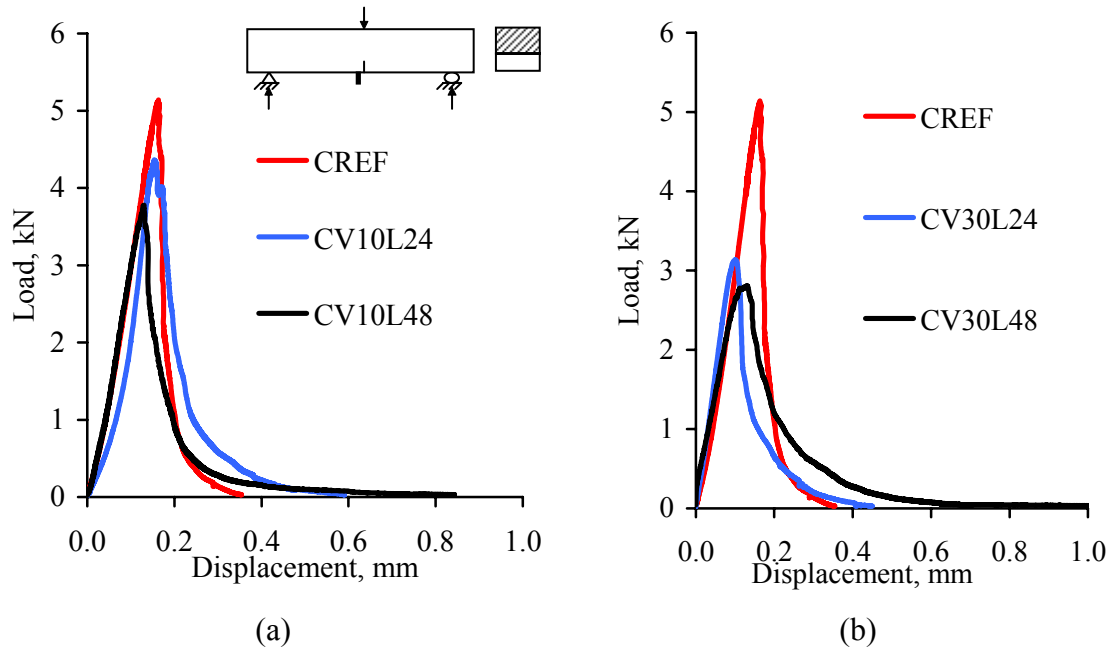


Figure 4.22: Effect of the size of used LWAs on load versus displacement curves for concrete in which the normal aggregate was replaced by LWAs with volume replacement ratios of (a) 10% and (b) 30%.

As presented in Figure 4.23 and Table 4.6 the volume concentration of LWAs had effects on fracture energy of mortars in a way similar to that observed on concrete samples. The 10% replacement of LWA increased the fracture energy of mortar, while further replacement decreased. In addition, it can be said from the figure that the displacement at peak load decreased with increasing LWA content.

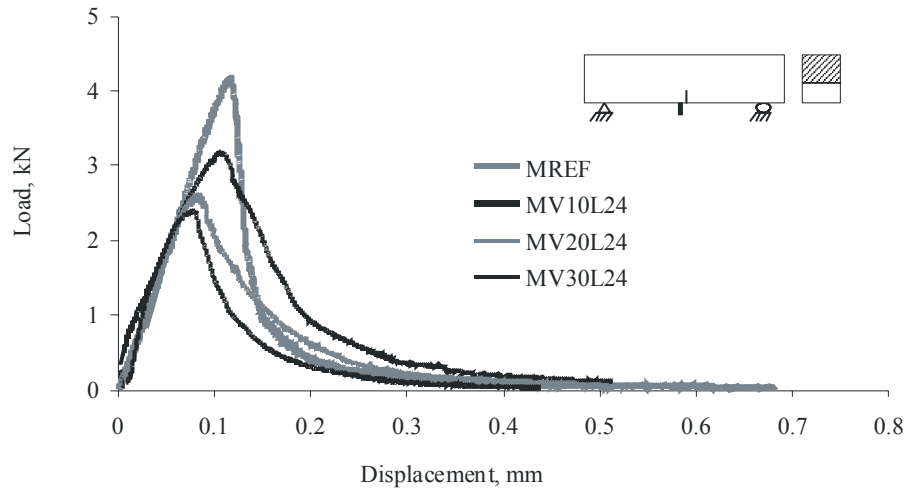


Figure 4.23: Typical load displacement curves for reference mortar and mortars with LWAs obtained from three point bending test.

The effect of variation of size and volume of LWAs on final displacement at midspan is shown in Figure 4.24. The final displacement increased significantly with the replacement volume of LWA, although after 10% replacement of LWA, the final displacement at midspan begins to decrease. This is probably due to the fact that there is not enough amount of stiffer normal aggregate around which the cracks could progress; thus the cracks can easily penetrate into the LWAs and matrix phases. For the mortar phases, the values of final displacement midspan have not been changed significantly with the increasing replacement ratio of LWAs, because the final displacement at midspan is governed by the maximum aggregate size. For the mortar samples, there were no large aggregates that could cause an obstacle to the crack.

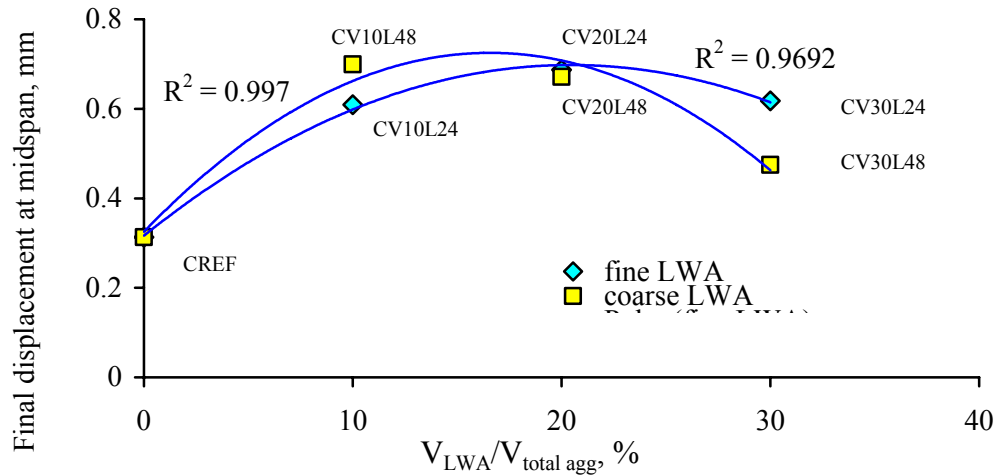


Figure 4.24: Final displacements at midspan for the concrete samples.

4.8.4 Characteristic Length

As shown in Table 4.6 and 4.7, the total aggregate content of composite increased with the characteristic length. In addition, the characteristic length of both mortars and concretes with LWA has been found higher than that of concrete without LWAs. The most fundamental effect of using LWAs was observed to have occurred on both the fracture energy and the characteristic length of concretes. The characteristic length, which is calculated using the Eq. (2.15), increased with the use of LWA, indicating that the material became more ductile. With decreasing the substituted mean particle size of LWA, the brittleness of concrete diminished. In Figure 4.25, the variations in the size of LWA with fracture energy and characteristic length are shown. The replacement of the 2-4 mm size of normal aggregate by LWAs by 10 and 20% volume fraction increased the fracture energy, while a replacement by 30% decreased. On the other hand, no significant effect of LWA replacement on fracture energy was observed when using the 4-8 mm of LWA and 10% replacement ratio, although a decrease in the fracture energy was observed with increasing the volume of the substitution to ratios greater than 10 percent. The use of LWAs in concrete had an effect of increasing the characteristic length of the material in all size and volume fraction of LWAs. The decrease in the brittleness was more significant in concretes with fine LWAs. It can be shown that replacement of normal aggregate by LWA even by 10% volume can play a significant role in decreasing the linear autogenous deformation of concrete at 28 days of age.

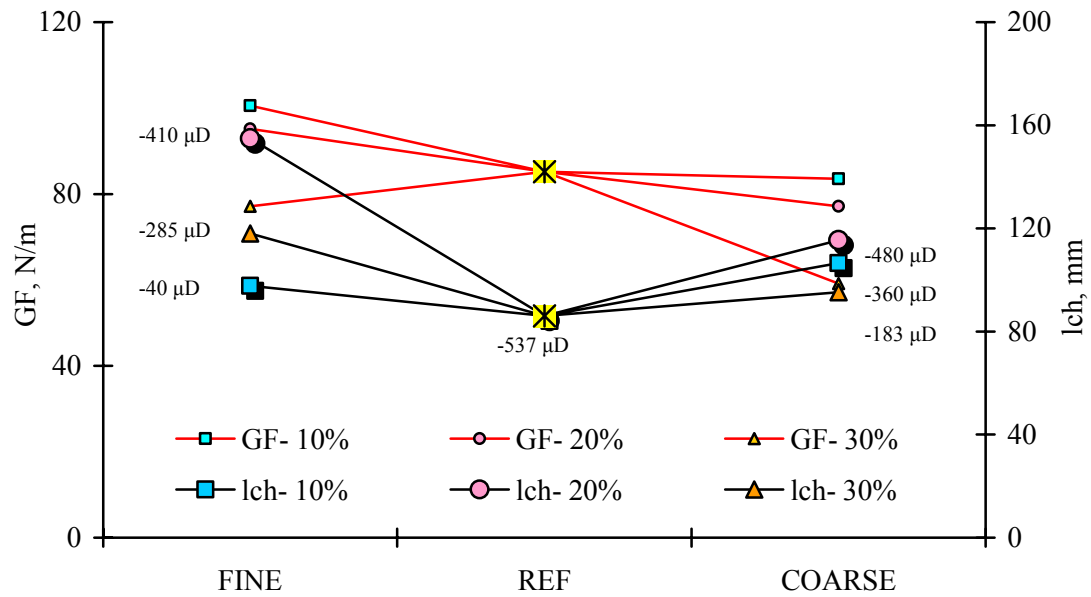


Figure 4.25: Effect of the size of LWA on both fracture energy and characteristic length (the values shown with arrow represent the linear autogenous deformation at the 28 days of age of concrete).

It can be seen that substituting the normal aggregates by LWAs by up to 30 volume percent prevented the autogenous deformation of reference concrete significantly, although such a practice caused also a marked loss in the mechanical properties of cementitious materials. However, the negative effect of this application on the mechanical properties of concrete is shown to be smaller in case of using fine LWAs. It should therefore be noted that in order to mitigate the autogenous deformation and cracking in early ages, the volume and size of the LWAs should also be optimized with taking the mechanical properties into account.

5 EFFECT OF SIZE AND TYPE OF AGGREGATES ON AUTOGENOUS DEFORMATION AND FRACTURE PROPERTIES OF CEMENTITIOUS MATERIALS

5.1 General

The size and volume of LWAs have significant effects on both autogenous deformation and fracture properties of cementitious materials as shown in previous chapters. This chapter presents the results of experimental studies conducted for determining the restraining effect of both LWAs and NWAs on autogenous deformation. The experiments were performed on five different cementitious composites with different type of aggregates. These composites contained 70% volume of paste and 30% volume of aggregate. Details of all mixtures proportioning and some of the fresh properties of composites are given in Table 5.1. The second letter in each code stands for the type of aggregate (e.g. N-normal and L-lightweight aggregate), while the following numbers denote the size fraction of aggregates such as 2-4 and 4-8 mm.

Table 5.1: Mixture properties of composites

	PN0-2	PN2-4	PN4-8	PL2-4	PL4-8
Cement, kg	1005	1005	1018	1010	1007
Silica Fume, kg	101	101	102	101	101
Water, kg	309	309	314	311	310
Pre-soaked water, kg	0	0		73	71
Superplasticizer, kg	6.3	5	3.7	5	3.7
Siliceous powder , kg	0	0	0	0	0
Natural sand (0-2), kg	765	0	0	0	0
Crushed sand (2-4), kg	0	765	0	0	0
Crushed stone No.I (4-8), kg	0	0	805	0	0
LWA 2-4 mm, kg	0	0	0	222	0
LWA 4-8 mm, kg	0	0	0	0	215
Air, %	2.3	2.4	1.7	2	2.3
Unit weight, kg/m ³	2186	2185	2243	1722	1708

5.2 Autogenous Deformation

5.2.1 Linear Autogenous Deformation

The linear autogenous deformation measurements of samples for 28 and 360 days are shown in Figure 5.1. The results of linear autogenous deformation are average of four samples. The autogenous deformation of cement paste at 28 days was $-760 \mu\text{D}$ ($1\mu\text{D}=1\times 10^{-6}$), while the paste with normal aggregate at the size fraction of 0-2 mm, 2-4 mm and 4-8 mm were measured as -453 , -414 and $-450 \mu\text{D}$, respectively.

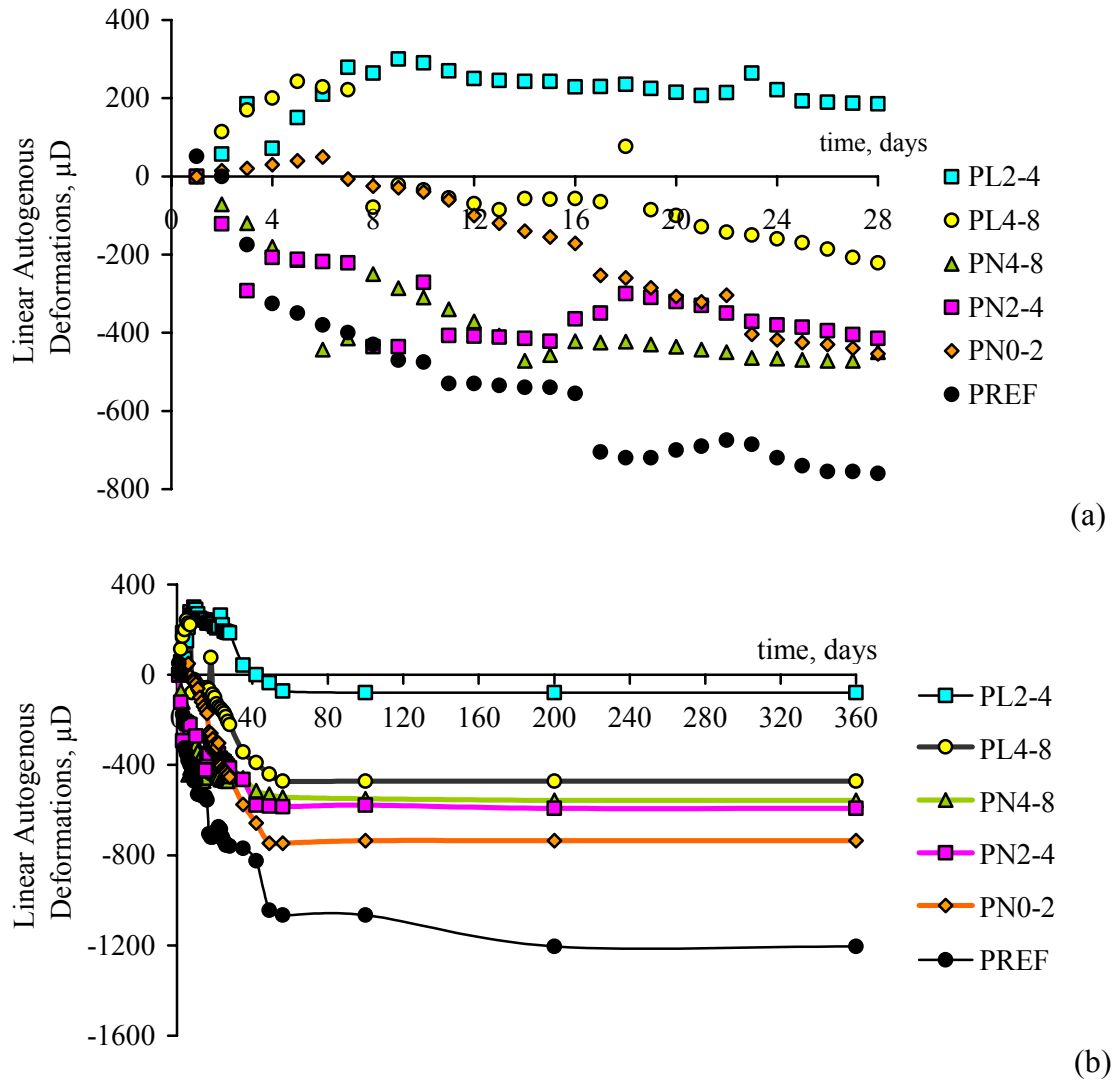


Figure 5.1: Effect of size and type of aggregate on linear autogenous deformation of composites until the age of 28 days (a) and 360 days (b).

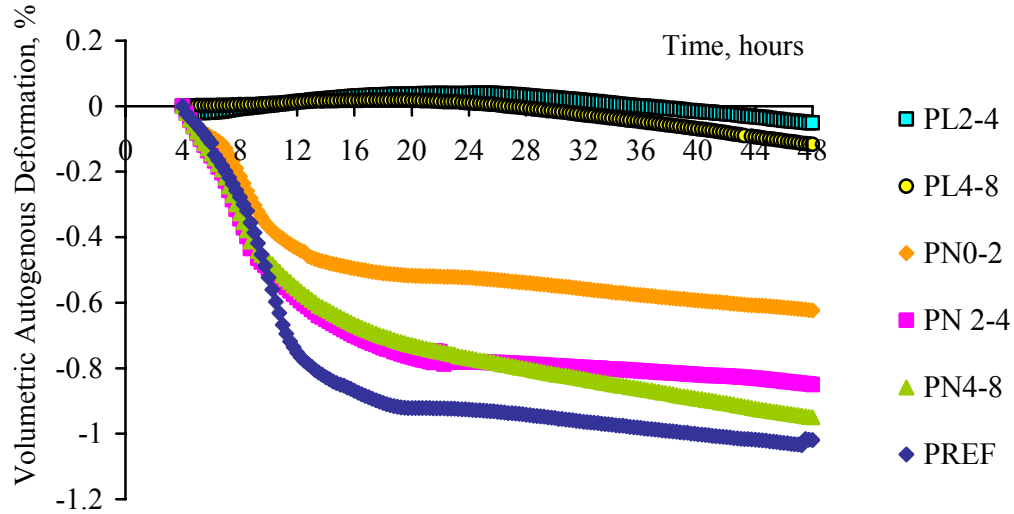
It is also shown in Figure 5.1 that the size of normal aggregates has no significant effect on autogenous deformation at 28 days, while the autogenous deformation of cement paste with 0-2 mm size fraction of normal aggregate has been found higher than that with 2-4 mm and 4-8 mm at the age of 360 days. Because the normal aggregates are stiffer than the cement paste, they mitigated the autogenous deformation by restraining the cement paste. In early ages, the finer NWAs (0-2 mm) efficiently mitigated the autogenous deformation of cement paste because the modulus of elasticity of cement paste was not too high. On the other hand, addition of coarser size aggregate easily restrained the shrinkage of cement paste at the later ages. Addition of 2-4 and 4-8 mm saturated LWAs into the cement paste reduced the autogenous deformation to -186 and -221 μD , respectively. The fine size of LWAs, as expected, was found to be more effective in mitigating the autogenous deformation of cement paste than the coarse LWAs, and even swelling was observed to occur by addition of finer LWAs at especially ages of <50 days.

5.2.2 Volumetric Autogenous Deformation and Temperature Development

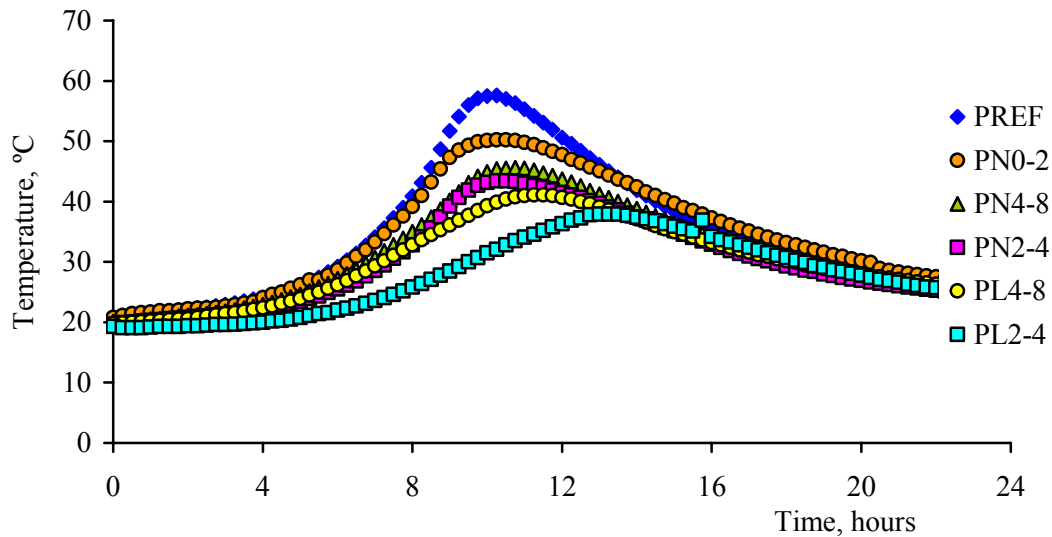
The variation of volumetric autogenous deformation with time for the composites is shown in Figure 5.2. The results shown are the average of two samples and normalized to the volume of cement paste content. The restraining effect of normal aggregates can also be seen in the volumetric autogenous deformation test results. In contrast to the linear autogenous deformation test result, the volumetric autogenous deformation of PN0-2 sample was found to be lower than that of PN2-4 and PN4-8 samples, while the values for PN2-4 and PN4-8 series were found similar to one another.

In addition, the test results also show that the addition of LWAs to the cement paste reduced the volumetric autogenous and also caused swelling. Approximately 28 hours after casting swelling behavior of autogenous deformation was followed by shrinkage. The possible reason for this, as explained in Section 4.2.1, is that the pore radius of cement paste at early ages is larger than at the later ages; and hence internal curing water can easily travel into the cement paste at early ages. With ongoing hydration, the probable travel distance will be decreased, thus the shrinkage is observed again in

mortars with LWAs. The use of fine size of LWA has been found to be more effective than coarse LWA in mitigating the volumetric autogenous deformation.



(a)



(b)

Figure 5.2: Volumetric autogenous deformation (a) and temperature development (b) of paste and mortar phases.

The temperature developments of paste and mortar phases in semi adiabatic condition are also shown in Figure 5.2. The test results shown are the average of two samples. It is found that, as expected, the maximum temperatures of composites decreased with the

decreasing size of LWAs. In addition, the time to reach the maximum temperature was getting longer with the decreasing size of LWA, while this time duration was found nearly similar for composites with different size of normal weight aggregates.

The new test series have been conducted to find out whether the LWAs have effects on autogenous deformation of cement paste other than water entraining. The cement paste sample was prepared using the water/cement ratio of 0.28 (without addition of silica fume), while another test sample was prepared replacing 30 percent by volume of reference cement paste using expanded clays (in particle size fractions 4.00-6.73 mm) saturated with water for 30 minutes. In the third series, all artificial expanded clay LWAs were coated by paraffin one by one to obstruct the water flow. All the autogenous deformation were tested in volumetric measurements and duplicated. The normalized results regarding the cement paste content are shown in Figure 5.3 where autogenous deformation of the cement paste with coated LWAs resembles to that of the plain cement paste.

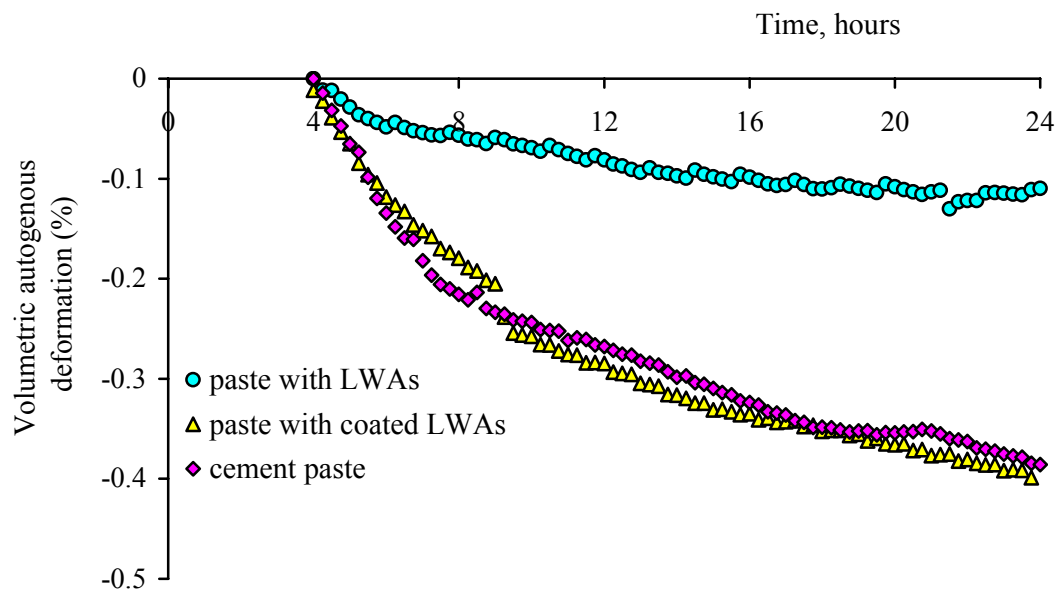


Figure 5.3: Volumetric autogenous deformation versus time diagram for plain cement paste, cement paste with expanded clays samples and paste containing paraffin coated expanded clays sample.

It can be easily seen from Figure 5.3 that the LWAs reduce the autogenous deformation by releasing the water to media. Because the LWAs used in these tests have modulus of

elasticity of approximately 5000 MPa (Müller-Rochholz J., 1979; Tasdemir, 1982) and their stiffness are low compared to those of normal weight aggregates, they cannot restrain the cement paste.

5.3 Heat of Hydration

The heat of hydration tests were conducted on series of PL2-4 and PL4-8. The details of the test procedure are given in Section 3.4.4. The results of heat of hydration tests for cement paste and cement paste with LWAs are compared in Figure 5.4. With addition of LWAs the heat of hydration increased with time compared to the reference paste samples. This is probably due to the fact that the amount of hydrated cement particles increased owing to internal curing which increased the heat of solution of cement paste. It was interesting to find that the heat of solution of paste with coarse LWAs was higher than that of paste with fine LWAs. However, this effect was diminished at later ages.

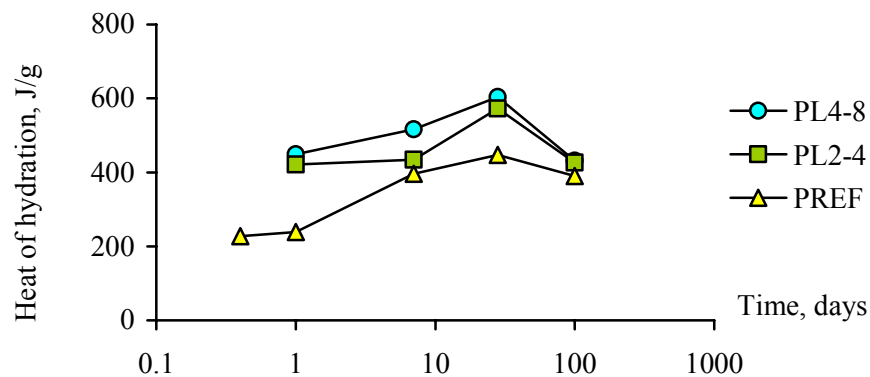


Figure 5.4: Effect of size of LWAs on heat of hydration of composites.

5.4 Non-evaporable Water Content and Degree of Hydration

The test results for the non evaporable water content (water/cement+silica fume by weight) are given in Table 5.2. The details of experiments can be found in Section 3.4.5. The non-evaporable water contents of series of PL2-4 and PL4-8 were found greater than that of reference paste sample.

Table 5.2: The variations of non evaporable water content (water / cement + silica fume by weight) of samples with time.

Non-evaporable water content (water/cement +silica fume by weight)				
	1 day	7 days	28 days	100 days
PREF	0.068	0.104	0.097	0.126
PL2-4	0.063	0.137	0.135	0.148
PL4-8	0.064	0.115	0.126	0.146

The effect of size of LWAs on cement paste can be clearly observed on the series of PL2-4 and PL4-8 as shown in Figure 5.5. Addition of LWAs to paste phases increased the degree of hydration, especially at early ages. The use of fine LWAs causes the water reservoirs to distribute in proximity and results in better internal curing. Therefore, the degree of hydration of cement paste with finer LWAs becomes greater than that with coarser LWAs.

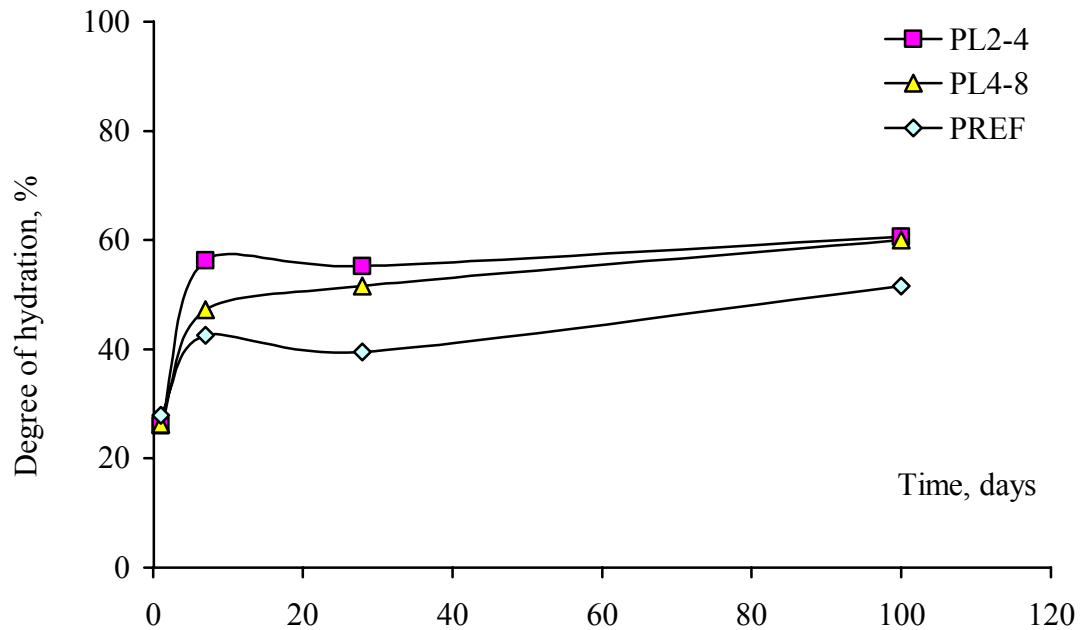


Figure 5.5: Effect of size of LWAs on degree of hydration of paste.

5.5 Mechanical Test Results

Table 5.3 summarizes the mechanical test results of produced series of cement paste and cement paste with aggregates.

Table 5.3: Fracture and strength properties of hardened cement paste series with cement paste and aggregates at the age of 28 days.

	PREF	PN0-2	PN2-4	PN4-8	PL2-4	PL4-8
Compressive strength, MPa	68.5	68.4	72.2	74.0	30.2	30.7
Modulus of elasticity, GPa	18	28	28	29	17	19
Area under the curve (W_0), Nmm	128	371	274	314	78	66
Fracture energy, N/m	27	70	49	57	16	13
Final disp. at midspan, mm	0.137	0.56	0.38	0.48	0.27	0.22
P_{max} , kN	1.6	3.1	3.2	3.0	1.0	1.0
Net bending strength, MPa	2.7	5.2	5.0	4.6	1.6	1.6
Splitting tensile strength, MPa	2.9	4.1	3.7	4.0	1.9	1.9
Characteristic length, l_{ch} , mm	55	115	102	104	77	73

5.5.1 Compressive Strength and Modulus of Elasticity

While the compressive strength of composites slightly increase with the increasing size of normal aggregate, the size of LWAs has no significant effect on compressive strength. As expected, the compressive strength decreased with the addition of LWAs, because the LWA behaves as a defect in matrix phase, as discussed in Section 4.8.1. In addition, as seen in Table 5.3 no substantial change was observed in the modulus of elasticity of composites with addition of LWAs. On the other hand, the modulus of elasticity increased with addition of normal weight aggregates. Also, the modulus of elasticity was not affected significantly by the size of aggregates (both NWA and LWA).

5.5.2 Bending and Splitting Tensile Strengths

The bending and splitting tensile strengths increased with addition of normal weight aggregate, while decreased significantly with addition of LWAs. The effect of size on the bending and splitting tensile strengths of composites has been found insignificant for both normal weight and lightweight aggregates.

5.5.3 Fracture Energy

The typical load-displacements at midspan curves for different series are shown in Figure 5.6. The results show that the addition of aggregate in cement paste phase

increased the area under the load-displacement curve. It has been found that the addition normal aggregate at the size fraction of 0-2 mm and the volume ratio of 30% increased the area under the curve about 3 times with respect to the PREF sample. On the other hand, the addition of same volume of LWAs at size fractions of 2-4 and 4-8 reduced the fracture energy. It can be seen in Table 5.3 that fracture energy of the cement paste with fine LWAs is greater than that of the cement with coarser LWAs.

The main reason why the fracture energy of composite is substantially greater than the plain cement paste is that the microcracks at the fracture process zone decrease the stress concentration. As a result, cracks are forced to incline into the aggregate, or near the aggregate, and to excess the aggregate obstacle, and hence the amount of consumed energy increases.

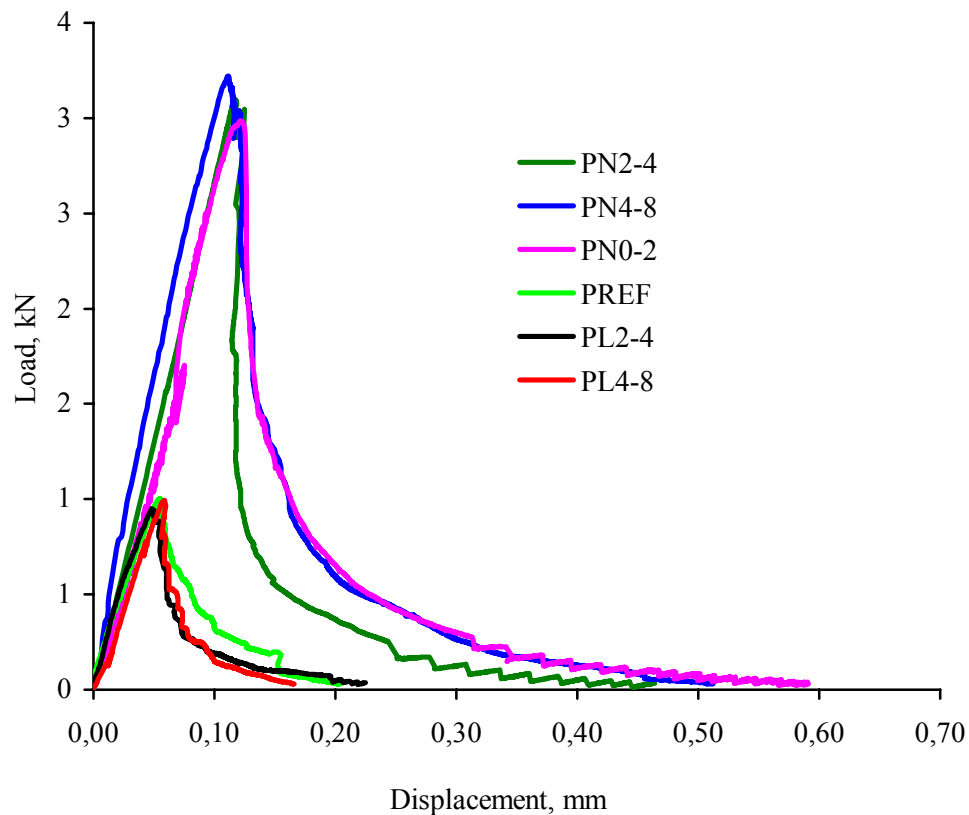


Figure 5.6: Typical load displacement curves for reference cement paste and composites of paste and aggregates.

5.5.4 Characteristic Length

It has been shown that the increase in total aggregate content of composite increased the characteristic length in comparison to the plain cement paste. The size of aggregate has also some effects on the brittleness of cementitious materials. Addition of fine sand aggregate at the size fraction of 0-2 mm increased the characteristic length significantly compared to the reference paste sample. The characteristic lengths of composites with 2-4 and 4-8 mm aggregate were found slightly smaller than that of with 0-2 mm fine sand. This slight difference is probably due to the interfacial transition zone between cement paste and normal aggregate. Since the stiffness of the crushed limestone is greater than that of cement paste, the crack is forced to travel around the aggregate near the transition zone which is the weakest zone of the aggregate. Thus, the energy consumed for fracture is likely to be lower. It has been also shown that the addition of aggregate to the reference paste at size fractions of 2-4 and 4-8 mm gave similar values of brittleness, while the fracture energy of paste with 4-8 mm aggregate was found greater than that with 2-4 mm.

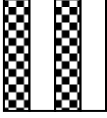
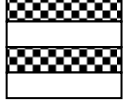
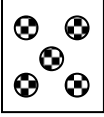

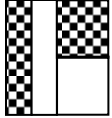
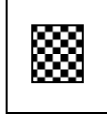
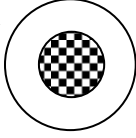
On the other hand, the addition of LWAs also increased the characteristic length of cement paste. The fracture energies of cement paste with LWAs were found smaller than that of reference cement paste. Although the stiffness of cement paste is significantly greater than that of LWA, the characteristic length of composites with LWAs was found remarkably greater than that of reference cement paste. Cement near the LWAs will be well-hydrated by internal curing. This enhanced transition zone increases the ductility of material with producing more microcracks. The composites with fine LWAs behave more ductile comparing to those with coarse LWAs. It can be concluded that the amount of micro cracks is governed by the low particle size of aggregate substituted, and a longer tail is an indication of many longer micro cracks.

5.6 Modeling of Modulus of Elasticity

A number of methods were proposed for modeling of elasticity of cementitious materials. These include: Parallel and Series phase model (Hansen 1960), Maxwell model (Holiday, 1966), Hirsch-Dougill model (Hirsch 1962; Holiday 1966), Popovics

model (Popovics and Erdey, 1970), Counto model (Counto, 1964), Hashin-Hansen model (Hansen, 1965), Bache and Nepper-Christansen model (Bache and Nepper-Christansen 1965), and Meso-mechanical modeling (Nielsen, 1990). These models and calculations are summarized in Table 5.4, where E_m and E_p are the modulus of elasticity of matrix and aggregate phases, respectively (Tanacan and Ersoy, 2000).

Table 5.4: Summary of models proposed to calculate modulus of elasticity of cementitious materials.

<p>Parallel phase model</p>  <p>(Hansen 1960)</p> $E_c = E_m V_m + E_p V_p$ $E_p \langle E_m$	<p>Series phase model</p>  $\frac{1}{E_c} = \frac{V_m}{E_m} + \frac{V_p}{E_p} \quad (\text{Hansen 1960})$ $E_p \rangle E_m$
<p>Dispersed Phase (Maxwell) model (Holiday, 1966)</p>  $E_c = E_m \left[\frac{1 + 2V_p (\alpha - 1) / (\alpha + 2)}{1 - V_p (\alpha - 1) / (\alpha + 2)} \right]$ $\alpha = E_p / E_m$	<p>Hirsch-Dougill model (Hirsch 1962; Holiday 1966)</p>  $\frac{1}{E_c} = \frac{1}{2} \left[\frac{1}{E_{c,Parallel}} + \frac{1}{E_{c,Seies}} \right]$
<p>Popovics model (Popovics and Erdey, 1970)</p>  $\frac{1}{E_c} = \frac{1}{2} [E_{c,Parallel} + E_{c,Seies}]$	<p>Counto model (Counto, 1964)</p>  $\frac{1}{E_c} = \frac{1 - \sqrt{V_p}}{E_m} + \left[\frac{1 - \sqrt{V_p}}{\sqrt{V_p}} E_m + E_p \right]^{-1}$
<p>Hashin-Hansen model</p>  <p>(Hansen, 1965)</p> $\frac{1}{E_c} = E_m \left[\frac{(E_m + E_p) + (E_p - E_m)V_p}{(E_m + E_p) - (E_p - E_m)V_p} \right]$	<p>Bache and Nepper-Christansen model</p> $E_c = E_m^{V_m} E_p^{V_p}$ <p>(Bache and Nepper-Christansen 1965)</p>

The experimental results and calculated values from each modelings are also given in Table 5.5. In these calculations moduli of elasticity of normal weight and lightweight aggregate have been taken as 74000 and 5000 MPa, respectively. It seems that the moduli of elasticity of composites with normal aggregates have been better predicted comparing to composites with LWAs by all models except Parallel and Series models.

The best correlated results have been obtained from the calculation by Hirsch-Dougill and Popovics model. On the other hand, Lydon and Balendran (1986) showed that Bache and Nepper-Christansen model can be reliably used to predict the modulus of elasticity of NWC and LWC. The reason why the predicted values have been found smaller than the experimental ones is that the effect of interfacial transition zone between the LWAs and cement paste has not been taken into account in calculations. Thus, meso-mechanical modeling will be applied to predict the modulus of elasticity of composites.

Table 5.5: Comparison of experimental and calculated value of modulus of elasticity of composites

Theoretical	cement paste with NWAs (GPa)			cement paste with LWAs (GPa)	
Parallel phase model	34.8			14.1	
Series phase mode	23.3			10.1	
Dispersed Phase (Maxwell) model	27.7			13.3	
Hirsch-Dougill model	27.9			11.8	
Popovics model	29.1			12.1	
Counto model	27.5			13.3	
Hashin-Hansen model	26.1			12.8	
Bache and Nepper-Christansen model	27.5			12.3	
Experimental	PN0-2	PN2-4	PN4-8	PL2-4	PL4-8
Modulus of elasticity, GPa	28	28	29	17	19

5.6.1 Meso-mechanical Modeling of the Modulus of Elasticity

Recent studies showed that the modulus of elasticity values for composites with normal aggregate can be successfully predicted by meso-mechanical modeling (Akçay et al, submitted; Mese et al, 2005; Aldikacti et al., 2005; Bayramov, 2004). In this study meso mechanical modeling was applied to the cement paste with silica fume and composites with both normal and LWAs.

5.6.1.1 Cement paste

Calculation of the modulus of elasticity was done according to the meso-mechanical relations using the model proposed by Nielsen (1990 and 1993) for plain concrete. In this model, a cement based material is considered as a two-phase system and the modulus of elasticity of the material is calculated using Eq. (5.1).

$$E = E_m \frac{n + \Theta + V\Theta(n-1)}{n + \Theta - V(n-1)} \quad (5.1)$$

where V is the volume fraction of the discrete phase, Θ is a geometric function used for the definition of discrete phase and n is the ratio of modulus of elasticity of the discrete phase to modulus of elasticity of the continuous phase E_m . If w/c ratio is greater than the value of $1.2\rho_w/\rho_c$ (ρ_w and ρ_c are the densities of water and cement, respectively), it is accepted that the cement paste consists of capillary pores embedded in the cement gel and n is equal to zero. In this case, V and Θ are calculated using the following equations

$$V = \frac{w/c - 1.2\rho_w/\rho_c}{w/c + \rho_w/\rho_c} \quad (5.2)$$

$$\Theta = \eta_k(1 - V) \quad (5.3)$$

where η_k is the shape factor of capillary pore. For $w/c < 1.2\rho_w/\rho_c$, cement paste is considered to be made up of unhydrated cement particles which are embedded in cement gel. In that case, V , Θ and n are given as

$$V = \frac{1 - 0.83(w/c)(\rho_c/\rho_w)}{1 + (w/c)(\rho_c/\rho_w)} \quad (5.4)$$

$$\Theta = 0.5 \cdot \left[\eta_u \sqrt{1 - V} (1 - n) + \sqrt{\eta_u^2 (1 - V)(1 - n)^2 + 4n} \right] \quad (5.5)$$

$$n = \frac{E_u}{E_m} \quad (5.6)$$

where η_u is the shape factor of an unhydrated cement particle. E_u and E_m are the moduli of elasticity of unhydrated cement particle and hydrated cement gel, respectively (Nielsen, 1993). E_m can be determined by the equation related to the degree of hydration,

α (Eq. 5.7). Modulus of elasticity of cement paste can be found using Eq. (5.8) by taking E equal to E_p .

$$E_m = 27200 \times \alpha \quad (5.7)$$

$$E_p = E_m \frac{n + \Theta + V\Theta(n-1)}{n + \Theta - V(n-1)} \quad (5.8)$$

5.6.1.2 Mortar

For determining the modulus of elasticity of mortar (E_r), the calculated modulus of elasticity of cement paste was used as the modulus of elasticity of continuous phase ($E_m = E_p$). In the calculations, the volume fraction of fine aggregate V_s was used instead of V . Thus, Eq. (5.8) was rearranged for mortar and was expressed in terms of a new n defined as the ratio of modulus of elasticity of fine aggregate (E_f) to that of cement paste as

$$n = \frac{E_f}{E_p} \quad (5.9)$$

$$E_r = E_p \frac{n + \Theta + V_s\Theta(n-1)}{n + \Theta - V_s(n-1)} \quad (5.10)$$

The geometry function of the discrete phase in mortar can be calculated as

$$\Theta = \frac{1}{2} \left[q + \sqrt{q^2 + 4n} \right] \quad (5.11)$$

$$q = \eta_f(1 - V_s) + n\eta_f(V_s - 1) \quad (5.12)$$

$$\eta_f = \frac{3A_f(1+A_f)}{1+A_f+4A_f^2} \quad (5.13)$$

where η_f and A_f are the shape factor and the aspect ratio of fine aggregate, respectively. The modulus of elasticity of aggregate can be determined according to the particle density of aggregate ρ_{agg} using the Müller-Rochholz (1979) formula (Eq. 5.14).

$$E_{agg} = 8.1\rho_{agg}^2 \quad (5.14)$$

5.6.1.3 Concrete

For concrete, modulus of elasticity of mortar, calculated by the above equation, was used as the modulus of elasticity of the continuous phase ($E_m=E_p$) and the volume fraction of coarse aggregate was taken instead of the volume fraction of the discrete phase ($V=V_c$) as shown in Eq. (5.15).

$$E = E_r \frac{n + \Theta + V_c \Theta(n-1)}{n + \Theta - V_c(n-1)} \quad (5.15)$$

The n value for concrete can be calculated as

$$n = \frac{E_c}{E_r} \left(1 - \beta^{\frac{7.5}{5 + \frac{E_c}{E_r}}} \right) \quad (5.16)$$

where E_c and E_r are the moduli of elasticity of coarse aggregate and mortar, respectively. β is the ratio of the surface area of the debonded coarse aggregate to its total surface area. Other parameters used for determining the modulus of elasticity of concrete are expressed in the equations below.

$$\Theta = \frac{1}{2} \left[q + \sqrt{q^2 + 4n} \right] \quad (5.17)$$

$$q = \eta_c (1 - V_c) + n \eta_c (V_c - 1) \quad (5.18)$$

$$\eta_c = \frac{3A_c(1 + A_c)}{1 + A_c + 4A_c^2} \quad (5.19)$$

where η_c and A_c are the shape factor and the aspect ratio of coarse aggregate, respectively. Following material parameters were chosen for the calculations: $\alpha=0.75$; $\eta_k=0.7$; $\eta_u=1.0$; $E_u=75000$ MPa; $A_f=A_c=1.0$ and $\beta=0.2$ (Lange-Kornbak. and Karihaloo, 1996).

The results obtained from both meso mechanical modeling and experiments are given in Table 5.6. Although the meso-mechanical modeling have been applied by not considering the size of aggregate, the results demonstrate that the modulus of elasticity values for composites with both NWA and LWAs can be successfully predicted by meso-mechanical modeling.

Table 5.6: The moduli of elasticity obtained from experiments and from meso-mechanical modeling

	PREF	PN0-2	PN2-4	PN4-8	PL2-4	PL4-8
Experimental, GPa	18	28	28	29	17	19
Meso-mechanical modeling, GPa	18.6	27.2			15.2	

5.7 Conclusions

1. It has been shown that the size of normal aggregates has no significant effect on autogenous deformation at 28 days, while the autogenous deformation of cement paste with 0-2 mm size fraction of normal aggregate has been found higher than that with 2-4 mm and 4-8 mm at the age of 360 days. In early ages, the finer NWAs (0-2 mm) restrained the autogenous deformation of cement paste, because the modulus of elasticity of cement paste was not too high. On the other hand,

addition of coarser size aggregate easily restrained the shrinkage of cement paste at the later ages. As opposite to the linear autogenous deformation test result, the volumetric autogenous deformation of PN0-2 sample was found to be lower comparing to those of PN2-4 and PN4-8 samples, while the values for PN2-4 and PN4-8 series were found similar to one another.

2. The fine size of LWAs, as expected, has been found to be more effective in mitigating the both linear and volumetric autogenous deformation of cement paste than coarse LWAs.
3. The autogenous deformation of the cement paste with paraffin coated LWAs has been found to be similar to that of the plain cement paste, indicating that the LWAs reduce the autogenous deformation by releasing the water to the media.
4. The addition of LWAs to paste phases increased the degree of hydration, especially at early ages. The use of fine LWAs causes the water reservoirs to be distributed in proximity and results in better internal curing, hence the degree of hydration of cement paste with finer LWAs is greater compared to that with coarser LWAs.
5. While the compressive strength of composites slightly increase with the increasing size of normal aggregate, the size of LWAs has no significant effect on compressive strength. Also, the modulus of elasticity was not affected significantly by the size of aggregates (both NWA and LWA).
6. The effect of size on the bending and splitting tensile strengths of composites has been found insignificant for both normal weight and lightweight aggregates.
7. It has been found that the addition of normal aggregate at the size fraction of 0-2 mm and the volume ratio of 30% increased the area under the curve about 3 times with respect to the PREF sample. On the other hand, the addition of same volume of LWAs at size fractions of 2-4 and 4-8 reduced the fracture energy.
8. Addition of fine sand aggregate at the size fraction of 0-2 mm increased the characteristic length significantly compared to the reference paste sample. The characteristic lengths of composites with 2-4 and 4-8 mm aggregate were found

slightly lower than that of with 0-2 mm fine sand. This slight difference is probably due to the interfacial transition zone between cement paste and normal aggregate.

9. The addition of LWAs increased the characteristic length of cement paste. The fracture energies of cement paste with LWAs were found smaller than that of reference cement paste.
10. It has been shown that the moduli of elasticity of composites with normal aggregates can be well predicted comparing to that of composites with LWAs by Hirsch-Dougill model (Hirsch 1962; Holiday 1966) and Popovics model (Popovics and Erdey, 1970). The results demonstrate that the modulus of elasticity values for composites with both NWA and LWAs can be successfully predicted by meso-mechanical modeling.

6 MECHANISM AND MODELING OF AUTOGENOUS DEFORMATION

6.1 General

In this chapter the most commonly used recent models of autogenous deformation are introduced. Some of these models are based on the mechanisms of autogenous deformation, while others are related to the cement compositions. Although the phenomenon of autogenous deformation has not been fully comprehended because of its complexity, it is known that the mechanism of autogenous deformation is the same as that of drying shrinkage. In literature, the autogenous deformation has been explained with the combination of three different mechanisms as (Hua et al., 1995)

1. variation of capillary depression
2. variation of surface tension of colloidal particles
3. variation of disjoining pressure

These mechanisms are considered to be the main driving forces of self-desiccation and are used by a number of authors (Jensen and Hansen, 2001; Pignat et al., 2002; Lura, 2003; Bentz and Jensen, 2004). Hua et al. (1995) modeled the autogenous deformation as self-desiccation shrinkage, and showed that capillary stresses in the pore water, which are affected largely by critical pore diameter, are the dominant physicochemical phenomenon of autogenous deformation. In addition, the mechanism of autogenous deformation can be considered in two different RH levels as high and low. At high RH level the autogenous deformation is governed by the capillary depression and disjoining pressure, whereas at low RH level ($< 45\%$), the surface tension of the C-S-H particles becomes the principal driving mechanism (Beltzung and Wittmann, 2002).

6.2 Mechanism of Shrinkage by Drying and Self-desiccation

Water saturated condition is always taken as a reference for porous materials in contact with water (Hanehara et al., 1999). The term ‘drying’ has the meaning of increasing the volume of gas in pores which are initially filled by water. It was accepted that this volume of gas has a similar mechanical effect on both drying and self-desiccation (Hua et al., 1995).

6.2.1 Mechanisms of Variation of Capillary Depression

The capillary tension occurs due to water-air menisci in the partially empty pores. The surface energy is given as (Alberty and Daniels, 1980):

$$\gamma = \frac{hg \rho_l r_{cap}}{2 \cos \theta} \quad (6.1)$$

where, h is the height of fluid pipe, g is the gravitational acceleration, ρ_l is the density of fluid, r_{cap} is the radius of capillarity, and θ is the contact angle.

In order to determine the effect of concavity on surface gas pressure, the relationship between the differential change of interface area and differential change of Gibbs free energy of system should be stated. The following equation is derived with the combination of the first and the second rules of thermodynamics (Alberty and Daniels, 1980):

$$dU = TdS_e - PdV + \gamma dA + \mu_c dn \quad (6.2)$$

where, U is internal energy, T is the temperature, P is the pressure, V is the volume, A is the surface area, S_e is the enthalpy, μ_c is the chemical potential and dn is the change in the mole number. The Gibbs free energy of system is found as follows (Alberty and Daniels, 1980):

$$G = U + PV - TS_e \quad (6.3)$$

$$dG = dU + PdV + VdP - TdS_e - S_e dT = -S_e dT + VdP + \gamma dA + \mu_c dn \quad (6.4)$$

If these equations are applied to the spherical drop, the equation shown below is obtained (Alberty and Daniels, 1980)

$$dG = -S_e dT + VdP + \left(\frac{2V_m \gamma}{r} + \mu_{planar} \right) dn \quad (6.5)$$

Here, V_m is the molar volume of fluid and μ_{planar} is the chemical potential in planar surface. From this equation the chemical potential of fluid in drop is derived as (Alberty and Daniels, 1980)

$$\mu = \frac{2V_m \gamma}{r} + \mu_{planar} \quad (6.6)$$

If the gas behaves like an ideal gas Eq(6.7) is achieved

$$\mu_c = \mu_{planar} + RT \ln \frac{P}{P^o} \quad (6.7)$$

where, P^o is the gas pressure of planar surface (atmospheric pressure) and R is the ideal gas constant. From combination of two equations, the well known Kelvin's equation is found (Alberty and Daniels, 1980)

$$\ln \left(\frac{P}{P^o} \right) = \frac{2V_m \gamma}{r RT} \quad (6.8)$$

This equation gives the gas pressure, P , in terms of radius of droplet, r . It is obvious that the droplet with the smaller radius has much higher gas pressure.

6.2.2 Mechanisms of Variation of Surface Tension of Colloidal Particles

Surface tension is a consequence of the asymmetry of attractive forces on atoms or molecules around the surfaces. Relaxation of the surface tension results from adsorption of water on solid surfaces during autogenous deformation. On the other hand, desorption of water prompts an increase in the surface tension, resulting in shrinkage. Some possible equations based on volume change and surface tension are summarized by Lura (2003). The surface tension mechanism has a slight influence on total shrinkage. According to Powers and Brownnyard (1948) almost all the adsorbed water is removed when hardened paste is dried to equilibrium with a very low vapor pressure. Hence, the possible change in volume may be computed from the thickness of the adsorbed layer and the particle-size of the solid phase. The thickness of the adsorbed layer may be conservatively estimated at one water-molecule diameter, or about 2.7 Å. From the relation of $\Delta V/V = 3\Delta r/r_c$, it was found that change in particle spacing corresponding to the addition or loss of one molecular layer per particle would, under the assumptions given, result in an over-all volume change of 16%.

Thus, it appears that the loss or gain of the first adsorbed layer can account for the observed amount of volume change (Powers and Brownnyard 1948). Lura et al. (2003), on the other hand, proposed that the changes in the surface tension of the solids due to adsorption of water molecules are of significance for the first three adsorbed layers only. Jensen (1995), however, suggests that this mechanism may not play a major role in autogenous deformation, unless the RH drops under 75%. It seems that the effect of alkalis on autogenous deformation must be considered with the surface tension mechanism because all of the above approximations are based on the assumption that the liquid is pure water. However, it should be noted that the pores in hardened cement paste are filled by water with dissolved salts (Powers and Brownnyard, 1948).

6.2.3 Mechanisms of Variation of Disjoining Pressure

This mechanism occurs where the adsorbed water exists in the interaction between two solid surfaces very close to one another. At a given temperature, the thickness of layer adsorbed water depends on the relative humidity (Hua et al., 1995), particularly at high level of RH (Lura, 2003), and the alkali concentration of water. This pressure occurs due

to van der Waals forces, double layer repulsion, and the structural forces. The pressure reaches its maximum in the saturated state, and when the system goes into an unsaturated state, shrinkage takes place because the disjoining pressure decreases and two surfaces move close together. Hua et al. (1995) mentioned that the disjoining pressure is practically constant when the RH varies from 80% to 100%. They suggested that both surface tension of colloidal particles and disjoining pressure can be neglected when considering the autogenous deformation of cement paste.

6.3 Modeling of Autogenous Deformation Based on its Mechanism

For modeling the shrinkage by drying and by self-desiccation, a real material is considered to be homogenous and isotropic and to contain randomly dispersed isolated spherical pores (Figure 6.1). When the big volumes are considered, elastic properties of materials will be independent of shapes of pores (MacKenzie, 1950). This method is based on the principle that any macroscopic volume (i.e. contain lots of big pores) can be substituted by equivalent homogenous material whose elastic properties are changed. Hence, displacements and average stresses at the boundary are equal to that of boundary of equivalent elastic area.

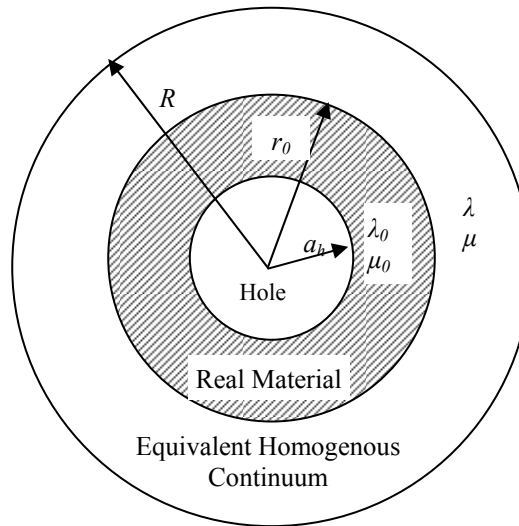


Figure 6.1: The model used for calculation (MacKenzie, 1950)

It can be seen from Figure 6.1 that every pore of radius a_h will be surrounded by a spherical shell of real material out to at least some radius r_0 , and this in turn is surrounded by a spherical shell of equivalent homogeneous material out to some large radius R . If $f(a_h)da_h$ is the proportion of pores, with radii rising in the range $(a_h, a_h + da_h)$ then the volume of pores per unit volume of the real material is given below:

$$\frac{1-\rho}{\rho} = \frac{4}{3} \pi n_p \int f(a_h) a_h^3 da_h = \frac{1}{\rho r_0^3} \int f(a_h) a_h^3 da_h \quad (6.9)$$

where, ρ and n_p are the relative density and number of pores per unit volume, respectively.

In addition, there will usually be terms of higher order which arise because the boundary and substituting conditions are neglected. The problem is considered in two parts: **(a)** the compressibility of a material containing small spherical pores of different sizes, and **(b)** the dilatation due to a distribution of pressures inside the pore boundaries (these pressures may be due to included gas or to surface tension in the boundary of the pores). To gain the compressibility, hydrostatic pressure \mathbf{P} is applied and then total dilation of homogenous elastic material will be $P(1/k-1/k_0)$ and the additional term is zero if the material is incompressible.

6.3.1 General Elastic Equations

The displacements of the model given when the (P) hydrostatic pressure applied and utilized on thick spherical shell, the radial displacement in the outer shell of equivalent homogeneous material is (Love, 1944).

$$u = \frac{r}{3k} \frac{p_0 r_0^3 - PR^3}{R^3 - r_0^3} + \frac{R^3 r_0^3}{4\mu_0 r^2} \frac{p_o - P}{R^3 - r_o^3} \quad (6.10)$$

$$k = \lambda + 2/3 \mu$$

The radial displacement in the inner shell of real material is

$$u = \frac{r}{3k_o} \frac{p_p a^3 - p_0 r_0^3}{r_0^3 - a^3} + \frac{a^3 r_0^3}{4\mu_0 r^2} \frac{p_p - p_0}{r_0^3 - a^3} \quad (6.11)$$

In above equations, λ and μ are Lamé's constants. In these equations, p_p is the pressure in the pores and P is the externally applied hydrostatic pressure. The values given with subscript 0 indices belong to either the real material or central boundary material. Thus, the others without subscript indices belong to equivalent homogenous material. The pressure at the intermediate boundary p_0 is calculated with neglecting the higher order terms; the equation given the radial displacement of the u/R volume is gained (Love, 1944).

$$\frac{U}{R} = -\frac{P}{3k} + (p_0 - P) \left[\frac{1}{3k} + \frac{1}{4\mu} \right] \frac{r_0^3}{R^3 - r_0^3} \quad (6.12)$$

6.3.2 Pressure applied internally

If there exist different pressures for the pores with same diameters, calculations can be made using the same average pressure, p . In this condition, when the p pressure is applied to the given model, by using the above equation, displacement at the outer boundary can be found as (MacKenzie, 1950)

$$u = R \left[\frac{1}{3k} + \frac{1}{4\mu} \right] \int p_0 f(a) da = \bar{p} R \left[\frac{1}{3k} - \frac{1}{3k_o} \right], \quad p_0(a) \quad (6.13)$$

The formulas given by MacKenzie (1950) provide the dimensional changes of fully saturated porous body. The equation gives the exact solution of solid since it behaves linear elastic. If there is negative pressure (hydrostatic stress), the displacements will be negative too, and the shrinkage will take place. Bentz et al. (1998) showed that the average capillary stress in the pores, σ_{cap} , can be used instead of \bar{p} when the porous solid part is partially saturated. They also inserted the saturation factor S in the equation. Consequently, deformation of partially saturated porous material becomes as

$$\frac{u}{R} = \varepsilon_{lin} = \frac{S\sigma_{cap}}{3} \left(\frac{1}{K} - \frac{1}{K_s} \right) \quad (6.14)$$

The saturation fraction, which is the ratio of evaporable water content, V_{ew} to the total pore volume, V_p , can be determined according to the hydration degree, α , using the following equation. (Powers and Brownyard,, 1948)

$$S = \frac{V_{ew}(\alpha)}{V_p(\alpha)}, \quad \alpha(t) \quad (6.15)$$

Powers' model can be used to determine the saturation fraction of Portland cement as

$$S = \frac{V_{ew}(\alpha)}{V_p(\alpha)} = \frac{V_{cw}(\alpha) + V_{gw}(\alpha)}{V_{cws}(\alpha) + V_{gw}(\alpha) + V_{cs}(\alpha)} = \frac{p - 0.7(1-p)\alpha}{p - 0.5(1-p)\alpha} \quad (6.16)$$

$$p = \frac{w/c}{(w/c) + (\rho_w / \rho_c)} \quad (6.17)$$

where, $V_{cw}(\alpha)$, $V_{gw}(\alpha)$ and $V_{cs}(\alpha)$ are capillary water, gel water and chemical shrinkage, respectively. Initial porosity, p , is given according to the water to cement ratio. There is a modification of Powers' volumetric model for using silica fume. In this case the equation will appear as (Jensen and Hansen, 1996)

$$S = \frac{V_{cw}(\alpha)}{V_p(\alpha)} = \frac{p - 0.8k(1-p)\alpha}{p - k(0.6 - 0.7(sf/c))(1-p)\alpha} \quad (6.18)$$

$$p = \frac{w/c}{(w/c) + (\rho_w / \rho_c) + (w\rho_s / \rho_{sf})(sf/c)} \quad (6.19)$$

$$k = \frac{1}{1 + 1.4(sf/c)} \quad (6.20)$$

where, sf/c is the ratio of silica fume to cement by weight.

6.4 Estimation of Stress and Deformation due to Self-desiccation Shrinkage

In order to calculate the capillary stress in the pore of cement paste, Kelvin's radius needs to be determined. The experiments on Vycor glass which has a similar behavior with cement paste showed that the above equation gives the exact solutions (Bentz et al., 1998). In addition, in a certain temperature, the ratio of partial pressure of vapor to that of saturated condition is defined as a relative humidity (RH). This means that the RH value can be taken as dimensionless P/P_0 fraction. Assuming the perfect wetting ($\cos\theta=1$), the RH_K due to the menisci formation can be calculated using the Kelvin's equation (Alberty and Daniels, 1980)

$$r = -\frac{2\gamma V_m}{\ln(RH_K)RT} \quad (6.21)$$

It was found that the initial value of internal RH of the cement paste is about 98% (Lura, 2003). Jensen (1993) claimed that this initial drop in RH value occurs due to the dissolved salts in pore fluid and can be estimated using Raoult's law.

$$RH_s = X_1 \quad (6.22)$$

Where, X_1 is the molar fraction of water in the pore fluid. When both menisci formation and the effect of dissolved salts are taken into account, the total RH can be determined using the following equation (Jensen, 1993).

$$RH = RH_s \cdot RH_K = X_1 \exp\left(-\frac{2\gamma V_m}{rRT}\right) \quad (6.23)$$

In order for the radius of the largest capillary pore filled with water to be calculated directly from the RH measurements, the influence of the dissolved salts also has to be taken into account. In this case the equation will be as

$$r = -\frac{2\gamma V_m}{\ln\left(\frac{RH}{RH_s}\right)RT} \quad (6.24)$$

The effect of dissolved salts on Kelvin's radius can be taken as constant value of 2% (Lura, 2003). It is well known that after determining the Kelvin radius, capillary stress can be calculated using the Laplace's equation as

$$\sigma_{cap} = -\frac{2\gamma}{r} \quad (6.25)$$

Using the founded capillary stress, deformation of self-desiccation can be calculated by Eq(6.14). For cement paste, bulk modulus of the solid material can be taken as $K_s = 44$ GPa (Lura, 2003). Figure 6.2 shows that the calculated values agree very well with the experimental result for RH values between 100 and 95%. Lura (2003) stated that, after this point, the measured values increase, while the calculated ones remain almost constant, which is due both to flattening out of the bulk stress in cement paste and to the increase of the modulus of elasticity and also pozzolanic effect of silica fume. It was concluded that calculation of self-desiccation shrinkage based on the capillary tension approach could explain only part of the measured shrinkage. It must be kept in mind that the modeling is based on the assumption that the cement paste behaves in an elastic manner. It has been mentioned that the proposed model together with the results from experimental studies can be used to investigate the change in the geometry of capillary pores and consequently contribute to the understanding of the development of the pore structure of cement paste (Lura, 2003).

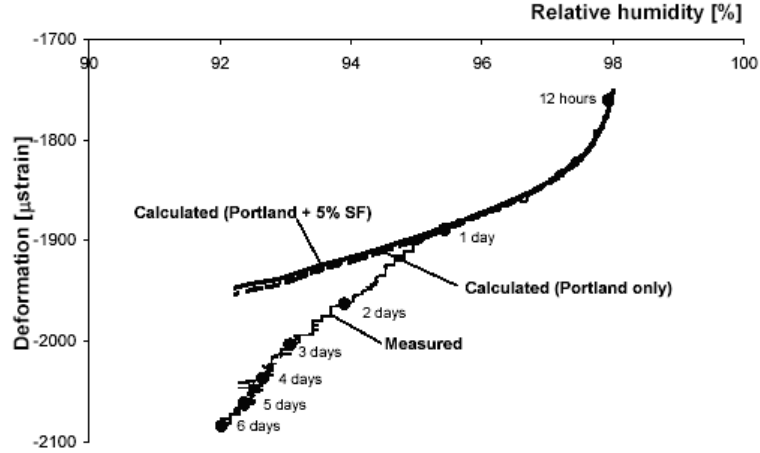


Figure 6.2: Measured and calculated autogenous deformation of Portland cement paste (w/c=0.37+5%sf) vs. internal relative humidity (Lura, 2003).

6.5 Other Studies on Modeling of Autogenous Deformation

Recently proposed models mainly related to the self-desiccation shrinkage and cement composition will be presented in this section.

6.5.1 Modeling of Self-desiccation Shrinkage at Macroscopic Scale

Hua et al. (1995) used similar elastic approach to determine autogenous deformation which is defined as self-desiccation shrinkage only. In their model, the pores smaller than Kelvin's radius, r , are filled with water, while those larger than r remain empty. Function of capillary stress $p_c(t)$ is defined as a function of the time during hydration. For estimating the $p_c(t)$, the results of mercury intrusion porosimetry (MIP) can be used. Because of the self-desiccation that results from Le Chatelier contraction, an unsaturated porous material whose gas volume is equal to $\Delta V(t_0)$ is used. The liquid phase is under the depression of $p_c(\Delta V(t_0))$ as given below (Hua et al., 1995)

$$p_c(\Delta V(t_0)) = \frac{\gamma_w \cos \theta_w}{\gamma_{Hg} \cos \theta_{Hg}} p_{Hg}(\Delta V(t_0)) \quad (6.26)$$

where, t_0 is the time of mercury penetration and p_{Hg} is the pressure caused by mercury penetration while θ_w and θ_{Hg} are the wetting angles for water and mercury, respectively.

6.5.1.1 Macroscopic stresses

The macroscopic stress of solid part of partially saturated porous materials can be determined as follows (Hua et al., 1995)

$$\sum_{ij}^s(X_g) = \frac{1}{V(X_g)} \int_{V_l(X_g)} \sigma_{ij}(y_l) dV_s(X_g) \quad (6.27)$$

- $\sum_{ij}^s(X_g)$:macroscopic stress of skeleton
 $\sigma_{ij}(y_l)$:real stress at microscopic level
 $V(X_g)$:representative elementary volume
 $V_s(X_g)$:volume of the solid part in $V(X_g)$
 $V_l(X_g)$:volume of the liquid part in $V(X_g)$
 X_g and y_l :global and local variables (vectors)

6.5.1.2 Definition of Autogenous Deformation

As long as there exists water in the media, the viscoelastic behavior of cement paste is characterized by the creep function, $J_{ijkl}(t, t')$. If the paste is homogenous and isotropic, the function can be separated into two components: volumetric, $J^v(t, t')$ and deviatoric $J^d(t, t')$. When the material is subject to a constant stress since time t' , the one-dimensional creep function, $J(t, t')$, at the time of t is given below.

$$\begin{cases} J^v(t, t') = 3(1 - 2\nu)J(t, t') \\ J^d(t, t') = 2(1 + \nu)J(t, t') \end{cases} \quad (6.28)$$

where, ν is the Poisson ratio which is assumed to remain constant. The solid skeleton of the hardening cement paste is macroscopically subject to a spherical internal stress due to the capillary depression. By Boltzmann's principle of superposition, the linear autogenous shrinkage of the material, $\varepsilon_r(t)$, can be defined as

$$\varepsilon_r(t, t') = \int_{\tau}^{t'} (1 - 2\nu) J(t, t') d \sum^s t' \quad (6.29)$$

where, $\sum^s t'$ is the macroscopic compression of the solid skeleton. The empirical form of the equation is given as (Hua et al., 1995)

$$J(t, t') = \frac{1}{E(t')} + \varepsilon_{\infty}^o(t') \frac{(t - t')^{a(t)}}{(t - t')^{a(t')} + b(t')} \quad (6.30)$$

$$\varepsilon_{creep}(t, t') = \varepsilon_{\infty}(t') \frac{(t - t')^{a(t')}}{(t - t')^{a(t')} + b(t')} \quad (6.31)$$

Here, $\varepsilon_{creep}(t, t')$ is the creep part for a non-unit load. Functions $\varepsilon_{\infty}(t')$, $a(t')$ and $b(t')$ are determined by a minimization for a series of specimens at different ages t' as given below (Hua et al., 1995).

$$\min_{\varepsilon, a, b} \sum_{j=1}^n \left[\varepsilon_{\infty}(t') \frac{(t_j - t')^{a(t')}}{(t_j - t')^{a(t')} + b(t')} - \varepsilon_{creep}^{\exp}(t_j, t') \right]^2 \quad (6.32)$$

It was shown that the capillary effects play the major role as compared to other physico-chemical phenomena and calculated results are in a very good agreement with the experimental results as shown in Figure 6.3.

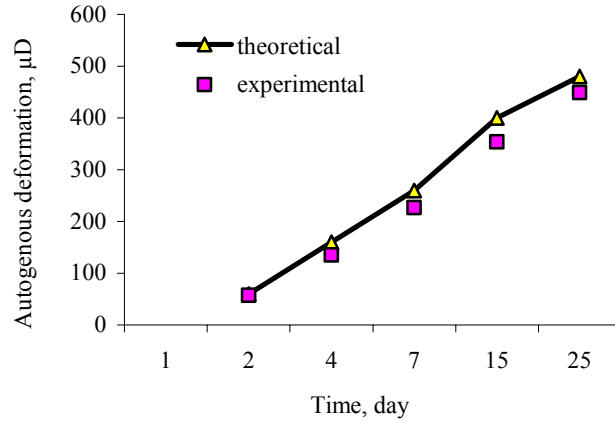


Figure 6.3: Comparison of theoretical and experimental results autogenous deformation of cement paste with $w/c=0.42$ (adopted from Hua et al., 1995). Note that in this modeling, autogenous deformation is considered as self-desiccation shrinkage.

6.5.2 A Model of Self-Desiccation in Concrete

Rodecea (1999) proposed a model for self-desiccation of concrete which is a function of the degree of hydration, cement content, and initial water content. In this model, mean radius of the equivalent pore as a function of degree of hydration and w/c -ratio can be given as

$$r = \frac{2(W_i - 0.1875\alpha C)}{k_1 \cdot \frac{0.26 \cdot 0.25\alpha C}{3.5 \cdot 10^{-10} \rho} \left(1 - \frac{W_i + 0.1875\alpha C}{\rho} \right)} \quad (6.33)$$

where, W_i is the initial water content, α is the degree of hydration, C is the cement content, ρ is the density of water, and k_1 is the coefficient. Using the mean radius of the equivalent pore, the RH reduction was found by the Laplace-Kelvin equation (6.24). The model is found to be in good agreement with the experimental results.

6.5.3 Modeling Autogenous Deformation Based on Type of Cement

It is well known that autogenous deformation of cement paste depends strongly upon mineral composition of cement paste. Miyazawa and Tazawa (2005) reported that autogenous shrinkage of cement paste with cements produced using Portland cement clinker can be estimated by the following equation (Miyazawa and Tazawa, 2005).

$$\begin{aligned} \varepsilon_p(t) = & A \cdot \alpha_{C_3S}(t) \cdot (C_3S\%) + B \cdot \alpha_{C_2S}(t) \cdot (C_2S\%) + C \cdot \alpha_{C_3A}(t) \cdot (C_3A\%) \\ & + D \cdot \alpha_{C_4AF}(t) \cdot (C_4AF\%) + E \cdot (Blaine) + F \end{aligned} \quad (6.34)$$

where, $\varepsilon_p(t)$ is the autogenous deformation of cement paste at age t , $\alpha(t)$ is the degree of hydration of compound i , ($i\%$) is the content of compound. Constants A , B , C , D , E and F were determined from regression analysis using experimental data. From these constants, it was conducted that autogenous deformation increases as the contents of C_3A and C_4AF increase.

For predicting the autogenous deformation from the time of initial setting, t_0 , the equation below can be used when the w/c ratio is between 0.2 and 0.6. The equation is also recommended by Standard Specification for Design and Construction of Concrete Structures by Japan Society for Civil Engineers (JSCE).

$$\begin{aligned} \varepsilon_c(t) &= k \cdot \varepsilon_{co}(w/c) \cdot \beta_a(t) \\ \text{for } 0.2 \leq w/c \leq 0.5 \quad \varepsilon_{co}(w/c) &= 3070 \exp(-7.2(w/c)) \\ \text{for } 0.5 < w/c \quad \varepsilon_{co}(w/c) &= 80 \end{aligned} \quad (6.35)$$

$$\beta_a(t) = \left[1 - \exp\left(-a/(t-t_0)^b\right) \right]$$

where, $\varepsilon_c(t)$ is the autogenous deformation of cement paste at age t (day), k is the coefficient of cement type ($k=1$ for OPC), $\varepsilon_{co}(w/c)$ is the ultimate autogenous deformation, $\beta_a(t)$ is the coefficient to describe the development of autogenous deformation with time, a and b are the constants related to w/c ratio. Miyazawa and Tazawa (2005) also obtained results of regression analysis of these constants as

$$a = 3.27 \exp\{-6.83 \times (w/c)\} \quad (6.36)$$

$$b = 0.251 \exp\{2.49 \times (w/c)\} \quad (6.37)$$

European Committee for standardization recommended a similar prediction model for autogenous deformation of concrete. In this recommendation, the ultimate autogenous deformation is obtained as a function of characteristic compressive strength at 28 days, f_{ck} .

$$\varepsilon_c(t) = \beta_{cc}(t) \cdot \varepsilon_{ca,\infty} \quad (6.38)$$

$$\beta_{cc}(t) = \exp\left[s \left\{1 - \left(\frac{28}{t}\right)^{0.5}\right\}\right] \quad (6.39)$$

$$\varepsilon_{ca,\infty} = -2.5(f_{ck} - 10) \quad (6.40)$$

where, $\varepsilon_c(t)$ is the autogenous deformation of cement paste at age t (day), s is the coefficient of cement type ($s=0.25$ for normal and rapid hardening cements, $s=0.38$ for slowly hardening cement, $s=0.2$ for rapid hardening high strength cement). In Figure 6.4, comparisons of models with the experiments of autogenous deformation of concrete with different w/c are given (Miyazawa and Tazawa, 2005). It can be easily said that the model proposed by Miyazawa and Tazawa (2005) gives the most accurate results of autogenous deformation for all w/c ratios and cement types tested. This model is also used by other researchers (Hashida and Yamazaki, 2002).

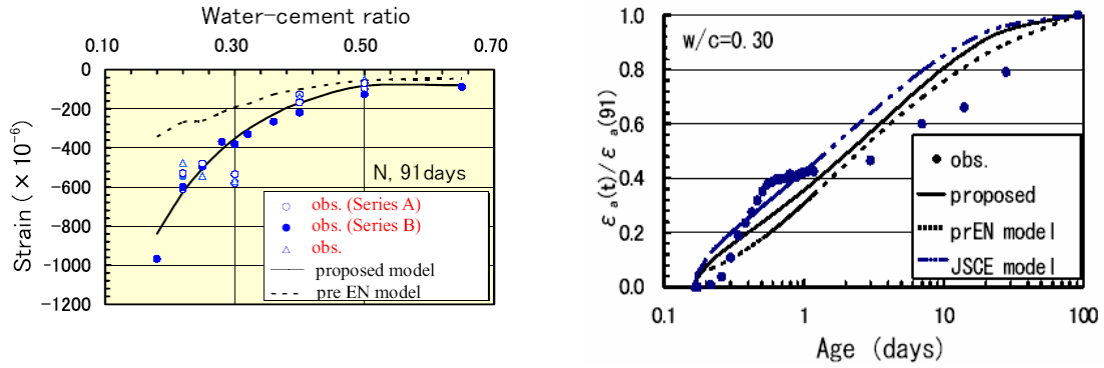


Figure 6.4: (a) Comparison of models of autogenous deformation of concrete, (b) Autogenous deformation vs. time diagram of concrete with the w/c of 0.3 where the observed value at the age of 91 days is taken to be 1.0 (Miyazawa and Tazawa, 2005).

6.5.4 A Macro-Model for Self-desiccation in High Performance Concrete

In another modeling of self-desiccation, which is based on remaining free water content in pores, the degree of hydration and curing temperature was presented by Norling and Mjörnell (1997). Using this model it is possible to determine the reaction of cement and the decrease in relative humidity (RH) resulted from self-desiccation in any composition. The decrease in RH is calculated from the sorption isotherm (the relation between state of moisture, RH and amount of evaporable water w_e) as is given in following equation and also seen in Figure 6.5.

$$RH_{self}(w_e) = RH(w_e = w_0 - w_n + \Delta w) \quad (6.41)$$

where, w_0 is the mixing water, w_n is the nonevaporable moisture content and w is any additional water contributed to the cement paste, for instance from internal curing. The amount of chemically bound water in HPC can be calculated from the degree of reaction of the cement, α_c , and the degree of reaction of the silica fume α_s as below

$$w_n = 0.25 \cdot \alpha_c \cdot C - 0.34 \cdot \alpha_s \cdot SF \quad (6.42)$$

where C and SF are the cement and silica fume contents, respectively. The rate of cement reaction is given as (Nilsson and Mjörnell, 2005).

$$\frac{\partial \alpha_c(t)}{\partial t} = \beta_{w/c} \cdot \beta_T \cdot \beta_\phi \cdot \frac{\partial \alpha_c(t)}{\partial t} \Big|_{ref} \quad (6.43)$$

where $\beta_{w/c}$, β_T , β_ϕ are the effects of w/c and reaction degree, temperature and the moisture, respectively. $\frac{\partial \alpha_c(t)}{\partial t} \Big|_{ref}$ is the rate of reaction for much “diluted” cement grains in a reference climate selected as +20°C and 100 % RH.

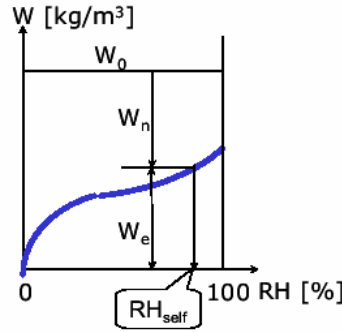


Figure 6.5: The self-desiccation in high performance concrete, in principle (Nilsson and Mjörnell, 2005).

The effect on the rate of reaction of increasingly smaller and smaller available space for further reaction products is given in Eq.(6.42) which is related to the maximum possible degree of cement reaction for the particular w/C, α_c , and the constant a.

$$\beta_{w/c} = \left(\frac{\alpha_{c,max} - \alpha_c}{\alpha_{c,max}} \right)^a \quad (6.44)$$

The effect of temperature is given as

$$\beta_T = e^{\theta \left(\frac{1}{T_{ref}} - \frac{1}{T+273} \right)} \quad (6.45)$$

$$\theta = \theta_{ref} \left(\frac{30}{T+10} \right)^{K_3} \quad (6.46)$$

where T_{ref} is the reference temperature $+20^{\circ}\text{C}$ and θ_{ref} and κ_3 are the empirical constants. Water in the capillary and gel pores which are strongly bounded may not be available as a reactant in the reaction or it might be at some distance from the cement granule. For expressing the combined effect $\beta_{\phi,w}$ is used as following equation

$$\beta_{\phi,w} = \left(\frac{\frac{w_e(\phi) - k_{wg} \cdot \alpha_c}{C}}{w_0/C - 0.19\alpha_c - k_{wg} \cdot \alpha_c} \right)^4 \quad (6.47)$$

where, k_{wg} is the amount of water in the gel at saturation and complete hydration. The moisture content $w_e(\phi)$ is determined from the desorption isotherm.

It was concluded that the model for self-desiccation seems very promising and potentially useful for many applications of HPC. The most uncertain part of the model is the moisture effect on rate of reaction, where more research is needed, especially at very early ages as shown in Figure 6.6.

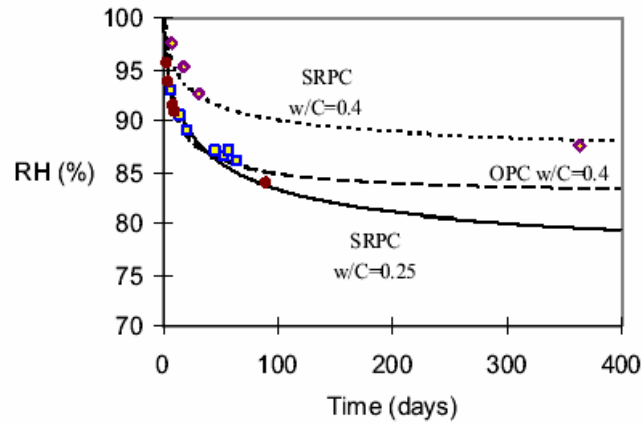


Figure 6.6: Comparison of predicted and measured RH due to pure self-desiccation of different concretes, SRPC-silica fume high performance concrete, OPC-ordinary Portland cement concrete (Nilsson and Mjörnell, 2005).

6.6 Results of Modeling Self-desiccation Shrinkage of Cement Paste

In this thesis, modeling of self-desiccation shrinkage has been determined based on its mechanism as explained in Sections 6.3 and 6.4. The below flow chart which is modified from Lura (2003) summarizes the modeling of the autogenous deformation (Figure 6.7). First of all, the saturation factor S was determined using the known degree of hydration obtained from the non evaporable water content experiments. The capillary stress σ_{cap} was calculated using the critical pore diameter of cement paste determined from MIP test. The self-desiccation of cement paste with silica fume was estimated using the Eq(6.14).

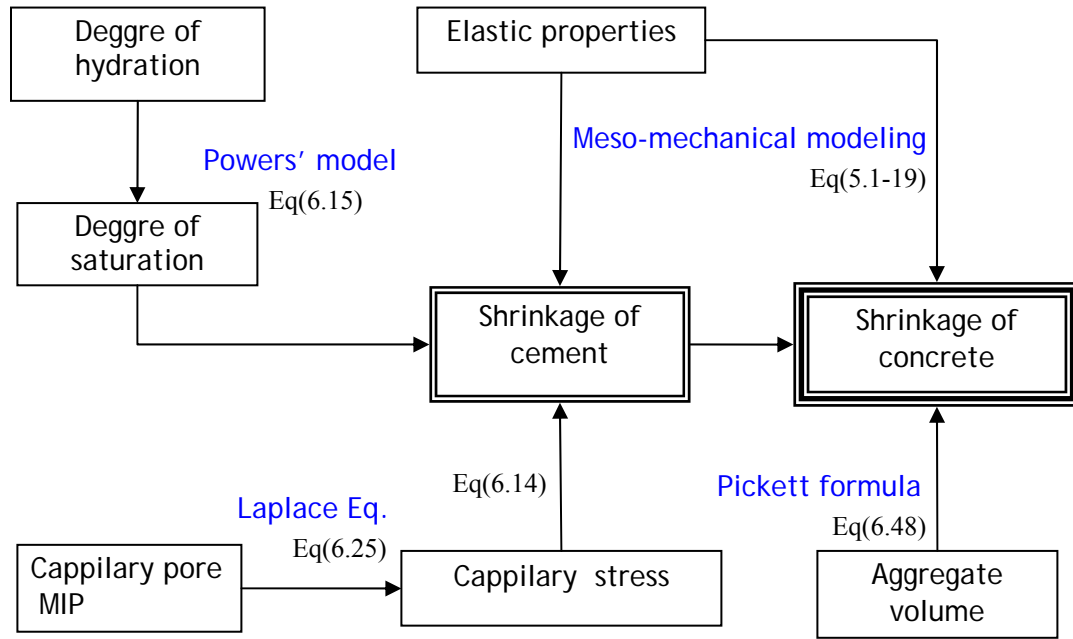


Figure 6.7: Flow chart for calculation of self-desiccation shrinkage of cement paste and concrete.

For calculating the Bulk modulus, the modulus of elasticity of cement paste was determined by meso-mechanical modeling as given in Section 5.6. In Figure 6.8 the results of modeling of autogenous deformation with time are compared with the results obtained from experimental studies. The similarity between the experimental and calculated results may indicate that the calculated values for self-desiccation shrinkage

correspond satisfactorily to the values of measured autogenous deformation. Lura (2003) also compared the measured autogenous deformation with the calculated self-desiccation shrinkage (capillary stress calculated with radius of the capillary pore directly from the RH measurements). Lura (2003) considers an effective elastic modulus equal to 1/3 of the measured one to obtain measured and calculated shrinkage curves close to one another. However, a much better correlation between the calculated and measured deformation values can be determined using the modulus of elasticity obtained from meso-mechanical modeling. As shown in Figure 6.8, the calculated results are getting closer to the measured results with time. The calculated deformations at early ages seem to be higher than the experimental results, and this is probably due to the fact that the unexpected swelling occurred on paste sample during the first day after water addition. As this effect has been diminished with time, the calculated and measured deformations become closer.

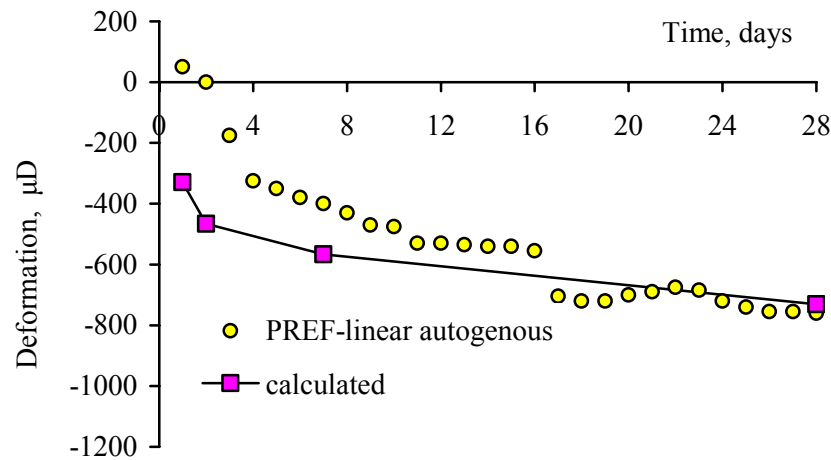


Figure 6.8: Comparison of experimental and calculated autogenous deformations for cement paste.

6.7 Modeling of Autogenous Deformation of Concrete

It is well known that the stiff aggregates restrain the shrinkage of cement paste. The shrinkage of concrete can be determined from the shrinkage of cement paste (Pickett, 1956). In particular, the restraining effect of aggregate on drying shrinkage and

autogenous deformation has been demonstrated by number of authors (Järvenpää, 2001; Pease, 2005 and Moon et al., 2005). On the other hand, in concrete and mortar both drying and autogenous shrinkage can result in tensile stresses and microcracking due to restraining of aggregate particles (Bisschop and van Mier, 1999; Dela 2000). Thus, it is vital to determine the autogenous deformation of concrete. The widely used Pickett expression (1956), which considers homogenous elastic concrete with embedded spherical aggregates (self-consistency principle), gives the shrinkage of concrete as

$$\varepsilon_c = \varepsilon_p (1 - V_{agg})^n \quad (6.48)$$

where ε_c and ε_p are the shrinkage of concrete and paste, respectively, V_{agg} is the volume fraction of aggregates (m^3/m^3), n is the parameter varies between 1.2 and 1.7 and defined as:

$$n = \frac{3(1 - \nu_c)}{1 + \nu_c + 2(1 - 2\nu_{agg})E_c/E_{agg}} \quad (6.49)$$

where, ν_c and ν_{agg} are the Poisson's ratios of the concrete and the aggregates, respectively, E_c and E_{agg} are the modulus of elasticity of concrete and aggregate, respectively. Detailed variation of parameter n is also available in literature (Moon et. al, 2005). In this thesis, ν_c and ν_{agg} were taken as 0.2 and 0.25 and E_{agg} was taken as 74 GPa, while modulus of elasticity of concrete was determined as 44.6 GPa by meso-mechanical modeling (see Section 5.6). The results for fine and coarse mortar and concrete phases are given in Table 6.1. While the calculated autogenous deformations values for FMREF and MREF samples have been found to be slightly higher than the experimental values, no difference is observed between the calculated and experimental results of autogenous deformation of concrete. The results from Table 6.1 show that the autogenous deformation of cementitious materials can be calculated using the above expressions.

Table 6.1: Calculated and measured autogenous deformation for the age of 28 days, μD .

	PREF	FMREF	MREF	CREF
measured	-760	-600	-543	-537
calculated		-632	-579	-536

Similar calculations were also applied to the composites of cement paste with different size fraction of normal aggregates (PN0-2, PN2-4, and PN4-8). These results are detailed in Chapter 5. In order to determine the time dependent variation of autogenous deformation for these series, the linear autogenous deformation results of PREF samples were used. The calculated restraining effect of 30% aggregate volume fraction on cement paste is shown in Figure 6.9.

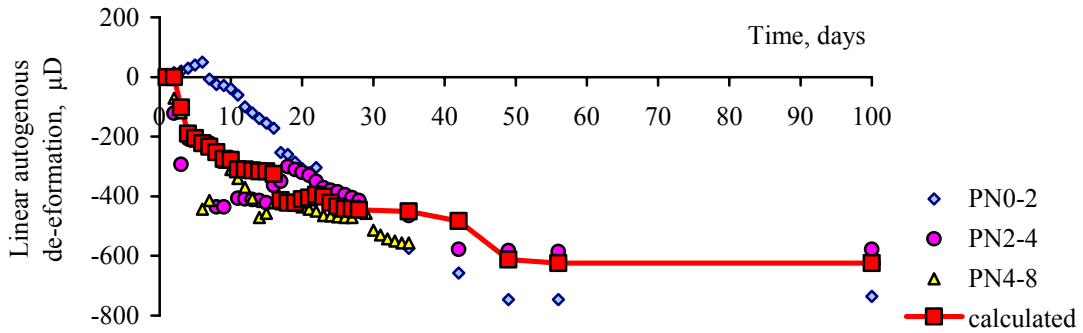


Figure 6.9: Comparison of experimental and calculated autogenous deformations for series of PN0-2, PN2-4, and PN4-8.

The results in Figure 6.9 indicate that the calculated values are greater than the values of PN0-2 series at the early ages, but smaller at the later ages. The comparisons of the calculated and measured results are given in Figure 6.10. The best fitted results were found for series PN4-8. The calculated deformation values have also been found to be close to the measured values for the series of cement paste with 2-4 mm normal aggregate. Since the calculation used considers the effect of aggregate volume only, the restraining effect of different size aggregate cannot be modeled. In addition, the modulus of elasticity, which was used for calculating the autogenous deformation of fine and coarse mortar and concrete, was based on meso-mechanical modeling. Thus, this may

explain why the calculated results for these composite phases have been found close to the measured values.

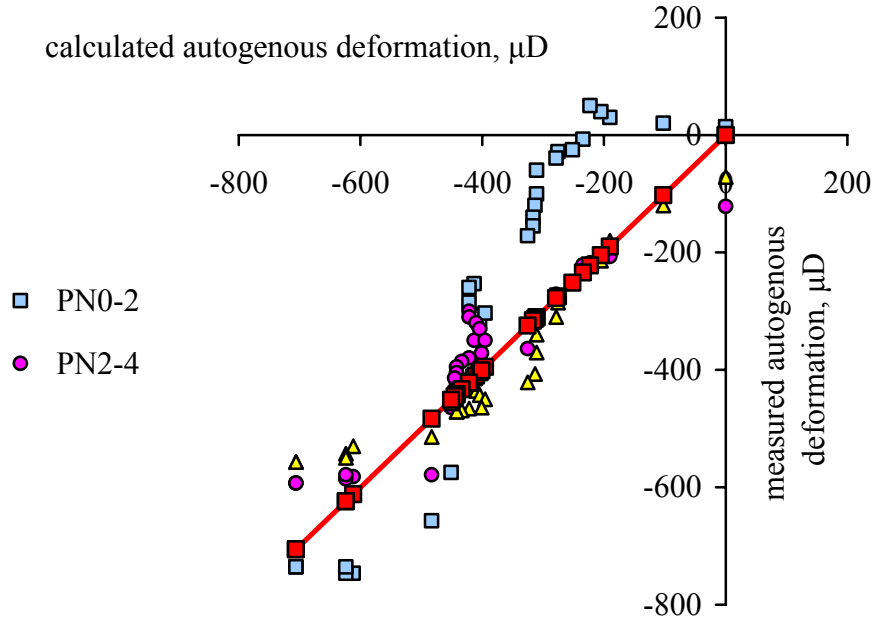


Figure 6.10: Comparison of experimental and calculated results autogenous deformation of series of PN0-2, PN2-4, and PN4-8.

6.8 Conclusion

It can be concluded that the self-desiccation shrinkage of cement paste can be determined by the known degree of hydration and capillary pore radius of cement paste. For cement paste, the results showed that the calculated self-desiccation shrinkage and the measured autogenous deformation are similar to one another.

If the self-desiccation shrinkage is accepted as a great portion of autogenous deformation, then using the above calculations the autogenous deformation of concrete or composites can be precisely determined according to the volume and elastic properties of aggregates. It has also been demonstrated that the modulus of elasticity obtained from the meso-mechanical modeling provides satisfactory predictions in calculating the autogenous deformation of both cement paste and concrete.

7 DISTRIBUTION OF LWAS

7.1 General

The efficiency of internal curing is affected by distribution of LWAs, as well as the size and volume of LWAs. Because the LWA can release water into the cement paste from a surface layer approximately 1mm thick, autogenous deformation will be mitigated only within this water entrained area in cement paste phases. It is obvious that the thickness of the water released rim is dependent of the pore volume and structure of LWA. If the porosity of LWA is high and the pores are open, the water absorption becomes more efficient. Consequently, water can penetrate easily through the cement paste. The distribution of reservoirs and their water entrainment in cement paste has been investigated as an approach of air entrained concrete. In the protected paste volume concept, the fraction of the cement paste within a given distance of an air void is determined. For the distribution of water reservoirs in cement paste, concerned property is being the fraction of cement paste within a given distance of a water reservoir (Bentz et al., 2006). In this point, it is being vital to identify the spacing equations of LWAs. In this chapter, first of all the flow distance of water from the cement paste will be investigated. Then, dispersion characteristics of LWAs and its effects on both the internal curing and the fracture properties will be examined.

7.2 Water Movement from LWA to the Cement Paste

Internal curing becomes more efficient if the water can travel throughout the cement paste easily. In order to demonstrate the water entrainment from LWA to cement paste, the solution with red concrete colored pigment was used. Artificial expanded clays with spherical surfaces were mixed with white cement after one-day absorption of pigmented water. When the microphoto taken from the surface of a sample was inversed, the image shown in Figure 7.1.b is obtained. Although water with pigments has a different surface tension compared to normal water, the 100 μm water flow from the LWA's outer surface

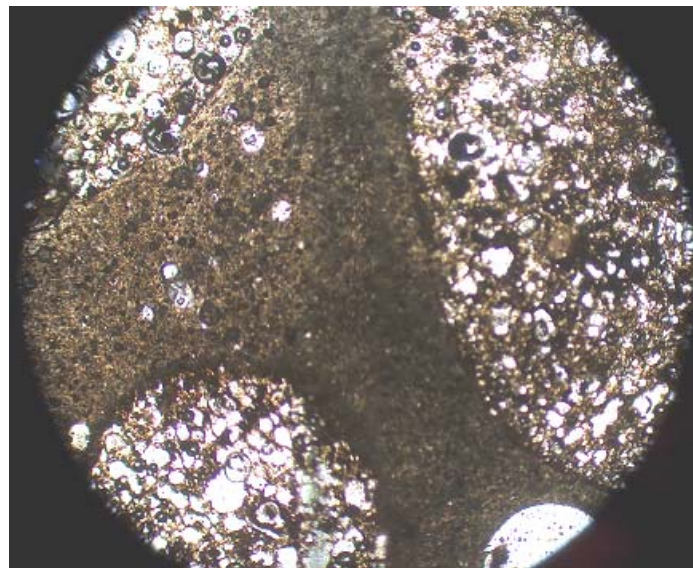
to the cement paste was determined at the age of one day, but it increased to 1 mm at three days. Recent studies have also shown similar results, suggesting that the LWA can release water into the cement paste from a surface layer approximately 1mm thick (Lura, 2003). The tests were also repeated for the age of 7 and 28 days after casting. The results show that no time dependent change in the distance of water flow is observed for any age, although some researchers argue that the length of water entraining rim varies with time (Bentz and Stutzman, 2006).



(a)



(b)



(c)

Figure 7.1: (a) Expanded clays saturated with concrete colored pigment; (b) water flow from LWA to cement paste; (c) optical image of LWA including cement paste.

In addition to this observation, thin sections were prepared for microscopic investigations. As shown in Figure 7.1.c, when the porous expanded clays are distributed in proximity, a continuous phase becomes visible and appears as a darker rim in thin section image. This may indicate that the distance between the aggregates is an important factor for preventing autogenous deformation of the cement paste.

It can be easily said that the water cannot effortlessly move through into the concrete with the increasing degree of hydration. Bentz et al. (2006) stated that penetration of water from LWA to the cement paste is dependent on the permeability of cementitious materials. The authors showed that the travel length of water varies depending on pore radius of paste and reservoir, water demand of concrete due to the ongoing chemical shrinkage and capillary porosity of concrete with the assuming water flow through a cylindrical pore. They also demonstrated the water flow for concrete with the cement dosage of 700 kg/m^3 and chemical shrinkage of 0.07 kg water/kg . They found that flow distances vary from tens of millimeters at early ages to millimeters at middle ages to hundreds of micrometers at later ages. The authors stated that the results are quite approximate in nature. However, the results obtained during the course of our study indicate a flow distance of only 1mm at ages of 3, 7 and 28 days for cement paste with w/c of 0.28, although this distance for concrete samples may be greater than one millimeter.

7.3 Distribution of LWAs

For air entrained concrete there are mainly two types of spacing definitions; paste-to-void proximity and void-to-void proximity. There are a number of spacing factors defined to estimate the paste-void proximity such as the definitions of Powers (1949), Philleo (1983), Pleau and Pigeon (1996), Lu and Torquato (1992). The equations for void-to-void proximity have been derived by a number of authors (e.g. Lu and Torquato (1992) and Attiogbe (1993, 1996)). The **paste to void** or **void to void** distances can be identified by their cumulative distribution and probability density functions. Snyder (1998) stated that the probability density function (PDF) represents the fraction of spacings found in the interval $[s, s + ds]$ for some differential element ds as shown in Figure 7.2. The associated cumulative distribution function (CDF) increases

monotonically from zero to unity and represents the fraction of spacings less than s . Because of the fact that there is not any single theoretical value defined for the spacings, following the approach by Snyder (1998), the 50th and the 95th percentiles of the spacing distributions were taken as representing the quantity of spacing. As the water movement from the LWAs into cement paste is conceptually similar to the air entrained concrete (Snyder, 1998), the distribution of water reservoirs will be defined here as the distribution of air voids in air entrained concrete.

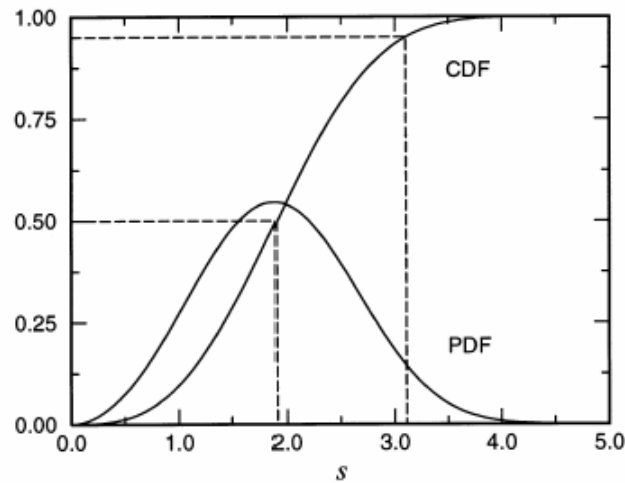


Figure 7.2: An idealized representation of a spacing cumulative distribution function (CDF) and the associated probability density function (PDF) for some distance s . The dashed lines demonstrate how to determine the 50th and the 95th percentiles from CDF data (Snyder, 1998).

7.3.1 Paste-Void Proximity

Paste-void proximity equations estimate the volume fraction of paste within some distance from the surface of the nearest air void. If the water release distance from the LWAs is known, water entrained volume fraction of cement paste can be determined.

Powers (1949) spacing factor attempts to calculate the distance from the surface of all the air void surfaces. It was assumed that the air voids are monosized. If there is very little paste for each air void, the spacing factor can be calculated as the ratio of the volume of the paste to the total surface area of air voids. On the other hand, if the paste volume fraction is larger it is assumed that the air voids are located in a simple cubic

lattice. In this condition, the Powers spacing factor is the distance from the center of a unit cell to the nearest air void surface.

Philleo (1983) spacing factor, which was modified from the Powers approach, is defined as the quantity of the volume fraction of paste within some distance of an air-void system. Philleo spacing factor approximates to characterize the paste-void spacings for finite-sized air voids.

The spacing factor proposed by Pleau and Pigeon (1996) uses the air void radii distribution and the distribution of distances between a random point in the paste and the nearest air void center.

Lu and Torquato (1992) proposed equations for both paste-void and void-void proximity. They examined the system in which a matrix contains solid spheres. In the paste-void equation, the probability that a point chosen at random throughout the entire system would have no part of an air void within a distance s from it. Their function represents the probability of finding the nearest void surface a distance s from a random point in the paste portion. In this point, the function has an equivalent meaning with the definition of the paste void proximity CDF.

7.3.2 Void-Void Proximity

The void-void proximity can be examined in two different ways as: the nearest neighbor and mean free path calculations (Snyder, 1998).

The nearest neighbor void-void proximity equations are based on the calculation of distance from the surface of air voids to the surface of the nearest neighbor air void. This calculation is repeated for a number of air voids and the nearest neighbor void-void distances are used to gain the cumulative distribution function. For the state of polydispersed particles, the void-void spacing differentiates with the particle dimension. Thus, the mean void-void spacing is defined.

Lu and Torquato (1992) proposed a void-void equation which is based on the calculation of the nearest air void surface in a condition that a point is located at the center of an air void with a chosen radius. Ensemble averages for polydispersed spheres of Lu and Torquato equation can be calculated based on either number density or volume density.

Attigbe (1993) put forward an equation to describe the mean spacing of air voids. This equation attempts to calculate the half of the minimum distance between surfaces of the nearest three neighbors. In Attigbe equation, if the air voids decrease to zero, the mean free path diverges toward infinity at low air contents.

One other definition of void-void proximity is the mean free path which is a numerical expression rather than a distribution. The mean free path is defined as the average length of paste between the closest air voids along an arbitrarily selected line, similar to the chord length given in ASTM C 457 (1998).

Snyder (1998) compared the above definitions for the systems containing both monosized spheres and the spheres with log-normally distributed air void radii. The results showed that the Powers spacing factor approximated some large percentile of the paste-void spacing distribution. The Philleo equation estimated the paste-void spacing distribution fairly well for the spheres with log-normally distributed void radii, and gave better results than the Pleau and Pigeon equation. The Pleau and Pigeon equation, however, performed well at very low air contents, especially for the polydispersed case, while the Attigbe equations estimated the void-void spacing quite poorly. Snyder (1998) proposed an alternative Attigbe equation which is based on the different air voids distribution. The performance of Lu and Torquato equations for both paste-void and void-void proximities were found to be the most accurate overall among the above mentioned approaches.

7.4 Application to the Internal Curing

In the light of above definitions and results, for the replacement of 10-20-30% volume and 2-4 mm and 4-8 mm size fraction of LWAs, the nearest surface distribution of LWAs were found by the image analysis on the pieces of broken beam specimens of flexural test. In addition, it is found from the images shown in Figure 7.3 that the LWAs can be well fitted to ellipses rather than circles.

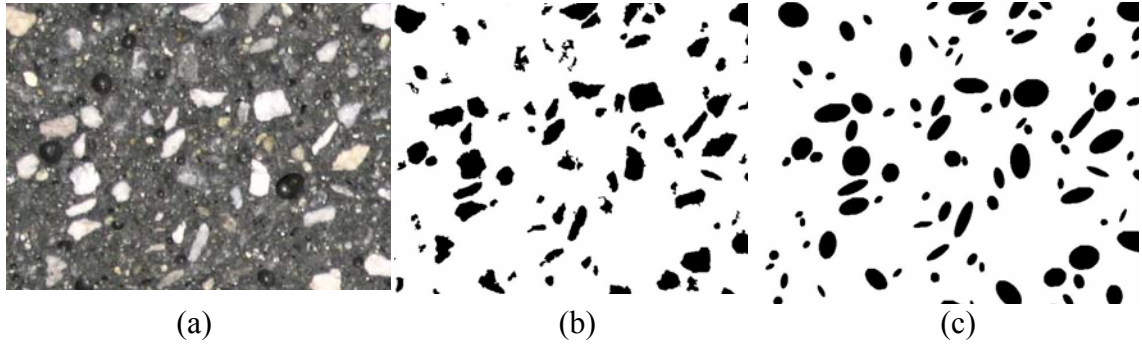


Figure 7.3: (a) Real image of concrete, (b) LWAs in binary image of concrete, (c) fitting ellipses of LWAs. It is shown that there is only very small amount of particles with circle geometries.

In order to calculate the protected paste volume, the area that corresponds to the cement paste was first calculated. The ellipses were then enlarged using the founded travel length of water as 0.5, 1 and 2 mm, and then the area of the cement paste and the protected area of cement paste were recalculated. In calculations, it is assumed that the normal aggregates were in water-saturated conditions, which means that water for internal curing was not absorbed by normal aggregates.

For the calculations of nearest LWA-LWA distribution, the image area was first divided into parallel lines with a distance of 10 mm, and then the nearest neighborhoods of LWAs for each line were obtained. The parallel lines were then rotated up to 90 degree with 15-degree intervals. For each interval, analysis of the nearest neighbor distance of LWAs was repeated as shown in Figure 7.4.

In this study, Powers and Attiogbe mean spacing factors were used. The **Powers spacing factor** \bar{L} , for paste to LWA proximity, was calculated using the following equation

$$\bar{L} = \begin{cases} \frac{P_v}{\alpha_v A_v} & , p_v / A_v < 4.342 \\ \frac{3}{\alpha_v} \left[1.4 \left(\frac{p_v}{A_v} + 1 \right)^{1/3} - 1 \right] & , p_v / A_v \geq 4.342 \end{cases} \quad (7.1)$$

where, A_v is the LWA volume fraction, p_v is the paste volume fraction and α_v is the specific surface area of LWAs. Using image analysis program (MicroImage and ImageJ), all the LWAs were fitted to ellipses, for which the area, the lengths of major and minor axes and the locations were known. For calculating α_v , the area of each ellipse was divided to its volume assuming that ellipses are represented by ellipsoids in three-dimension. The mean value of α_v for all ellipses was used in calculating the spacing factor.

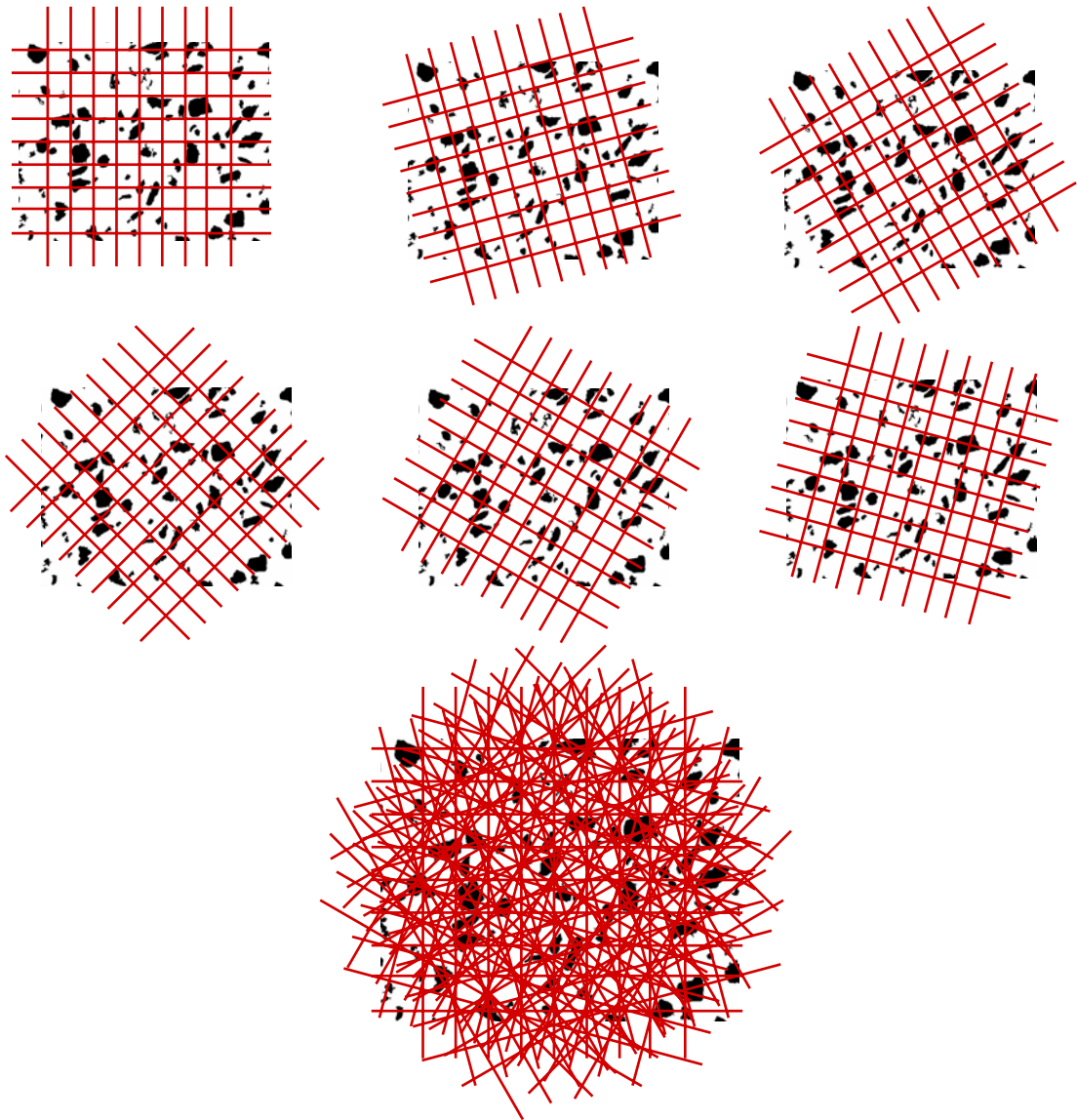


Figure 7.4: Calculation steps of nearest distance of LWA-LWA surfaces.

Attiogbe mean spacing factors, which were originally defined for void-to-void proximity in air entrained concrete, were used to calculate the LWA-LWA proximity. Attiogbe defined two different spacings, which are termed in this thesis as \bar{s}_1 and \bar{s}_2 with the following equations (Attiogbe, 1993 and 1996).

$$\bar{s}_1 = 2 \frac{p_v^2}{\alpha_v A_v} \quad (7.2)$$

$$\bar{s}_2 = 2F \frac{p_v^2}{\alpha_v A_v} \quad (7.3)$$

$$F_v = \frac{8}{p_v / A_v + 1} \leq 1 \quad (7.4)$$

where p_v , α_v , A_v and F_v are the paste volume fraction, specific surface area of LWAs, volume fraction of LWAs and the fraction of the total paste volume within distance of \bar{s} from the edges of LWAs.

7.5 Results of Image Analysis

7.5.1 Concrete

The cumulative and probability distribution function of the nearest neighbor LWA-LWA proximities are given in Figure 7.5 a and b, respectively. As expected, the distance of the nearest neighbor of LWAs decreased with the volume of the LWAs. The distance between the nearest neighbors for coarse LWAs was shorter than that of finer LWAs when the replacement ratio of 10% is applied, although at higher volume of replacements the effect of size of LWAs on the nearest neighbor LWA-LWA proximities became less significant. The results of image analysis show that the well distributed LWAs in the sample CV10L48 may explain why the characteristic length of this sample (107 mm) was unexpectedly greater than that of the sample CV10L24 (98 mm), suggesting that the distribution of LWAs can affect the fracture properties of concrete, especially the characteristic length.

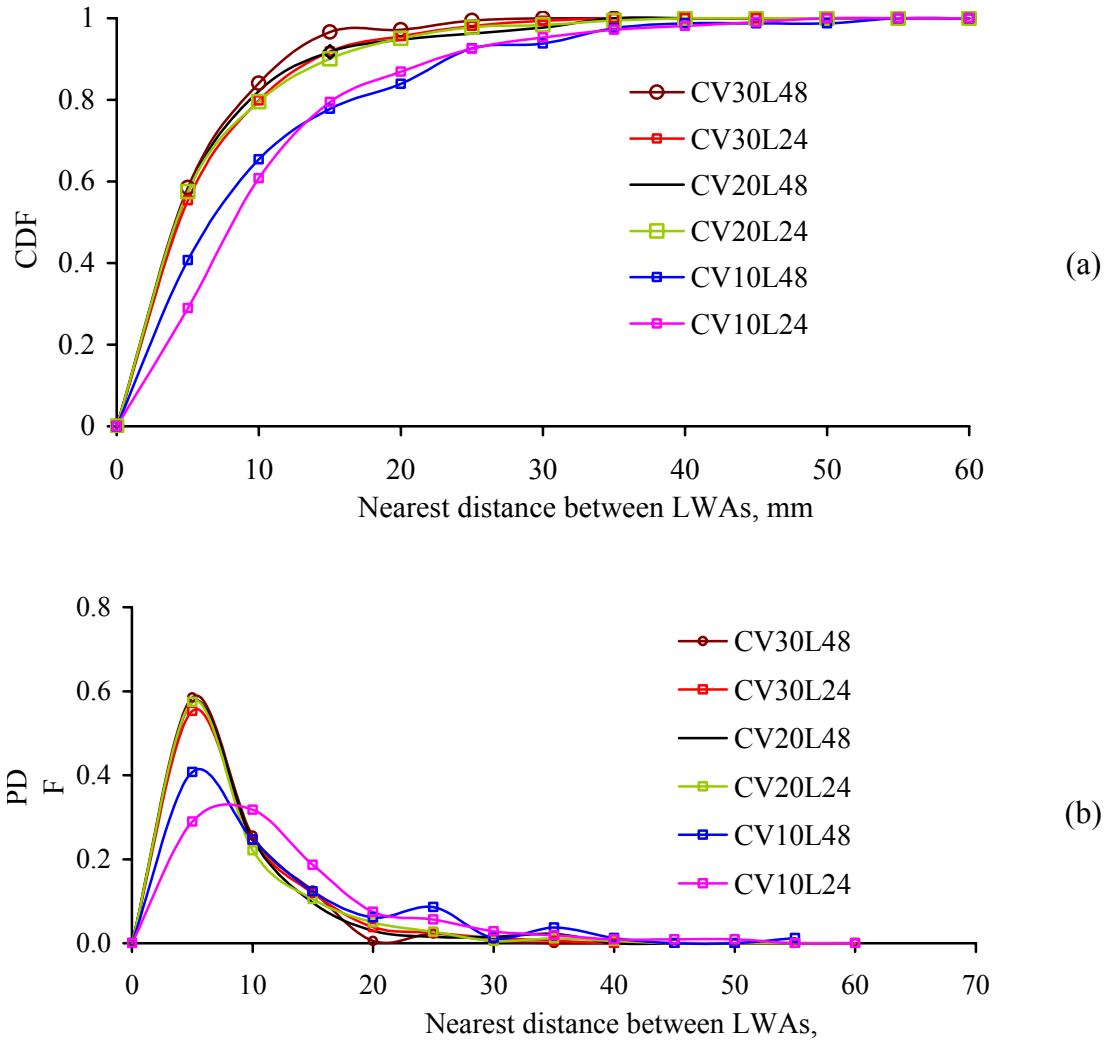


Figure 7.5: (a) The cumulative distribution function (CDF) and (b) the probability distribution function (PDF) for the 838 nearest neighbor LWA-LWA proximities.

The CDF values corresponding to the 50th and the 95th percentiles of the LWA-LWA proximity distributions were used to provide a comparison with the Powers and Attiogbe spacing factors. The results from the image analyses are given in Table 7.1. As seen from Table 7.1, since the Powers spacing factor estimates the large percentile of the paste to LWA spacing distribution (Snyder, 1998), the results have been found higher than the 95th percentile of the nearest neighbor LWA-LWA proximity distribution. On the other hand, the Attiogbe mean spacing of s_2 has been found to be similar to the calculated value of 95th percentile of the nearest neighbor LWA-LWA proximity distribution of LWAs as shown in Figure 7.6.

Table 7.1: The results of Powers and Attiogbe mean spacings calculations and the image analysis of the distance of the nearest neighbor LWA-LWA proximities.

		CV10L24	CV20L24	CV30L24	CV10L48	CV20L48	CV30L48
Number of LWAs, n		66	162	238	40	74	98
Total area of LWAs, mm ²		272.4	836	1182	294.5	529.6	1128.9
Area fraction of LWAs, %		3.1	9.5	13.9	3	6.2	11.2
Image area, mm ²		8787	8800	8504	9817	8542	10080
Powers	\bar{L} , mm	43.686	22.383	14.488	57.149	26.307	17.597
Attiogbe	\bar{s}_1 , mm	30.580	15.668	10.142	40.004	18.415	12.318
	F	1.253	2.167	2.862	1.253	2.167	2.862
	\bar{s}_2 , mm	19.159	16.974	14.515	25.063	19.949	17.629
Image analysis	average, mm	10.440	6.289	6.250	9.895	6.317	5.467
	50th, mm	3.850	3.800	4.250	6.850	3.850	3.750
	95th, mm	20.900	19.900	17.550	31.050	20.900	14.450
Autogenous def. (28 days), μD		-410	-285	-40	-480	-360	-183

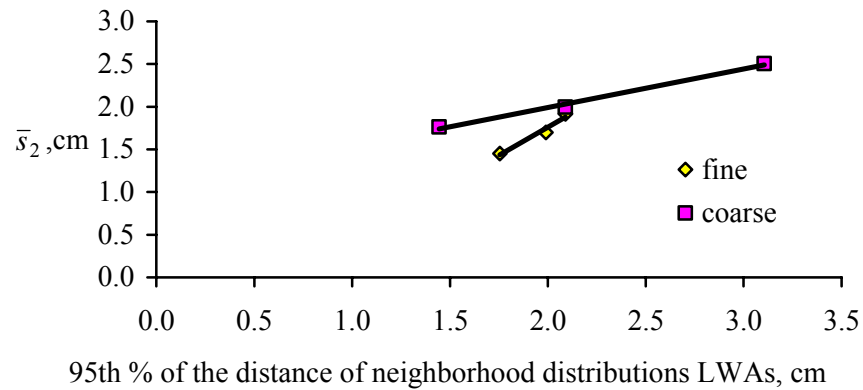


Figure 7.6: Comparison of the results of 95th percentile of the nearest neighbor LWA-LWA proximity distribution with the Attiogbe spacing factor \bar{s}_2 for the mortars with fine and coarse LWAs.

It is demonstrated in Figure 7.7 that the 95th percentile of the nearest neighbor LWA-LWA proximity distribution was in close agreement with the magnitude of autogenous deformation at 28 days of age. Since the LWA-LWA proximity is affected by both size and volume, variation of autogenous deformation results can be easily correlated with

this proximity. Although the distance of the nearest neighbor of fine and coarse LWAs were closer at the replacement volume ratio of 20%, the fracture energy of concrete with fine LWAs were greater than that of concrete with coarse LWAs.

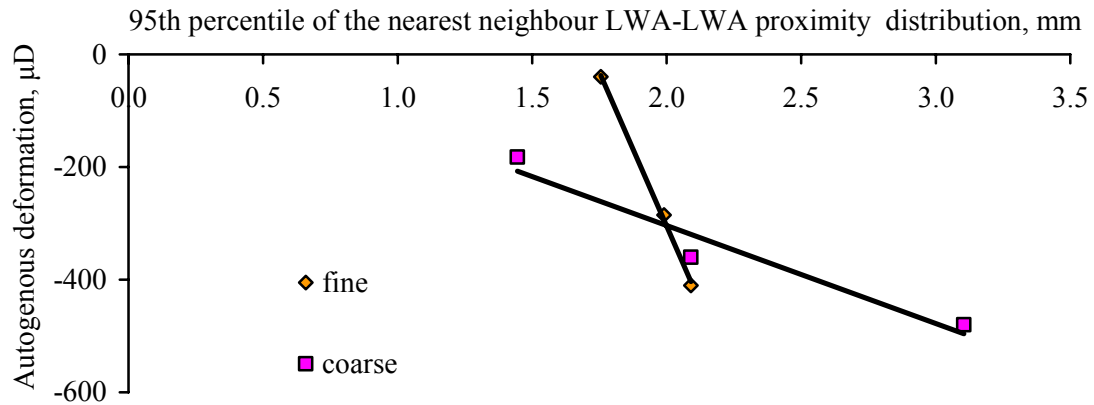


Figure 7.7: Comparison of the results of 95th percentile of the nearest neighbor LWA-LWA proximity distribution with the autogenous deformation of concretes with LWAs at the age of 28 days.

The results of protected paste volume approach, which were calculated for the 0.5, 1 and 2 mm distances of water release, are shown in Figure 7.8. The rate of mitigation of autogenous deformation for each series with respect to the reference concrete is also shown as dashed lines. As shown in figure, the best-fitted values of concretes with LWAs were found to be at water flow of 1 mm. In addition, the water flow from LWAs to the cement paste has been shown previously as 1 mm (Akçay et al., 2005; Akçay and Tasdemir, 2006b). As shown in the figure, the values of protected paste volume for the sample CV20L24 were unexpectedly greater than those of the sample CV30L48, especially for water flow length of >1 mm. For the replacement by high volume of LWAs, the protected paste volume was found to exceed 100% for water travel length of >1 mm, meaning that all the cement paste would be protected and even swelling may occur.

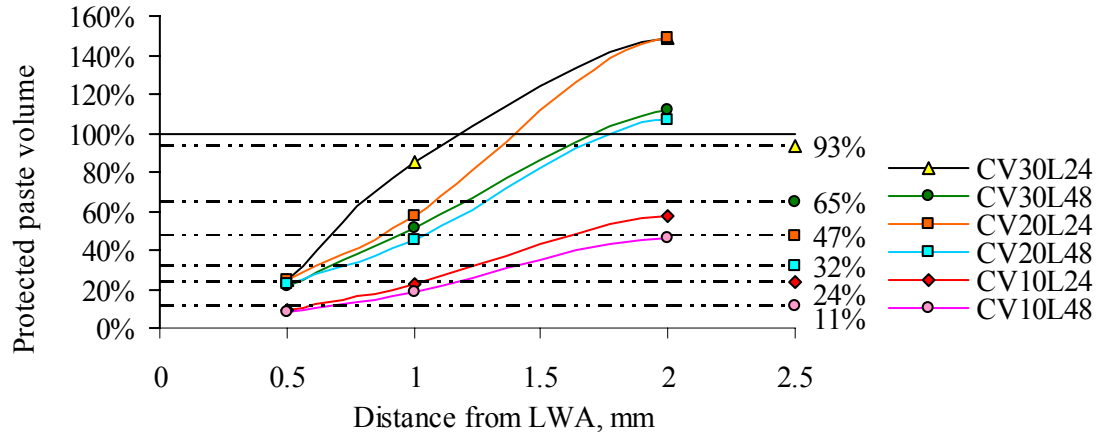


Figure 7.8: Fraction of paste within distance from the LWA.

In Figure 7.9, for different series of concrete, the mitigation ratios of autogenous deformation with respect to the reference concrete at the age of 28 days were compared with the calculated protected paste volume for water flow distance of 1 mm. The mitigation ratios corresponding to longer and shorter periods than 28 days were also compared with the results of protected paste volume for water flow distances of 0.5, 1 and 2 mm, but no significant correlation were found (Figure 7.8).

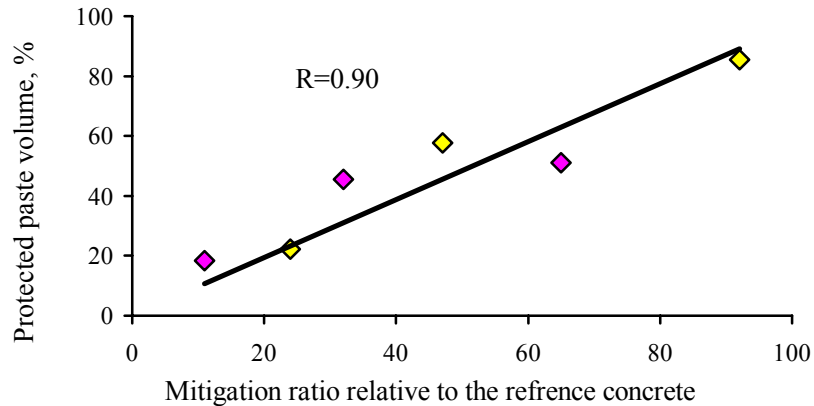


Figure 7.9: Comparison of the mitigation ratio of autogenous deformation according to the reference concrete with the protected paste volume calculated with the water travel distance of 1 mm.

7.5.2 Mortar

The cumulative and probability distribution function of the nearest neighbor LWA-LWA proximities for the MV10L24, MV20L24 and MV30L24 series are given in Figure 7.10 a and b, respectively. As expected, the distance between the nearest neighbors for LWAs decreased with the volume of the LWAs.

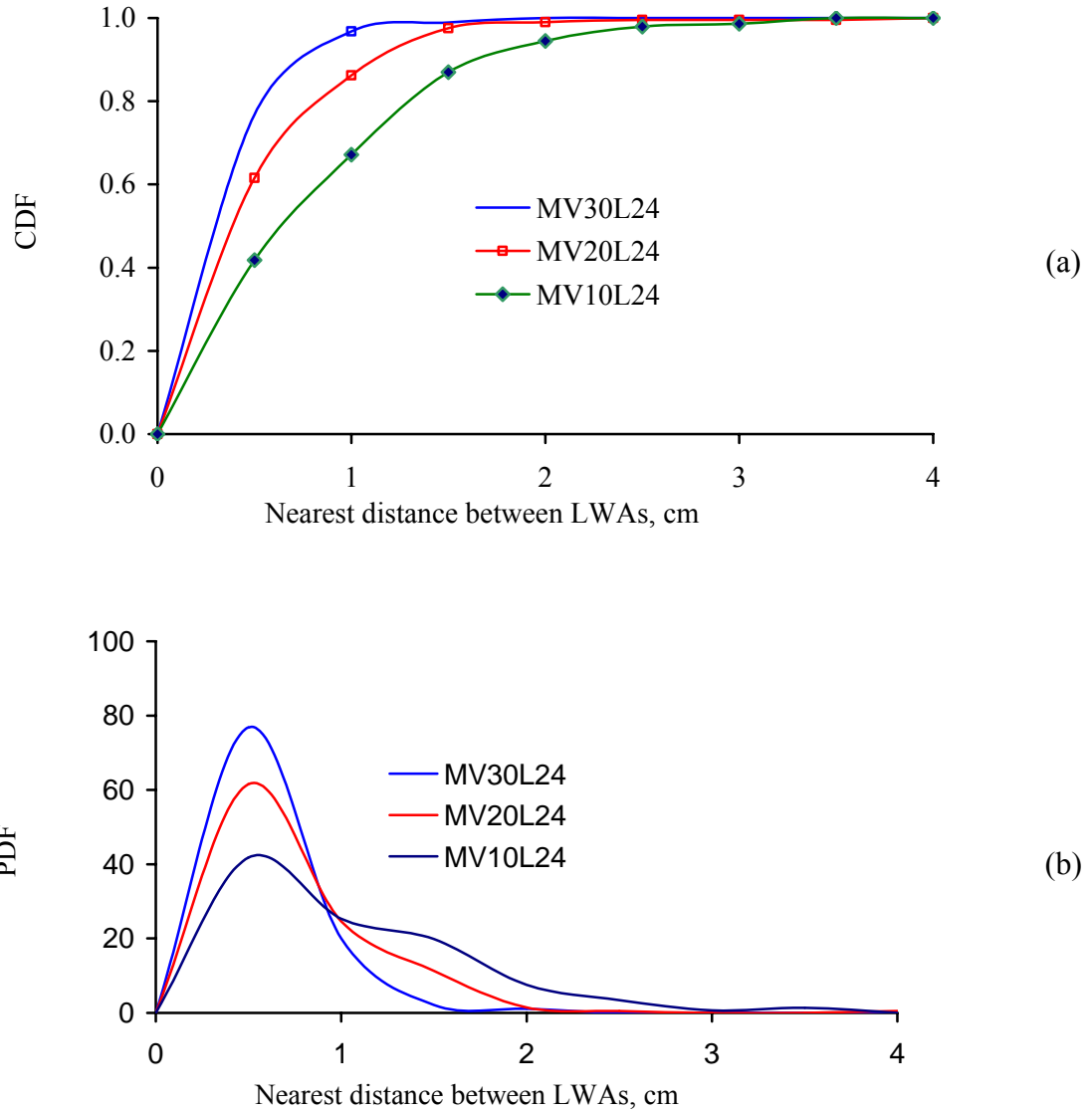


Figure 7.10: (a) The cumulative distribution function (CDF) and (b) the probability distribution function (PDF) for the 623 nearest neighbor LWA-LWA proximities.

The CDF values corresponding to the 50th and the 95th percentiles of the LWA-LWA proximity distributions were used to provide a comparison with the Powers and Attiogbe spacing factors. The results from the image analyses are given in Table 7.2.

Table 7.2: The results of Powers and Attiogbe mean spacings calculations and the image analysis of the distance of the nearest neighbor LWA-LWA proximities.

		MV10L24	MV20L24	MV30L24
number of LWAs, n		107	158	239
total area of LWAs, mm ²		4012	8549	11792
area fraction of LWAs, %		4.8	11.1	15.7
image area		8358.0	77018.0	75108.0
α , 1/mm		1.341	1.169	1.251
Powers	\bar{L} , mm	41.00	23.52	14.66
Attiogbe	\bar{s}_1 , mm	36.081	20.694	12.898
	G	1.231	2.133	2.824
	\bar{s}_2 , mm	22.204	22.073	18.209
Image analysis	average, mm	8.105	5.256	3.538
	50th, mm	6.550	3.700	2.550
	95th, mm	20.400	14.450	9.300
Autogenous def. (28 days), μD		-450	-240	210

The results show that the Attiogbe mean spacing of \bar{s}_2 gave closer approximation than Powers spacing to the calculated value of 95th percentile of the nearest neighbor LWA-LWA proximity distribution of LWAs. The Attiogbe mean spacing \bar{s}_2 for the MV20L24 sample was found similar to that for the MV10L24 sample, although the results were taken as the average of two different images from each series. It is demonstrated in Figure 7.11 that the 95th percentile of the nearest neighbor LWA-LWA proximity distribution was in close agreement with the magnitude of autogenous deformation at 28 days. A similar correlation was observed in the experiments with concrete samples (Figure 7.7). Since the LWA-LWA proximity is affected by both size and volume, variation in autogenous deformation results can be easily correlated with this proximity.

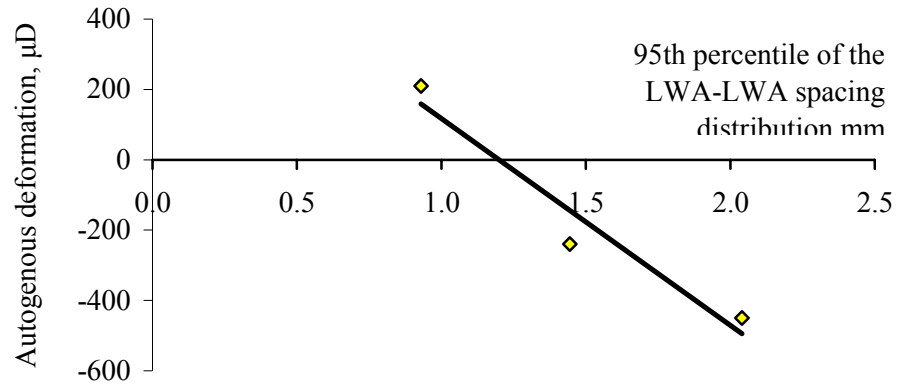


Figure 7. 11: Comparison of the results of 95th percentile of the nearest neighbor LWA-LWA proximity distribution with the autogenous deformation of mortars with LWAs at the age of 28 days.

The values of protected paste volume, which are calculated for water flow distances of 0.5, 1, and 2 mm are shown in Figure 7.12. The rate of mitigation of autogenous deformation for each series with respect to the reference mortar is also shown as dashed lines. As shown in Figure 7.12, the best correlated values of mortars with LWAs were found to be at water flow of 1 mm, although the experiments with concrete specimens gave much satisfactory results.

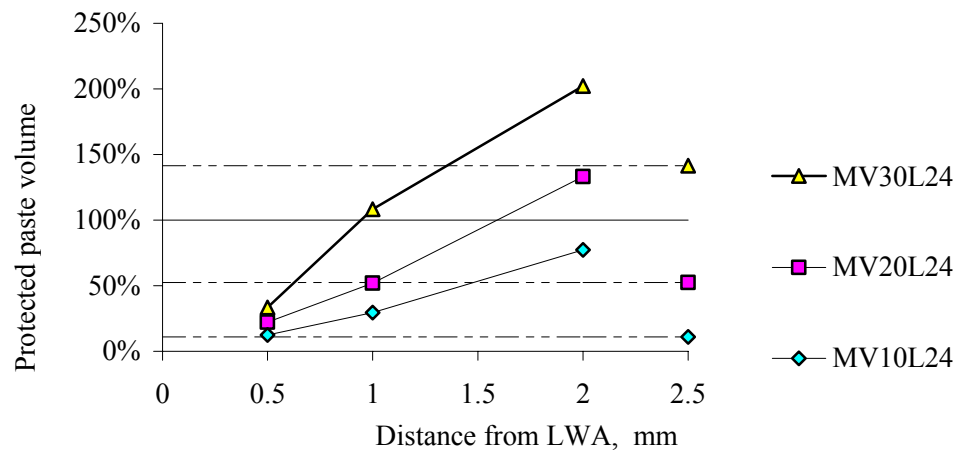


Figure 7.12: Fraction of paste within distance from the LWA.

Although the values of protected paste volume were found greater than the experimentally determined values of mitigation ratios of autogenous deformation, a well defined correlation was observed between the two values. (Figure 7.13).

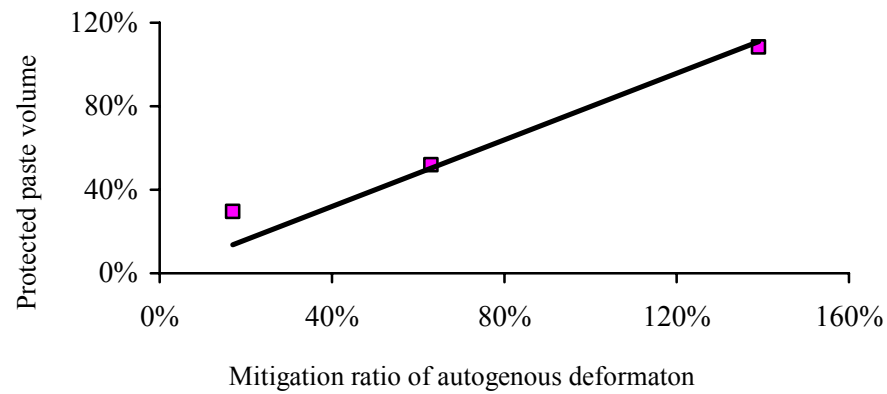


Figure 7. 13: Comparison of the mitigation ratio of autogenous deformation according to the reference mortar with the protected paste volume calculated with the water travel distance of 1 mm.

7.6 Comparison of Results of Image Analysis with Fracture Properties

It is shown in Figure 7.14 that the results from the image analysis are also well correlated with the results of fracture energy and characteristic length of mortar, as is the case for the result of autogenous deformation.

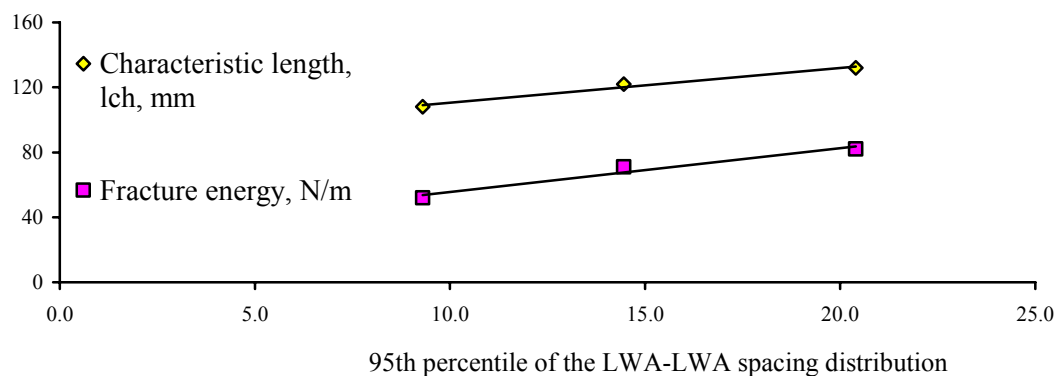


Figure 7.14: Comparison of the fracture energy and characteristic length of mortars with the 95th percentile of the nearest neighbor LWA-LWA proximity distribution.

Examining the fracture energy using image analysis for concrete specimens with fine and coarse LWAs showed that the fracture parameters of concretes were highly dependent on the distribution of LWAs (Figure 7.15).

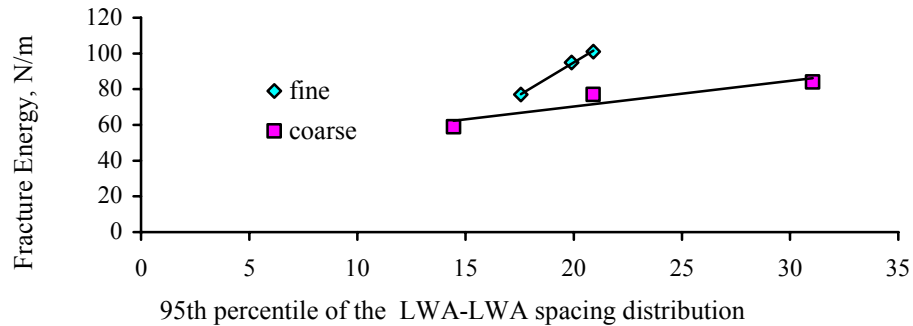


Figure 7.15: Comparison of the fracture energy of concrete with the 95th percentile of the nearest neighbor LWA-LWA proximity distribution.

The value of 95th percentile of the nearest neighbor LWA-LWA proximity distribution reflects the effects of both volume and size of LWAs. Comparison of this single value with the fracture properties of concrete (Figure 7.16) shows that although the correlation coefficient is not significantly high, the similar values of 95th percentile of the nearest neighbor LWA-LWA proximity distribution for concrete with fine and coarse LWAs resulted in similar fracture properties.

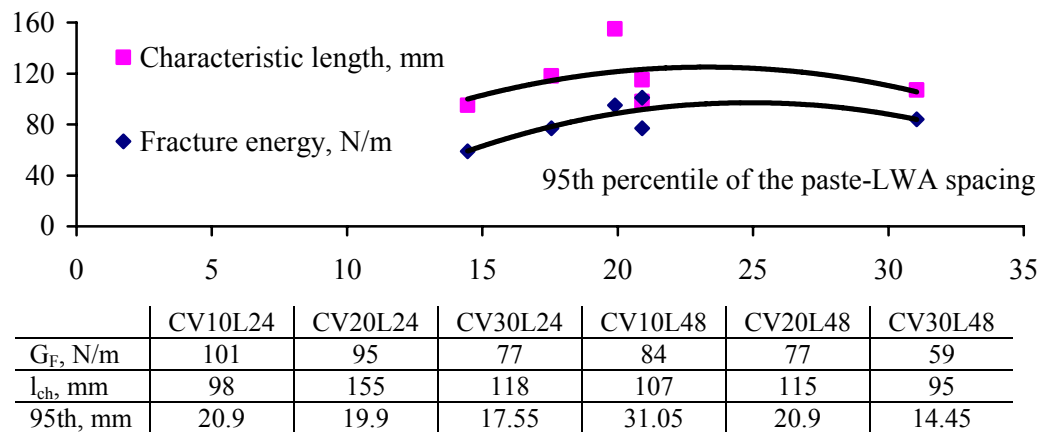


Figure 7.16: Comparison of the fracture energy and characteristic length of concretes with the 95th percentile of the nearest neighbor LWA-LWA proximity distribution.

7.7 Conclusion

On the basis of the results of experimental studies described in this chapter the following conclusions can be drawn:

1. The values corresponding to the 50th and the 95th percentiles of the LWA-LWA proximity distributions were used to provide comparison with the Powers and Attiogbe spacing factors. The Attiogbe mean spacing of \bar{s}_2 were found to be similar to the calculated value of 95th percentile of the nearest neighbor LWA-LWA proximity distribution of LWAs.
2. The distance between the nearest neighbors for coarse LWAs was shorter than that of finer LWAs when the replacement ratio of 10% is applied, and this can explain why the characteristic length of the CV10L48 sample (107 mm) was found greater than that of the CV10L24 sample (98 mm). The well distribution of LWAs for the CV10L48 series was found to be effective on its fracture properties, especially the characteristic length.
3. The 95th percentile of the nearest neighbor LWA-LWA proximity distribution was found to be in close agreement with the magnitude of autogenous deformation of concretes and mortars at 28 days. Since the LWA-LWA proximity is affected by both size and volume, variation of autogenous deformation results can be easily correlated with this proximity.
4. The comparison between the mitigation ratios of autogenous deformation of concrete series relative to the reference concrete at the age of 28 days and the calculated protected paste volume for the 1 mm of water flow gives the satisfactory results. Thus, the results indicate that the protected paste volume in internal curing can be determined by image analysis.
5. It can be concluded that the distribution of LWAs strongly affects the fracture properties of cementitious materials. In addition, the value of autogenous deformation has been found to be well correlated with the distribution of LWAs.

8. OPTIMUM DESIGN OF CONCRETES

8.1 General

In this chapter, the compressive strength, modulus of elasticity, fracture energy, characteristic length, splitting tensile strength, net bending strength, and autogenous deformation of concretes have been defined according to the size and volume of substituted LWAs. A multi-objective simultaneous optimization technique, in which the Response Surface Method (RSM) is incorporated, is used. The experimental programs are designed to find the optimum solutions as a combination of a number of factors estimated by fitting a polynomial model by using analysis of variance (ANOVA).

8.2 Response Surface Modeling

Because of the fact that the concrete has a non linear behavior and there are some microstructural parameters and mechanical properties, the nonlinear optimization problems should be solved. Analysis of response surface over the simplex region involves the collection of experimental data, choosing a proper model that fits the data, and testing the adequacy of the fitted model (Bayramov et al., 2004). A response surface is the graph of system response as a function of one or more variables. These graphs analyze the effect and significance of each variable. The RSM has been used by several researchers to find optimum solutions in cement and concrete industry (Soares et al., 2002; Bayramov et al., 2004; Grabiec and Piasta, 2004; Duprat and Sellier, 2006).

The main aim of this chapter is to provide the optimization by maximizing the characteristic length (l_{ch}), splitting tensile strength (f_{st}), compressive strength (f_c), fracture energy (G_F) and the mitigation ratio of the autogenous deformation relative to the reference concrete. For this purpose, above mentioned statistical RSM, which combines statistical and mathematical methods of experiment design, regression analysis

and optimization to provide useful approaches to the problem development, improvement or optimization has been used.

A response surface can simultaneously represent two or more independent and one dependent variable (response) when the mathematical relationship between the variables is known, or can be assumed. In this analysis, the dependent responses are characteristic length (l_{ch}), splitting tensile strength (f_{st}), compressive strength (f_c), fracture energy (G_F) and autogenous deformation. Two factors (or independent x_k design variables) that can be selected to describe this system are average size fraction ($x_1=d_{avr}$), and volume fraction ($x_2=V_f$) of LWAs. The chosen ranges are as follows:

$$\begin{aligned} 3\text{ mm} \leq x_1(d_{avr}) &\leq 6\text{ mm} \\ 6.5\% \leq x_2(V_f) &\leq 19.5\% \end{aligned} \quad (8.1)$$

In this chapter, the volume of LWAs is considered to be represented by the ratio of volume of total LWAs content to the total volume of concretes. In the designation codes of concretes, the ratio of volume of LWAs to the total aggregate content has been used. Thus, it should be noted that the value of LWAs volume of 6.5% is equal to the 10% replacement value which is the ratio of LWAs to the total aggregate content.

A quadratic model for each response has been established. The quadratic model for two independent variables, which has 6 coefficients that are b_0 , b_1 , b_2 , b_3 , b_4 , and b_5 , is shown below:

$$y = b_0 + b_1(\text{volume}) + b_2(\text{size}) + b_3(\text{volume})^2 + b_4(\text{size})^2 + b_5(\text{volume}) * (\text{size}) \quad (8.2)$$

8.3 Regression Analysis

Each response of concretes is analyzed individually by examining summary plots of the data, fitting a quadratic model using ANOVA, validating the model by examining the residuals for trends and outliers, and interpreting the model graphically. The quadratic

model can be simplified using a backward stepwise technique to ignore the insignificant terms if necessary (Bayramov et al., 2004).

Thus, six experimental data were fitted to a polynomial type of mathematical model by adjusting parameters until calculated values were in close agreement with the experimental values. Model fitting results for each response are shown in Table 8.1.

Table 8.1: Model fitting results for each response.

Responses	coefficients						correlation coefficient
	b ₀	b ₁	b ₂	b ₃	b ₄	b ₅	r
f _c	93	-2.77	1.69	-0.006	-0.69	0.23	0.9967
E	46	1.15	-5.14	-0.05	0.70	-0.123	0.9953
G _F	85	1.66	8.61	-0.14	-1.61	-	0.9998
l _{ch}	86	22.77	-44.33	-0.72	5.44	-0.82	0.9389
f _{st}	6.7	-0.33	0.75	0.007	-0.11	0.0077	0.9780
f _{net}	8.6	-0.38	0.46	0.002	-0.12	0.036	0.9937
autogenous def. at 28 days	0	1.08	8.05	0.2			0.9993

For example the fitted regression model for fracture energy (G_F in N/m) is as follows

$$G_F = 85 + 1.61 * (volume) + 8.61 * (size) - 0.14 * (volume)^2 - 1.61 * (size)^2$$

In this case (volume), (size), (volume)², (size)², are the significant terms. Since the LWAs were added to the reference concrete to mitigate autogenous deformation of this concrete, the effects of CREF series were taken into account in fitting analysis. It is obvious that the b₀ terms of each response belong to the experimental results of reference concrete. The comparison between the results obtained from both regression models and experiments are given in Table 8.2.

Table 8.2: The results of experimental and model fitting of each concrete.

		f_c	E	G_F	l_{ch}	f_{st}	f_{net}	Mitigation ratio of autogenous def
CV10L24	experimental	79	40	101	98	6.4	7.1	24
	fitted	78	40	101	103.5	6.3	7.2	23.2
CV20L24	experimental	62	37	95	155	4.8	6	47
	fitted	64	39	95	144	5.1	5.8	48.7
CV30L24	experimental	50	32	77	118	4.6	4.4	92
	fitted	49	33	77	123.5	4.5	4.5	91.2
CV10L48	experimental	68	40	84	107	5.6	6.1	11
	fitted	69	41	84	101.5	5.7	6	11.8
CV20L48	experimental	61	37	77	115	5.0	5	32
	fitted	59	37	77	126	4.7	5.2	30.3
CV30L48	experimental	48	27	59	95	4.1	4.8	65
	fitted	49	29	59	89.5	4.2	4.7	65.8

Response surfaces of fracture energy, compressive strength, characteristic length, splitting tensile strength, modulus of elasticity, net bending strength, and the value of the mitigation ratio of autogenous deformation at 28 days are given in Figure 8.1 to 8.7, respectively.

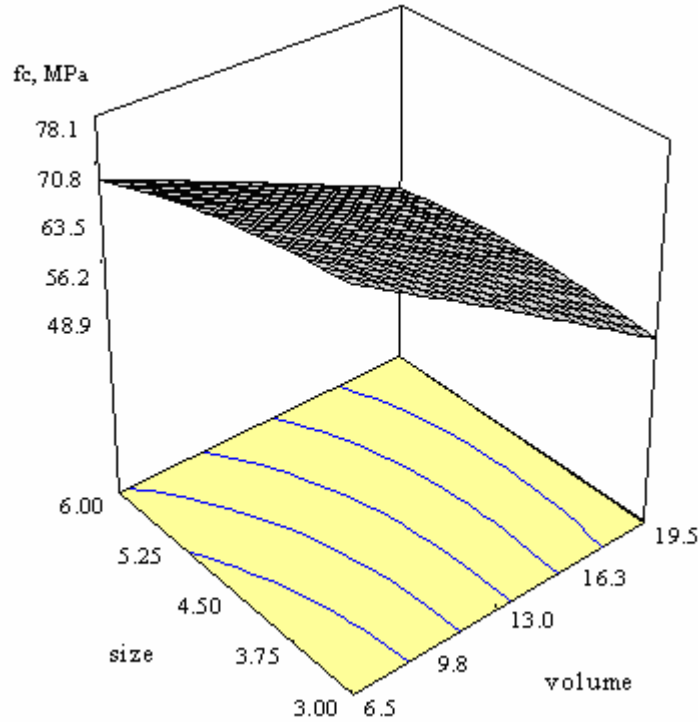


Figure 8.1: The variation of compressive strength f_c with volume and size of LWAs.

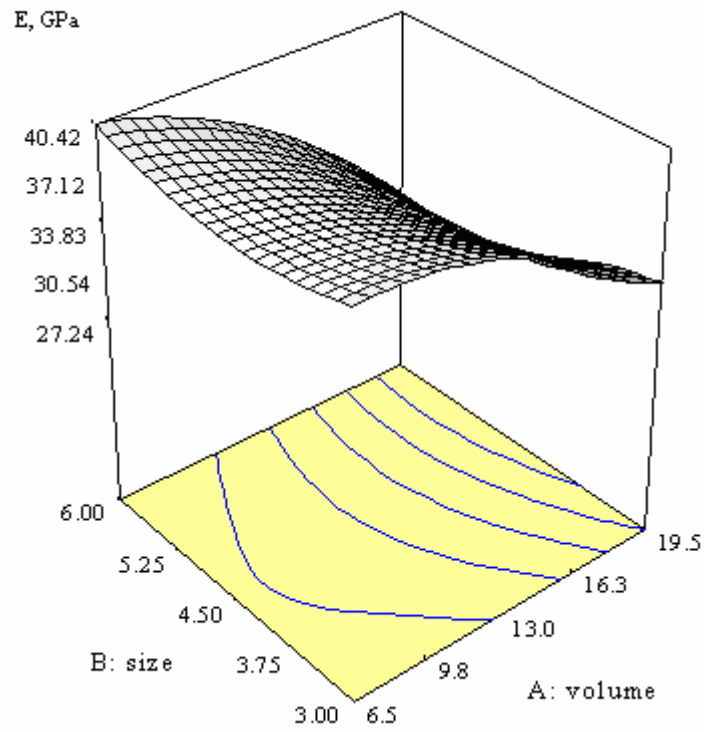


Figure 8.2: The variation of modulus of elasticity E with volume and size of LWAs.

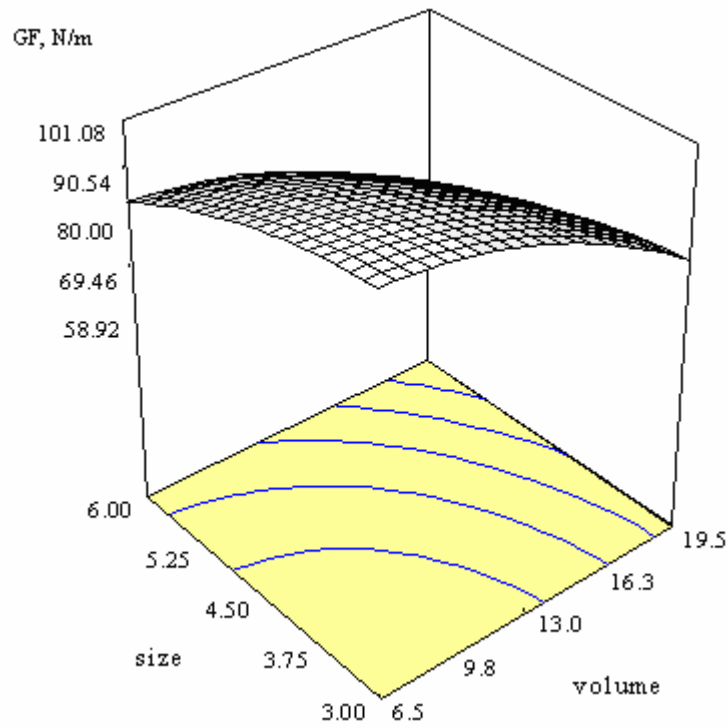


Figure 8.3: The variation of fracture energy G_F with volume and size of LWAs.

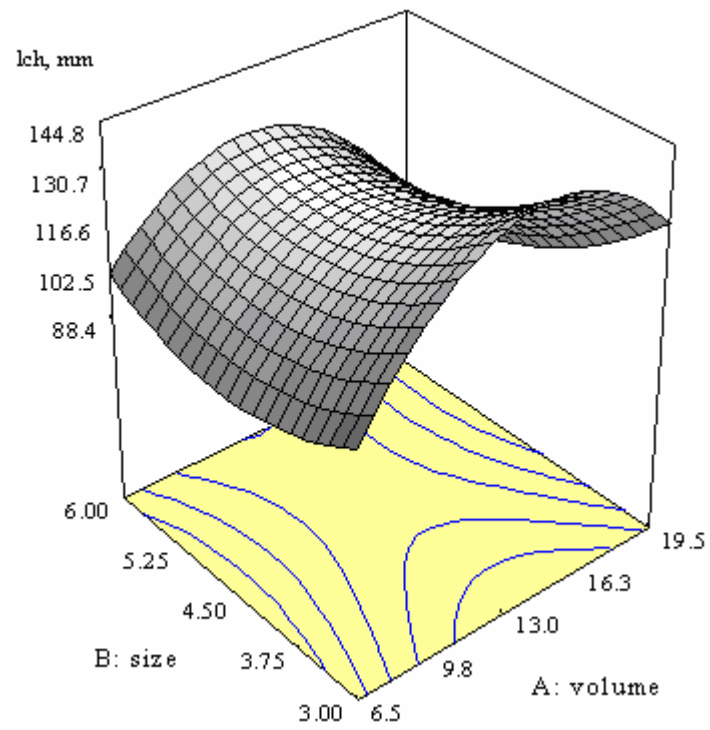


Figure 8.4: The variation of characteristic length l_{ch} with volume and size of LWAs.

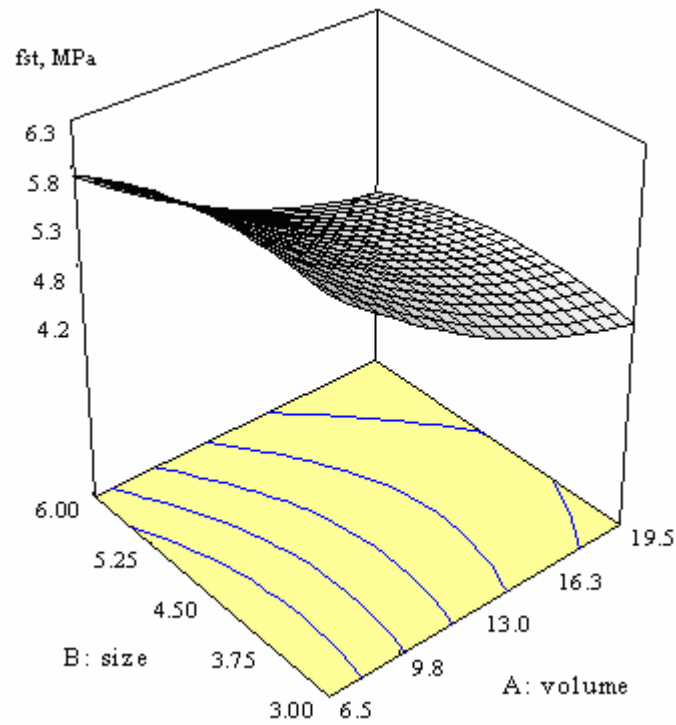


Figure 8.5: The variation of splitting tensile strength f_{st} with volume and size of LWAs.

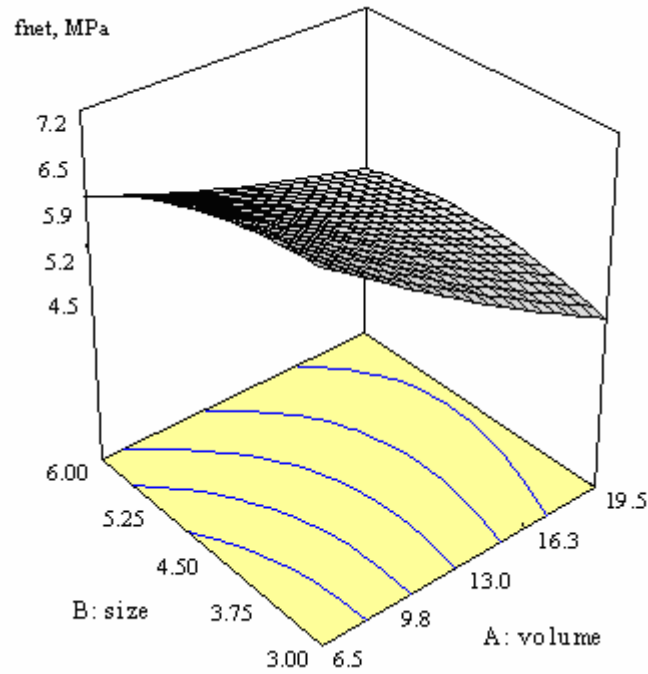


Figure 8.6: The variation of net bending strength f_{net} with volume and size of LWAs.

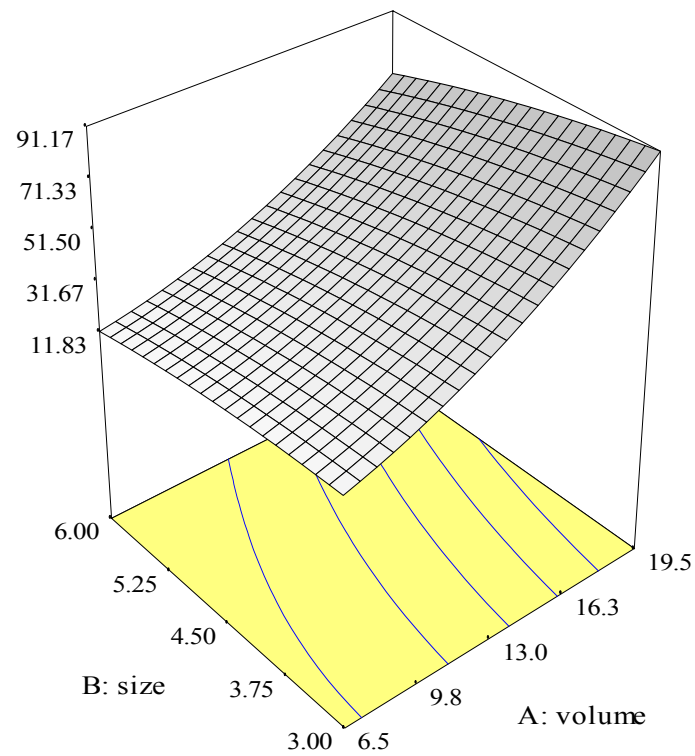


Figure 8.7: The variation of the value of the mitigation ratio of autogenous deformation according to the CREF series at 28 days of age with volume and size of LWAs.

8.4 Optimization

Optimization naturally requires simultaneous assessment of several responses. Thus, in order to optimize the objective functions, the regression model and relationships between mix design variables and the responses are established (Table 8.2). Simultaneous and independent variations between all independent variables are assorted. The objective of optimization is to find the “best settings” that maximize a particular response or responses. A numerical optimization technique using desirability functions (d_j), which are defined for each response, can be used to optimize the responses simultaneously (Derringer and Suich, 1980). A desirability function (d_j) varies over the range of $0 \leq d_j \leq 1$ and each response can be mapped onto the function. By using the single composite response (D) given in Eq.(8.3), which is the geometric mean of the individual desirability functions, the multiobjective optimization problem is solved. D is maximized over the feasible region of the design variables given in Eq. (8.1) (Myers and Montgomery, 2002):

$$D = (d_1 \times d_2 \times d_3 \times \dots \times d_n)^{\frac{1}{n}} \quad (8.3)$$

where n is the number of responses included in the optimization. If any of the responses or factors fall outside their desirability range, the overall function becomes zero. In cases of the maximizing and minimizing of individual responses, the desirability will be defined by the formulas given in Eqs. (8.4) and (8.5), respectively.

$$d_j = \begin{cases} 0 & Y_j \leq \min f_j \\ \left[\frac{Y_j - \min f_j}{\max f_j - \min f_j} \right]^{wt_j} & \text{and } 0 < d_j < 1, \min f_j < Y_j < \max f_j \\ 1 & Y_j \geq \max f_j \end{cases} \quad (8.4)$$

$$d_j = \begin{cases} 1 & Y_j \leq \min f_j \\ \left[\frac{\max f_j - Y_j}{\max f_j - \min f_j} \right]^{wt_j} & \text{and } 0 < d_j < 1, \min f_j < Y_j < \max f_j \\ 0 & Y_j \geq \max f_j \end{cases} \quad (8.5)$$

where d_j , Y_j , $\min f_j$ and $\max f_j$ are the desirability function, the fitted value, and minimum and maximum actual (experimental) values of j_{th} response included in the optimization, respectively. The power value wt_j is weighting factor of the j_{th} response. In this work, for optimization, a commercially available Design-Expert software package was used.

Three different optimizations were conducted such as: i) Concrete with higher strength and minimum autogenous deformation; ii) The less brittle concrete with minimum autogenous deformation; and iii) Concrete with minimum autogenous deformation, maximum strength and less brittleness.

- i) To attain higher strength concrete with a minimum autogenous deformation, a concrete with the highest compressive strength (f_c) and the maximum mitigation ratio of autogenous deformation should be obtained. Thus, these two responses are considered to be of equal importance, i.e. $wt_j=1$ and maximized simultaneously. The solution of this multiobjective optimization is shown in Figure 8.8. The figure shows that, the optimal values of design variables are as follows; volume:12.9% and size:3.0 mm. The predicted response values and associated uncertainties (at 95% confidence level) are as follows; the compressive strength (f_c)=61.5 MPa, and the mitigation ratio of autogenous deformation=48.2%. The solution indicates that the addition of LWAs in concrete has a decreasing effect on the mechanical properties of concrete. In addition, this effect can be minimized by using fine LWAs.

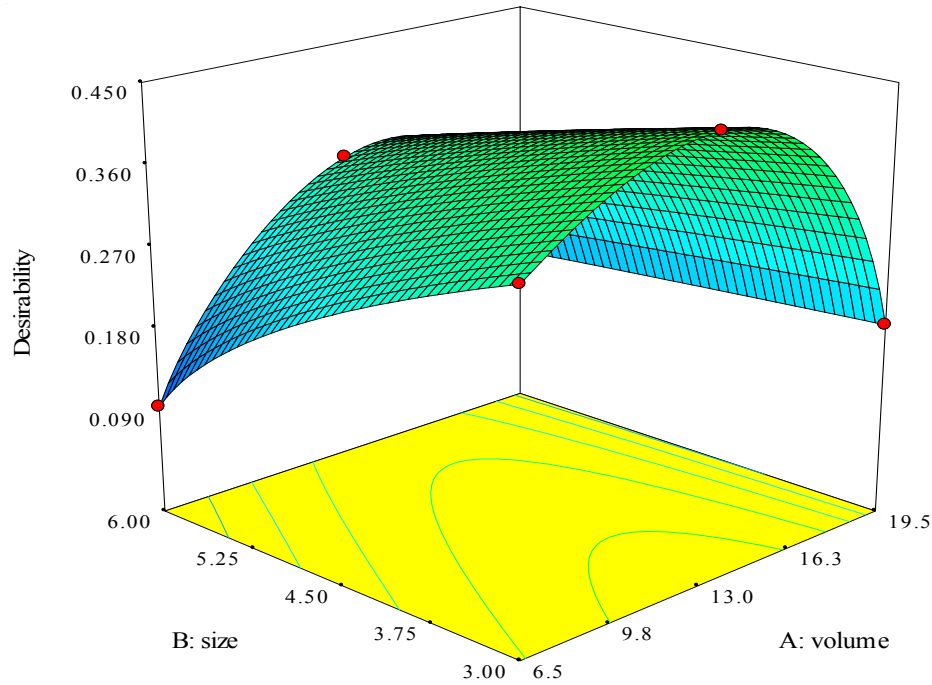


Figure 8.8: Response surface plot of the composite desirability (D) when the mitigation ratio of autogenous deformation and f_c are maximized simultaneously.

- ii) To attain less brittle concrete, a concrete with the highest characteristic length (l_{ch}), the highest splitting tensile strength (f_{st}), the highest net bending strength (f_{net}), and the maximum mitigation ratio of autogenous deformation should be obtained. The three responses l_{ch} , f_{net} and f_{st} are considered to be of equal importance, i.e. $wt_j=1$, while the response of the mitigation ratio of autogenous deformation according to the CREF series is considered to be of greater importance of $wt_j=2$. The solution of this multiobjective optimization is shown in Figure 8.9. The figure shows that the optimal values of design variables are as follows; volume:13.3% and size:3 mm. The predicted response values and associated uncertainties (at 95% confidence level) are as follows; the mitigation ratio of autogenous deformation=50.4%, $l_{ch}=115$ mm, $f_{st}=5.0$ MPa, and $f_{net}=5.6$ MPa. It is also concluded from the above two optimization that while the addition of LWAs has a negative effect on compressive strength, the fracture properties can be enhanced by addition of fine LWAs.

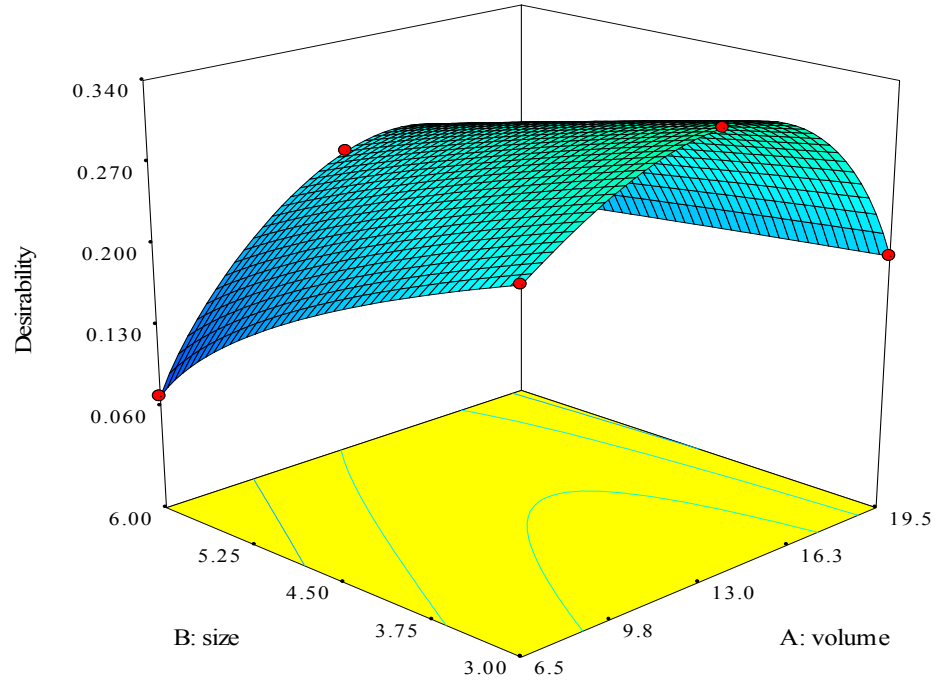
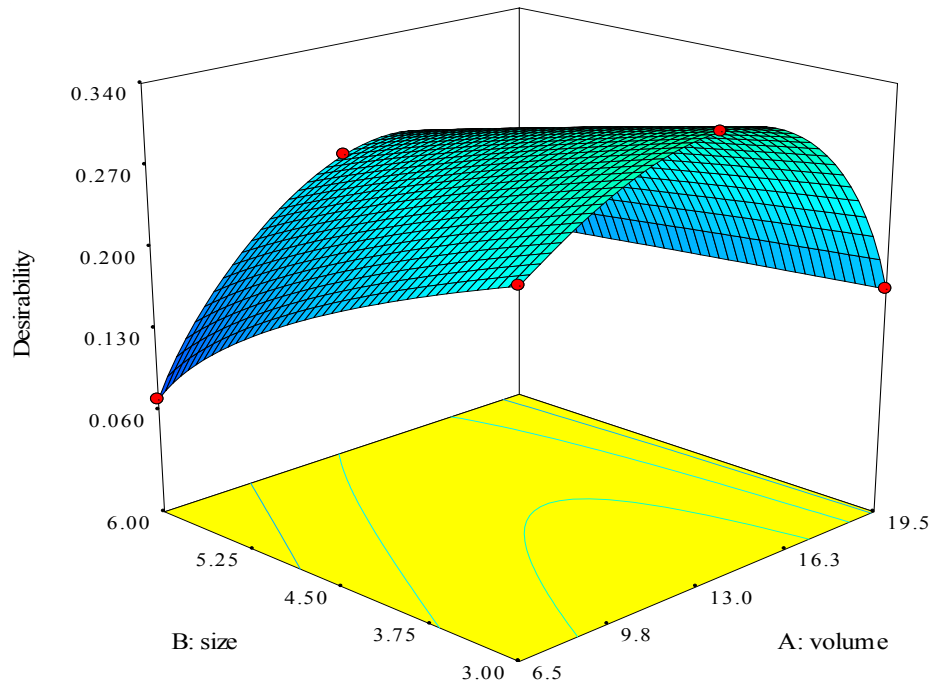
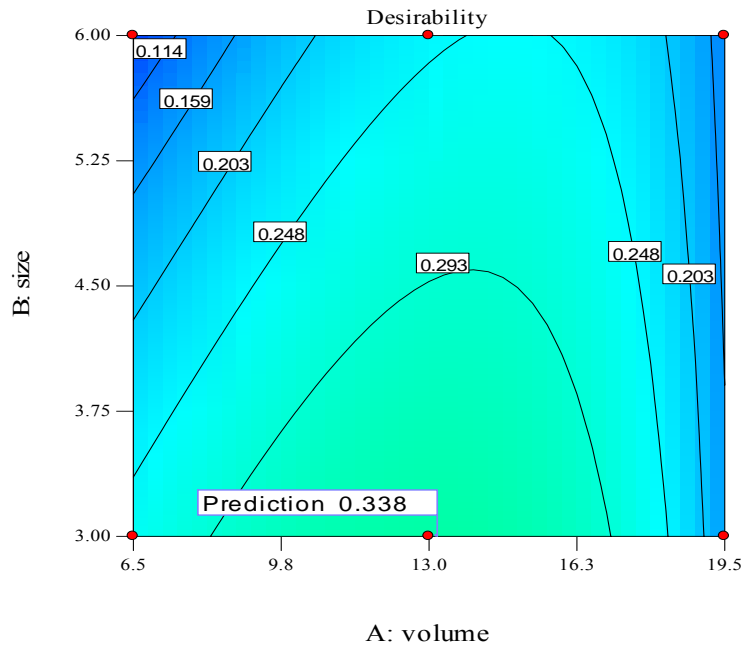


Figure 8.9: Response surface plot of the composite desirability (D) when l_{ch} , f_{st} , and f_{net} are maximized simultaneously.

iii) One of the purposes of this thesis is to find out the necessary volume and size of LWAs to prevent the autogenous deformation of concretes. On the other hand, it is equally important to save and also enhance the mechanical and fracture properties of concretes. Thus, third optimization conducted to attain a concrete with minimum autogenous deformation, maximum strength and less brittleness, a concrete with the minimum autogenous deformation, maximum characteristic length (l_{ch}), the maximum splitting tensile strength (f_{st}), and also the maximum compressive strength (f_c) should be obtained. The three responses l_{ch} , f_c and f_{st} are considered to be of equal importance, i.e. $wt_j=1$, while the response of the mitigation ratio of autogenous deformation is considered to be of greater importance of $wt_j=2$. The solution of this multiobjective optimization is shown in Figure 8.10. The figure shows that the optimal values of design variables are as follows; volume:13.1% and size:3 mm. The predicted response values and associated uncertainties (at 95% confidence level) are as follows; the mitigation ratio of autogenous deformation =49.4%, l_{ch} =115 mm, f_{st} =5.1 MPa, and f_c =61.1 MPa.



(a)



(b)

Figure 8.10: (a) Response surface and contour plot of the composite desirability (D) when the mitigation ratio of autogenous deformation, l_{ch} , f_{st} , and f_c are maximized simultaneously.

In above optimization the response values of CREF reference concrete have been ignored because of the ranges given in Eq(8.1), although in quadratic fitting model they

have been taken into account. In the first situation, effect of LWAs on toughening mechanism has also been discarded. For example, the characteristic length of CV10L24 series is significantly higher than that of CREF series. If the CREF is included as a design point, it is obvious that the area of $0 < d_{avr} < 3$ and $0 < \text{volume} < 6.5$ will be included in optimization. However, CREF has been inserted in the design layout as a design point. In this situation, the optimal values of design variables have been found as; volume:17% and size:2.2 mm. The predicted response values and associated uncertainties (at 95% confidence level) are; mitigation ratio of autogenous deformation =49.5%, l_{ch} =117 mm, f_{st} =5.4 MPa, and f_c =67.4 MPa.

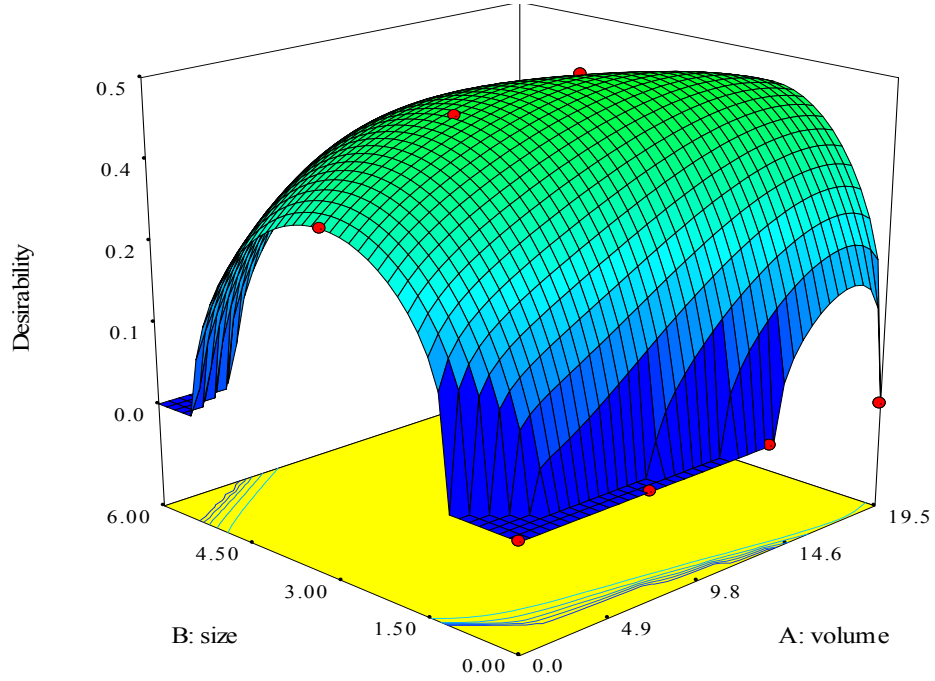


Figure 8.11: Response surface plot of the composite desirability (D) when mitigation of autogenous deformation (with $w_{tj} = 2$), l_{ch} , f_{st} , and f_c are maximized simultaneously.

Since the prevention of autogenous deformation is being more important for the high strength and high performance concrete, the response of autogenous deformation is considered to be at the maximum importance of $w_{tj} = 10$ and the optimization was repeated. The solution of this multiobjective optimization is shown in Figure 8.12. The

figure shows that, the optimal values of design variables are; volume:17.3% and size:3.13 mm. The predicted response values and associated uncertainties at 95% confidence level are; mitigation ratio of autogenous deformation =79.6%, l_{ch} =116 mm, f_{st} =4.84 MPa and, f_c =57.9 MPa

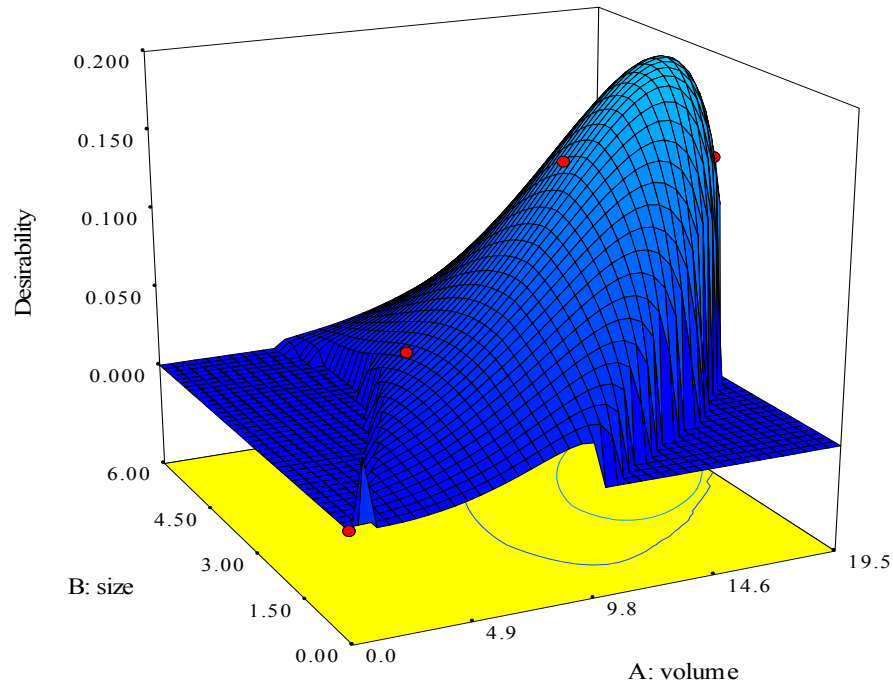


Figure 8.12: Response surface plot of the composite desirability (D) when autogenous deformation is minimum (with $w_{tj} = 10$), l_{ch} , f_{st} , and f_c are maximized simultaneously.

8.5 Conclusions

Response surface method is a promising approach for optimizing concrete with LWAs to meet several performance criteria such as maximum strength, minimum brittleness, and minimum autogenous deformation. In order to provide an adequate representation of the responses, fitting quadratic models that are usually assumed to represent each concrete property of interest, can be applied in identifying optimal mixes. The conclusion can be summarized as follows.

1. The results show that the predictiveness of the polynomial regression model is satisfactory. For each response, the value of r of regression model has been found greater than 0.93. It has also been shown that the values obtained from model calculations are very close to those obtained from experiments.
2. The volume of LWAs has been found more effective on compressive strength of concrete than the size of LWAs. As the volume and size of the LWAs increased the compressive strength decreased.
3. The effect of size of LWAs on modulus of elasticity of concrete was found insignificant. On the other hand, with increasing the volume of LWA, the modulus of elasticity decreased slightly.
4. The size of LWAs has been found to be more effective on the splitting tensile strength of concrete comparing to the volume of LWAs.
5. The low volume of LWAs increased the fracture energy, while further addition decreased. The size of LWAs has been found more effective than its volume on fracture energy of concrete.
6. As being the indicator of toughness, the characteristic length behaves different from other parameters. The model established shows that there is a certain maximum point for characteristic length of concrete, and both the size and volume of LWAs have significant effect on it. The ductility first increased with the volume of LWAs and then decreased. It can be roughly said that as the size of LWAs decreased the characteristic length increased, since the toughening mechanism will change with the variation in volume and size of LWAs. While the 10% replacement of total aggregate content by coarse aggregate resulted in higher ductility comparing to replacement by fine aggregate, for the 20% replacement the concrete with fine LWAs behaves more ductile than that with coarse LWAs. Thus, it can be said that the usage of LWAs should be carefully optimized considering the toughness of concrete.
7. The volume and size of LWAs have been found to have similar effects on both splitting tensile strength and net bending strength. When the volume of LWAs

increased strength of concrete decreased. The use of finer LWAs resulted in higher strength than coarse aggregate.

8. The model shows that the autogenous deformation decreased with increasing volume and decreasing size of LWAs. The size of LWAs has been found more effective than the volume of LWAs on preventing autogenous deformation of concrete.
9. It has been shown that the possible optimum solutions for desired mechanical, fracture properties, and also the value of autogenous deformation of concretes can be obtained using the variable size and volume of LWAs.
10. The experimental design assigned using RSM provides a thorough examination of properties over the selected range of volume and size of LWAs.
11. The multi-objective simultaneous optimization analysis, which considers also the desirability function (d_j), has been proven to be a good approach to obtain maximum strength, maximum ductility, and minimum autogenous deformation.
12. It is shown that the autogenous deformation of concretes can be prevented by using LWAs; it is also possible to increase the fracture properties of concretes while reducing their mechanical properties. The optimization was made with two different importance factor of autogenous deformation. Initially, the three responses l_{ch} , f_c , and f_{st} , are considered to be of equal importance, i.e. $wt_j=1$, while the response of autogenous deformation is considered to be importance of $wt_j=2$. The solution of this multiobjective optimization showed that the optimal values of design variables are; volume:12.3% and size:3 mm.
13. Since the prevention of autogenous deformation is important for high strength and high performance concrete, the response of autogenous deformation is considered to be at the highest importance of $wt_j=10$. The solution showed that the optimal values of design variables are; volume:17.3% and size:3.13 mm, when the series of CREF has been inserted in the design layout as a design point.
14. After analyzing the data obtained from the experiments, a decision might be made to perform another experimental program to obtain the desired responses.

As a further study, a wider range of variables can be used, and the concretes with different water to cement ratios can be investigated by using optimization based mixture design.

9 CONCLUSIONS

In this chapter, a general summary of the results documented in previous chapters will be presented.

Autogenous deformation

- It is shown that the linear and volumetric autogenous deformation of cementitious materials can reach significant values in a couple of days after production. The great proportion of volumetric autogenous deformation for PREF sample (reference cement paste used in this study) has been completed before 24 hours of age. Within the first few hours the volumetric autogenous deformation is increased with a gradually decreasing rate, after 9 hours, the slope of deformation begins to increase. After this point, the hydration products with lower specific volumes begin to form, and the rate of autogenous deformation begins to decrease.
- The volumetric autogenous deformation increases with increasing the cement content, while an increase in aggregate content (especially coarser ones) restrains the deformation of cement paste.
- The results show that the fine lightweight aggregates (LWAs) are more effective than the coarse LWAs in reducing the autogenous deformation of cement based materials. It has been indicated that the capability of LWAs in mitigating autogenous deformation decreased with time due to the enhancing impermeable character of cement paste. This is because the pores through which the LWAs transport water are getting smaller as the hydration products continue to form.

Chemical shrinkage and temperature development in semi-adiabatic condition

- The most important part of the chemical shrinkage is completed in 24 hours after the addition of water. It was shown that at early ages the main driving mechanism of autogenous deformation is chemical shrinkage. The linear relationship between the autogenous deformation and chemical shrinkage has been corrupted at about 11 hours after addition of water. Beyond this point, no relationship between the autogenous deformation and chemical shrinkage was observed.
- The maximum temperatures of mortars decreased with increasing volume content of LWAs. In addition, the time to reach the maximum temperature was getting longer with increasing LWA content.

Heat of hydration

- The heat of hydration tests were conducted on cement paste, fine mortar and coarse mortar samples. The heat of hydration of PREF samples were found smaller than those of FMREF (reference fine mortar) and MREF (reference coarse mortar) samples at early ages, while the trends changed reversely at later ages.
- As the amount of LWAs increased, the heat of hydration also increased slightly. The cement particles can easily find water to hydrate from LWAs, and consequently the degree of hydrated increased due to internal curing.

Non-evaporable water content and degree of hydration

- The results show that at early ages the rate of hydration reaction for the MREF sample is greater than those of mortars with LWAs. Using LWAs causes a delay in the time to reach approximately the asymptotic value of the non evaporable water content. This is probably due to the fact that with higher degree of hydration the products will be larger in size and the diffusion of water through the denser C-S-H products will take little more time. The amount of hydrated cement particles increased with increasing LWA content.

Mercury intrusion porosimetry (MIP)

- The critical pore diameters of PREF sample were found larger than those of FMREF and MREF samples at the age of one day, but smaller at later ages. It is found that the cement paste in fine mortar and coarse mortar were more porous than the PREF sample.
- The results show that the addition of aggregate to the cement paste caused a decrease in the total intruded mercury volume because of the diminishing content of cement paste. On the other hand, substituting the normal aggregate by LWAs increased the total intruded mercury volume. Using LWAs decreased the critical pore diameter significantly compared to the reference mortar, especially at later ages.

Pore size distribution

- In order to determine the distribution of pores, the normalized porosity was calculated from the cumulative intruded mercury curves. It was found that the amount of very fine pores (<10 nm) of PREF sample increased with time, while the volume of capillary pores decreased. The partial 10-100 nm porosity of PREF sample at the age of one day was found much greater comparing to those at later ages and in other pore width ranges.
- It was shown that the addition of aggregates had no significant effect on the amount of pores greater than 200 nm. At the capillary pore width range of 100-200 nm, the porosity of the MREF sample was found smaller than that of FMREF finer mortar. The bond of interfacial transition zone between cement paste and quartz sand is weaker than that with the limestone which results in more porous microstructure.
- The major contribution of using LWAs was observed at the large capillaries. The amount of large capillaries decreased with increasing LWA content, while very fine pore volume increased at the age of 28 days and 100 days. It is indicated that the hydrated cement ratio and the amount of gel pores increased by means of internal curing.

- With the decreasing amount of LWA content the volume ratio of fine (10-100 nm) capillaries increased due to self desiccation. The pore structure of mortars smaller than 200 nm became even finer with increasing LWA content, which means that the internal curing provided an enhancement in the hydration kinetics.

Mechanical properties

- It was shown that the addition of aggregate to the cement paste had an initial effect of decreasing the compressive, bending, and splitting tensile strengths.
- Since the stiffness of LWA is lower than that of normal aggregate, a significant reduction in compressive strength for mortars and concretes with LWAs was observed with respect to the reference mortar. In addition, the compressive strength of mortars and concretes with LWAs decreased with increasing the particle size and volume of the substituted LWA. A slight decrease in the modulus of elasticity was recorded with increasing the replacement volume of the LWAs, although the change in the size of LWA had no significant effect on the modulus of elasticity of mortars and concretes. The size and volume concentration of LWAs had effects on bending and splitting tensile strengths in a way similar to that observed on the compressive strength results. The effect of the size of LWA on bending and compression has been modeled. It can be concluded that LWAs in concrete behave as defects.
- The use of fine LWA to prevent autogenous deformation of mortar and concrete was found more effective in terms of the mechanical properties of concrete.

Fracture properties

- The addition of aggregate in cement paste phase increased the area under the load-displacement curve. It was found that the area under the curve increased about 3.5 times with respect to the PREF sample when the aggregate concentration is $0.65 \text{ m}^3/\text{m}^3$. The main reason for this substantial increase in the fracture energy of concrete with increasing aggregate volume concentration is that the microcracks at the fracture process zone decrease the stress concentration. The more microcracks result in more fracture energy.

- The most fundamental effect of using LWAs was observed to have occurred on both the fracture energy and the characteristic length of concretes. In cases of using both fine and coarse fractions, the area under the load vs. displacement curve increased with increasing the replacement volume of LWA, although the peak load decreased with especially the use of fine LWA. Because the LWAs produce more microcracks, the concrete containing these aggregates behaves more ductile (i.e. less brittle) than the reference concrete. The fracture energy decreased with increasing volume of the LWAs while the displacement at peak load decreased with increasing content of LWA.
- The final displacement increased significantly with the replacement volume of LWA. On the other hand, for mortar phases, the values of final displacement midspan did not change significantly with increasing replacement ratio of LWAs because the final displacement at midspan is governed by the maximum aggregate size.
- The use of LWAs in concrete had an effect of increasing the characteristic length of the material in all size and volume fraction of LWAs. The characteristic length of both mortars and concretes with LWA were found higher than that of without LWAs. The decrease in the brittleness was more significant in concretes with fine LWAs.

Effect of size and type of aggregates

- The experiments were performed on five different composites with different type of aggregates. The composites contain 70% volume of paste and 30% volume of aggregate. The size of normal aggregates has no significant effect on autogenous deformation at 28 days. At early ages, the finer NWAs (0-2 mm) mitigated the autogenous deformation of cement paste efficiently, because the modulus of elasticity of cement paste was not too high. On the other hand, addition of coarser size aggregate easily restrained the shrinkage of cement paste at later ages.

- The fine size of LWAs, as expected, was found to be more effective in mitigating the autogenous deformation of cement paste compared to coarse LWAs. It has been shown that the LWAs reduce the autogenous deformation by releasing water to the media.
- The addition of LWAs to paste phases increased the degree of hydration, especially at early ages. Although it is expected that the use of fine LWAs causes the water reservoirs to distribute in proximity and results in better internal curing, the degree of hydration of cement paste with coarser LWAs was found greater than that with finer LWAs.
- While the compressive strength of composites slightly increase with increasing size of normal aggregate, the size of LWAs has no significant effect on compressive strength. Also, the modulus of elasticity was not affected significantly by the size of aggregates (both NWA and LWA).
- The effect of size on the bending and splitting tensile strengths of composites has been found insignificant for both normal weight and lightweight aggregates.
- The addition of fine sand aggregate at size fraction of 0-2 mm increased the characteristic length significantly compared to the reference paste. The characteristic lengths of composites with 2-4 and 4-8 mm aggregate were found slightly smaller than that of fine sand with 0-2 mm.
- The addition of LWAs increased the characteristic length of cement paste. The fracture energies of cement paste with LWAs were found lower than that of reference cement paste.

Modeling of modulus of elasticity

- Although the meso-mechanical modeling have been applied by not considering the size of aggregate, the results demonstrate that the modulus of elasticity values for composites with both NWA and LWAs can be successfully predicted by meso-mechanical modeling.

Modeling of autogenous deformation based on its mechanism

- The self-desiccation shrinkage of cement paste was determined by the known degree of hydration and capillary pore radius of cement paste. If the self-desiccation shrinkage is accepted as a great portion of autogenous deformation, the autogenous deformation of concrete (or composites) has been precisely determined according to the volume and elastic properties of aggregates. It was also demonstrated that using the modulus of elasticity, obtained from the meso-mechanical modeling, provides satisfactory predictions in calculating the autogenous deformation for both cement paste and concrete.

Distribution of LWAs and image analysis

- The distribution of LWAs was found to be effective on both the magnitude of autogenous deformation and fracture properties of concrete.
- The distance between the nearest neighbors for coarse LWAs was found shorter than that for finer LWAs for the replacement ratio of 10%, and this can explain why the characteristic length of the CV10L48 sample (107 mm) was found greater than that of the CV10L24 sample (98 mm). The well distribution of LWAs for the CV10L48 series was found to be effective on its fracture properties, especially the characteristic length.
- The 95th percentile of the nearest neighbor LWA-LWA proximity distribution was found to be in close agreement with the magnitude of autogenous deformation of concretes and mortars at 28 days of age. Since the LWA-LWA proximity is affected by both size and volume, the variation of autogenous deformation results has been easily correlated with this proximity.
- The comparison between the mitigation ratios of autogenous deformation of concrete series (relative to the reference concrete at 28 days) and the protected paste volume calculated for the 1 mm of water flow gives satisfactory results. Thus, the results indicate that the protected paste volume in internal curing can be determined by image analysis.

Optimum design of concretes

- It has been shown that mitigation ratio of autogenous deformation according to the reference concrete, the mechanical, and fracture properties of concretes with LWAs can be correctly predicted using quadratic regression models and Response Surface Method (RSM) in the ranges chosen.
- The possible optimum solutions for desired mechanical and fracture properties and also the value of autogenous deformation of concretes can be obtained by using the variable size and volume of LWAs. The experimental design assigned using quadratic regression models and Response Surface Method (RSM) provides a thorough examination of properties over the selected range of volume and size of LWAs ($3\text{ mm} \leq x_1(d_{avr}) \leq 6\text{ mm}$ and $6.5\% \leq x_2(V) \leq 19.5\%$).
- The optimization was made with two different importance factor of autogenous deformation. Initially, the three responses l_{ch} , f_c and f_{st} are considered to be of equal importance, i.e. $wt_j = 1$, while the response of autogenous deformation is considered to be importance of $wt_j = 2$. The solution of this multiobjective optimization showed that the optimal values of design variables are as follows; volume: 13.1 % and size: 3.0 mm.
- Since the prevention of autogenous deformation is more important for the high strength and high performance concrete, the response of autogenous deformation is considered to be at the highest importance of $wt_j = 10$. The solution showed that the optimal values of design variables are; volume: 17.3% and size: 3.13 mm, when the series of CREF was inserted in the design layout as a design point.

REFERENCES

- Abdalla, H.M. and Karihaloo, B.L.**, 2003. Determination of size-independent specific fracture energy of concrete from three-point bend and wedge splitting tests, *Magazine of Concrete Research*, **55**, 133-141.
- Ai, H.**, 2000. Investigation of the dimensional stability in DSP cement paste, *PhD Thesis*, University of Illinois at Urbana-Champaign, Urbana, Illinois, USA.
- Aitcin, P.C.**, 1999. Autogenous shrinkage measurement, in *Proceedings of International Workshop Autoshrink'98*, Ed. Tazawa, E-I., Hiroshima, Japan, E&FN SPON, London, 13-14 June, 257-268.
- Akcay, B. and Tasdemir, M.A.**, 2006a. Effects of Lightweight Aggregates on Autogenous Deformation in Concrete, *plenary lecture in 16th European Conference of Fracture (ECF16), Measuring, Monitoring, and Modeling Concrete Properties: MMMCP in Honor of Surendra P. Shah*, Eds. Konsta-Gdoutos, Greece, 3-7 July, 163-170.
- Akcay, B. and Tasdemir, M.A.**, 2006b. Influence of lightweight aggregates on internal curing and fracture of concrete, *Proceedings of the International RILEM Conference, Volume Changes of Hardening Concrete: Testing and Mitigation*, Eds. Jensen, Lura, and Kovler, Lyngby, Denmark, PRO 52, 20-23 August, 31-40.
- Akcay, B., Agar, A.S., Bayramov, F., Atahan, H.N., Sengul, C. and Tasdemir, M.A.**, submitted, Modeling of the size-independent specific fracture energy of concrete, *ACI Materials Journal*.
- Akcay, B., Pekmezci, B.Y. and Tasdemir, M.A.**, 2005. Utilization of artificial lightweight aggregates in hardened cement paste for internal water curing, *Proc. of fib Keep Concrete Attractive*, Budapest, 23-25 May, Eds., Balazs and Borosnyoi, 1, pp 374-380.
- Alaee, F.J.**, 2002. Retrofitting of concrete structures using high performance fibre reinforced cementitious composite, *PhD Thesis*, Department of Civil Engineering, Cardiff University, Cardiff.
- Alberty, R.A. and Daniels, F.**, 1980. Physical Chemistry, John Wiley & Sons, New York.
- Aldikacti, K.V., Sengul, C., Akcay, B. and Tasdemir, C.**, 2005. Meso-mechanical modeling of concrete as a composite material, in *6th National Concrete Congress, High Performance Concrete*, Istanbul, Turkey, 16-18 November 2005, pp. 257-271 (in Turkish with English summary).

- Arisoy, B.**, 2002. Development and fracture evaluation of high performance fiber reinforced lightweight concrete, *PhD Thesis*, Wayne State University, Detroit, Michigan.
- ASTM C186**, 1998. Standard Test Method for Heat of Hydration of Hydraulic Cement.
- ASTM C330**, 2005. Standard Specification for Lightweight Aggregates for Structural Concrete.
- ASTM C457**, 1998. Standard test method for microscopical determination of parameters of the air-void system in hardened concrete.
- Atahan, H.N.**, 2002. Sensitivity of properties to pore structure of cement paste of concretes with low water - cement ratio, *PhD Thesis*, Istanbul Technical University, Turkey (in Turkish with English summary).
- Attiogbe, E.K.**, 1993. Mean spacing of air voids in hardened concrete, *ACI Materials Journal*, **90**, 174-181.
- Attiogbe, E.K.**, 1996. Predicting freeze-thaw durability of concrete-A new approach, *ACI Materials Journal*, **93**, 457-464.
- Bache, H. and Nepper-Christansen, P.**, 1965. Observations on strength and fracture in lightweight and ordinary concrete-the structure of concrete and it's behaviour under load. *Proc., Int. Conf. on the Struct. of Concrete, Cement and Concrete Assoc.*, London, pp. 1-16.
- Barcelo, L., Boivin, S., Rigaud, S., Acker, P., Clavaud, B. and Boulay, C.**, 1999. Linear vs. volumetric autogenous shrinkage measurement: Material behaviour or experimental artifact?, *Self-Desiccation and Its Importance in Concrete Technology Proceedings of the 2nd International Research Seminar in Lund*, 18 June, 109-125.
- Barenblatt, G. I.**, 1959. The formation of equilibrium cracks during brittle fracture, *Journal of Applied Mathematics and Mechanics*, **23**, 622-636.
- Baroghel-Bouny, V.**, 1997. Experimental investigation of self-desiccation in high-performance materials-Comparison with drying behaviour, *Self-Desiccation and Its Importance in Concrete Technology Proceedings of an International Research Seminar in Lund*, 10 June, 72-87.
- Baroghel-Bounya, V., Mounanga, P., Khelidj, A., Loukili, A. and Rafai N.**, 2006. Autogenous deformations of cement pastes Part II. W/C effects, micro-macro correlations, and threshold values, *Cement and Concrete Research*, **36**, 123-136.
- Bayramov, F, Tasdemir, C. and Tasdemir, M.A.**, 2004. Optimisation of steel fibre reinforced concretes by means of statistical response surface method, *Cement and Concrete Research*, **26**, 665-675.
- Bayramov, F.**, 2004. Optimum Design of Cement-Based Composite Materials, *PhD Thesis*, Istanbul Technical University, Turkey (in Turkish with English summary).

- Bažant, Z. P. and Kazemi, M.T.**, 1990. Determination of fracture energy, process zone length and brittleness number from size effect, with application to rock and concrete, *International Journal of Fracture*, **44**, 111-131.
- Bažant, Z. P. and Oh, B. H.**, 1983. Crack band theory for fracture of concrete, *Materials and Structures* **16**, 155-157.
- Bažant, Z.P.**, 1984. Size Effect in Blunt Fracture- Concrete, Rock, Metal, *ASCE Engineering Mechanics*, **110**, 518-535.
- Beltzung, F. and Wittmann, F.H.**, 2002. Influence of cement composition on endogenous shrinkage, *Self-Desiccation and Its Importance in Concrete Technology Proceedings of the 3rd International Research Seminar in Lund*, 14-15 June, 113,126.
- Bendoudjema, F., Meftah, F. and Torrenti, J.M.**, 2001. Drying creep; An elasto-plastic damage approach of the structural effect, *Proc. Fourth Int. Conference on Fracture Mechanics of Concrete and Concrete Structures (Framcos)*, de Borst et al. (Eds), 1, Cachan, France, 28 May- 2 June, 169-168,
- Bentur, A., Igarashib, S-I. and Kovler, K.**, 2001. Prevention of autogenous shrinkage in high-strength concrete by internal curing using wet lightweight aggregates, *Cement Concrete Research*, **31**, 1587–1591.
- Bentz, D.P. and Garboczi, E.J.**, 1991. Percolation of phases in a three-dimensional cement paste microstructural model, *Cement and Concrete Research*, **21**, 325–344.
- Bentz, D.P. and Jensen, O.M.**, 2004. Mitigation strategies for autogenous shrinkage cracking, *Cement and Concrete Composites*, **26**, 677-685.
- Bentz, D.P. and Snyder, K.A.**, 1999. Protected paste volume in concrete extension to internal curing using saturated lightweight fine aggregate, *Cement and Concrete Research*, **29**, 1863–1867.
- Bentz, D.P. and Stutzman, P.E.**, 2006. Curing, hydration and microstructure of cement paste, *ACI Materials Journal*, **103(5)**, 348-356.
- Bentz, D.**, 2005a. Self-desiccation and its importance in concrete, *Proceedings of the 4th International Research Seminar*, Eds. Persson,B., Bentz, D. and Nilsson, L-O. Gaithersburg, Maryland, USA, June, 2005.
- Bentz, D.P.**, 2005b. Replacement of coarse cement particles by inert fillers in low w/c ratio concretes II. Experimental validation, *Cement and Concrete Research*, **35**, 185-188.
- Bentz, D.P.**, 2005c. Capitalizing on self-desiccation for autogenous distribution of chemical admixtures, *Self-Desiccation and Its Importance in Concrete Technology Proceedings of the 4th International Research Seminar in Lund*, June, 189-196.

- Bentz, D.P., Garbozci, E.J. and Quenard, D.A.,** 1998. Modeling drying shrinkage in reconstructed porous materials: Application to porous Vycor glass, *Model. Simul. Mater. Sci. Eng.* **6**, 211-236.
- Bentz, D.P., Geiker, M. and Jensen, O.M.,** 2002. On the mitigation of early age cracking. *Self-Desiccation and Its Importance in Concrete Technology Proceedings of the 3rd International Research Seminar in Lund*, 14-15 June, 195-204.
- Bentz, D.P., Geiker, M.R. and Hansen, K.K.,** 2001a. Shrinkage-reducing admixtures and early-age desiccation in cement pastes and mortars, *Cement and Concrete Research*, **31**, 1075-1085.
- Bentz, D.P., Koenders, E.A.B., Mönnig S., Reinhardt, H.-W., van Breugel, K. and G. Ye.,** 2006. Materials Science-Based Models in Support of Internal Water Curing to be published as part of a RILEM state-of-the-art report.
- Bentz, D.P., Jensen, O.M., Hansen, K.K., Olesen, J.F., Stang, H. and Haecker, C.J.,** 2001b. Influence of cement particle size distribution on early age autogenous strains and stresses in cement-based materials, *Journal of American Ceramic Society*, **84**(1), 129-35.
- Berry, E.E., Hemmings, R.T. and Cornelius, B.J.,** 1990. Mechanisms of hydration reactions in high volume fly ash pastes and mortars, *Cement and Concrete Composites*, **12**, 253-261.
- Bisschop, J. and Van Mier, J.G.M.,** 1999. Time evolution of shrinkage microcracking in young mortar as observed with environmental scanning electron microscopy, in *Symposium 'Transport Properties and Microstructure of Cement-Based Systems' of MRS 1999 Fall meeting*, Boston, November 29-30.
- Bjøntegaard, Ø. and Sellevold, E.J.,** 1999. Thermal dilation-autogenous shrinkage: How to separate?, in *Proceedings of International Workshop Autoshrink'98*, Ed. Tazawa, E-I., Hiroshima, Japan, E&FN SPON, London, 13-14 June, 245-256.
- Bjøntegaard, Ø., Hammer T.A. and Sellevold, E.J.,** 2004. On the measurement of free deformation of early age cement paste and concrete, *Cement and Concrete Composites*, **26**, 427-435.
- Brooks, J.J. and Megat Johari, M.A.,** 2001. Effect of metakaolin on creep and shrinkage of concrete, *Cement and Concrete Composites*, **23**, 495-502.
- Brooks, J.J., Cabrera, J.G. and Megat Johari, M.A.,** 1999. Factors affecting the autogenous shrinkage of silica fume high-strength concrete, in *Proceedings of International Workshop Autoshrink'98*, Ed. Tazawa, E-I., Hiroshima, Japan, E&FN SPON, London, 13-14 June, 195-202.
- Brunauer, S., Yudenfreund, M., Odler, I. and Skalny, J.,** 1973. Hardened Portland cement pastes of low porosity VI. Mechanism of the hydration process, *Cement and Concrete Research*, **3**, 129-147.

- Chan, Y.W., Liu, C.Y. and Lu, Y.S.,** 1999. Effects of slag and fly ash on the autogenous shrinkage of high-performance concrete, in *Proceedings of International Workshop Autoshrink'98*, Ed. Tazawa, E-I., Hiroshima, Japan, E&FN SPON, London, 13-14 June, 221-228.
- Chang, T.-P. and Shieh, M.-M.,** 1996. Fracture properties of lightweight concrete, *Cement and Concrete Research*, **26**, 181-188.
- Cook, R.A. and Hover, K.C.,** 1999. Mercury porosimetry of hardened cement pastes, *Cement and Concrete Research*, **29**, 933-943.
- Counto, U.J.,** 1964. The effect of elastic modulus of the aggregate on the elastic modulus, creep and creep recovery of concrete, *Magazine of Concrete Research*, **16**, 129-138.
- Curti E., Kulik A.D. and Tits J.,** 2005. Solid solutions of trace Eu(III) in calcite: thermodynamic evaluation of experimental data over a wide range of pH and pCO₂, *Geochimica Cosmochimica Acta*, **69(7)**, 1721-1737.
- Dela, B.F. and Stang, H.,** 1997. Internal eigenstresses in concrete due to autogenous shrinkage, *Self-Desiccation and Its Importance in Concrete Technology Proceedings of an International Research Seminar in Lund*, 10 June, 46-55.
- Derringer, G. and Suich, R.,** 1980. Simultaneous optimization of several response variables. *Journal of Quality and Technology*, **12(4)**, 214-219.
- Dhir, R.K., Hewlett, P.C., Lota, J.S. and Dyer, T.D.,** 1994. An investigation into the feasibility of formulating self-cure concrete, *Materials and Structure*, **27**, 606-615.
- Diamond, S.,** 2000. Mercury porosimetry: An inappropriate method for the measurement of pore size distributions in cement-based materials, *Cement and Concrete Research*, **30**, 1517-1525.
- Diamond, S.,** 2004. The microstructure of cement paste and concrete—a visual primer, *Cement and Concrete Composites*, **26**, 919-933.
- DIN 4226,** 1983. Aggregates for Concrete, Deutsche Norm.
- Du, L. and Folliard, K.J.,** 2005. Mechanisms of air entrainment in concrete, *Cement and Concrete Research*, **35**, 1463-1471.
- Duan, K., Hu, X.Z., Wittmann, F.H.,** 2003. Boundary effect on concrete fracture and non-constant fracture energy distribution, *Engineering Fracture Mechanics*, **70**, 2257-2268.
- Dugdale, D.S.,** 1960. Yielding of steel sheets containing slits, *Journal of the Mechanics and Physics of Solids*, **8**, 100-104.
- Duprat, F. and Sellier, A.,** 2006. Probabilistic approach to corrosion risk due to carbonation via an adaptive response surface method, *Probabilistic Engineering Mechanics*, **21**, 207-216.

- EuroLightCon/R2**, 1998. LWAC Material Properties State-of-the-Art EuroLightCon, Economic Design and Construction with Light Weight Aggregate Ed. van Bruegel, K. The European Union – Brite EuRam III, Document BE96-3942/R2, December 1998.
- Faber, K.T., Evans, A.G., and Drory, M.D.**, 1983. A Statistical Analysis of Crack Deflection as a Toughening Mechanism in Ceramic Materials, *Fracture Mechanics of Ceramics*, **6**, 77-91.
- Farhat, F.A.**, 2004. Performance of concrete structures retrofitted with CARDIFRC[®] after thermal cycling, *PhD Thesis*, Cardiff University, Wales.
- Farhat, F.A., Nicolaides, D., Kanellopoulos, A., and Karihaloo, B.L.**, 2007. High performance fibre-reinforced cementitious composite (CARDIFRC)-Performance and application to retrofitting, *Engineering Fracture Mechanics*, **74**, 151-167.
- Faust, T.**, 1997. Stress Strain Curves of High Strength Lightweight Concrete, *LACER*, **2**, 103-108.
- Feylessoufi, A., Tenoudji, F.C., Marin, V. and Richard, P.**, 2001. Early ages shrinkage mechanisms of ultra-high-performance cement based materials, *Cement and Concrete Research*, **31**, 1573-1579.
- Frias, M. and Cabrera, J.**, 2000. Pore size distribution and degree of hydration of metakaolin-cement pastes, *Cement and Concrete Research*, **30**, 561-569.
- Geiker, M.R., Bentz, D.P. and Jensen, O.M.**, 2004. Mitigating autogenous Shrinkage by Internal Curing in High-Performance Structural Lightweight Concrete, *SP 218*, Eds Ries, J.P. and Holm, T.A., American Concrete Institute, 1 February, 143-148.
- Glisic, B. and Simon, N.**, 2000. Monitoring of concrete at very early age using stiff SOFO sensor, *Cement and Concrete Composites*, **22**, 115-119.
- Grabiec, A.M. and Piasta, Z.**, 2004. Study on compatibility of cement-superplasticiser assisted by multicriteria statistical optimisation, *Journal of Materials Processing Technology*, **152**, 197-203.
- Grasley Z.C., Lange, D.A. and D'Ambrosia, M.D.**, 2003. Drying Stresses and Internal Relative Humidity in Concrete, *Materials Science of Concrete VII*, ed. Jan Skalny, 2003, in press.
- Griffith, A.A.**, 1920. The phenomena of rupture and flow in solids, *Philosophical Transactions of Royal Society of London*, **221**, 163-198.
- Halamickova, P., Detwiler, R.J., Bentz, D.P. and Garboczi, E.J.**, 1995. Water permeability and chloride ion diffusion in Portland cement mortars: Relationship to sand content and critical pore diameter, *Cement and Concrete Research*, **25**, 790-802.
- Hammer, T.A. and Heese, C.**, 1999. Early age chemical shrinkage and autogenous deformation of cement paste, *Self-Desiccation and Its Importance in*

Concrete Technology Proceedings of the 2nd International Research Seminar in Lund, 18 June, 7-14.

- Han, M-C., and Han, C-G.,** 2005. The effect of specimen size on the shrinkage properties of high performance concrete, *Self-Desiccation and Its Importance in Concrete Technology Proceedings of the 4th International Research Seminar in Lund*, June, 153-164.
- Hanehara, S., Hirao, H. and Uchikawa, H.,** 1999. Relationships between autogenous shrinkage, and the microstructure and humidity changes at inner part of hardened cement paste at early age, The influence of cement characteristics on chemical shrinkage, in *Proceedings of International Workshop Autoshrink'98*, Ed. Tazawa, E-I., Hiroshima, Japan, E&FN SPON, London, 13-14 June, 93-104.
- Hansen, K.K. and Jensen, O.M.,** 1997. Equipment for measuring autogenous RH change and autogenous deformation in cement paste and concrete, *Self-Desiccation and Its Importance in Concrete Technology Proceedings of an International Research Seminar in Lund*, 10 June, 27-30.
- Hansen, T.C.,** 1960. Strength, elasticity and creep as related to the internal structure of concrete, *Chem. of Cement, Proc., 4th Int. Symp., Monograph 43*, Washington, D.C., 709-723.
- Hansen, T.C.,** 1965. Influence of aggregate and voids on modulus of elasticity of concrete, cement mortar and cement paste, *ACI Journal*, **62**, 193-215.
- Hansen, T.C.,** 1986. Physical structure of hardened cement pastes. A classical approach. *Materials and Structures*, **19**, 423-436.
- Hashida, H. and Yamazaki, N.,** 2002. Deformation composed of autogenous shrinkage and thermal expansion due to hydration of high strength concrete and stress in reinforced structures, *Self-Desiccation and Its Importance in Concrete Technology Proceedings of the 3rd International Research Seminar in Lund*, 14-15 June, 77-92.
- Hillerborg, A., Modeer, M. and Peterson, P.E.,** 1976. Analysis of crack formation and crack growth in concrete by means of fracture mechanics and finite elements, *Cement and Concrete Research*, **6**, 773-782.
- Hirsch., T.J.,** 1962. Modulus of elasticity of concrete affected by elastic moduli of cement paste matrix and aggregate, *ACI J*, **59**, 427-451.
- Holiday, L.,** 1966. Composite Materials. Elsevier Science, Amsterdam.
- Holt, E.,** 2002. Very early age autogenous shrinkage: Governed by chemical shrinkage or self-desiccation, *Self-Desiccation and Its Importance in Concrete Technology Proceedings of the 3rd International Research Seminar in Lund*, 14-15 June, 1-25.
- Holt, E.E. and Leivo, M.T.,** 1999. Autogenous shrinkage at very early ages, in *Proceedings of International Workshop Autoshrink'98*, Ed. Tazawa, E-I., Hiroshima, Japan, E&FN SPON, London, 13-14 June, 133-140.

- Holt, E.E.**, 2001. Early ages autogenous shrinkage of concrete, *PhD Thesis*, University of Washington, Washington, USA.
- Hori, A., Morioka, M., Sakai, E. and Daimon, M.**, 1999. Influence of expansive additives on autogenous shrinkage in *Proceedings of International Workshop Autoshrink'98*, Ed. Tazawa, E-I., Hiroshima, Japan, E&FN SPON, London, 13-14 June, 187-194.
- Hu, X.Z., and Wittman, F.H.**, 2000. Size effect on toughness induced by crack close to free surface," *Engineering Fracture Mechanics*, **65**, 209-211.
- Hua, C., Acker, P. and Ehlacher, A.**, 1995. Analyses and models of the autogenous shrinkage of hardening cement paste I. Modeling at macroscopic scale, *Cement and Concrete Research*, **25**, 1457-1468.
- Irwin, G.R.**, 1957. Analysis of stresses and strains near the end of a crack transversing a plate, *Journal of Applied Mechanics*, **24**, 361-364.
- Jennings, H.M.**, 1988. Design of high strength cement based materials: Part 2 Microstructure, *Material Science and Technology*, **4**, 285-290.
- Jennings, H.M., and Parrot, L.J.**, 1986. Microstructure analyses of hardened alite paste, *Journal of Material Science*, **21**, 4048-4052.
- Jennings, H.M., Dalglish, B.J., and Pratt, P.L.**, 1981. Morphological development of hydrating C_3S as examined by electron microscopy techniques, *Journal of the American Ceramic Society*, **64**, 567
- Jenq, Y. and Shah, S.P.**, 1985. Two parameter fracture model for concrete, *ASCE Journal of Engineering Mechanics*, **11**, 1227-1241.
- Jensen, O.M. and Hansen, P.F.**, 1995. A dilatometer for measuring autogenous deformation in hardening Portland cement paste, *Materials and Structures*, **28**, 406-409.
- Jensen, O.M. and Hansen, P.F.**, 1996. Autogenous deformation and change of the relative humidity in silica fume-modified cement paste, *ACI Materials Journal*, **93**, 539-543.
- Jensen, O.M. and Hansen, P.F.**, 1999. Influence of temperature on autogenous deformation and relative humidity change in hardening cement paste, *Cement and Concrete Research*, **29**, 567-575.
- Jensen, O.M. and Hansen, P.F.**, 2001a. Autogenous deformation and RH-change in perspective, *Cement and Concrete Research*, **31**, 1859-1865.
- Jensen, O.M. and Hansen, P.F.**, 2001b. Water-entrained cement-based materials I. Principles and theoretical background, *Cement and Concrete Research*, **31**, 647-654.
- Jensen, O.M. and Hansen, P.F.**, 2002. Water-entrained cement-based materials II. Experimental observations, *Cement and Concrete Research*, **32**, 973-978.

- Jensen, O.M.**, 1993. Autogenous deformation and RH-change—self-desiccation and self-desiccation shrinkage (in Danish), *PhD Thesis*, The Technical University of Denmark, Lyngby, Denmark,
- Jensen, O.M.**, 1995. Thermodynamic limitation of self-desiccation, *Cement and Concrete Research*, **25**, 157-164.
- Jiang, Z., Sun, Z. and Wang, P.**, 2005. Autogenous relative humidity change and autogenous shrinkage of high-performance cement pastes, *Cement and Concrete Research*, **35**, 1539-1545.
- Justice, J.M.**, 2005. Evaluation of metakaolins for use as supplementary cementitious materials, *MSc Thesis*, Georgia Institute of Technology, Georgia, USA.
- Justnes, H., Sellevold, E.J., Reyniers, B., Van Loo, D., Van Gemert, A., Verboven, F. and Van Gemert, D.**, 1999a. The influence of cement characteristics on chemical shrinkage, in *Proceedings of International Workshop Autoshrink'98*, Ed. Tazawa, E-I., Hiroshima, Japan, E&FN SPON, London, 13-14 June, 71-80.
- Justnes, H., Sellevold, E.J., Reyniers, B., Van Loo, D., Van Gemert, A., Verboven, F. and Van Gemert, D.**, 1999b. Chemical shrinkage of cementitious pastes with mineral additives *Self-Desiccation and Its Importance in Concrete Technology Proceedings of the 2nd International Research Seminar in Lund*, 18 June, 73-84.
- Kaplan, M.E.**, 1961. Crack propagation and fracture of concrete, *Journal of American Concrete Institute*, **58**, 591-610.
- Karihaloo, B.L. and Nallathambi, P.**, 1989. An improved effective crack model for the determination of fracture toughness of concrete, *Cement and Concrete Research*, **19**, 603-610.
- Karihaloo, B.L.**, 1995. *Fracture Mechanics and Structural Concrete*, Longman Group Ltd., Essex, England.
- Kayali, O., Haque, M.N. and Zhu, B.**, 1999. Drying shrinkage of fibre-reinforced lightweight aggregate concrete containing fly ash, *Cement and Concrete Research*, **29**, 1835-1840.
- Kishi, T. and Maekawa, K.**, 1995. Thermal and mechanical modeling of young concrete based on hydration process of multi-component cement minerals, in *Proceedings of the International RILEM Symposium on Thermal Cracking in Concrete at Early Ages*, pp 11-18, Ed. Springenschmid, R., E & EF Spon, London, 10–12 October, June, 11-18,
- Koenders, E.A.B. and van Breugel, K.**, 1997. Numerical modelling of autogenous shrinkage of hardening cement paste, *Cement and Concrete Research*, **27**, 1489-1499.
- Kohno, K., Okamoto, T., Isikawa, Y., Sibata, T. And Mori, H.**, 1999. Effects of artificial lightweight aggregate on autogenous shrinkage of concrete, *Cement and Concrete Research*, **29**, 611-614.

- Kolluru, V.S., Roman, G.S, Shah, S.P., Karthik, O. and Russell, H.,** 2005. Influence of Ultrafine Fly Ash on the Early Age Response and the Shrinkage Cracking Potential of Concrete, *Journal of Materials in Civil Engineering*, **17(1)**, 45-53.
- Kumar, R. and Bhattacharjee, B.,** 2003. Study on some factors affecting the results in the use of MIP method in concrete research, *Cement and Concrete Research*, **33**, 417-424.
- Lam, H. and Hooton, R.D.,** 2005. Effects of internal curing methods on restrained shrinkage and permeability, *Self-Desiccation and Its Importance in Concrete Technology Proceedings of the 4th International Research Seminar in Lund*, June, 210-228.
- Lam, H.,** 2005. Effects of internal curing methods on restrained shrinkage and permeability, *Master of Applied Science Thesis*, University of Toronto, Canada.
- Lange-Kornbak, D. and Karihaloo, B.L.,** 1996. Design of Concrete Mixes for Minimum Brittleness, *Advanced Cement Based Materials*, **3**, 124-132.
- Le Chatelier, H.** 1900. Sur les changements de volume qui accompagnent le durcissement des ciments, *Bull. Soc. Encour. Ind. Natl.*, **5**, 54-57.
- Lee, H.K., Lee, K.M. and Kim, B.G.,** 2003. Autogenous shrinkage of high-performance concrete containing fly ash, *Magazine of Concrete Research*, **55 (6)**, 507-515.
- Lee, K.M., Lee, H.K., Lee, S.H. and Kim, G.Y.,** 2006, Autogenous shrinkage of concrete containing granulated blast-furnace slag, *Cement and Concrete Research*, **36 (7)**, 1279-1285.
- Li, V.C. and Maalej, M.,** 1996. Toughening in cement based composites. Part I: Cement, mortar, and concrete,” *Cement and Concrete Composites*, **18**, 223-237.
- Li, V.L. and Huang, J.,** 1990. Crack Trapping and Bridging as Toughening Mechanisms in High Strength Concrete, in *Micromechanics of Failure of Quasi-Brittle Materials*, Eds. S.P. Shah, et al., Elsevier, London, 6-8 June, 579-588.
- Lim, S.N., and Wee, T.H.,** 2000. Autogenous shrinkage of ground-granulated blast-furnace slag concrete, *ACI Materials Journal*, **97 (5)**, 587-593.
- Lo, T.Y. and Cui, H.Z.,** 2004. Effect of porous lightweight aggregate on strength of concrete, *Materials Letters*, **58**, 916– 919.
- Loukili, A., Chopin, D., Khelidj A. and Le Touzo, J-Y.,** 2000. A new approach to determine autogenous shrinkage of mortar at an early age considering temperature history, *Cement and Concrete Research*, **30**, 915-922.
- Loukili, A., Khelidj, A. and Richard, P.,** 1999. Hydration kinetics, change of relative humidity, and autogenous shrinkage of ultra-high-strength concrete, *Cement and Concrete Research*, **29**, 577-584.

- Love, A.E.H.**, 1944. Theory of Elasticity, 4th edition, Dover, New York.
- Lu, B. and Torquato, S.**, 1992. Nearest-surface distribution functions for polydispersed particle system, *Phys. Rev. A*, **45**, 5530-5544.
- Lura, P. and Jensen, O.M.**, 2005. Discussion on "On the measurement of free deformation of early age cement paste and concrete [Bjøntegaard Ø, Hammer TA, Sellevold EJ. Cement & Concrete Composites 2004;26:427-435]" *Cement and Concrete Composites*, **27**, 854-856.
- Lura, P.**, 2003. Autogenous deformation and internal curing of concrete, *PhD Thesis*, Technical University of Delft, The Netherlands.
- Lura, P., Bentz, D.P., Lange, D.A., Kovler, K. and Bentur, A.**, 2004. Pumice aggregates for internal water curing, *Proceedings of International RILEM Conference on the Advances in Concrete Through Science and Engineering*, Illinois, 21-24 March.
- Lura, P., Jensen, O.M. and Van Breugel, K.**, 2003, Autogenous shrinkage in high-performance cement paste: An evaluation of basic mechanisms, *Cement and Concrete Research*, **33**, 223-232.
- Lura, P., Van Breugel, K. and Maruyama, I.**, 2001. Effect of curing temperature of cement type of cement on early-age shrinkage of high-performance concrete, *Cement and Concrete Research*, **31**, 1867-1872.
- Lydon, F.D. and Balendran, R.V.**, 1980. Some properties of higher strength light-weight concrete under short-term tensile stress, *The International Journal of Lightweight Concrete*, **2**, 125-139.
- Lydon, F.D. and Balendran, R.V.**, 1986. Some observations on elastic properties of plain concrete, *Cement and Concrete Research*, **16**, 314-324.
- Lynam, C.G.**, 1934. Growth and Movement in Portland Cement Concrete, Oxford University Press, London.
- MacKenzie, J.K.**, 1950. The elastic constants of a solid containing spherical holes, *Proc. Phys. Soc. A*, **224**, 526-544.
- Maruyama, I. and Sato, R.**, 2005. A trial of reducing autogenous shrinkage by recycled aggregate, *Self-Desiccation and Its Importance in Concrete Technology Proceedings of the 4th International Research Seminar in Lund*, June, 264-270.
- Mese, O., Sengul, C., Akcay, B. and Tasdemir, M.A.**, 2005. Meso-mechanical modeling of fracture parameters of cement paste, mortar and concrete, *XIV. National Mechanical Conference*, Hatay, Turkey, 12-16 September 2005, (in Turkish with English Summary).
- Meshab, H.A., Buyle-Badin, F. and Acker, P.**, 2000. Early age shrinkage, mechanical behaviour and cracking of fibre reinforced mortar containing recycled aggregates, *Concrete Science and Engineering*, **2**, 71-77.
- Mindess, S. and Diamond, S.**, 1982. The cracking and fracture of mortar, *Materials and Structures*, **15**, 107-113.

- Miyazawa, S. and Tazawa, E-I.**, 2005. Prediction model for autogenous shrinkage of concrete with different type of cement, *Self-Desiccation and Its Importance in Concrete Technology Proceedings of the 4th International Research Seminar in Lund*, June, 125-138.
- Mohr, B.J., Premenko1, L., Nanko, H. and Kurtis, K.E.**, 2005. Examination of wood-derived powders and fibers for internal curing of cement-based materials, *Self-Desiccation and Its Importance in Concrete Technology Proceedings of the 4th International Research Seminar in Lund*, June, 229-244.
- Mönnig, S.**, 2003. Modelling of the hydration of high performance concrete with normal- and lightweight aggregates, *Otto-Graf-Journal*, **14**, 79-90.
- Moon, J-H., Rajabipour, F., Pease, B. and Weiss, J.**, 2005. Autogenous shrinkage, residual stress, and cracking in cementitious composites: The influence of internal and external restraint, *Self-Desiccation and Its Importance in Concrete Technology Proceedings of the 4th International Research Seminar in Lund*, June, 1-20.
- Morin, V., Tenoudji, F.C., Feylessoufi, A. and Richard, P.**, 2002. Evolution of the capillary network in a reactive powder concrete during hydration process, *Cement and Concrete Research*, **32**, 1907-1914.
- Morioka, M., Hori, A., Hagiwara, H., Sakai, E. and Daimon, M.**, 1999. Measurements of autogenous length changes by laser sensors equipped with digital computer system, in *Proceedings of International Workshop Autoshrink'98*, Ed. Tazawa, E-I., Hiroshima, Japan, E&FN SPON, London, 13-14 June, 191-200.
- Müller-Rochholz, J.**, 1979. Determination of the elastic properties of lightweight aggregate by ultrasonic pulse velocity measurement, *The International Journal of Lightweight Concrete*, **1**, 87-90.
- Myers, R.H. and Montgomery, D.C.**, 2002. Response Surface Methodology: Process and Product Optimization Using Designed Experiments, New York: John Wiley&Sons.
- Nallathambi, P., and Karihaloo, B.L.**, 1990. Fracture of concrete: Application of effective crack model, in *9th International Conference on Experimental Mechanics*, Volume. 4, Lyngby, Denmark, 20-24 August, 1413-1422.
- Navalurkar, R.K., Hsu, C.T., Kim, S.K. and Wecharanta, M.**, 1999. True Fracture Energy of Concrete, *ACI Materials Journal*, **96**, 213-225.
- Neville, A.M.**, 1997. Properties of concrete, 4th Edition, John Wiley & Sons Inc., New York.
- Nielsen, L.F.**, 1990. Technical Report No. 208, Institute of Building Materials, Technical University of Denmark, (in Danish).
- Nielsen, L.F.**, 1993. Technical Report No. 287, Institute of Building Materials, Technical University of Denmark, (in Danish).

- Nilsson, L-O. and Mjörnell, K.,** 2005. A macro-model for self-desiccation in high performance concrete, *Self-Desiccation and Its Importance in Concrete Technology Proceedings of the 4th International Research Seminar in Lund*, June, 49-66.
- Nokken, M.R.,** 2004. Development of discontinuous capillary porosity in concrete and its influence on durability, *PhD Thesis*, University of Toronto, Canada.
- Norling Mjörnell, K.,** 1997. A model on self-desiccation in high performance concrete, *Self-Desiccation and Its Importance in Concrete Technology Proceedings of an International Research Seminar in Lund*, 10 June, 141-157.
- Østregaard, L.,** 2003. Early-age fracture mechanics and cracking of concrete: Experiments and modeling, *PhD Thesis*, Technical University of Denmark.
- Pane, I. and Hansen, W.,** 2002. Early age creep and stress relaxation of concrete containing blended cements, *Materials and Structures*, **35**, 92-96.
- Park, K.B., Noguchi, T. and Tomosawa, F.,** 1999. A study on the hydration ratio and autogenous shrinkage of cement paste, in *Proceedings of International Workshop Autoshrink'98*, Ed. Tazawa, E-I., Hiroshima, Japan, E&FN SPON, London, 13-14 June, 299-308.
- Persson, B.,** 1999a. Evaluation of under-pressure in the pore water of sealed high-performance concrete, *Self-Desiccation and Its Importance in Concrete Technology Proceedings of the 2nd International Research Seminar in Lund*, 18 June, 135-151
- Persson, B.,** 1999b. Influence of mix design on self-desiccation in concrete, *Self-Desiccation and Its Importance in Concrete Technology Proceedings of the 2nd International Research Seminar in Lund*, 18 June, 85-108.
- Persson, B.,** 2001. A NORDTEST method for verification of self-desiccation in concrete, *Cement and Concrete Research*, **31**, 199-203.
- Persson, B.,** 2005. On the temperature effect on self desiccation on concrete, *Self-Desiccation and Its Importance in Concrete Technology Proceedings of the 4th International Research Seminar in Lund*, June, 95-124.
- Philleo, R.E.,** 1991. Concrete science and reality in *Material Science of Concrete II*, pp. 1-8, Eds. Skalny, J.P. and Mindess, S., Westerville, American Ceramic Society.
- Philleo, R.E.,** 1983. A method for analyzing void distribution in air-entrained concrete, *Cement Concrete and Aggregate*, **5**, 128-130.
- Pignat, C., Navi, P. and Scrivener, K.,** 2002. Characterization of the pore space in hardening cement paste to predict the autogenous shrinkage, *Self-Desiccation and Its Importance in Concrete Technology Proceedings of the 3rd International Research Seminar in Lund*, 14-15 June, 217-228.
- Pleau, R. and Pigeon, M.,** 1996. The use of the flow length concept to assess the efficiency of air entrainment with regards to frost durability: Part 1-

- Description of the test method, *Cement Concrete and Aggregate*, **18**, 19-29.
- Popovics, S. and Erdey, M.**, 1970. Estimation of the modulus of elasticity of concrete-like composite materials, *Materials and Structure*, **3**, 253-260.
- Postacıoğlu, B.**, 1986. Beton: Bağlayıcı Maddeler, Agregalar, Beton, Cilt 1, İstanbul, in Turkish.
- Powers, T.C. and Brownard, T.L.**, 1948. Studies of the physical properties of hardened Portland cement paste (Bulletin 22), *Research Laboratories of the Portland Cement Association, Part 3 and 4*.
- Powers, T.C.**, 1949. The air requirement of frost-resistant concrete, *Proc. Highway Res. Board*, **29**, 184-202.
- Powers, T.C.**, 1964. The physical structure in portland cement paste, *The Chemistry of Cements*, T.C.Powers (Ed.), Academic Press, London and New York, **1**, 391-416.
- Radocea, A.**, 1999. A model of self-desiccation in concrete, *Self-Desiccation and Its Importance in Concrete Technology Proceedings of the 2nd International Research Seminar in Lund*, 18 June, 153-162.
- Richardson, I.G.**, 2004. Tobermorite/jennite- and tobermorite/calcium hydroxide-based models for the structure of C-S-H: applicability to hardened pastes of tricalcium silicate, β -dicalcium silicate, Portland cement, and blends of Portland cement with blast-furnace slag, metakaolin, or silica fume, *Cement and Concrete Research*, **34 (9)**, 1733-1777.
- Richardson, I.G.**, 2000. The nature of the hydration products in hardened cement paste, *Cement and Concrete Composites*, **22**, 97-113.
- RILEM Technical Committee 50-FMC**, 1985. Draft Recommendation: Determination of the fracture energy of mortar and concrete by means of three-point bend test on notched beams, *Materials and Structures*, **18 (106)**, 287-291.
- Roberts, J.W.**, 2005. Current and future trends in the application of internal curing of concrete, *Self-Desiccation and Its Importance in Concrete Technology Proceedings of the 4th International Research Seminar in Lund*, June, 197-209.
- Sadouki, H. and Wittmann, F.H.**, 2001. Numerical Investigations on damage in cementitious composites under combined drying and shrinkage and mechanical load, *Proc. Fourth Int. Conference on Fracture Mechanics of Concrete and Concrete Structures (Framcos)*, de Borst et al. (Eds), Cachan, France, 95-98.
- Sanchez de Rojas, M.I. and Frias, M.**, 1996. The pozzolanic activity of different materials, its influence on the hydration heat an mortars. *Cement and Concrete Research*, **26**, 203-213.

- Sarkar, S., Chandra, S. and Berntsson, L.,** 1992. Interdependence of microstructure and strength of structural lightweight aggregate concrete, *Cement and Concrete Composites*, **14**, 239-248.
- Sato, R., Tanaka, S., Hayakawa, T. and Tanimura, M.,** 1999. Experimental studies on reduction of autogenous shrinkage and its induced stress in HSC, *Self-Desiccation and Its Importance in Concrete Technology Proceedings of the 2nd International Research Seminar in Lund*, 18 June, 163-171
- Scherer, G.W.,** 1999. Crystallization in pores, *Cement and Concrete Research*, **29**, 1347-1358.
- Schindler, A.K.,** 2002. Concrete Hydration, Temperature Development, and Setting at Early-Ages, *PhD Thesis*, University of Texas at Austin, US.
- Scrivener, K.L.,** 2004. Backscattered electron imaging of cementitious microstructures: understanding and quantification, *Cement and Concrete Composites*, **26**, 935-945.
- Shah, S.P., Swartz, S.E. and Ouyang, C.,** 1995. Fracture Mechanics of Concrete: Applications of Fracture Mechanics to Concrete, Rock, and Other Quasi-Brittle Materials, John Wiley & Sons, Inc., New York.
- Snyder, K.A.,** 1998. A numerical test of air void spacing equations, *Advanced Cement Based Materials*, **8**, 28-44.
- Soares, R.C., Mohamed, A., Venturini, W.S. and Lemaire, M.,** 2002. Reliability analysis of non-linear reinforced concrete frames using the response surface method, *Reliability Engineering and System Safety*, **75**, 1-16.
- Staquet, S. and Espion, B.,** 2004. Evolution of the thermal expansion coefficient of UHPC incorporating ver fine fly ash and metakaolin *Advances in Concrete Through Science and Engineering, Rilem Spring Meeting*, March-21-26, Northwestern University, Evanston, Illinois.
- Swamy, R.N. and Lixian, W.,** 1995. The ingredients for high performance, in *Proceedings of International Symposium on Structural Lightweight Aggregate Concrete*, Eds. Ivar Holand et al., Sanderfjord, Norwegian Concrete Association, Oslo, 20-24 June, 628-639.
- Takada, K., Van Bruegel, K., Koenders, E.A.B. and Kaptijn, N.,** 1999. Experimental evaluation of autogenous shrinkage of lightweight aggregate concrete in *Proceedings of International Workshop Autoshrink'98*, Ed. Tazawa, E-I., Hiroshima, Japan, E&FN SPON, London, 13-14 June, 229-239.
- Tanacan, L. and Ersoy, H.Y.,** 2000. Mechanical properties of fired clay-perlite as composite material, *Journal of Materials in Civil Engineering*, **12**, 55-59.
- Tangtermsirikul, S.,** 1999. Effects of chemical composition and particle size of fly ash on autogenous shrinkage of paste, in *Proceedings of International Workshop Autoshrink'98*, Ed. Tazawa, E-I., Hiroshima, Japan, E&FN SPON, London, 13-14 June, 175-186.

- Tanimura, M., Mitami, Y. and Sato, R.,** 2005. An investigation of prediction model for autogenous shrinkage/expansion strain of low-shrinkage HSC. *Self-Desiccation and Its Importance in Concrete Technology Proceedings of the 4th International Research Seminar in Lund*, June, 245-263.
- Tasdemir, M.A. and Karihaloo, B.L.,** 2001. Effect of aggregate volume fraction on the parameters of concrete: A meso-mechanical approach, *Magazine of Concrete Research*, **53**, 405-415.
- Tasdemir, M.A.,** 1982. Elastic and Inelastic Behaviour of Structural Lightweight Aggregate Concrete”, *PhD Thesis*, Istanbul Technical University, Istanbul, (in Turkish with English summary).
- Tasdemir, M.A., Tasdemir, C., Grimm, R. and König, G.,** 2002. Role of aggregate fraction in the fracture of semi-lightweight high strength concrete, *Proceedings of the 6th International Symposium on Utilization of High Strength/High Performance Concrete*, Leipzig, June, 1453-1466.
- Tazawa, E.-I. and Miyazawa, S.,** 1995. Influence of cement and admixture on autogenous shrinkage of cement paste, *Cement and Concrete Research*, **25**, 281-287.
- Tazawa, E.-I.,** 1999. Technical Committee on Autogenous Shrinkage of Concrete, Japan Concrete Institute, Japan Concrete Institute Committee report, in *Proceedings of International Workshop Autoshrink’98*, Ed. Tazawa, E.-I., Hiroshima, Japan, E&FN SPON, London, 13-14 June, 1-67.
- Tazawa, E.-I. and Miyazawa, S.,** 1997. Effect of self-desiccation on volume change and flexural strength of cement paste and mortar, *Self-Desiccation and Its Importance in Concrete Technology Proceedings of an International Research Seminar in Lund*, 10 June, 8-14.
- Termkhajornkit, P., Nawa, T., Nakai, M. and Saito, T.,** 2005. Effect of fly ash on autogenous shrinkage, *Cement and Concrete Research*, **35**, 473-482.
- Theodorakopoulus, D.D. and Swamy, R.N.,** 1993. Contribution of steel fibers to the strength characteristics of lightweight concrete slab-column connections failing in punching shear, *ACI Structural Journal*, **90 (4)**, 342-355.
- Tixier, R. and Mobasher, B.,** 2003. Modeling of damage in cement-based materials subjected to external sulfate attack. II: Comparison with experiments, *Journal of Materials in Civil Engineering ASCE*, **15 (4)**, 314-322.
- Voigt, T., Ye, G., Sun, Z.H., Shah, S.P. and van Breugel, K.,** 2005. Early age microstructure of Portland cement mortar investigated by ultrasonic shear waves and numerical simulation, *Cement and Concrete Research*, **35**, 858-866.
- Wang, S. and Li, V.C.,** 2003. Lightweight engineered cementitious composites (ECC) in *HPFRCC4 Workshop*, Ann Arbor, USA, June, 279-390.

- Way, S.J. and Shayan, A.,** 1989. Early hydration of a Portland cement in water and sodium hydroxide solutions: Composition of solutions and nature of solid phases, *Cement and Concrete Research*, **19**, 759-769.
- Weber, S. and Reinhardt, H.W.,** 1997. A new generation of high performance concrete: Concrete with autogenous curing, *Advanced Cement Based Materials*, **6**, 59-68.
- Weiss, J.W.,** 1999. Prediction of early age shrinkage cracking in concrete, *PhD Thesis*, Northwestern University, Illinois, USA.
- Wild, S., Khatib, J.M. and Roose, L.J.,** 1998. Chemical shrinkage and autogenous shrinkage of Portland cement metakaolin pastes, *Advances in Cement Research*, **10(3)**, 109-119.
- Wille, K. and Dehn, F.,** 2003. Fracture mechanics of different lightweight Concretes (LWC), *LACER*, **8**, 81-97.
- Wittmann, F.H.,** 1983. Structure of concrete with respect to crack formation, in *Fracture Mechanics of Concrete*, pp. 43-74, Eds. Wittmann, F.H., Elsevier Applied Science Publishers, Amsterdam.
- Yang, C.C., Cho, S.W. and Wang, L.C.,** 2006. The relationship between pore structure and chloride diffusivity from ponding test in cement-based materials, *Materials Chemistry and Physics*, **100 (2-3)**, 203-210.
- Yogendran, V., Langan, B.W. and Ward, M.A.,** 1991. Hydration of cement and silica fume paste, *Cement and Concrete Research*, **21**, 691-708.
- Zhang, D. and Wu, K.,** 1999. Fracture process zone of three-point-bending concrete beams, *Cement and Concrete Research*, **29**, 1887-1892.
- Zhang, M.H. and Gjorv, O.E.,** 1990. Microstructure of the interfacial zone between lightweight aggregate and cement paste, *Cement and Concrete Research*, **20**, 610-618.
- Zhang, M.H. and Gjorv, O.E.,** 1992. Penetration of cement paste into lightweight aggregate, *Cement and Concrete Research*, **22**, 47-55.
- Zhang, M.H., Tam, C.T. and Leow, M.P.,** 2003. Effect of water-to-cementitious materials ratio and silica fume on the autogenous shrinkage of concrete, *Cement and Concrete Research*, **33**, 1687-1694.
- Zhutovsky, S., Kovler, K. and Bentur, A.,** 2002a. Autogenous curing of high-strength concrete using pre-soaked pumice and perlite sand, *Self-Desiccation and Its Importance in Concrete Technology Proceedings of the 3rd International Research Seminar in Lund*, 14-15 June, 161-174.
- Zhutovsky, S., Kovler, K. and Bentur, A.,** 2002b. Efficiency of lightweight aggregates for internal curing of high strength concrete to eliminate autogenous shrinkage, *Materials and Structures*, **35**, 97-101.

APPENDIX A

Mechanical and Fracture Test Results

Table A1. Results of compressive strength and modulus of elasticity of produced cementitious materials.

		Compressive Strength, MPa		Modulus of Elasticity, MPa		
		Average	Cov		Average	Cov
PREF-1	77.67	68.50	16.7	19592	17935	17.2
PREF-2	78.56			15471		
PREF-3	55.39			15234		
PREF-4	62.39			21443		
FMREF-1	78.33	74.93	4.3	30447	31027	3.3
FMREF-2	72.87			30874		
FMREF-3	71.51			32526		
FMREF-4	77.01			30261		
MREF-1	93.17	87.98	6.8	39578	39438	3.9
MREF-2	86.58			37385		
MREF-3	92.05			41132		
MREF-4	80.12			39658		
MV10L24-1	56.1	59.14	5.6	31295	31817	4.8
MV10L24-2	61.16			33906		
MV10L24-3	56.53			31781		
MV10L24-4	62.78			30285		
MV20L24-1	45.72	46.37	2.1	27329	28211	6.1
MV20L24-2	45.91			27106		
MV20L24-3	47.49			30199		
MV30L24-1	40.67	40.55	0.4	23054	23940	5.4
MV30L24-2	40.62			25794		
MV30L24-3	40.36			23897		
MV30L24-4				23016		
CREF-1	104.96	93.06	14.1	45466	45666	1.9
CREF-3	95.24			46636		
CREF-4	78.98			44895		
CV10L24-1	83.42	79.37	7.4	39743	39612	0.8
CV10L24-2	84.76			39968		
CV10L24-3	72.03			39475		
CV10L24-4	77.26			39261		
CV20L24-1	68.75	62.07	6.9	37320	35565	12.5
CV20L24-2	57.08			31052		
CV20L24-3	61.75					
CV20L24-4	62.52			37196		
CV20L24-5	60.26			36692		
CV30L24-1	47.76	49.51	2.6	29239	30494	4.9
CV30L24-2	49.71			29277		
CV30L24-3	50.92			32240		
CV30L24-4	49.66			31221		
CV10L48-1	62.91	68.11	5.1	42502	39965	8.4
CV10L48-2	67			40146		
CV10L48-3	71.97					
CV10L48-4	70.17			35172		
CV10L48-5	68.48			42039		

Table A1. Continued.

		Compressive Strength, MPa			Modulus of Elasticity, MPa	
		Average	Cov		Average	Cov
CV20L48-1	63.03	61.13	2.2	35091	36372	7.4
CV20L48-2	61.66			35077		
CV20L48-3	61.9			40383		
CV20L48-4	59.84			34938		
CV30L48-1	46.49	47.64	5.2	30177	27746	9.1
CV30L48-2	49.57			24357		
CV30L48-3	44.25			27389		
CV30L48-4	49.11			29062		
PN0-2-1	71.3	68.42	5.5	28420	27425	6.7
PN0-2-2	63.28			25421		
PN0-2-3	67.98			26394		
PN0-2-4	71.11			29466		
PN2-4-1	72.42	72.21	1.8	27616	28009	5.5
PN2-4-2	70.81			28877		
PN2-4-3				29518		
PN2-4-4	73.41			26026		
PN4-8-1	81.49	74.00	15.1	29002	29283	1.0
PN4-8-2	61.12			29281		
PN4-8-3	79.4			29567		
PL2-4-1	27.54	29.23	10.4	15301	16492	8.2
PL2-4-2	29.86					
PL2-4-3	26.32			16204		
PL2-4-4	33.21			17970		
PL4-8-1	30.07	30.69	3.2	17275	19784	24.4
PL4-8-2	30.7			20489		
PL4-8-3	32.09			26220		
PL4-8-4	29.9			15150		

Table A2. Results of splitting tensile strength of produced cementitious materials.

	splitting strength (MPa)				splitting strength (MPa)		
		average	Cov			average	Cov
PREF-1	2.63	2.94	25.2	FMREF-1	5.45	5.06	8.3
PREF-2	2.4			FMREF-2	4.61		
PREF-3	3.78			FMREF-3	5.12		
MREF-1	5.81	6.09	5.6	MV10L24-1	4.06	4.45	7.8
MREF-2	5.98			MV10L24-2	4.59		
MREF-3	6.47			MV10L24-3	4.71		
MV20L24-1	4.81	4.07	23.2	MV30L24-1	3.35	3.38	6.6
MV20L24-2	3			MV30L24-2	3.18		
MV20L24-3	4.39			MV30L24-3	3.62		
CREF-1	6.01	6.79	8.6	CV10L24-1	7.1	6.38	11.9
CREF-2	7.81			CV10L24-2	5.45		
CREF-3	6.62			CV10L24-3	6.54		
CREF-4	6.72			CV10L24-4	5.42		
CREF-5	6.72			CV10L24-5	6.85		
CREF-6	6.84			CV10L24-6	6.94		
CV20L24-1	4.77	4.81	16.3	CV30L24-1	4.2	4.52	11
CV20L24-2	5.88			CV30L24-2	4.54		
CV20L24-3	5.65			CV30L24-3	4.73		
CV20L24-4	4.12			CV30L24-4	5.38		
CV20L24-5	4.46			CV30L24-5	4.28		
CV20L24-6	4.01			CV30L24-6	3.99		
CV10L48-1	5.59	5.56	9.5	CV20L48-1	5.28	4.95	5.6
CV10L48-2	4.68			CV20L48-2	4.7		
CV10L48-3	5.56			CV20L48-3	4.66		
CV10L48-4	5.43			CV20L48-4	4.87		
CV10L48-5	5.81			CV20L48-5	4.88		
CV10L48-6	6.3			CV20L48-6	5.3		
CV30L48-1	3.93	4.06	7.9	PN0-2-1	3.57	4.08	15
CV30L48-2	4.1			PN0-2-2	3.54		
CV30L48-3	4.59			PN0-2-3	4.52		
CV30L48-4	3.81			PN0-2-4	4.69		
CV30L48-5	4.23						
CV30L48-6	3.71						
PN2-4-1	3.32	3.68	13	PN4-8-1	4.2	3.99	7.3
PN2-4-2	3.41			PN4-8-2	4.37		
PN2-4-3	3.59			PN4-8-3	3.96		
PN2-4-4	4.37			PN4-8-4	3.65		
				PN4-8-5	3.79		
PL2-4-1	2.08	1.87	14.9	PL4-8-1	1.77	1.88	23.2
PL2-4-2	2.12			PL4-8-2	1.46		
PL2-4-3	1.71			PL4-8-3	1.79		
PL2-4-4	1.56			PL4-8-4	2.49		

Table A3. Fracture properties of produced cementitious materials.

	Area under the curve (W_0), Nmm	Final def., mm	P_{max} , kN	Fracture energy G_F , N/m	Net bending strength (f_{net}), MPa
CREF-1	552	0.359	5.74	95	9.22
CREF-2	524	0.353	5.14	83	8.06
CREF-3	448	0.227	4.96	78	8.33
Average	508	0.313	5.28	86	8.54
Cov	10.6	23.9	7.7	10.4	7.1
CV10L24-1	576	0.590	4.37	104	7.11
CV10L24-2	600	0.595	4.74	109	7.79
CV10L24-3	532	0.468	4.00	105	8.02
CV10L24-4	584	0.766	4.10	95	6.55
CV10L24-5	508	0.598	4.05	107	6.65
CV10L24-6	577	0.637	4.81	90	6.45
Average	563	0.609	4.34	102	7.09
Cov	7.4	14.4	9.9	8.5	1.4
CV20L24-1	571	0.704	4.11	99	6.26
CV20L24-2	545	0.554	3.49	92	5.37
CV20L24-3	538	0.804	3.40	49	6.30
Average	551	0.687	3.67	80	5.97
Cov	3.1	18.3	10.5	33.5	8.8
CV30L24-1	437	0.588	2.87	79	4.54
CV30L24-2	464	0.822	2.91	88	4.63
CV30L24-3	396	0.444	3.04	129	3.87
Average	432	0.618	2.94	99	4.35
Cov	8.0	30.9	3.1	27.2	9.6
CV10L48-1	400	0.641	3.47	83	6.11
CV10L48-2	472	0.843	3.78	89	5.89
CV10L48-3	480	0.614	4.18	82	6.12
Average	451	0.699	3.81	85	6.04
Cov	9.8	17.9	9.3	4.3	2.2
CV20L48-1	416	0.559	3.18	75	5.13
CV20L48-2	493	0.855	3.06	90	4.77
CV20L48-3	383	0.543	2.97	71	4.85
CV20L48-4	385	0.675	2.74	75	4.61
CV20L48-5	432	0.725	3.20	80	5.21
Average	422	0.671	3.03	78	4.92
Cov	6.5	14.0	7.7	6.1	6.2
CV30L48-1	326	0.434	3.02	61	4.98
CV30L48-2	287	0.386	3.12	52	5.00
CV30L48-3	271	0.427	3.05	51	4.86
CV30L48-4	404	0.652	2.86	102	4.59
Average	322	0.475	3.01	66	4.86
Cov	22.6	30.1	4.5	44.2	4.2
PREF-1	104	0.13	1.8	17	3.28
PREF-2	172	0.17	1.9	30	3.86
PREF-3	93	0.11	1.3	16	1.85
PREF-4	144		1.5	42	1.76
Average	128	0.137	1.60	27	2.69
Cov	37.5	42.1	45.2	46.3	38.9

Table A3. Continued.

	Area under the curve (W_0), Nmm	Final def., mm	P_{\max} , kN	Fracture energy G_F , N/m	Net bending strength (f_{net}), MPa
FMREF-1	304	0.494	2.85	58	4.67
FMREF-2	313	0.495	2.92	57	4.60
FMREF-3	351	0.593	3.10	66	5.02
FMREF-4	341	0.602	2.65	66	4.37
Average	327	0.546	2.88	62	4.67
Cov	6.8	10.9	6.5	8.2	5.8
MREF-1	446	0.425	4.14	82	7.06
MREF-2	381	0.428	4.32	70	7.23
MREF-3	411	0.681	4.16	79	6.95
Average	413	0.512	4.21	77	7.08
Cov	7.8	28.7	2.2	8.4	2.0
MV10L24-1	478	0.425	3.15	85	5.07
MV10L24-2	400	0.508	2.83	76	4.55
MV10L24-3	429	0.711	2.93	82	4.91
MV10L24-4	462	0.768	2.92	86	4.87
Average	442	0.603	2.96	82	4.85
Cov	7.9	27.0	4.5	5.5	4.5
MV20L24-1	342	0.547	2.96	63	4.79
MV20L24-2	401	0.716	2.51	76	4.16
MV20L24-3	346	0.593	2.62	66	4.32
MV20L24-4	430	0.706	2.80	81	4.64
Average	380	0.640	2.73	71	4.48
Cov	11.3	13.0	7.2	11.8	6.4
MV30L24-1	262	0.556	2.21	50	3.57
MV30L24-2	295	0.751	2.11	58	3.42
MV30L24-3	247	0.430	2.39	46	3.88
MV30L24-4	279	0.598	2.44	53	3.92
Average	271	0.584	2.29	52	3.70
Cov	7.7	22.7	6.8	10.0	6.5
PN0-2-1	394	0.42	3.6	71	5.97
PN0-2-2	353	0.59	3.0	67	4.99
PN0-2-3	320	0.50	2.7	63	4.95
PN0-2-4	417	0.74	3.0	79	4.92
Average	371	0.561	3.06	70	5.21
Cov	11.6	24.2	11.8	9.7	9.8
PN2-4-1	313	0.37	3.2	53	4.79
PN2-4-2	263	0.46	3.1	51	5.22
PN2-4-3	272	0.34	3.0	50	4.83
PN2-4-4	248	0.32	3.4	43	5.07
Average	274	0.376	3.18	49	4.98
Cov	10.2	16.4	4.6	8.6	4.1
PN4-8-1	297	0.54	3.1	56	4.82
PN4-8-2	297	0.46	2.8	54	4.30
PN4-8-3	276	0.41	2.9	50	4.44
PN4-8-4	386	0.51	3.2	69	4.81
Average	314	0.479	3.03	57	4.59
Cov	15.6	12.1	5.7	13.9	5.7

Table A3. Continued.

	Area under the curve (W_0), Nmm	Final def., mm	P_{\max} , kN	Fracture energy G_F , N/m	Net bending strength (f_{net}), MPa
PL2-4-1	59	0.22	0.9	12	1.53
PL2-4-2	73	0.23	1.0	15	1.72
PL2-4-3	99	0.34	0.9	21	1.40
PL2-4-4	83	0.29	1.0	17	1.65
Average	78	0.270	0.96	16	1.57
Cov	21.3	20.7	8.0	21.7	8.7
PL4-8-1	49	0.16	1.0	10	1.54
PL4-8-2	99	0.24	1.2	18	1.89
PL4-8-3	57	0.26	0.8	12	1.28
PL4-8-4	60	0.21	1.0	12	1.61
Average	66	0.218	1.02	13	1.58
Cov	33.4	19.6	16.2	28.9	15.9

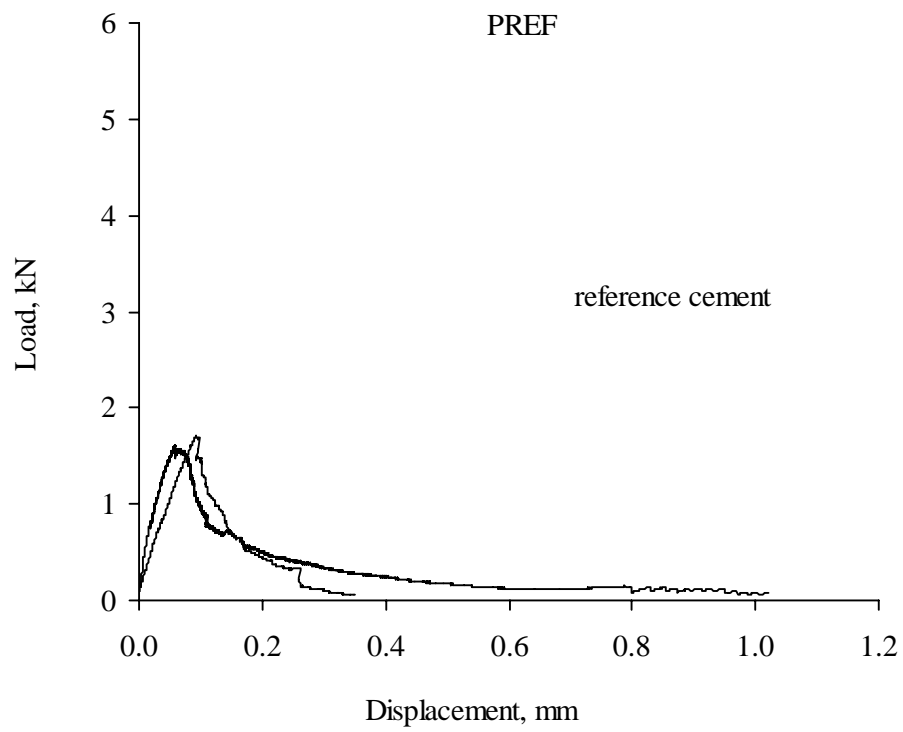


Figure A1. Load displacement diagram for PREF samples.

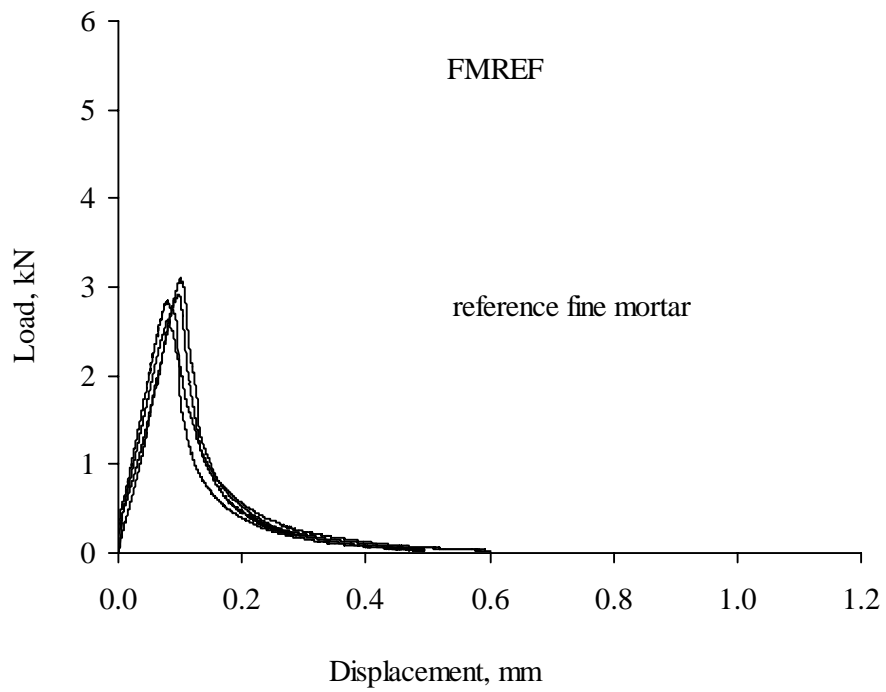


Figure A2. Load displacement diagram for FMREF samples.

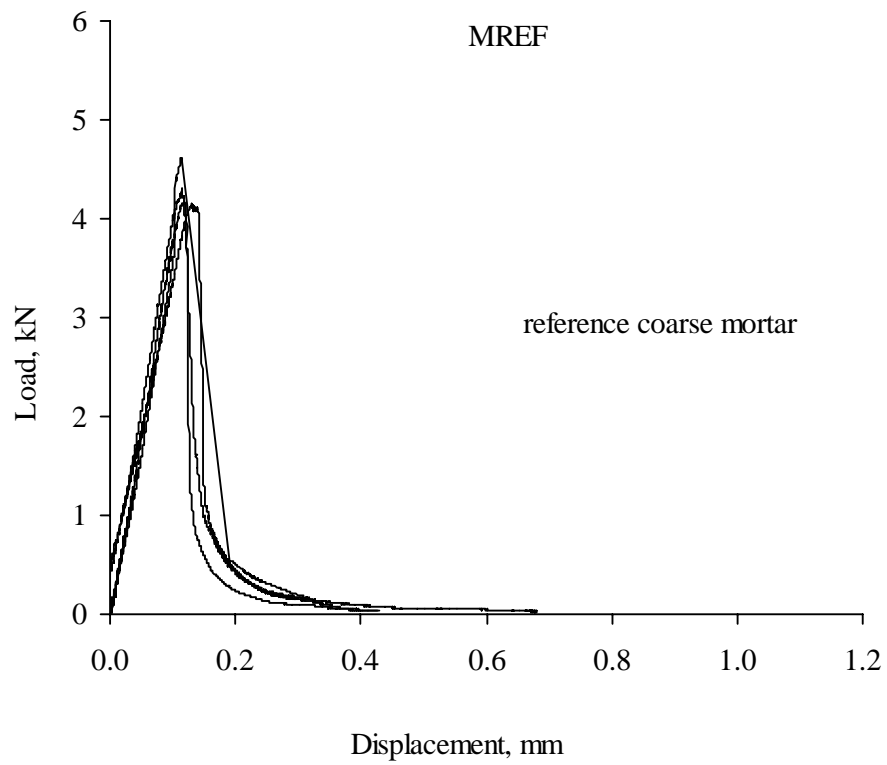


Figure A3. Load displacement diagram for MREF samples.

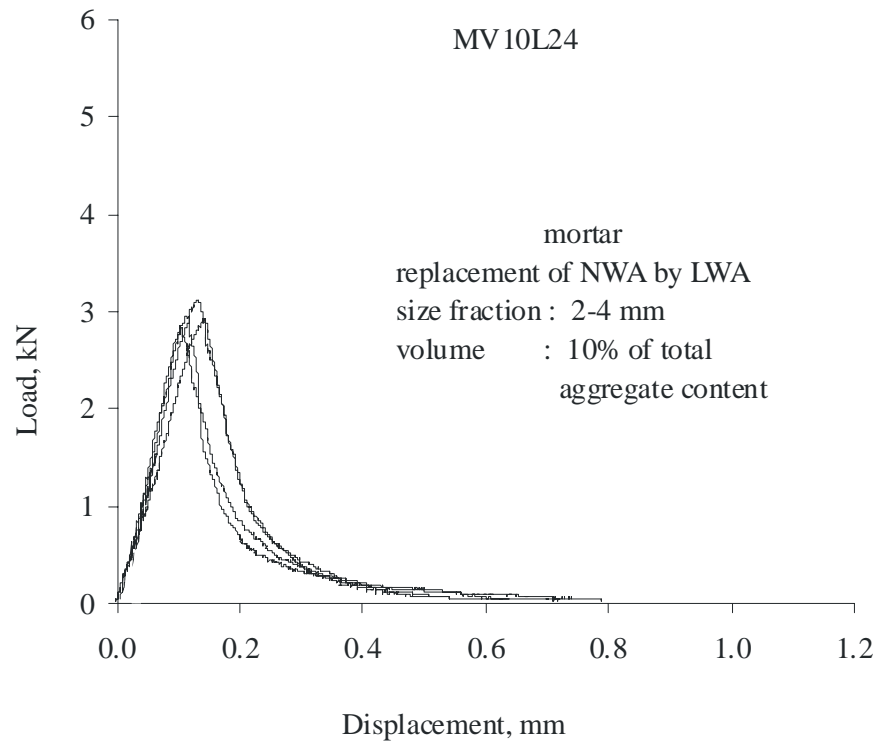


Figure A4. Load displacement diagram for MV10L24 samples.

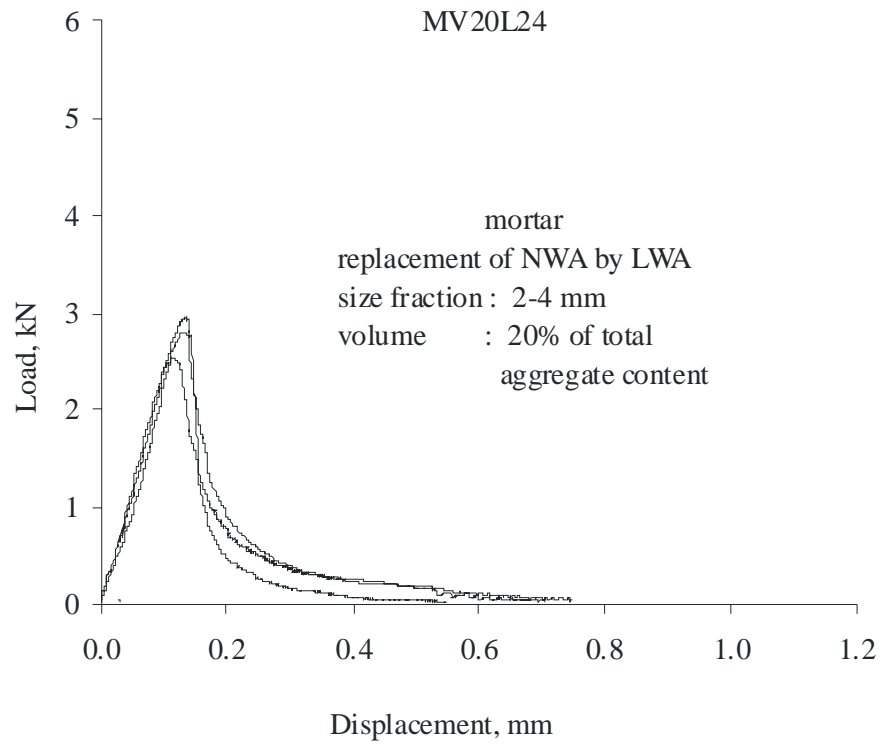


Figure A5. Load displacement diagram for MV20L24 samples.

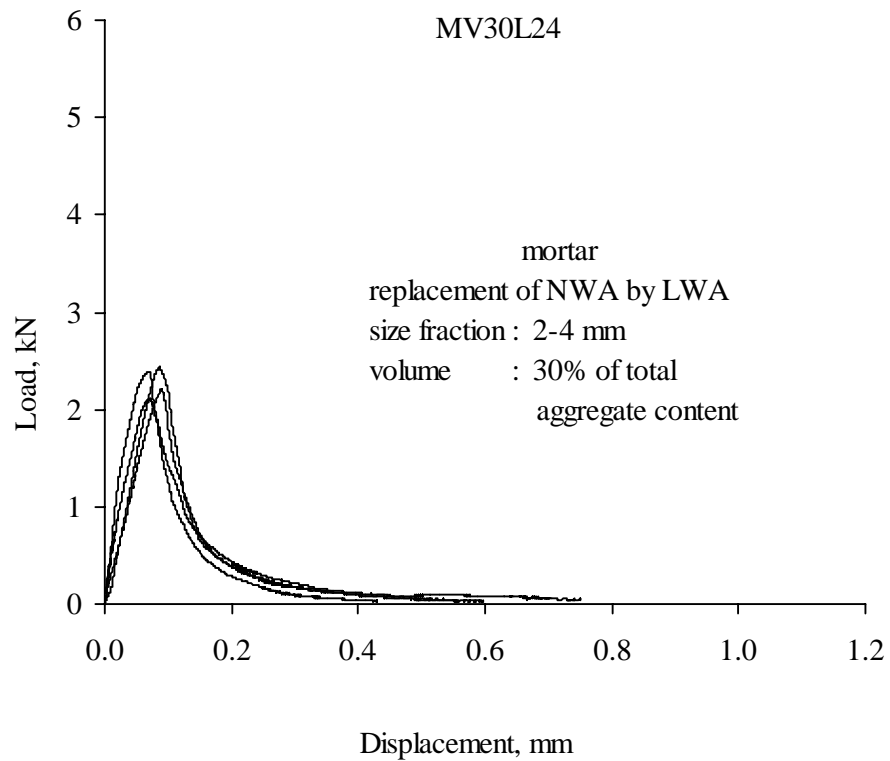


Figure A6. Load displacement diagram for MV30L24 samples.

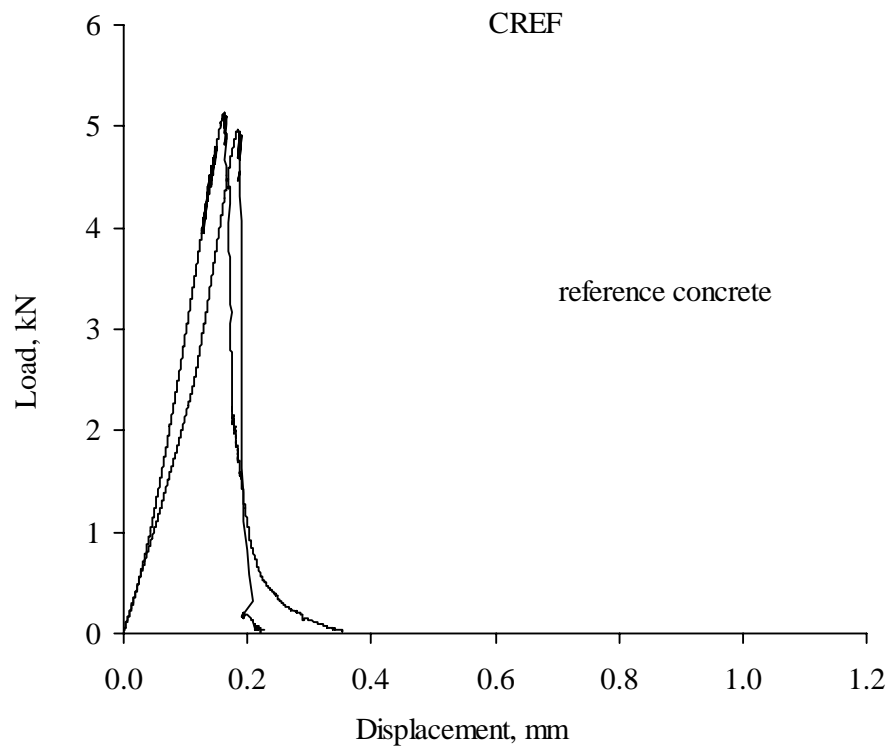


Figure A7. Load displacement diagram for CREF samples.

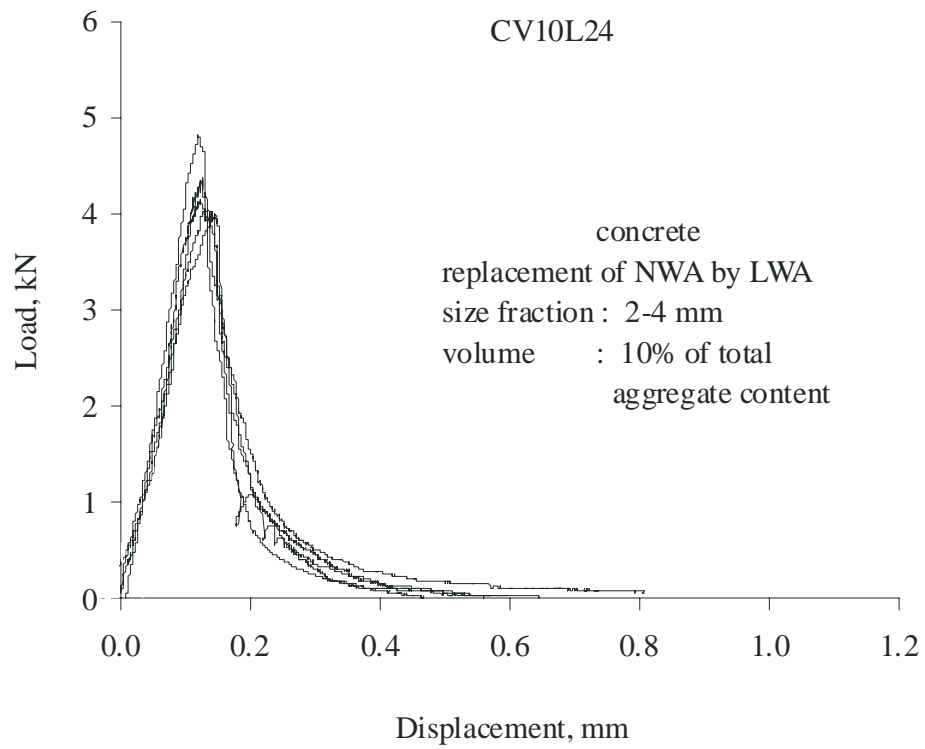


Figure A8. Load displacement diagram for CV10L24 samples.

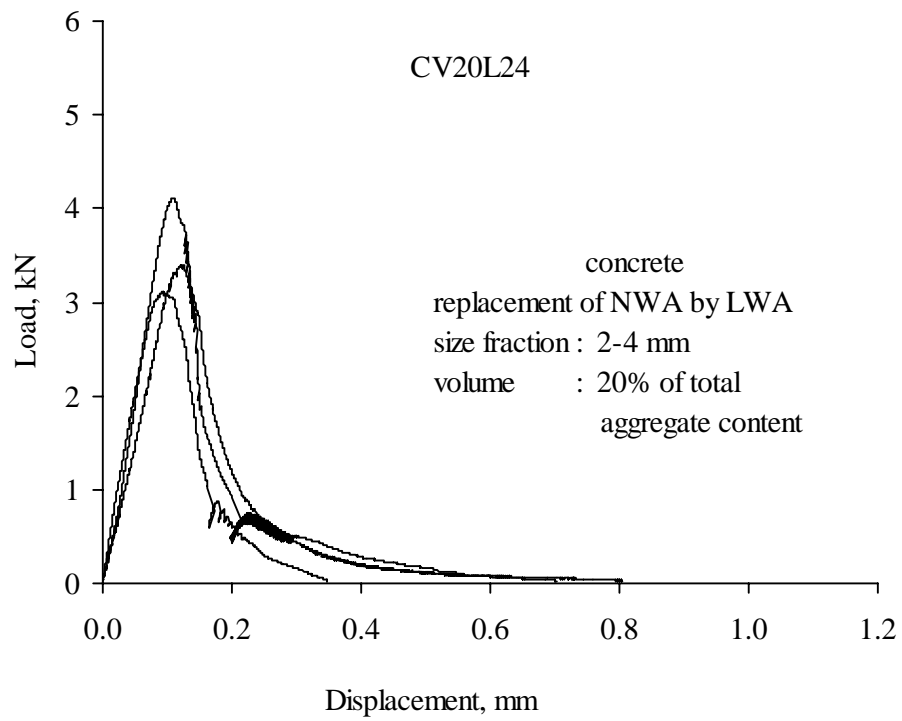


Figure A9. Load displacement diagram for CV20L24 samples.

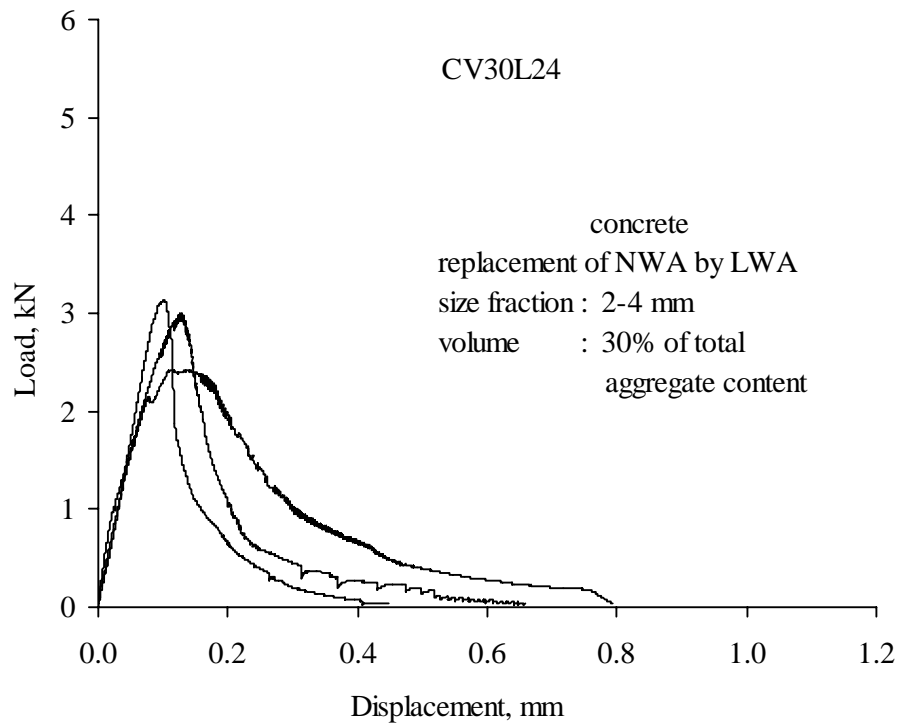


Figure A10. Load displacement diagram for CV30L24 samples.

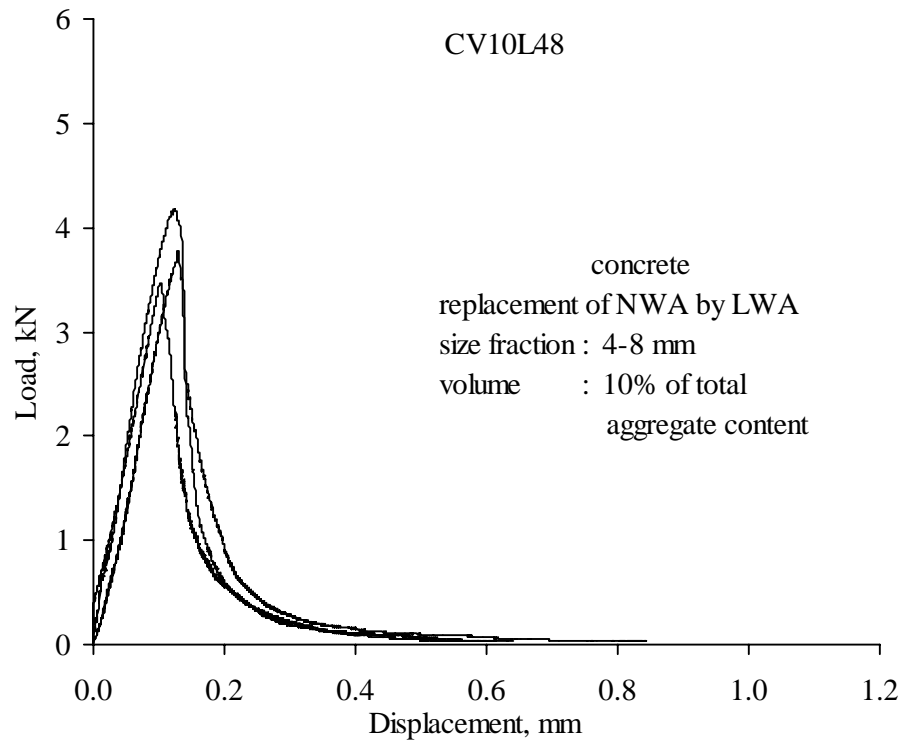


Figure A11. Load displacement diagram for CV10L48 samples.

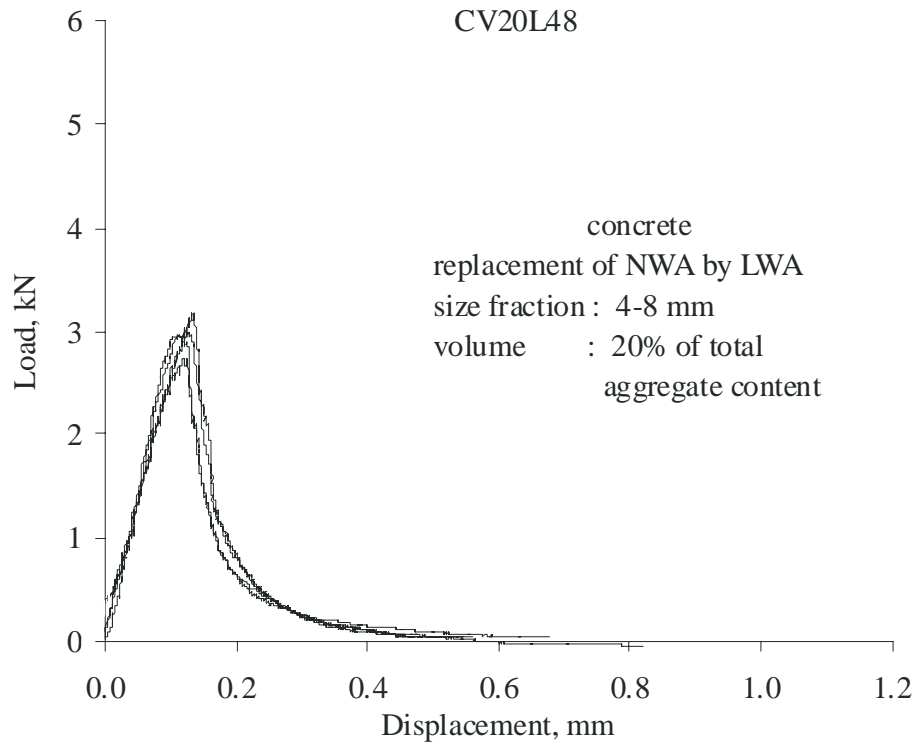


Figure A12. Load displacement diagram for CV20L48 samples.

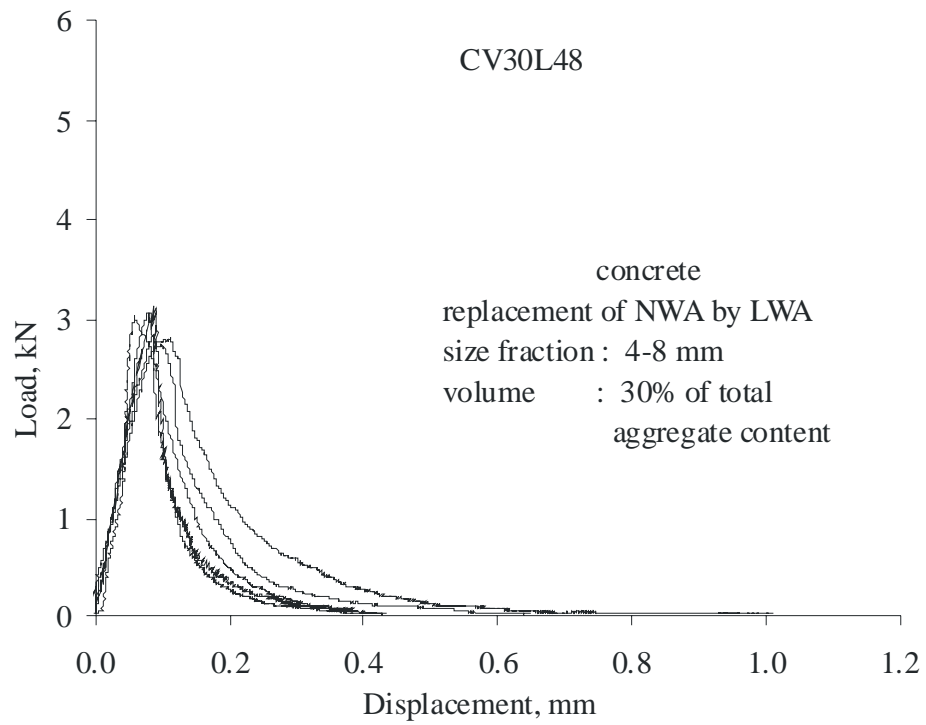


Figure A13. Load displacement diagram for CV30L48 samples.

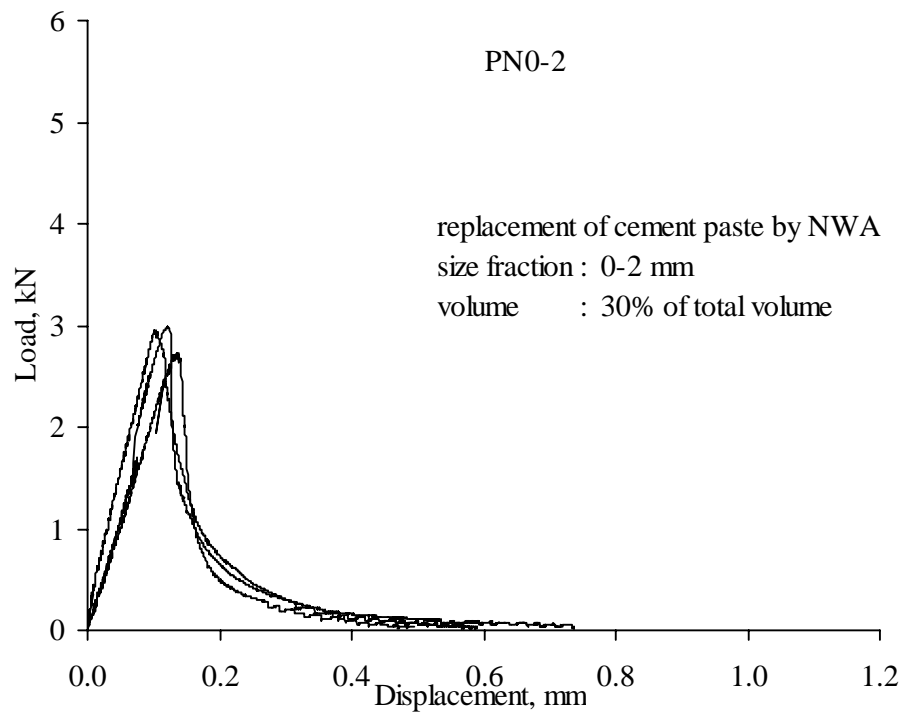


Figure A14. Load displacement diagram for PN0-2 samples.

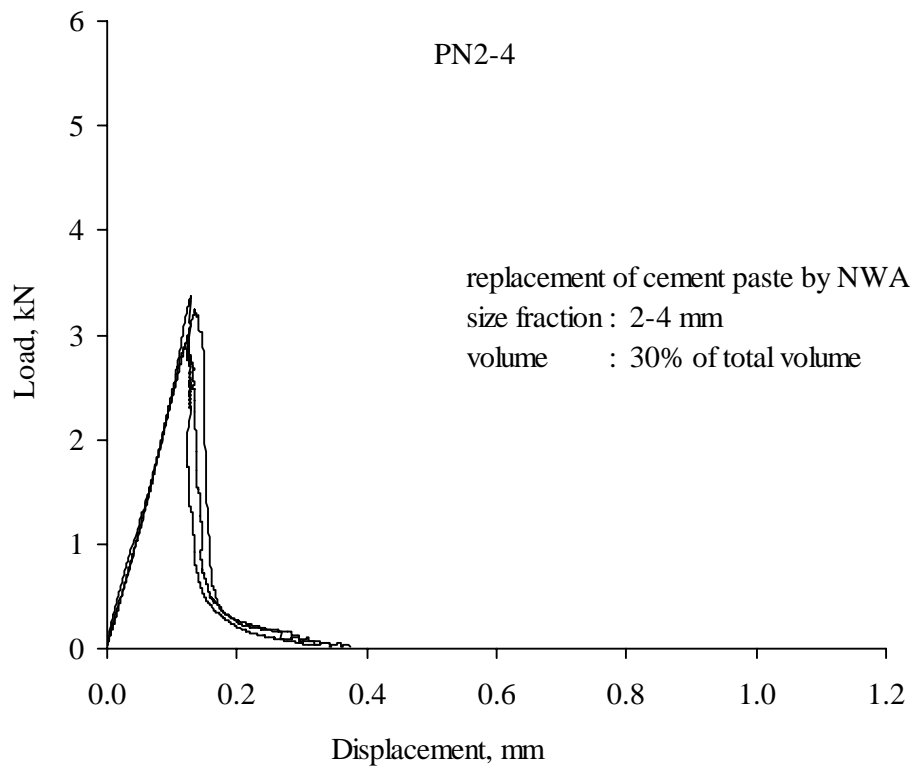


Figure A15. Load displacement diagram for PN2-4 samples.

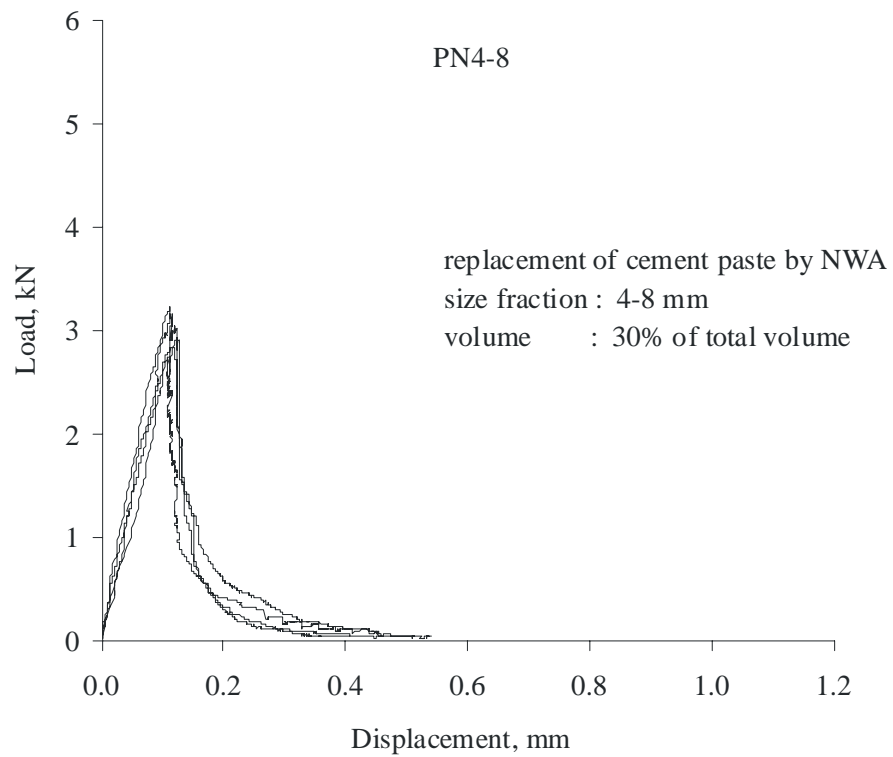


Figure A16. Load displacement diagram for PN4-8 samples.

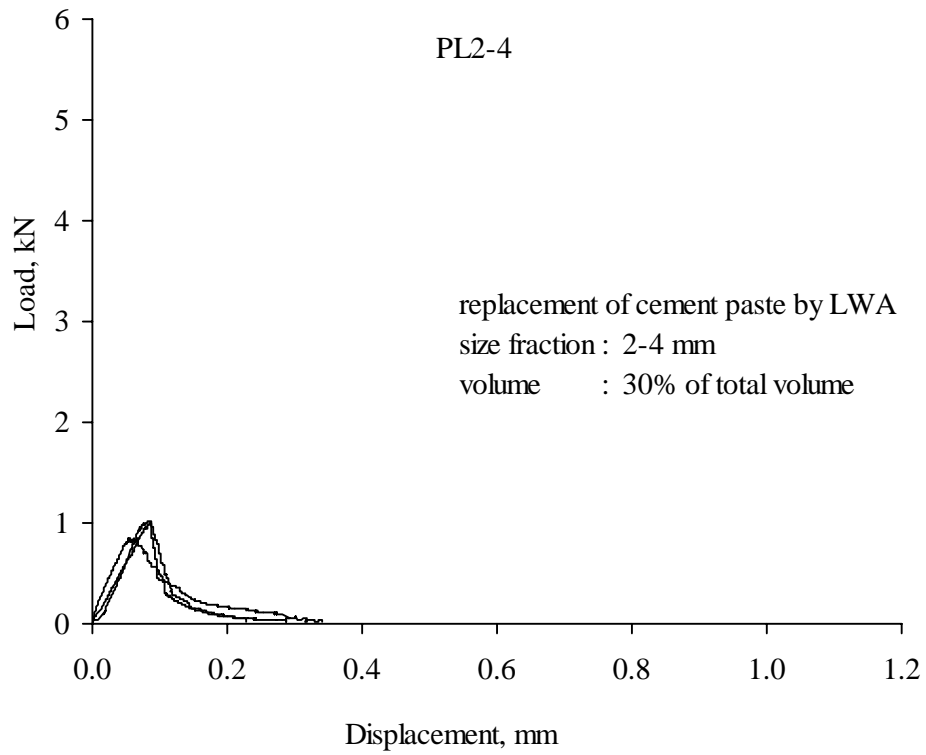


Figure A17. Load displacement diagram for PL2-4 samples.

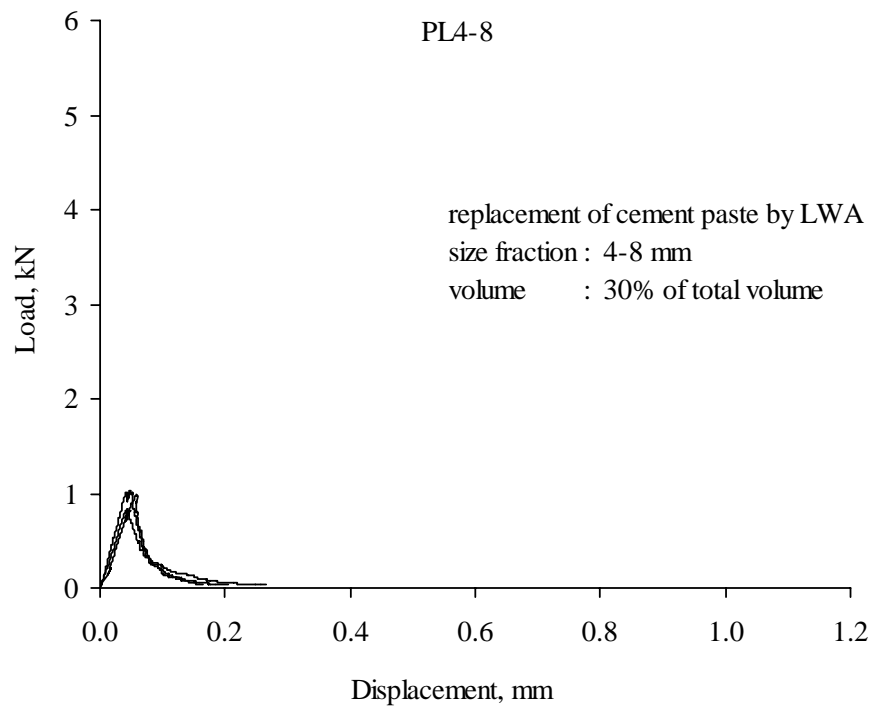


Figure A18. Load displacement diagram for PL4-8 samples.

APPENDIX B

Mercury Intrusion Porosimetry Test Results

Table B1. MIP test results of PREF (reference paste) sample at 1day, 2 and 7 days.

PREF 1 day			PREF 2 days			PREF 7 days		
pore diameter, nm	dv/dD	volume intruded cc/g	pore diameter, nm	dv/dD	volume intruded cc/g	pore diameter, nm	dv/dD	volume intruded cc/g
10840.49	1.646	0.0864	10551.62	3.657	0.0003657	10277.75	3.316	0
438.15	2.552	0.0855	451.55	2.379	0.002379	448.07	3.397	0.0014
141.61	1.539	0.0827	143.12	3.147	0.003147	144.49	5.483	0.004
80.28	7.953	0.0732	79.62	6.729	0.006729	80.06	5.928	0.0054
55.72	1.672	0.0529	54.23	1.526	0.01526	54.32	6.64	0.0064
42.29	1.938	0.0295	40.61	2.773	0.02773	40.61	8.645	0.0074
33.27	1.264	0.0122	31.99	4.125	0.04125	32.2	1.161	0.0084
27.26	4.927	0.0053	26.36	4.905	0.04905	26.33	1.63	0.0096
22.91	1.379	0.0034	22.31	5.427	0.05427	22.16	2.18	0.0111
19.63	6.171	0.0029	19.22	6.244	0.06244	19.07	2.626	0.0126
17.08	6.608	0.0025	16.81	6.471	0.06471	16.65	3.655	0.0145
15.05	5.553	0.0022	14.86	6.527	0.06527	14.71	4.259	0.0166
13.38	5.286	0.0019	13.24	5.469	0.05469	13.12	4.82	0.019
11.89	6.713	0.0016	11.72	4.537	0.04537	11.7	5.077	0.0214
10.38	6.518	0.0012	10.24	3.429	0.03429	10.26	5.509	0.0245
9.06	6.099	0.0008	8.97	2.293	0.02293	8.99	4.935	0.0276
7.99	8.404	0.0004	7.93	1.762	0.01762	7.95	3.648	0.0298
7.11	7.389	0				7.08	3.259	0.0315

Table B2. MIP test results of PREF sample at 28 and 100 days.

PREF 28 days			PREF 100days		
pore diameter, nm	dv/dD	volume intruded cc/g	pore diameter, nm	dv/dD	volume intruded cc/g
10551.62	9.681	0	10017.69	3.096	0
739.64	6.991	0.0003	2850.92	3.691	0.0002
178.4	2.987	0.0013	1236.41	6.226	0.0004
90.35	4.381	0.0025	521.21	1.937	0.0008
59.15	7.186	0.0034	216.48	1.67	0.0017
43.35	9.131	0.0046	110.1	1.64	0.0021
33.55	1.401	0.0058	68.99	2.728	0.0025
26.69	1.87	0.0076	48.89	4.268	0.0031
22.35	1.711	0.009	37.28	8.349	0.0037
19.2	1.947	0.0102	29.64	1.058	0.0048
16.74	2.429	0.0115	24.63	1.399	0.0057
14.77	2.853	0.0129	21.14	1.352	0.0067
13.16	2.217	0.0142	18.25	1.028	0.0074
11.71	3.321	0.0155	15.97	1.165	0.008
10.23	4.042	0.0178	14.12	1.603	0.0088
8.95	4.405	0.0201	12.61	2.092	0.0096
7.92	5.798	0.0229	11.18	2.976	0.0111
7.06	7.028	0.0261	9.72	3.045	0.0129
			8.53	3.666	0.0147
			7.56	5.803	0.0173

Table B3. MIP test results of FMREF (reference fine mortar) sample at 1day, 28 and 100 days.

FMREF 1 day			FMREF 28 days			FMREF 100 days		
pore diameter, nm	dv/dD	volume intruded cc/g	pore diameter, nm	dv/dD	volume intruded cc/g	pore diameter, nm	dv/dD	volume intruded cc/g
227644.93	7.51	0	10017.71	1.386	0.0001	9535.25	1.428	0.0001
30445.87	2.989	0.0055	455.81	2.249	0.0007	1238.16	7.929	0.0002
15277.29	2.368	0.0058	144.61	7.729	0.0033	240.44	4.707	0.0018
10227.19	3.238	0.0058	80.47	1.014	0.0054	106.34	8.636	0.0043
7971.37	2.225	0.0058	54.66	1.435	0.0076	66.21	9.737	0.0062
6205.42	5.952	0.0058	40.77	1.922	0.0097	47.32	1.141	0.0078
643.77	3.903	0.0081	32.07	2.432	0.012	36.12	1.367	0.0091
170.28	5.012	0.0109	26	3.309	0.0146	28.81	2.038	0.0108
88.15	9.793	0.0128	21.99	3.771	0.0172	23.93	2.44	0.0128
58.23	1.881	0.0154	18.97	3.929	0.0197	20.42	2.281	0.0143
42.92	3.187	0.0187	16.66	4.456	0.022	17.72	2.432	0.0159
33.58	4.449	0.0229	14.79	4.542	0.0245	15.58	4.177	0.0175
27.44	5.637	0.0273	13.18	4.554	0.0267	13.83	3.56	0.0198
23.05	6.081	0.0318	11.6	4.313	0.0292	12.32	2.83	0.0214
19.78	5.885	0.0359	10.13	4.121	0.0317	10.87	2.167	0.0227
17.22	4.99	0.0392	8.92	3.156	0.0337	9.52	1.617	0.0234
15.18	4.065	0.0416	7.91	3.206	0.0353	8.38	4.362	0.0254
13.5	4.172	0.0437	7.08	2.978	0.0368	7.44	3.073	0.0272
12.01	3.371	0.0456				6.68	2.071	0.0305
10.52	2.637	0.0474						
9.18	1.084	0.0484						
8.09	1.151	0.049						
7.2	2.437	0.0493						

Table B4. MIP test results of MREF (reference fine mortar) sample at 1day, 28 and 100 days.

MREF 1 day			MREF 28 days			MREF 100 days		
pore diameter, nm	dv/dD	volume intruded cc/g	pore diameter, nm	dv/dD	volume intruded cc/g	pore diameter, nm	dv/dD	volume intruded cc/g
10017.7	4.249	0	10551.62	4.778	0	10551.6	6.401	0
2372.6	1.792	0.0002	549.96	5.514	0.0002	650.01	6.718	0.00073
885.86	2.586	0.0003	160.77	1.78	0.0008	172.56	1.761	0.002649
339.12	6.773	0.0005	87.89	2.384	0.0014	90.64	2.254	0.004324
149.93	2.193	0.0009	58.65	3.648	0.0019	59.51	6.966	0.005081
85.46	4.696	0.0017	43.06	4.637	0.0024	43.5	3.871	0.005189
57.59	1.381	0.0031	33.6	6.48	0.0031	34.01	5.894	0.005622
42.64	3.411	0.0062	27.14	6.725	0.0037	27.8	1.309	0.008568
33.27	5.437	0.0111	22.57	7.112	0.0042	23.3	3.782	0.010297
27.14	5.937	0.0163	19.36	1.147	0.0048	19.92	8.489	0.010514
22.87	5.072	0.0205	16.88	1.264	0.0056	17.3	9.173	0.010649
19.61	3.561	0.0234	14.89	1.62	0.0063	15.22	2.28	0.010865
17.06	2.716	0.0251	13.23	1.672	0.0072	13.53	2.104	0.011243
15.02	2.187	0.0265	11.77	2.314	0.0081	12.02	1.167	0.011432
13.36	1.685	0.0274	10.26	3.293	0.0099	10.54	1.382	0.011622
11.96	1.018	0.0282	9	3.751	0.0119	9.2	2.818	0.011946
10.55	2.077	0.0283	7.96	3.414	0.014	8.12	3.166	0.012432
9.2	2.982	0.0285	7.09	3.061	0.0154	7.22	2.796	0.012811
8.11	3.638	0.0287						
7.21	3.114	0.0288						

Table B5. MIP test results of MV10L24 (10% total aggregate content replaced by 2-4 mm LWA- mortar) sample at 1day, 28 and 100 days.

MV10L24 1 day			MV10L24 28 days			MV10L24 100 days		
pore diameter, nm	dv/dD	volume intruded cc/g	pore diameter, nm	dv/dD	volume intruded cc/g	pore diameter, nm	dv/dD	volume intruded cc/g
10277.71	2.42	0	10277.69	6.492	0	10551.6	6.401	0
2602.24	3.68	0.0002	1137.3	2.498	0.0012	650.01	6.718	0.0027
1014.16	2.736	0.0004	330.7	3.798	0.003	172.56	1.761	0.0098
386.48	4.647	0.0004	140.85	7.676	0.0047	90.64	2.254	0.016
164.36	3.191	0.0009	81.8	1.856	0.0077	59.51	6.966	0.0188
90.94	1.267	0.0027	55.96	3.54	0.0121	43.5	3.871	0.0192
60.31	2.969	0.0063	41.86	3.649	0.0172	34.01	5.589	0.0208
43.96	8.347	0.0133	32.97	2.695	0.0203	27.8	1.309	0.0317
34.07	9.495	0.0253	26.92	5.417	0.0239	23.3	3.782	0.0381
27.19	6.018	0.032	22.66	3.715	0.0271	19.92	8.489	0.0389
22.76	5.485	0.0365	19.51	7.394	0.0311	17.3	9.173	0.0394
19.51	3.846	0.0396	17.04	2.952	0.0341	15.22	2.28	0.0402
16.97	3.204	0.0417	15.03	1.996	0.0353	13.53	2.104	0.0416
14.94	1.995	0.0431	13.37	1.496	0.0361	12.02	1.167	0.0423
13.28	1.494	0.0439	11.92	1.9	0.037	10.54	1.382	0.043
11.82	9.779	0.0445	10.45	1.721	0.038	9.2	2.818	0.0442
10.39	9.249	0.0451	9.14	2.814	0.0393	8.12	3.166	0.046
9.07	6.703	0.0455	8.08	3.307	0.041	7.22	2.796	0.0474
8	7.16	0.0459	7.2	2.869	0.0425			
7.11	1.069	0.0463						

Table B6. MIP test results of MV20L24 (20% total aggregate content replaced by 2-4 mm LWA- mortar) sample at 1day, 28 and 100 days.

MV10L24 1 day			MV10L24 28 days			MV10L24 100 days		
pore diameter, nm	dv/dD	volume intruded cc/g	pore diameter, nm	dv/dD	volume intruded cc/g	pore diameter, nm	dv/dD	volume intruded cc/g
10551.6	1.01	0	9770.5	4.769	0	10551.63	1.113	0
4044.99	1.124	0.0005	2103.35	1.009	0.0004	3544.63	2.223	0.0008
2440.4	1.307	0.0007	731.32	5.686	0.0013	1679.89	2.971	0.0016
1411.96	1.726	0.0011	277.2	1.625	0.0068	831.73	4.421	0.0027
726.93	1.873	0.0016	129.65	1.275	0.0113	371.46	8.17	0.0048
339.41	3.795	0.0025	77.66	5.079	0.0159	168.78	1.589	0.0087
158.87	8.62	0.0044	54.38	1.238	0.0319	94.96	2.326	0.0143
89.74	1.975	0.0078	41.06	4.897	0.0438	62.48	1.163	0.0173
59.64	2.605	0.0122	32.46	5.357	0.0458	45.35	3.473	0.0193
43.71	2.063	0.0155	26.73	7.257	0.0539	34.74	1.05	0.0292
33.96	9.299	0.017	22.52	2.251	0.0562	27.85	2.677	0.0359
27.3	1.057	0.0179	19.33	3.079	0.0576	23.2	1.129	0.0367
22.69	5.169	0.0186	16.83	6.906	0.061	19.79	1.408	0.0376
19.38	4.892	0.0188	14.83	2.597	0.0635	17.16	1.592	0.0385
16.82	7.291	0.0193	13.2	2.977	0.065	15.08	1.804	0.0395
14.79	3.667	0.0196	11.78	2.868	0.0664	13.39	1.931	0.0404
13.13	2.16	0.0197	10.29	3.16	0.0682	11.95	2.863	0.0417
11.71	2.936	0.0198	8.99	2.562	0.0699	10.47	3.915	0.0435
10.3	3.053	0.02	7.94	2.764	0.0713	9.13	3.165	0.0458
9	3.179	0.0202	7.07	3.449	0.0729	8.04	4.192	0.0476
7.92	5.343	0.0204				7.14	4.493	0.0476
7.04	1.729	0.0209						

Table B7. MIP test results of MV30L24 (30% total aggregate content replaced by 2-4 mm LWA- mortar) sample at 1day, 28 and 100 days.

MV30L24 1 day			MV30L24 28 days			MV30L24 100 days		
pore diameter, nm	dv/dD	volume intruded cc/g	pore diameter, nm	dv/dD	volume intruded cc/g	pore diameter, nm	dv/dD	volume intruded cc/g
9311.02	2.267	0.0001	10840.51	7.478	0	10840.49	2.093	0
669.81	2.511	0.0103	650.3	3.246	0.0227	4090.57	6.093	0.0014
184.04	6.717	0.0346	171.36	1.449	0.0389	2055.7	1.011	0.004
96.04	1.726	0.0638	88.75	8.764	0.0416	1081.66	1.244	0.0073
64.86	2.592	0.1087	58.52	1.443	0.0434	522.89	1.667	0.0118
47.31	4.724	0.127	43.04	2.832	0.0465	235.52	2.478	0.0191
36.38	1.539	0.1293	33.63	1.65	0.0488	119.78	2.457	0.0266
28.87	9.671	0.1304	27.75	3.694	0.0508	73.85	2.269	0.0317
24.04	1.135	0.1313	23.99	3.877	0.0537	51.85	1.856	0.0348
20.49	7.465	0.1319	20.59	1.827	0.0553	39.15	2.944	0.0373
17.76	1.436	0.1326	17.89	1.864	0.0563	30.91	9.598	0.0426
15.61	6.05	0.1332	15.74	2.904	0.0576	26.93	2.709	0.0524
13.86	6.566	0.1335	13.98	6.86	0.06	23.86	1.94	0.0683
12.35	1.244	0.134	12.47	4.692	0.0637	20.81	6.67	0.073
10.85	1.499	0.1348	10.95	2.313	0.065	18.17	4.655	0.077
9.47	9.801	0.1355	9.54	2.44	0.0664	15.95	1.628	0.0783
8.33	1.654	0.1362	8.4	2.883	0.0678	14.12	1.681	0.0791
7.4	1.157	0.137	7.46	3.997	0.0696			

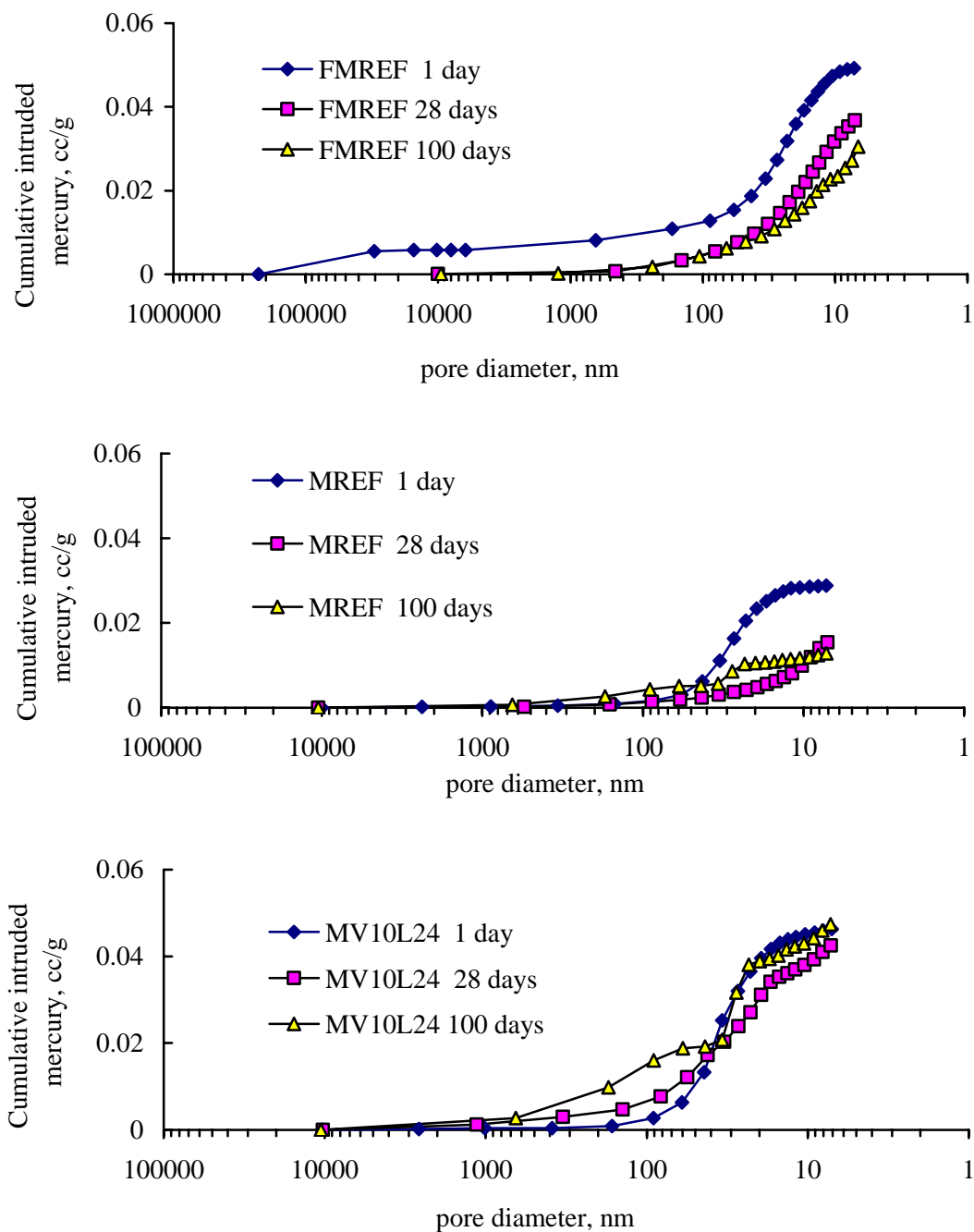


Figure B1. The variations of cumulative introduced mercury volume of FMREF, MREF and MV10L24 samples at 1, 28 and 100 days of ages, respectively.

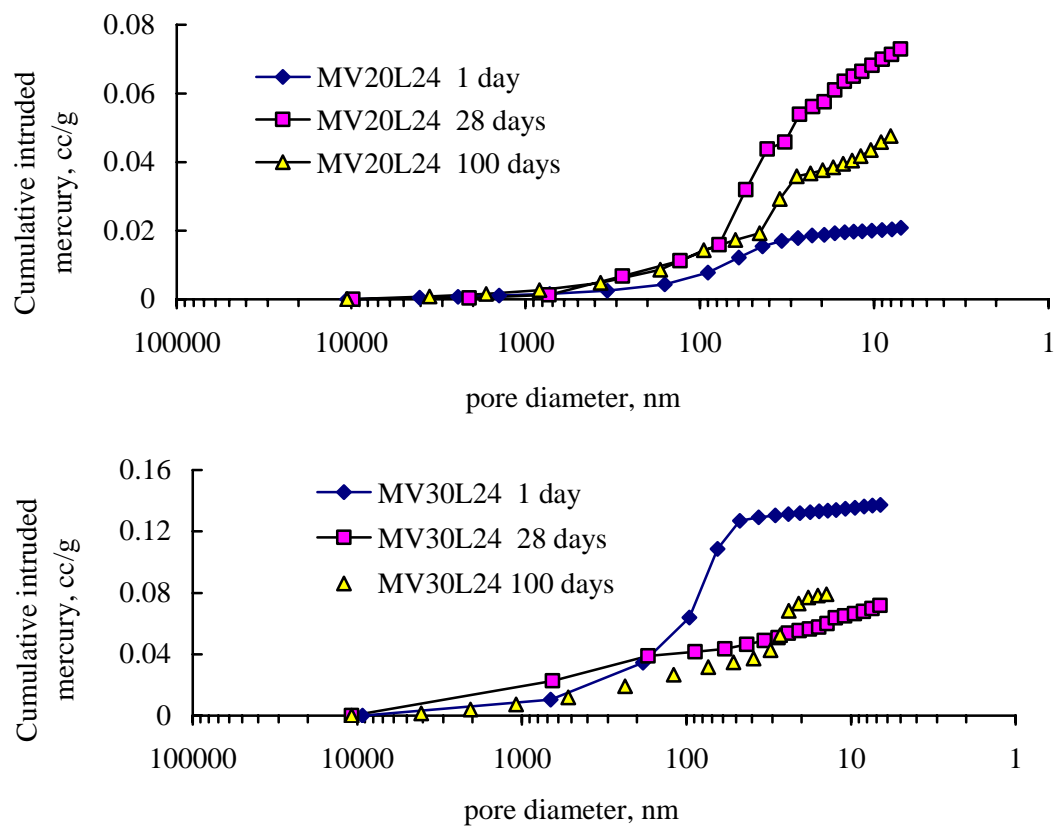
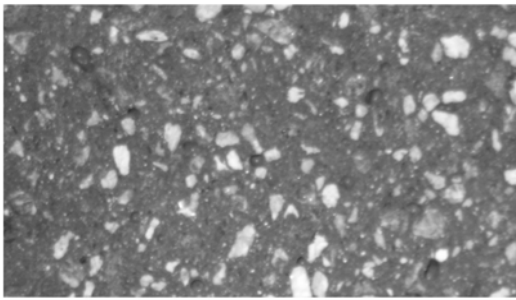


Figure B2. The variations of cumulative introduced mercury volume of MV20L24 and MV30L24 samples at 1, 28 and 100 days of ages, respectively.

APPENDIX C

Image Analysis Data



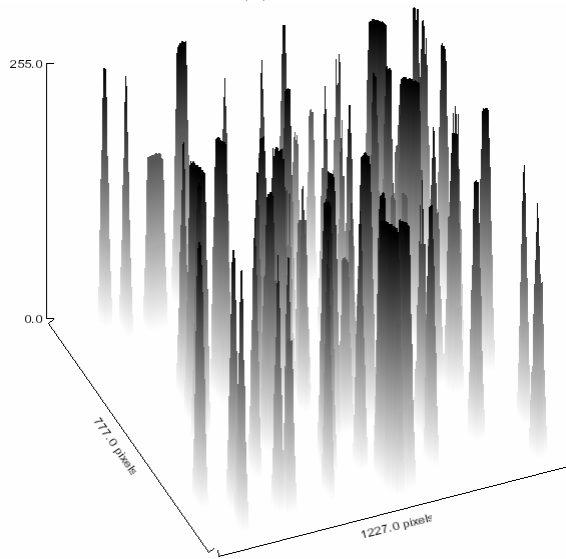
(a)



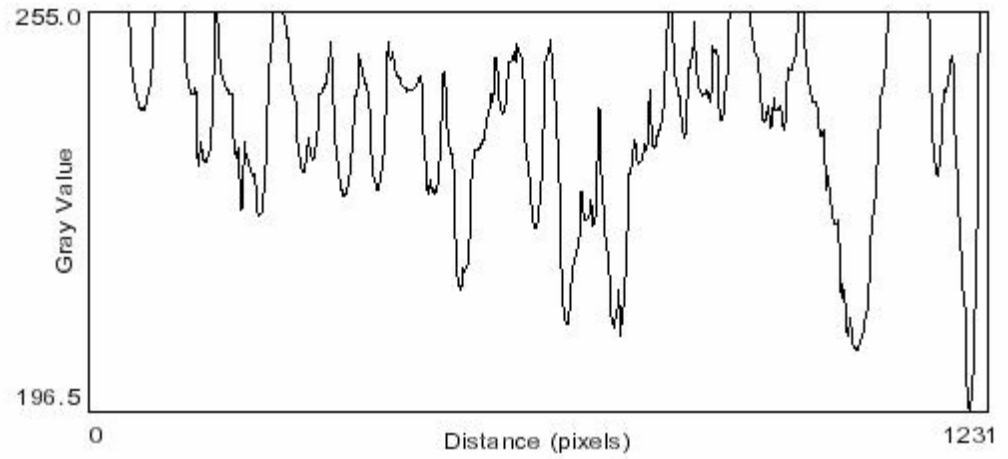
(b)



(c)



(d)



(e)

Figure C1. a) Image of CV10L24, b) selected pumices in binary image of CV10L24, c) ellipses mask, d) surface of pumices and (e) plot drawing of CV10L24.

Table C1. Image analysis results for CV10L24 series.

	Area	xm	ym	major	minor	angle		Area	xm	ym	major	minor	angle		Area	xm	ym	major	minor	angle
1	0.068	4.652	0.558	0.385	0.226	13.4	24	0.024	3.307	2.469	0.19	0.159	24	47	0.023	6.071	3.935	0.194	0.152	168.7
2	0.026	2.767	0.645	0.197	0.167	50.8	25	0.027	7.159	2.584	0.306	0.114	25	48	0.037	3.713	4.239	0.399	0.12	63.5
3	0.03	6.963	0.706	0.249	0.152	75.1	26	0.077	4.057	2.652	0.388	0.253	26	49	0.125	5.253	4.469	0.623	0.256	59.8
4	0.013	7.49	0.854	0.157	0.11	20.4	27	0.023	9.53	2.759	0.304	0.097	27	50	0.021	7.557	4.388	0.257	0.106	98.0
5	0.02	3.071	0.921	0.226	0.114	86.9	28	0.049	4.976	2.74	0.347	0.182	28	51	0.084	6.497	4.564	0.466	0.23	58.5
6	0.015	9.563	0.908	0.201	0.096	159.1	29	0.018	5.49	2.841	0.255	0.092	29	52	0.051	2.179	4.564	0.365	0.177	63.9
7	0.052	3.725	0.969	0.464	0.142	179.6	30	0.103	3.213	3.057	0.506	0.259	30	53	0.028	9.801	4.625	0.255	0.142	64.6
8	0.032	9.841	1.03	0.246	0.168	103.1	31	0.021	8.172	2.969	0.171	0.154	31	54	0.038	8.611	4.692	0.236	0.205	31.4
9	0.129	8.854	1.145	0.462	0.355	156.3	32	0.031	5.753	2.976	0.254	0.156	32	55	0.024	5.875	4.686	0.2	0.15	17.0
10	0.02	7.956	1.111	0.246	0.106	109.8	33	0.02	7.902	2.983	0.204	0.127	33	56	0.036	2.767	4.847	0.289	0.157	74.7
11	0.025	6.051	1.233	0.215	0.147	45.7	34	0.055	5.104	3.091	0.347	0.203	34	57	0.013	6.658	4.814	0.162	0.101	128.4
12	0.016	6.84	1.206	0.2	0.104	163.7	35	0.025	4.868	3.152	0.251	0.126	35	58	0.023	4.044	4.882	0.211	0.139	38.4
13	0.021	5.159	1.246	0.2	0.133	43.7	36	0.018	6.328	3.165	0.179	0.127	36	59	0.034	7.375	4.935	0.253	0.172	82.2
14	0.04	9.8	1.314	0.298	0.171	132.2	37	0.024	5.557	3.287	0.188	0.16	37	60	0.033	4.862	5.037	0.342	0.123	61.7
15	0.022	4.374	1.26	0.23	0.124	167.3	38	0.05	9.807	3.361	0.267	0.237	38	61	0.151	6.219	5.172	0.563	0.341	102.6
16	0.032	9.861	1.908	0.324	0.127	87.5	39	0.045	2.997	3.415	0.289	0.197	39	62	0.088	6.551	5.192	0.429	0.262	92.4
17	0.043	6.125	1.969	0.241	0.225	69.9	40	0.023	4.368	3.429	0.197	0.147	40	63	0.02	3.625	5.111	0.187	0.139	39.3
18	0.058	8.814	2.003	0.403	0.183	4.4	41	0.031	8.544	3.429	0.273	0.146	41	64	0.028	2.645	5.28	0.26	0.137	77.2
19	0.045	8.415	2.091	0.268	0.214	89.1	42	0.017	6.557	3.455	0.191	0.113	42	65	0.019	3.827	5.212	0.207	0.116	0.6
20	0.039	8.064	2.138	0.293	0.17	88.6	43	0.085	6.733	3.679	0.389	0.276	43							
21	0.021	6.922	2.097	0.188	0.14	162.7	44	0.044	8.834	3.659	0.305	0.183	44							
22	0.017	7.226	2.239	0.172	0.125	88.3	45	0.059	5.807	3.841	0.393	0.192	45							
23	0.108	8.706	2.429	0.522	0.262	140.0	46	0.05	4.307	3.909	0.295	0.218	46							

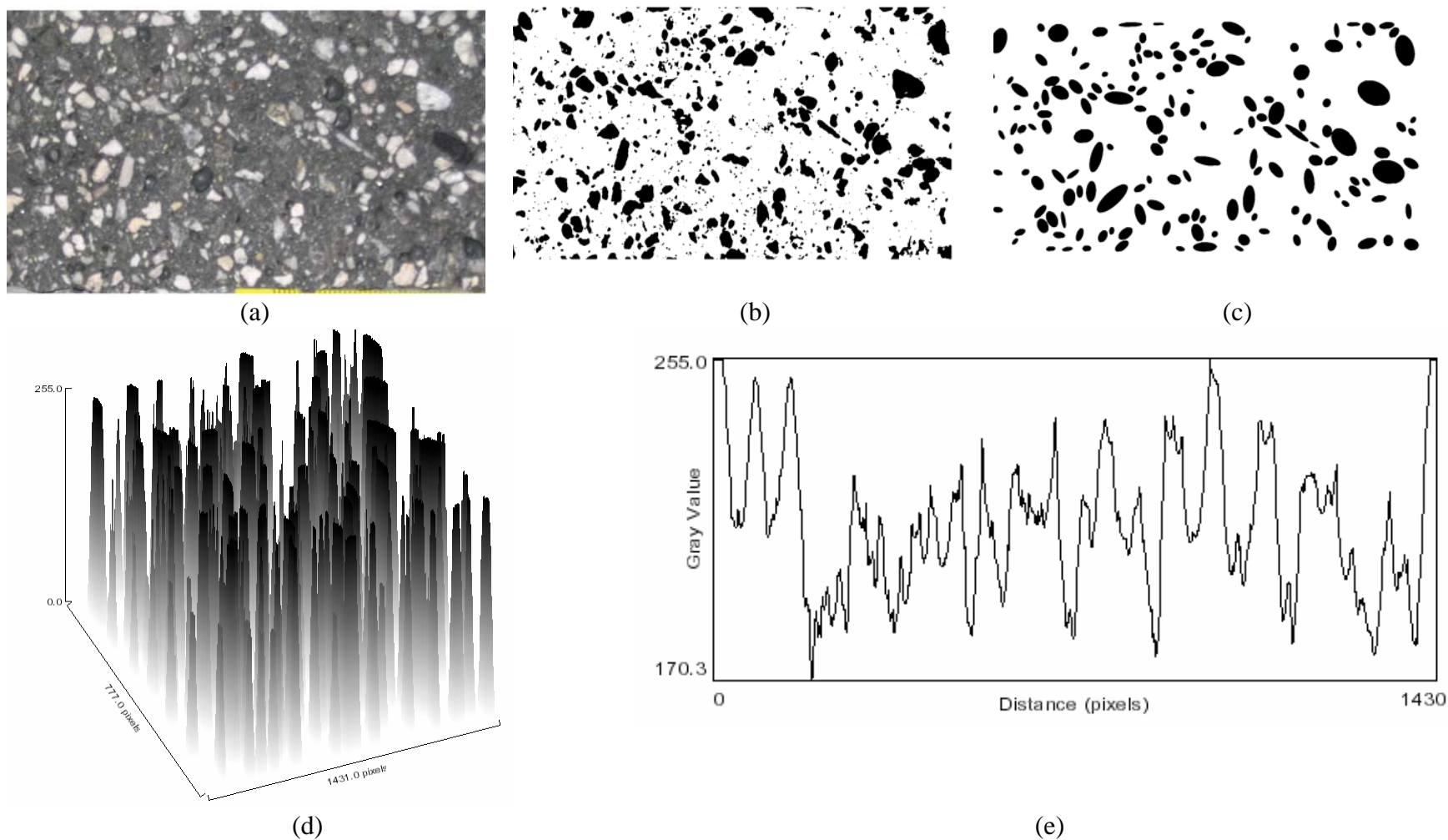


Figure C2. a) Image of CV20L24, b) selected pumices in binary image of CV20L24, c) ellipses mask, d) surface of pumices and (e) plot drawing of CV20L24.

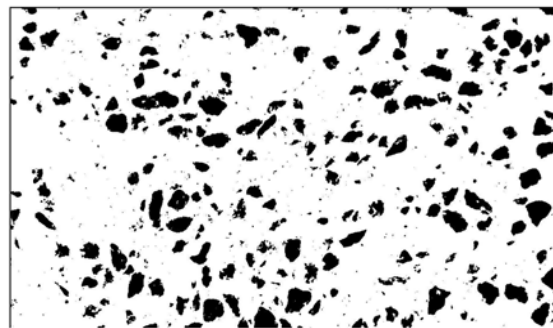
Table C2. Image analysis results for CV20L24 series.

	Area	xm	ym	major	minor	angle		Area	xm	ym	major	minor	angle		Area	xm	ym	major	minor	angle
1	0.107	6.185	0.517	0.542	0.251	157.6	53	0.046	2.051	2.043	0.351	0.166	157.6	105	0.028	2.659	3.733	0.321	0.11	36.8
2	0.04	9.551	0.449	0.336	0.151	8.3	54	0.143	3.665	2.057	0.642	0.284	8.3	106	0.02	1.009	3.699	0.209	0.123	163.9
3	0.041	3.922	0.428	0.522	0.101	2.0	55	0.027	3.084	2.024	0.238	0.142	2.0	107	0.028	5.165	3.774	0.296	0.12	119.5
4	0.021	8.82	0.421	0.294	0.091	0.9	56	0.028	4.828	2.132	0.308	0.118	0.9	108	0.052	4.881	3.855	0.31	0.212	161.3
5	0.012	4.534	0.415	0.248	0.064	0.4	57	0.066	6.55	2.185	0.401	0.211	0.4	109	0.016	4.334	3.855	0.186	0.113	103.7
6	0.066	9.159	0.53	0.328	0.256	138.3	58	0.027	6.962	2.091	0.22	0.158	138.3	110	0.066	1.882	3.929	0.346	0.241	123.1
7	0.028	8.449	0.557	0.319	0.112	95.3	59	0.06	2.949	2.239	0.39	0.195	95.3	111	0.028	8.847	3.888	0.245	0.147	137.3
8	0.024	1.956	0.496	0.192	0.156	118.7	60	0.028	8.233	2.165	0.2	0.175	118.7	112	0.022	9.097	3.909	0.228	0.12	132.4
9	0.14	2.334	0.618	0.449	0.397	16.9	61	0.018	1.855	2.226	0.187	0.124	16.9	113	0.081	3.057	4.118	0.469	0.219	85.6
10	0.057	3.253	0.591	0.341	0.212	7.9	62	0.138	7.125	2.395	0.523	0.336	7.9	114	0.033	4.125	4.044	0.273	0.152	27.4
11	0.037	9.713	0.604	0.263	0.177	47.0	63	0.051	5.125	2.314	0.308	0.211	47.0	115	0.216	3.524	4.274	0.868	0.317	42.3
12	0.156	1.03	0.787	0.581	0.343	71.9	64	0.015	1.435	2.273	0.165	0.115	71.9	116	0.032	2.807	4.118	0.284	0.145	91.9
13	0.042	5.409	0.631	0.312	0.17	41.3	65	0.014	0.956	2.307	0.177	0.099	41.3	117	0.127	6.524	4.287	0.619	0.262	85.4
14	0.03	4.192	0.726	0.24	0.157	88.5	66	0.03	4.138	2.294	0.264	0.143	88.5	118	0.046	8.847	4.111	0.313	0.186	137.3
15	0.228	9.949	1.003	0.698	0.416	102.5	67	0.033	4.766	2.382	0.243	0.175	102.5	119	0.081	2.578	4.246	0.388	0.267	85.7
16	0.015	6.497	0.766	0.173	0.107	58.6	68	0.045	2.036	2.415	0.331	0.174	58.6	120	0.016	8.462	4.179	0.184	0.108	117.4
17	0.089	8.388	0.902	0.407	0.279	170.3	69	0.034	6.807	2.49	0.236	0.182	170.3	121	0.038	9.382	4.28	0.328	0.149	9.3
18	0.037	5.605	0.847	0.31	0.153	9.5	70	0.117	4.456	2.645	0.446	0.335	9.5	122	0.097	6.165	4.524	0.481	0.257	87.7
19	0.013	8.942	0.868	0.159	0.106	106.5	71	0.031	6.584	2.591	0.267	0.149	106.5	123	0.066	4.476	4.422	0.405	0.206	160.4
20	0.024	4.895	0.895	0.229	0.135	34.7	72	0.014	10.132	2.544	0.16	0.111	34.7	124	0.017	8.645	4.388	0.186	0.118	146.4
21	0.025	4.084	0.942	0.228	0.139	86.6	73	0.035	7.699	2.665	0.27	0.168	86.6	125	0.035	10.03	4.557	0.349	0.129	94.6
22	0.029	7.523	0.935	0.201	0.185	101.0	74	0.051	2.084	2.692	0.32	0.204	101.0	126	0.084	4.138	4.625	0.484	0.221	106.3
23	0.019	2.693	1.023	0.221	0.107	71.5	75	0.02	5.523	2.672	0.202	0.126	71.5	127	0.046	1.943	4.564	0.362	0.16	48.3
24	0.028	5.327	1.037	0.224	0.157	3.3	76	0.034	9.868	2.699	0.262	0.167	3.3	128	0.027	7.544	4.536	0.204	0.171	71.8
25	0.029	4.307	1.077	0.219	0.17	165.8	77	0.026	1.362	2.739	0.273	0.122	165.8	129	0.022	1.009	4.523	0.219	0.129	173.7
26	0.055	5.01	1.118	0.317	0.221	147.9	78	0.016	1.766	2.699	0.206	0.1	147.9	130	0.04	5.355	4.638	0.297	0.171	74.4
27	0.028	4.523	1.104	0.225	0.158	141.7	79	0.065	7.578	2.828	0.618	0.134	141.7	131	0.07	2.199	4.733	0.38	0.236	115.6
28	0.013	5.753	1.137	0.164	0.098	74.9	80	0.027	1.537	2.746	0.219	0.155	74.9	132	0.028	2.449	4.746	0.382	0.093	99.7

	Area	xm	ym	major	minor	angle		Area	xm	ym	major	minor	angle		Area	xm	ym	major	minor	angle
29	0.019	4.118	1.185	0.237	0.101	106.8	81	0.285	8.554	2.993	0.865	0.419	106.8	133	0.017	6.645	4.685	0.18	0.122	66.6
30	0.047	1.962	1.212	0.329	0.184	134.7	82	0.058	7.036	2.807	0.457	0.161	134.7	134	0.036	7.794	4.732	0.273	0.168	61.9
31	0.072	6.219	1.213	0.446	0.207	158.1	83	0.017	6.294	2.794	0.221	0.097	158.1	135	0.042	5.098	4.719	0.26	0.207	19.4
32	0.042	5.49	1.28	0.247	0.217	35.7	84	0.02	10.104	2.807	0.193	0.131	35.7	136	0.02	5.51	4.733	0.192	0.133	68.1
33	0.019	3.962	1.28	0.18	0.137	115.2	85	0.101	2.895	2.895	0.441	0.292	115.2	137	0.061	1.996	4.881	0.335	0.233	114.8
34	0.134	5.834	1.409	0.506	0.336	13.0	86	0.017	1.091	2.868	0.223	0.099	13.0	138	0.071	8.179	4.909	0.459	0.198	130.7
35	0.023	2.916	1.348	0.24	0.123	29.1	87	0.034	4.632	2.962	0.228	0.192	29.1	139	0.043	4.713	4.936	0.326	0.166	74.3
36	0.031	4.956	1.395	0.211	0.186	0.6	88	0.015	7.968	3.084	0.246	0.079	0.6	140	0.081	5.395	5.03	0.402	0.258	107.8
37	0.096	7.679	1.49	0.369	0.333	42.7	89	0.138	3.172	3.355	0.696	0.252	42.7	141	0.015	3.51	4.989	0.173	0.113	81.0
38	0.013	3.361	1.53	0.141	0.113	22.6	90	0.059	4.503	3.185	0.32	0.236	22.6	142	0.06	3.814	5.051	0.357	0.215	39.3
39	0.027	4.03	1.577	0.212	0.163	100.6	91	0.038	1.463	3.172	0.251	0.192	100.6	143	0.035	2.808	5.077	0.308	0.144	70.9
40	0.014	0.874	1.557	0.164	0.107	124.7	92	0.016	3.476	3.132	0.162	0.127	124.7	144	0.024	6.861	5.003	0.239	0.13	173.0
41	0.026	4.584	1.571	0.198	0.164	20.8	93	0.068	9.449	3.26	0.348	0.249	20.8	145	0.027	1.497	5.023	0.25	0.138	21.5
42	0.15	2.308	1.841	0.639	0.298	129.7	94	0.058	6.625	3.395	0.456	0.161	129.7	146	0.042	3.314	5.111	0.288	0.187	62.3
43	0.015	1.281	1.665	0.2	0.097	54.2	95	0.057	7.989	3.429	0.313	0.233	54.2	147	0.015	5.773	5.064	0.15	0.13	57.6
44	0.068	2.719	1.807	0.384	0.227	134.1	96	0.045	8.328	3.435	0.313	0.183	134.1	148	0.03	2.354	5.084	0.264	0.144	173.7
45	0.306	9.267	1.949	0.747	0.522	155.4	97	0.089	5.609	3.442	0.593	0.192	155.4	149	0.051	6.415	5.192	0.273	0.238	139.2
46	0.037	3.179	1.841	0.289	0.164	134.2	98	0.059	10.084	3.496	0.359	0.209	134.2	150	0.033	7.577	5.199	0.26	0.159	105.9
47	0.071	1.489	1.882	0.438	0.206	143.3	99	0.29	9.591	3.686	0.713	0.517	143.3	151	0.043	9.584	5.206	0.253	0.214	88.9
48	0.016	3.496	1.807	0.169	0.119	151.6	100	0.072	7.118	3.639	0.421	0.218	151.6	152	0.049	8.348	5.28	0.324	0.193	79.0
49	0.019	3.949	1.848	0.173	0.14	18.5	101	0.025	6.72	3.665	0.234	0.136	18.5	153	0.078	9.125	5.273	0.43	0.23	17.4
50	0.029	4.166	1.902	0.277	0.132	36.6	102	0.101	7.848	3.888	0.567	0.227	36.6	154	0.013	1.389	5.226	0.177	0.093	47.6
51	0.027	7.659	1.949	0.229	0.151	104.3	103	0.019	1.618	3.692	0.181	0.135	104.3	155	0.066	10.091	5.294	0.324	0.261	164.0
52	0.015	5.239	1.915	0.165	0.114	170.0	104	0.049	2.341	3.78	0.395	0.157	170.0	156	0.05	3.733	5.327	0.342	0.185	36.9



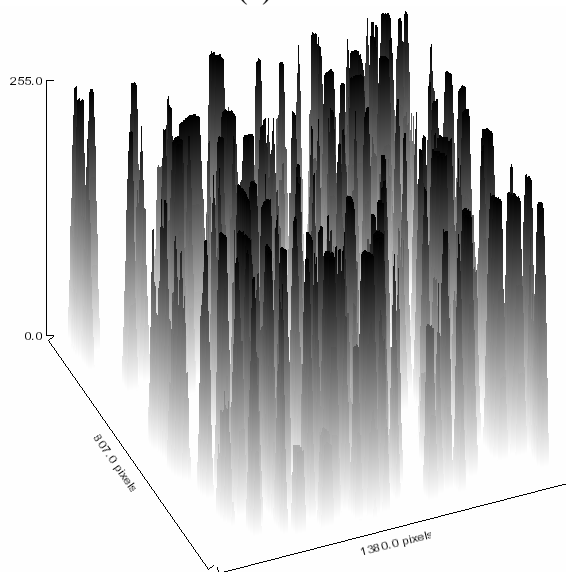
(a)



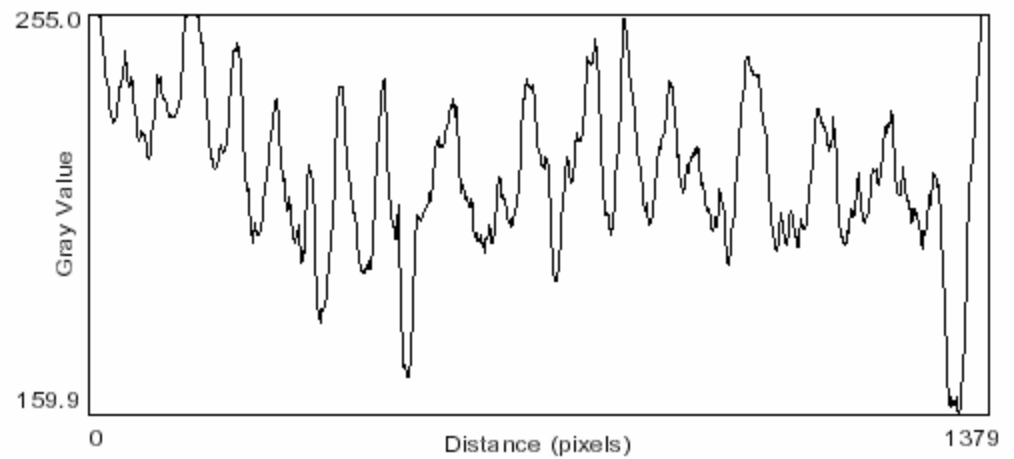
(b)



(c)



(d)



(e)

Figure C3. a) Image of CV30L24, b) selected pumices in binary image of CV30L24, c) ellipses mask, d) surface of pumices and (e) plot drawing of CV30L24.

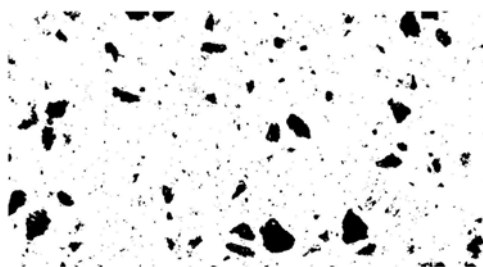
Table C3. Image analysis results for CV30L24 series.

	Area	xm	ym	major	minor	angle		Area	xm	ym	major	minor	angle		Area	xm	ym	major	minor	angle
1	0.381	0.909	1.325	3.237	0.15	90.2	81	0.034	3.544	1.942	0.334	0.129	32.3	161	0.075	6.662	3.894	0.498	0.192	26.9
2	0.043	2.12	0.27	0.291	0.188	178.2	82	0.136	4.841	2.142	0.664	0.261	16.2	162	0.016	7.286	3.867	0.253	0.082	15.8
3	0.028	3.082	0.285	0.248	0.146	25.7	83	0.021	10.163	1.942	0.197	0.135	130.9	163	0.026	4.829	3.996	0.278	0.118	142.0
4	0.017	4.224	0.234	0.211	0.102	28.7	84	0.078	6.666	2.148	0.42	0.235	60.5	164	0.044	6.14	4.053	0.361	0.157	27.7
5	0.016	8.54	0.21	0.3	0.067	174.8	85	0.016	9.533	1.974	0.195	0.106	44.6	165	0.098	5.648	4.06	0.411	0.303	91.9
6	0.041	9.391	0.279	0.279	0.188	132.3	86	0.052	5.771	2.031	0.325	0.203	117.9	166	0.016	1.07	3.988	0.249	0.084	106.4
7	0.052	8.971	0.37	0.361	0.185	24.5	87	0.051	8.041	2.042	0.349	0.186	137.5	167	0.076	5.29	3.95	0.341	0.284	179.9
8	0.014	2.826	0.337	0.166	0.108	138.8	88	0.019	7.331	2.061	0.207	0.117	101.2	168	0.063	1.814	4.097	0.319	0.253	126.5
9	0.043	1.289	0.408	0.272	0.2	16.2	89	0.012	1.816	2.007	0.139	0.114	63.4	169	0.04	3.877	3.95	0.297	0.174	41.6
10	0.011	10.094	0.373	0.128	0.108	156.7	90	0.022	5.513	2.116	0.263	0.108	101.5	170	0.012	9.288	3.964	0.189	0.083	31.0
11	0.114	4.926	0.518	0.436	0.334	137.7	91	0.078	3.819	2.178	0.432	0.229	178.2	171	0.014	8.704	3.999	0.174	0.099	74.4
12	0.04	6.655	0.429	0.287	0.175	178.3	92	0.122	4.329	2.24	0.581	0.268	162.8	172	0.081	2.202	4.142	0.331	0.311	11.5
13	0.044	5.297	0.475	0.3	0.185	176.4	93	0.014	8.528	2.096	0.18	0.101	108.4	173	0.069	4.148	4.319	0.436	0.203	54.8
14	0.01	6.421	0.457	0.155	0.079	131.9	94	0.011	3.203	2.095	0.153	0.09	58.7	174	0.091	2.757	4.105	0.475	0.245	108.7
15	0.085	1.767	0.464	0.43	0.253	44.6	95	0.081	8.2	2.377	0.361	0.284	81.4	175	0.042	7.812	4.133	0.275	0.195	10.8
16	0.102	7.461	0.685	0.561	0.232	80.8	96	0.041	9.279	2.144	0.248	0.213	153.7	176	0.011	2.986	4.145	0.147	0.097	53.4
17	0.115	9.3	0.635	0.494	0.296	60.3	97	0.065	6.305	2.303	0.311	0.268	10.9	177	0.041	7.49	4.21	0.251	0.208	38.6
18	0.032	3.314	0.531	0.24	0.167	0.6	98	0.081	7.417	2.361	0.474	0.218	48.6	178	0.035	9.809	4.191	0.255	0.176	64.1
19	0.013	3.963	0.51	0.141	0.115	78.6	99	0.015	5.293	2.22	0.16	0.122	146.3	179	0.035	8.292	4.216	0.346	0.129	33.7
20	0.132	9.708	0.685	0.602	0.279	30.6	100	0.021	6.982	2.241	0.222	0.122	38.3	180	0.068	6.281	4.278	0.318	0.272	59.4
21	0.024	4.518	0.513	0.239	0.13	9.9	101	0.038	7.174	2.318	0.262	0.187	67.2	181	0.037	4.963	4.244	0.253	0.185	103.1
22	0.029	4.242	0.565	0.337	0.111	143.5	102	0.019	5.698	2.316	0.265	0.09	22.1	182	0.037	10.211	4.263	0.307	0.154	91.2
23	0.068	6.956	0.686	0.518	0.166	47.5	103	0.039	5.941	2.395	0.262	0.19	75.0	183	0.019	3.201	4.31	0.184	0.134	102.6
24	0.012	5.516	0.562	0.143	0.104	101.6	104	0.03	8.678	2.413	0.253	0.151	69.9	184	0.026	3.818	4.321	0.206	0.159	32.8
25	0.073	2.613	0.557	0.356	0.263	178.4	105	0.089	9.888	2.428	0.415	0.274	21.8	185	0.014	9.49	4.253	0.22	0.084	35.5
26	0.062	8.949	0.674	0.334	0.236	130.0	106	0.098	8.842	2.626	0.589	0.211	29.5	186	0.07	5.91	4.32	0.362	0.247	88.1
27	0.059	1.223	0.688	0.307	0.245	138.7	107	0.012	4.784	2.46	0.158	0.1	60.0	187	0.036	7.785	4.393	0.24	0.189	166.5
28	0.032	3.826	0.742	0.221	0.184	174.3	108	0.057	5.084	2.505	0.366	0.197	11.9	188	0.034	8.664	4.4	0.233	0.187	18.6
29	0.015	5.532	0.769	0.239	0.082	51.4	109	0.011	5.704	2.529	0.143	0.1	29.8	189	0.028	2.48	4.377	0.236	0.149	39.5
30	0.02	4.55	0.86	0.172	0.149	62.2	110	0.056	6.755	2.617	0.386	0.184	177.6	190	0.06	4.534	4.553	0.341	0.226	43.0
31	0.049	3.255	0.798	0.34	0.183	4.4	111	0.058	6.097	2.747	0.563	0.131	27.9	191	0.011	1.811	4.389	0.141	0.097	71.7
32	0.066	5.802	0.835	0.319	0.264	52.9	112	0.036	9.294	2.688	0.292	0.158	22.6	192	0.021	2.933	4.424	0.201	0.135	47.3
33	0.111	8.815	0.939	0.45	0.314	94.4	113	0.025	2.387	2.716	0.25	0.125	90.4	193	0.052	4.265	4.695	0.384	0.171	92.7
34	0.036	8.138	0.831	0.248	0.184	39.4	114	0.098	6.877	2.844	0.49	0.256	48.2	194	0.073	9.961	4.564	0.338	0.275	84.0
35	0.014	2.525	0.872	0.144	0.12	88.7	115	0.038	4.134	2.71	0.296	0.165	161.5	195	0.04	2.58	4.544	0.31	0.162	78.0
36	0.056	6.296	0.977	0.288	0.247	159.8	116	0.031	3.248	2.738	0.23	0.172	53.4	196	0.024	5.482	4.467	0.207	0.149	149.6
37	0.032	1.205	0.985	0.225	0.182	67.6	117	0.015	5.425	2.758	0.309	0.06	38.4	197	0.093	3.044	4.659	0.473	0.251	67.7
38	0.053	9.105	1.041	0.293	0.23	93.1	118	0.041	1.408	2.842	0.264	0.199	79.5	198	0.01	5.662	4.512	0.137	0.092	105.7

	Area	xm	ym	major	minor	angle		Area	xm	ym	major	minor	angle		Area	xm	ym	major	minor	angle
39	0.049	3.262	1.018	0.364	0.171	11.9	119	0.093	9.613	2.895	0.414	0.286	29.6	199	0.073	7.354	4.586	0.567	0.163	6.1
40	0.02	9.698	1.003	0.185	0.137	18.4	120	0.056	1.894	2.956	0.342	0.207	53.2	200	0.015	9.022	4.538	0.189	0.102	31.4
41	0.012	2.87	1.034	0.17	0.089	98.2	121	0.034	3.842	2.844	0.316	0.136	172.7	201	0.042	5.014	4.566	0.285	0.188	137.5
42	0.11	8.075	1.155	0.548	0.255	168.3	122	0.052	6.322	2.894	0.289	0.23	140.2	202	0.043	8.603	4.638	0.291	0.188	58.0
43	0.011	7.545	1.071	0.142	0.101	171.2	123	0.037	3.004	2.904	0.235	0.202	79.9	203	0.119	9.41	4.767	0.416	0.365	30.4
44	0.032	9.464	1.096	0.272	0.149	17.7	124	0.022	6.57	2.923	0.233	0.12	73.4	204	0.04	2.275	4.624	0.279	0.183	172.9
45	0.032	6.757	1.161	0.242	0.168	110.8	125	0.082	8.905	2.941	0.491	0.213	163.5	205	0.06	3.463	4.65	0.306	0.25	108.0
46	0.011	3.549	1.144	0.145	0.1	71.4	126	0.042	7.93	2.979	0.275	0.193	54.6	206	0.01	4.01	4.658	0.139	0.095	76.9
47	0.011	9.858	1.148	0.186	0.075	51.5	127	0.1	1.552	3.221	0.559	0.227	106.0	207	0.103	8.919	4.787	0.41	0.32	127.2
48	0.022	3.727	1.186	0.188	0.15	41.9	128	0.027	4.239	3.085	0.215	0.162	105.9	208	0.024	1.825	4.736	0.348	0.09	133.0
49	0.033	5.875	1.291	0.384	0.11	48.8	129	0.109	3.72	3.083	0.433	0.322	86.9	209	0.01	5.386	4.644	0.22	0.059	172.8
50	0.199	4.466	1.545	0.715	0.354	56.5	130	0.049	5.021	3.117	0.293	0.215	167.6	210	0.016	10.154	4.725	0.262	0.079	41.9
51	0.03	8.947	1.266	0.243	0.158	111.0	131	0.018	7.395	3.125	0.214	0.107	66.3	211	0.127	8.059	4.906	0.49	0.331	65.0
52	0.039	3.102	1.288	0.272	0.182	77.2	132	0.061	8.276	3.184	0.372	0.21	50.8	212	0.024	6.339	4.777	0.191	0.162	121.1
53	0.026	3.963	1.33	0.223	0.146	49.1	133	0.047	6.21	3.12	0.287	0.21	174.1	213	0.137	5.87	4.97	0.482	0.361	43.6
54	0.127	7.207	1.408	0.562	0.288	19.1	134	0.01	2.969	3.102	0.136	0.094	77.2	214	0.031	9.767	4.853	0.242	0.161	66.6
55	0.053	2.077	1.302	0.348	0.194	130.7	135	0.026	0.983	3.083	0.263	0.126	161.9	215	0.034	4.058	4.943	0.338	0.128	84.6
56	0.086	8.616	1.428	0.417	0.263	176.8	136	0.116	8.734	3.299	0.589	0.251	144.3	216	0.068	10.114	5.003	0.376	0.229	68.1
57	0.02	9.178	1.375	0.165	0.153	24.5	137	0.121	3.383	3.393	0.664	0.233	86.4	217	0.064	4.54	4.89	0.431	0.189	119.6
58	0.05	9.906	1.428	0.287	0.22	149.1	138	0.024	4.05	3.203	0.182	0.166	115.1	218	0.02	2.119	4.905	0.251	0.103	37.9
59	0.039	6.747	1.441	0.299	0.168	8.9	139	0.021	7.6	3.245	0.192	0.139	25.6	219	0.053	3.813	4.994	0.321	0.212	75.0
60	0.011	1.592	1.454	0.138	0.102	147.2	140	0.078	7.04	3.383	0.351	0.282	72.2	220	0.013	5.382	4.925	0.156	0.11	92.2
61	0.191	3.32	1.62	0.821	0.297	4.8	141	0.032	9.45	3.271	0.303	0.133	7.8	221	0.02	2.547	4.98	0.188	0.134	164.5
62	0.06	1.745	1.561	0.306	0.251	6.6	142	0.061	4.697	3.472	0.374	0.208	72.4	222	0.119	4.328	5.078	0.414	0.365	57.0
63	0.024	3.897	1.562	0.248	0.124	69.0	143	0.038	5.299	3.348	0.256	0.19	147.0	223	0.034	6.038	5.049	0.316	0.137	55.8
64	0.156	8.126	1.543	0.844	0.236	4.9	144	0.015	3.164	3.34	0.216	0.09	80.2	224	0.09	9.798	5.149	0.422	0.273	61.2
65	0.01	9.077	1.522	0.179	0.071	13.5	145	0.184	10.036	3.629	0.641	0.366	150.6	225	0.08	2.348	5.094	0.399	0.254	5.3
66	0.02	9.701	1.543	0.179	0.14	54.7	146	0.056	4.347	3.437	0.294	0.243	63.8	226	0.05	7.35	5.163	0.283	0.223	96.7
67	0.011	1.297	1.566	0.134	0.102	42.5	147	0.045	8.011	3.426	0.291	0.196	48.8	227	0.103	5.195	5.22	0.402	0.327	153.6
68	0.042	2.647	1.684	0.281	0.191	57.7	148	0.019	7.526	3.429	0.191	0.127	38.0	228	0.01	7.702	5.103	0.203	0.064	130.4
69	0.056	7.303	1.713	0.298	0.238	55.0	149	0.013	7.743	3.417	0.14	0.117	114.2	229	0.022	8.512	5.159	0.211	0.134	67.9
70	0.028	5.741	1.674	0.219	0.161	126.2	150	0.057	6.74	3.453	0.349	0.209	7.9	230	0.034	2.927	5.197	0.274	0.16	99.6
71	0.024	1.445	1.724	0.235	0.132	86.1	151	0.123	8.187	3.48	0.497	0.315	144.4	231	0.038	7.576	5.26	0.263	0.185	41.2
72	0.046	2.38	1.779	0.403	0.146	110.8	152	0.052	1.703	3.757	0.459	0.145	140.1	232	0.021	7.05	5.249	0.231	0.116	61.1
73	0.047	5.343	1.77	0.37	0.162	26.8	153	0.06	3.016	3.642	0.316	0.241	45.4	233	0.021	4.833	5.296	0.166	0.16	2.0
74	0.04	8.488	1.807	0.261	0.195	9.7	154	0.101	3.779	3.649	0.473	0.271	20.0	234	0.012	9.981	5.27	0.183	0.081	58.6
75	0.015	4.875	1.774	0.196	0.095	171.8	155	0.048	8.859	3.654	0.316	0.194	39.2	235	0.023	5.527	5.294	0.222	0.13	150.6
76	0.053	3.907	1.874	0.347	0.195	177.3	156	0.038	5.421	3.651	0.376	0.13	32.4	236	0.026	6.785	5.304	0.239	0.14	3.7
77	0.115	9.85	2.007	0.471	0.31	58.9	157	0.022	6.162	3.605	0.204	0.138	3.9	237	0.019	4.029	5.325	0.294	0.081	4.6
78	0.053	2.969	1.962	0.324	0.208	54.0	158	0.053	9.413	3.711	0.301	0.223	37.8	238	0.012	3.321	5.333	0.247	0.064	5.0
79	0.012	2.219	1.894	0.158	0.094	66.3	159	0.009	2.15	3.657	0.174	0.066	41.6	161	0.075	6.662	3.894	0.498	0.192	26.9
80	0.106	2.734	1.99	0.388	0.346	2.4	160	0.026	4.117	3.784	0.29	0.115	66.0	162	0.016	7.286	3.867	0.253	0.082	15.8



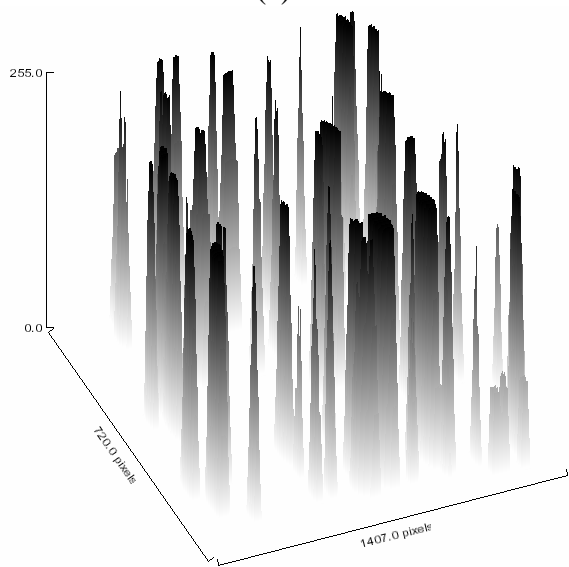
(a)



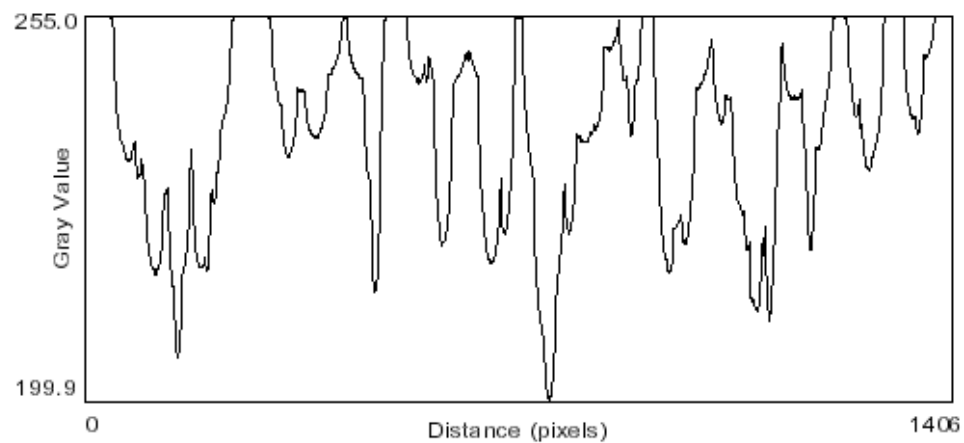
(b)



(c)



(d)



(e)

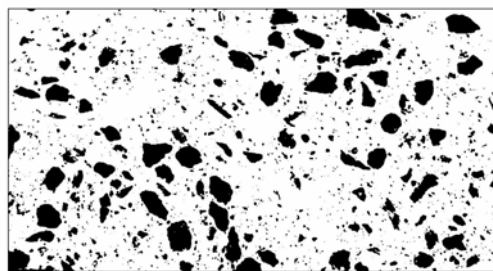
Figure C4. a) Image of CV10L48, b) selected pumices in binary image of CV10L48, c) ellipses mask, d) surface of pumices and (e) plot drawing of CV10L48.

Table C4. Image analysis results for CV10L48 series.

	Area	xm	ym	major	minor	angle		Area	xm	ym	major	minor	angle		Area	xm	ym	major	minor	angle
1	0.058	3.285	0.539	0.421	0.176	1.0	19	0.123	6.264	2.595	0.552	0.284	136.4	37	0.035	4.363	4.722	0.277	0.162	33.4
2	0.054	3.75	0.538	0.394	0.175	8.2	20	0.07	5.813	2.715	0.35	0.255	77.6	38	0.03	2.13	4.799	0.225	0.17	19.7
3	0.047	8.7	0.538	0.363	0.163	176.0	21	0.083	1.637	2.799	0.431	0.247	89.1	39	0.084	5.192	4.869	0.574	0.185	161.9
4	0.027	2.087	0.538	0.263	0.131	169.1	22	0.025	8.186	2.961	0.212	0.149	152.3	40	0.053	7.546	4.87	0.369	0.183	23.4
5	0.137	8.334	0.722	0.49	0.356	107.5	23	0.027	9.348	3.172	0.232	0.147	69.9	40	5.257	4.532	0.443	0.267	0.235721	155.9
6	0.045	4.644	0.68	0.28	0.206	72.6	24	0.084	7.954	3.236	0.464	0.232	7.9	41	6.75	4.615	0.185	0.175	0.113334	50.3
7	0.065	8.947	0.954	0.371	0.224	128.9	25	0.034	8.827	3.306	0.278	0.157	100.4	42	9.546	4.806	0.414	0.252	0.217859	74.1
8	0.03	1.883	0.926	0.263	0.144	136.9	26	0.045	5.18	3.757	0.374	0.153	55.2	43	4.363	4.722	0.277	0.162	0.135549	33.4
9	0.035	5.912	1.045	0.218	0.206	163.3	27	0.052	3.848	3.841	0.342	0.192	105.5	44	3.905	4.749	0.235	0.131	0.113028	112.4
10	0.058	2.834	1.201	0.389	0.191	130.1	28	0.107	1.053	3.968	0.492	0.276	60.7	45	2.13	4.799	0.225	0.17	0.123441	19.7
11	0.076	4.693	1.144	0.502	0.194	177.7	29	0.059	1.954	3.926	0.364	0.207	140.4	46	5.192	4.869	0.574	0.185	0.233922	161.9
12	0.026	8.398	1.799	0.277	0.118	90.8	30	0.05	10.025	4.264	0.337	0.19	114.4	47	7.546	4.87	0.369	0.183	0.171073	23.4
13	0.028	5.384	1.855	0.235	0.15	83.0	31	0.181	1.44	4.398	0.58	0.397	57.6	48	8.355	4.855	0.153	0.117	0.087842	72.1
14	0.086	3.065	2.031	0.554	0.199	160.3	32	0.224	7.292	4.468	0.604	0.472	100.9	49	6.519	4.89	0.293	0.083	0.109522	22.1
15	0.031	4.658	2.074	0.232	0.171	147.1	33	0.278	5.862	4.637	0.684	0.517	136.2	50	8.883	5.143	0.204	0.095	0.093556	1.7
16	0.121	1.785	2.299	0.489	0.314	44.1	34	0.093	5.257	4.532	0.443	0.267	155.9	51	8.636	5.144	0.251	0.08	0.09913	0.1
17	0.107	8.13	2.306	0.447	0.305	131.7	35	0.025	6.75	4.615	0.185	0.175	50.3	52	9.431	5.151	0.221	0.087	0.094849	170.8
18	0.07	1.299	2.482	0.436	0.204	50.2	36	0.082	9.546	4.806	0.414	0.252	74.1	37	0.035	4.363	4.722	0.277	0.162	33.4



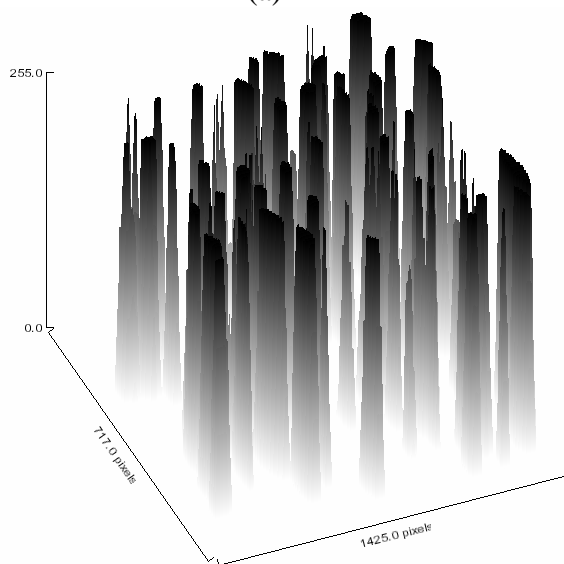
(a)



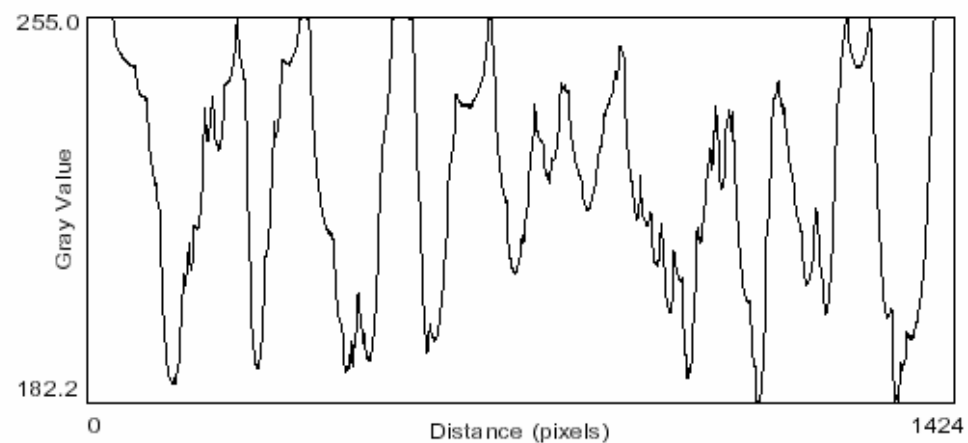
(b)



(c)



(d)



(e)

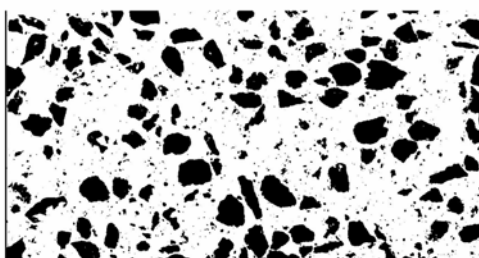
Figure C5. a) Image of CV20L48, b) selected pumices in binary image of CV20L48, c) ellipses mask, d) surface of pumices and (e) plot drawing of CV20L48.

Table C5. Image analysis results for CV20L48 series.

	Area	xm	ym	major	minor	angle		Area	xm	ym	major	minor	angle		Area	xm	ym	major	minor	angle
1	0.035	7.536	0.676	0.328	0.137	147.168	34	0.065	2.903	2.623	0.353	0.233	151.626	67	0.026	4.617	4.316	0.26	0.129	72.716
2	0.148	8.843	0.77	0.574	0.329	166.504	35	0.068	8.423	2.663	0.301	0.287	32.914	68	0.056	8.33	4.416	0.318	0.225	90.029
3	0.106	6.269	1.016	0.582	0.231	153.594	36	0.04	4.056	2.663	0.299	0.169	137.349	69	0.069	1.73	4.376	0.497	0.177	6.835
4	0.067	5.703	1.036	0.322	0.265	138.602	37	0.07	5.876	2.73	0.364	0.244	131.659	70	0.087	8.73	4.476	0.4	0.277	179.444
5	0.031	4.763	1.07	0.309	0.13	144.027	38	0.023	7.95	2.729	0.188	0.155	115.167	71	0.091	9.737	4.57	0.452	0.257	131.144
6	0.023	7.556	1.096	0.183	0.158	135.246	39	0.151	3.65	2.957	0.532	0.362	25.773	72	0.073	5.563	4.723	0.414	0.223	143.585
7	0.034	2.177	1.143	0.309	0.142	30.564	40	0.094	7.41	3.043	0.384	0.312	52.832	73	0.072	8.203	4.776	0.344	0.265	179.844
8	0.102	3.937	1.276	0.405	0.32	31.542	41	0.121	4.71	3.083	0.428	0.361	60.978	74	0.033	9.037	4.783	0.265	0.158	34.081
9	0.076	2.83	1.317	0.365	0.265	51.848	42	0.036	2.183	3.023	0.253	0.179	141.585	75	0.07	2.79	3.876	0.498	0.18	0.208213
10	0.142	7.184	1.35	0.709	0.254	14.667	43	0.071	6.995	3.103	0.556	0.162	152.982	76	0.304	9.99	4.103	0.908	0.427	0.545352
11	0.111	5.11	1.39	0.513	0.275	148.131	44	0.071	2.783	3.23	0.372	0.243	167.054	77	0.034	7.616	3.856	0.236	0.183	0.131086
12	0.025	6.49	1.356	0.239	0.131	1.098	45	0.071	3.816	3.303	0.37	0.243	138.695	78	0.144	1.836	4.036	0.47	0.391	0.310836
13	0.098	8.99	1.47	0.458	0.271	25.235	46	0.109	1.937	3.39	0.43	0.324	55.235	79	0.016	1.35	3.923	0.2	0.099	0.093886
14	0.029	2.116	1.443	0.213	0.174	28.649	47	0.027	7.93	3.35	0.261	0.131	53.57	80	0.034	7.723	4.109	0.267	0.16	0.131974
15	0.103	9.889	1.49	0.531	0.247	164.383	48	0.041	2.343	3.403	0.323	0.164	66.511	81	0.02	8.164	4.096	0.255	0.098	0.106438
16	0.075	7.45	1.677	0.359	0.266	161.389	49	0.025	9.129	3.316	0.245	0.13	179.957	82	0.029	8.803	4.096	0.254	0.144	0.122598
17	0.024	4.057	1.67	0.219	0.14	46.187	50	0.025	6.036	3.423	0.303	0.107	121.157	83	0.182	4.063	4.37	0.543	0.426	0.365118
18	0.157	6.497	1.777	0.552	0.362	12.236	51	0.112	8.217	3.537	0.628	0.227	46.392	84	0.022	7.029	4.21	0.2	0.142	0.107388
19	0.033	1.843	1.716	0.327	0.128	4.554	52	0.025	2.983	3.476	0.205	0.157	174.873	85	0.018	7.249	4.23	0.217	0.108	0.100822
20	0.031	6.923	1.769	0.239	0.163	81.386	53	0.026	3.796	3.59	0.318	0.103	134.835	86	0.026	4.617	4.316	0.26	0.129	0.118802
21	0.119	8.203	1.91	0.447	0.339	73.27	54	0.031	9.05	3.596	0.257	0.153	117.639	87	0.019	2.25	4.289	0.191	0.124	0.099447
22	0.121	5.603	1.93	0.428	0.361	60.978	55	0.033	3.131	3.616	0.31	0.135	31.283	88	0.056	8.33	4.416	0.318	0.225	0.172818
23	0.07	7.25	1.997	0.434	0.204	107.339	56	0.035	7.123	3.643	0.246	0.179	138.43	89	0.017	3.429	4.329	0.184	0.115	0.094954
24	0.103	2.003	1.95	0.472	0.277	174.354	57	0.142	3.63	3.83	0.627	0.287	131.437	90	0.069	1.73	4.376	0.497	0.177	0.206274
25	0.058	1.468	1.936	0.459	0.16	167.569	58	0.121	4.797	3.79	0.428	0.361	60.978	91	0.022	5.23	4.383	0.178	0.156	0.105636
26	0.098	9.69	2.043	0.407	0.305	108.692	59	0.07	2.79	3.876	0.498	0.18	82.406	92	0.087	8.73	4.476	0.4	0.277	0.224667
27	0.039	7.863	2.123	0.328	0.15	97.587	60	0.304	9.99	4.103	0.908	0.427	97.33	93	0.017	3.31	4.469	0.188	0.113	0.095334
28	0.046	2.456	2.156	0.249	0.237	163.643	61	0.034	7.616	3.856	0.236	0.183	121.146	94	0.091	9.737	4.57	0.452	0.257	0.233902
29	0.05	4.743	2.204	0.459	0.139	141.391	62	0.144	1.836	4.036	0.47	0.391	139.463	95	0.016	7.368	4.602	0.212	0.098	0.096379
30	0.038	5.99	2.356	0.318	0.153	35.763	63	0.034	7.723	4.109	0.267	0.16	100.51	96	0.073	5.563	4.723	0.414	0.223	0.203882
31	0.097	7.65	2.45	0.367	0.336	34.142	64	0.029	8.803	4.096	0.254	0.144	146.611	97	0.072	8.203	4.776	0.344	0.265	0.198574
32	0.029	9.396	2.57	0.276	0.136	137.413	65	0.182	4.063	4.37	0.543	0.426	99.967	98	0.033	9.037	4.783	0.265	0.158	0.130679
33	0.023	9.702	2.536	0.205	0.141	169.799	66	0.022	7.029	4.21	0.2	0.142	171.465	99	0.018	8.722	4.769	0.2	0.113	0.098282



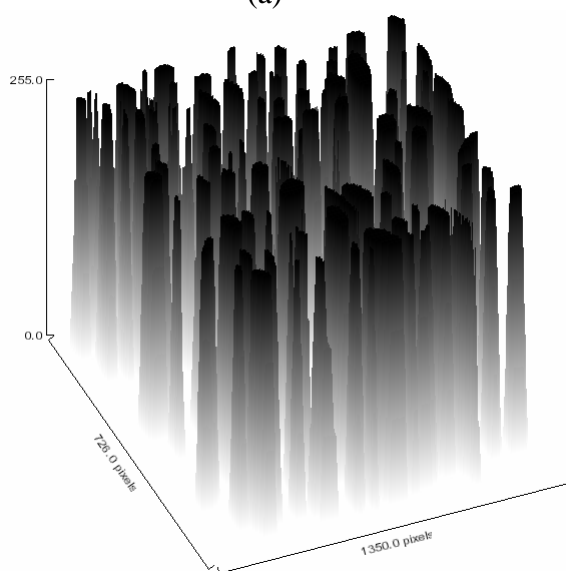
(a)



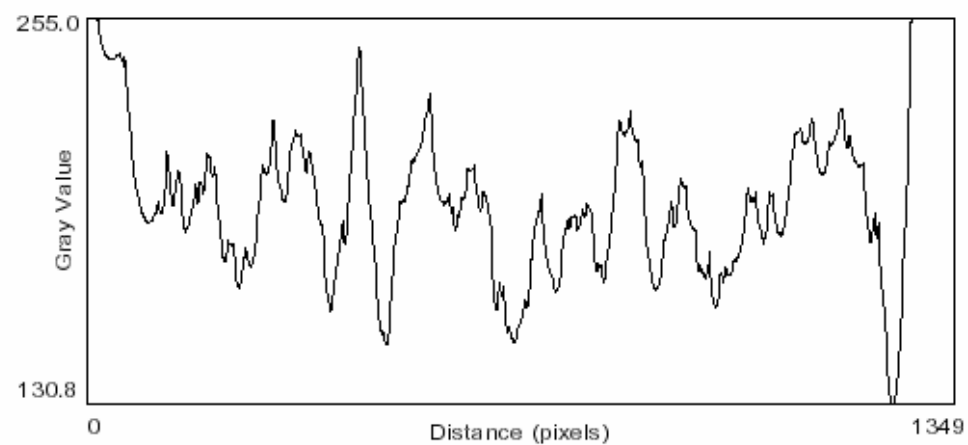
(b)



(c)



(d)



(e)

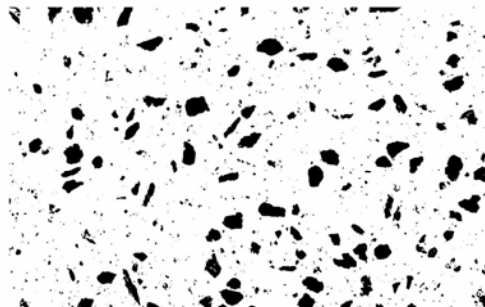
Figure C6. a) Image of CV130L48, b) selected pumices in binary image of CV30L48, c) ellipses mask, d) surface of pumices and (e) plot drawing of CV30L48.

Table C6. Image analysis results for CV30L48 series.

	Area	xm	ym	major	minor	angle		Area	xm	ym	major	minor	angle		Area	xm	ym	major	minor	angle
1	0.054	3.692	1.228	0.31	0.221	73.151	38	0.042	7.633	2.467	0.31	0.171	73.151	75	0.271	5.88	4.96	0.625	0.552	100.878
2	0.149	4.235	1.228	0.63	0.3	175.924	39	0.105	4.301	2.634	0.424	0.315	175.924	76	0.174	2.316	4.88	0.801	0.277	27.986
3	0.058	6.148	1.192	0.344	0.214	4.694	40	0.042	10.308	2.626	0.348	0.152	4.694	77	0.084	7.38	4.793	0.412	0.259	0.107
4	0.035	8.49	1.169	0.324	0.139	14.65	41	0.086	2.699	2.714	0.398	0.276	14.65	78	0.086	10.177	4.837	0.355	0.31	136.042
5	0.076	2.096	1.336	0.548	0.177	158.411	42	0.151	7.851	2.771	0.532	0.36	158.411	79	0.073	4.742	5.09	0.442	0.211	118.204
6	0.126	3.003	1.409	0.532	0.302	149.214	43	0.149	10.569	2.916	0.586	0.324	149.214	80	0.042	4.431	5.126	0.369	0.145	76.425
7	0.139	10.518	1.453	0.509	0.346	148.408	44	0.151	6.184	2.822	0.622	0.31	148.408	81	0.1	3.069	5.264	0.441	0.287	105.406
8	0.062	1.75	1.409	0.32	0.247	144.053	45	0.117	6.974	2.815	0.512	0.29	144.053	82	0.08	7.815	5.242	0.4	0.255	72.227
9	0.126	7.25	1.482	0.437	0.368	58.415	46	0.091	9.206	2.851	0.387	0.298	58.415	83	0.117	9.852	5.308	0.477	0.312	45.694
10	0.064	6.714	1.489	0.389	0.21	102.542	47	0.101	2.569	3.09	0.44	0.291	102.542	84	0.192	8.337	5.395	0.589	0.416	140.169
11	0.054	3.46	1.482	0.448	0.152	141.675	48	0.091	4.083	3.039	0.403	0.288	141.675	85	0.113	3.598	5.431	0.506	0.284	86.504
12	0.164	9.307	1.554	0.642	0.326	172.931	49	0.054	4.822	3.083	0.38	0.18	172.931	86	0.138	10.489	5.366	0.536	0.327	21.452
13	0.145	5.003	1.59	0.639	0.288	2.392	50	0.082	6.366	3.17	0.545	0.192	2.392	87	0.137	7.228	5.395	0.491	0.356	168.819
14	0.067	4.22	1.568	0.406	0.21	171.976	51	0.176	2.17	3.286	0.572	0.392	171.976	88	0.392	6.585	5.591	0.982	0.508	157.085
15	0.026	2.699	1.597	0.228	0.148	64.179	52	0.062	4.345	3.249	0.383	0.207	64.179	89	0.105	8.815	5.598	0.75	0.178	116.431
16	0.17	2.127	1.808	0.645	0.337	56.017	53	0.224	9.518	3.373	0.674	0.423	56.017	90	0.076	2.67	5.481	0.352	0.273	73.576
17	0.071	8.54	1.691	0.42	0.215	2.996	54	0.265	8.554	3.402	0.691	0.488	2.996	91	0.118	5.736	5.692	0.487	0.309	58.682
18	0.061	3.38	1.793	0.403	0.192	138.718	55	0.03	7.271	3.286	0.241	0.161	138.718	92	0.15	3.119	5.699	0.561	0.341	154.459
19	0.074	6.27	1.742	0.48	0.196	173.397	56	0.1	10.511	3.424	0.507	0.252	173.397	93	0.042	4.192	5.619	0.272	0.199	3.56
20	0.151	5.547	1.953	0.588	0.327	119.902	57	0.081	3.3	3.59	0.427	0.243	119.902	94	0.086	7.744	5.641	0.61	0.179	14.459
21	0.051	10.348	1.771	0.556	0.118	171.763	58	0.072	5.496	3.655	0.52	0.176	171.763	95	0.046	7.301	5.706	0.284	0.205	31.209
22	0.112	7.489	1.88	0.482	0.296	28.46	59	0.102	4.018	3.576	0.446	0.291	28.46	96	0.051	4.714	5.677	0.424	0.153	5.5
23	0.072	2.496	1.974	0.427	0.215	68.249	60	0.19	4.83	3.663	0.571	0.425	68.249	97	0.039	6.127	5.778	0.272	0.183	89.308
24	0.07	6.742	1.924	0.416	0.214	142.926	61	0.165	9.185	3.757	0.517	0.407	142.926	98	0.038	4.85	5.843	0.434	0.112	178.711
25	0.172	4.771	2.061	0.617	0.355	119.57	62	0.043	2.38	3.807	0.276	0.198	119.57	99	8.815	5.598	0.75	0.178	0.281894	116.431
26	0.125	2.866	2.032	0.495	0.321	70.255	63	0.075	8.496	3.88	0.327	0.293	70.255	100	2.67	5.481	0.352	0.273	0.20496	73.576
27	0.44	8.815	2.243	0.938	0.597	67.455	64	0.337	5.243	4.192	0.87	0.493	67.455	101	4.982	5.474	0.187	0.127	0.099341	85.796
28	0.094	8.271	1.974	0.428	0.281	169.998	65	0.24	10.172	4.185	1.037	0.294	169.998	102	5.736	5.692	0.487	0.309	0.274501	58.682
29	0.058	3.271	2.032	0.336	0.218	147.576	66	0.18	7.946	4.315	0.571	0.401	147.576	103	3.119	5.699	0.561	0.341	0.323185	154.459
30	0.052	3.807	2.032	0.34	0.193	153.89	67	0.19	6.243	4.656	0.941	0.257	153.89	104	4.192	5.619	0.272	0.199	0.147837	3.56
31	0.136	10.612	2.271	0.67	0.259	84.43	68	0.116	3.772	4.496	0.418	0.354	84.43	105	7.744	5.641	0.61	0.179	0.240987	14.459
32	0.056	10.142	2.119	0.362	0.198	32.692	69	0.288	6.757	4.598	0.795	0.461	32.692	106	9.467	5.619	0.173	0.143	0.100432	140.857
33	0.224	8.069	2.322	0.62	0.46	171.144	70	0.224	3.264	4.547	0.598	0.477	171.144	107	7.301	5.706	0.284	0.205	0.153876	31.209
34	0.053	4.069	2.199	0.348	0.192	11.58	71	0.064	4.265	4.59	0.334	0.246	11.58	108	4.714	5.677	0.424	0.153	0.172914	5.5
35	0.076	5.975	2.351	0.362	0.266	85.836	72	0.03	9.207	4.583	0.284	0.133	85.836	109	6.127	5.778	0.272	0.183	0.141909	89.308
36	0.12	7.112	2.416	0.427	0.359	8.788	73	0.086	9.735	4.655	0.426	0.259	8.788	110	2.633	5.836	0.179	0.12	0.095205	162.848
37	0.113	6.366	2.467	0.44	0.326	23.85	74	0.039	5.12	4.663	0.341	0.145	23.85	111	4.85	5.843	0.434	0.112	0.155279	178.711



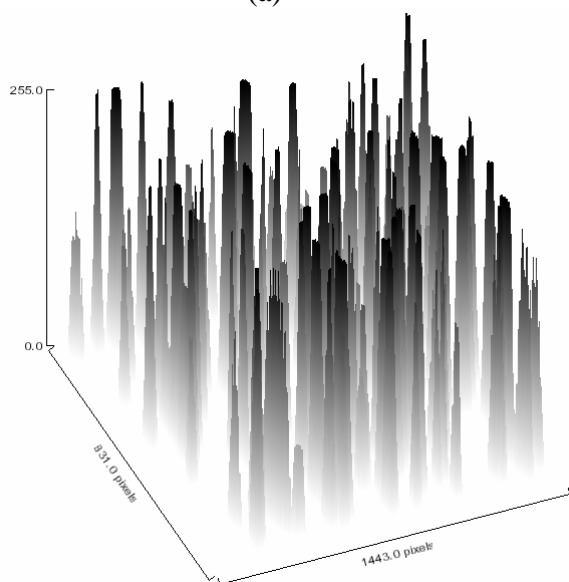
(a)



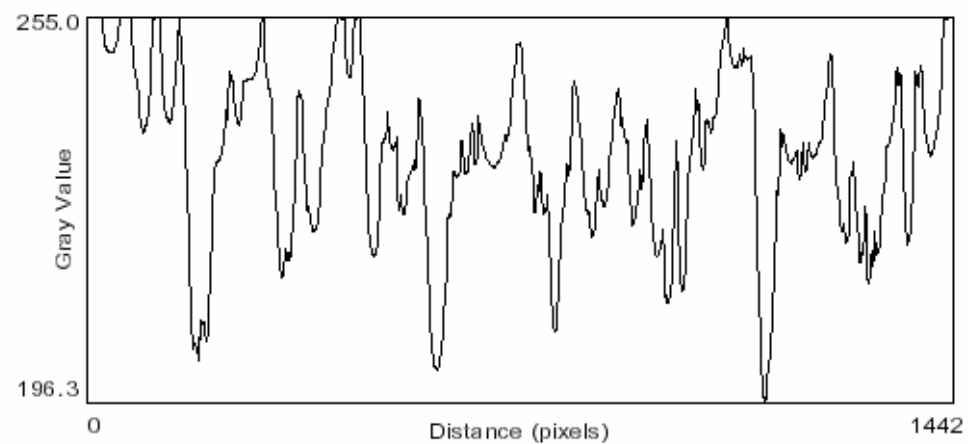
(b)



(c)



(d)



(e)

Figure C7. a) Image of MV10L24, b) selected pumices in binary image of MV10L24, c) ellipses mask, d) surface of pumices and (e) plot drawing of MV10L24.

Table C7. Image analysis results for MV10L24 series.

	Area	xm	ym	major	minor	angle		Area	xm	ym	major	minor	angle		Area	xm	ym	major	minor	angle
1	0.034	1.652	0.306	0.259	0.166	13.247	36	0.041	2.902	2.238	0.348	0.149	52.232	1	73	0.037	4.35	3.919	0.246	0.193
2	0.075	2.094	0.385	0.341	0.28	59.3	37	0.016	8.089	2.067	0.162	0.124	4.311	2	74	0.022	8.198	3.912	0.182	0.153
3	0.05	2.896	0.337	0.378	0.168	75.63	38	0.018	2.005	2.228	0.216	0.106	110.656	3	75	0.026	6.308	4.04	0.219	0.15
4	0.015	4.858	0.239	0.155	0.124	21.391	39	0.016	9.082	2.12	0.177	0.118	52.285	4	76	0.029	9.496	4.079	0.287	0.129
5	0.036	7.132	0.215	0.532	0.087	87.248	40	0.059	4.939	2.351	0.394	0.191	145.56	5	77	0.023	4.966	4.125	0.192	0.154
6	0.015	9.218	0.258	0.227	0.084	159.066	41	0.038	1.433	2.433	0.257	0.187	80.332	6	78	0.046	6.77	4.182	0.285	0.204
7	0.038	10.018	0.371	0.228	0.212	179.615	42	0.063	3.945	2.578	0.388	0.208	76.602	7	79	0.054	7.115	4.185	0.282	0.245
8	0.015	1.098	0.348	0.257	0.074	102.946	43	0.064	7.344	2.478	0.372	0.218	85.27	8	80	0.014	7.738	4.144	0.196	0.088
9	0.023	4.008	0.503	0.238	0.123	156.322	44	0.074	2.061	2.577	0.325	0.291	172.179	9	81	0.019	7.869	4.181	0.186	0.131
10	0.017	9.346	0.582	0.173	0.128	109.432	45	0.061	6.202	2.725	0.332	0.235	83.281	10	82	0.02	5.776	4.229	0.181	0.14
11	0.026	9.787	0.699	0.244	0.136	48.018	46	0.042	9.759	2.876	0.382	0.139	162.511	11	83	0.022	3.157	4.259	0.219	0.129
12	0.022	8.244	0.653	0.182	0.152	163.961	47	0.089	8.22	2.968	0.436	0.261	167.65	12	84	0.058	4.265	4.352	0.328	0.226
13	0.058	3.329	0.78	0.407	0.181	44.441	48	0.027	2.453	2.707	0.203	0.171	63.82	13	85	0.057	6.459	4.263	0.341	0.211
14	0.086	5.277	0.83	0.415	0.265	131.862	49	0.038	7.131	2.708	0.264	0.183	60.112	14	86	0.076	9.246	4.552	0.46	0.21
15	0.047	10.101	0.825	0.31	0.192	166.839	50	0.041	7.653	2.739	0.312	0.168	97.907	15	87	0.02	5.57	4.448	0.296	0.085
16	0.013	6.876	0.898	0.207	0.078	87.432	51	0.013	3.706	2.776	0.217	0.079	58.909	16	88	0.013	2.03	4.55	0.227	0.074
17	0.034	5.892	0.984	0.337	0.127	76.175	52	0.071	6.016	2.94	0.365	0.249	64.3	17	89	0.057	2.94	4.775	0.592	0.123
18	0.034	8.275	1.059	0.227	0.193	4.449	53	0.03	2.02	2.88	0.355	0.106	64.806	18	90	0.047	2.613	4.5	0.3	0.2
19	0.016	1.908	1.053	0.183	0.115	89.308	54	0.07	8.71	2.988	0.365	0.245	35.807	19	91	0.04	9.019	4.72	0.294	0.175
20	0.059	6.377	1.121	0.344	0.22	89.165	55	0.036	4.601	2.965	0.363	0.126	16.642	20	92	0.045	6.78	4.729	0.337	0.17
21	0.027	4.682	1.225	0.237	0.147	162.617	56	0.043	2.027	3.101	0.32	0.17	75.611	21	93	0.017	7.555	4.66	0.235	0.09
22	0.027	7.031	1.271	0.322	0.105	88.744	57	0.032	9.404	3.132	0.25	0.162	125.646	22	94	0.063	5.983	4.71	0.368	0.217
23	0.057	8.287	1.43	0.355	0.203	139.484	58	0.019	3.079	3.157	0.224	0.106	38.432	23	95	0.032	4.688	4.698	0.226	0.18
24	0.021	8.95	1.515	0.293	0.09	104.009	59	0.034	3.224	3.287	0.425	0.103	81.443	24	96	0.013	7.335	4.746	0.177	0.095
25	0.017	1.47	1.508	0.178	0.119	74.296	60	0.012	6.529	3.125	0.18	0.088	62.11	25	97	0.024	9.867	4.94	0.343	0.09
26	0.044	7.363	1.795	0.336	0.166	95.228	61	0.081	9.169	3.306	0.404	0.256	102.292	26	98	0.069	4.646	4.912	0.367	0.238
27	0.046	3.376	1.708	0.369	0.16	101.559	62	0.035	7.162	3.474	0.389	0.113	92.4	27	99	0.031	8.769	4.935	0.258	0.151
28	0.094	4.068	1.791	0.394	0.303	5.55	63	0.067	8.56	3.402	0.331	0.257	43.738	28	100	0.057	5.86	5.011	0.3	0.241
29	0.037	7.033	1.771	0.301	0.154	118.862	64	0.077	5.297	3.51	0.474	0.207	77.497	29	101	0.033	9.47	5.018	0.305	0.14
30	0.012	5.968	1.799	0.169	0.092	101.137	65	0.018	5.696	3.499	0.184	0.121	1.043	30	102	0.029	4.204	4.92	0.195	0.189
31	0.033	4.809	1.89	0.26	0.161	104.017	66	0.013	1.728	3.485	0.155	0.109	15.692	31	103	0.041	2.127	5.059	0.268	0.195
32	0.033	2.122	1.914	0.233	0.182	8.162	67	0.019	7.356	3.581	0.217	0.109	15.692	32	104	0.023	6.52	5.058	0.237	0.122
33	0.018	2.996	1.943	0.248	0.093	39.229	68	0.024	8.314	3.594	0.237	0.128	15.692	33	105	0.018	3.346	5.063	0.213	0.105
34	0.039	8.529	1.897	0.261	0.192	117.373	69	0.068	4.682	3.687	0.335	0.258	15.692	34	106	0.014	7.59	5.084	0.172	0.107
35	0.031	4.654	2.142	0.42	0.095	127.84	70	0.064	9.577	3.738	0.3	0.273	15.692	35	107	0.015	4.517	5.093	0.222	0.084
36	0.041	2.902	2.238	0.348	0.149	52.232	71	0.02	6.711	3.817	0.247	0.105	15.692	36	73	0.037	4.35	3.919	0.246	0.193

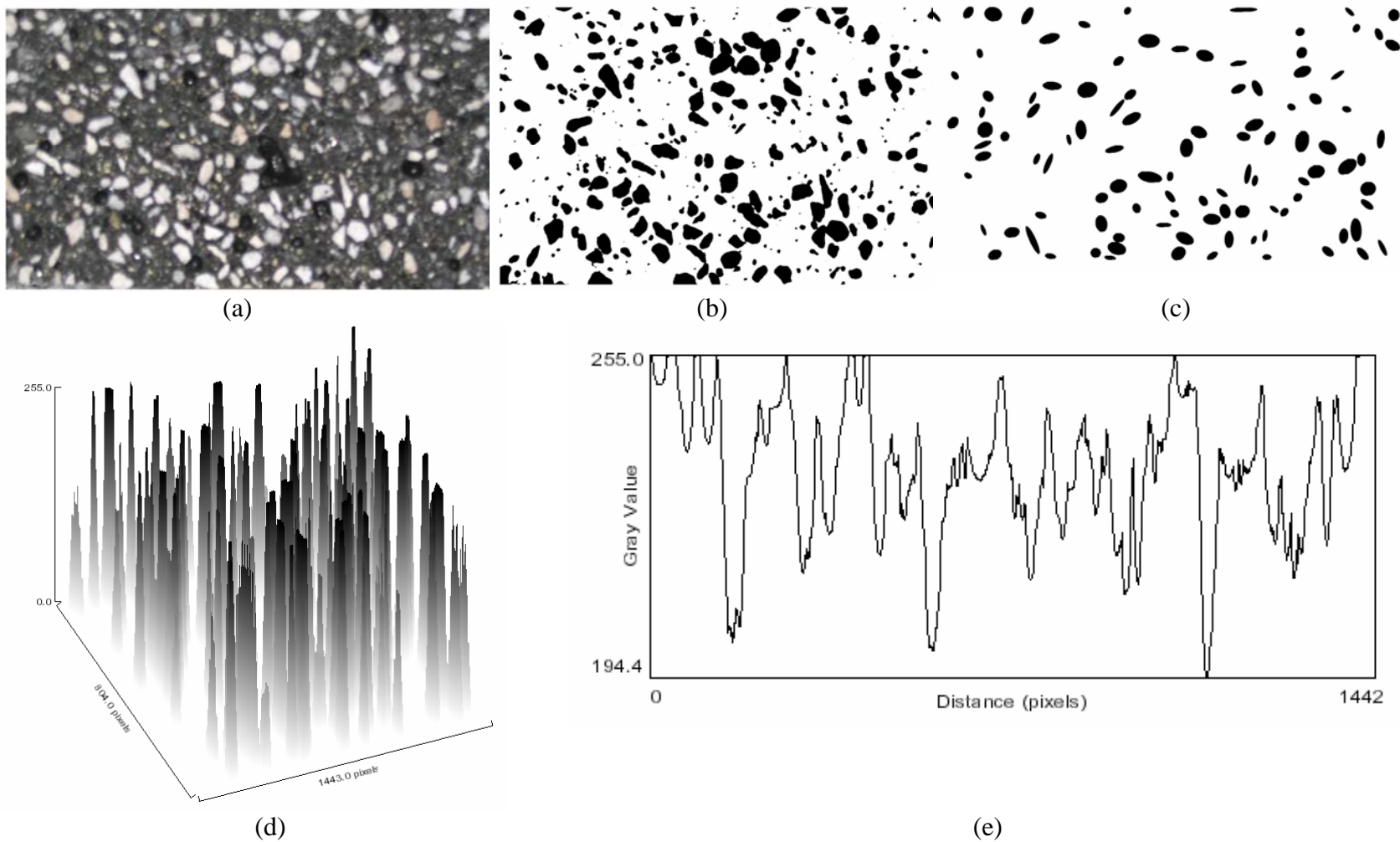


Figure C8. a) Image of MV20L24, b) selected pumices in binary image of MV20L24, c) ellipses mask, d) surface of pumices and (e) plot drawing of MV20L24.

Table C8. Image analysis results for MV20L24 series.

	Area	xm	ym	major	minor	angle		Area	xm	ym	major	minor	angle		Area	xm	ym	major	minor	angle
1	0.018	1.931	0.195	0.302	0.075	0.3	53	0.027	1.906	1.713	0.254	0.137	130.6	105	0.088	3.034	3.587	0.441	0.255	44.6
2	0.032	7.122	0.222	0.296	0.139	178.6	54	0.043	2.595	1.764	0.244	0.225	171.5	106	0.106	6.416	3.629	0.456	0.296	29.8
3	0.067	8.953	0.292	0.315	0.272	24.3	55	0.141	4.442	2.072	0.64	0.28	94.1	107	0.021	7.699	3.623	0.343	0.078	79.2
4	0.083	6.154	0.308	0.45	0.236	18.5	56	0.025	7.21	1.863	0.301	0.106	108.2	108	0.093	3.393	3.7	0.366	0.322	83.4
5	0.05	6.808	0.33	0.352	0.18	127.8	57	0.077	5.974	1.987	0.381	0.259	107.3	109	0.059	9.116	3.696	0.311	0.242	92.0
6	0.029	2.9	0.297	0.256	0.146	143.4	58	0.043	5.257	1.977	0.307	0.179	163.4	110	0.201	5.206	3.896	0.634	0.403	110.4
7	0.035	1.106	0.318	0.239	0.184	150.6	59	0.016	6.296	1.981	0.26	0.08	123.2	111	0.057	9.478	3.784	0.395	0.185	110.4
8	0.019	2.196	0.331	0.19	0.124	7.5	60	0.015	6.86	1.973	0.182	0.104	122.6	112	0.074	7.205	3.885	0.474	0.198	99.5
9	0.06	4.014	0.4	0.348	0.221	159.2	61	0.05	1.153	2.015	0.336	0.189	152.5	113	0.031	4.875	3.789	0.245	0.159	149.6
10	0.025	4.386	0.375	0.231	0.135	89.8	62	0.031	2.469	1.985	0.229	0.173	27.1	114	0.06	2.513	3.845	0.335	0.229	145.1
11	0.044	7.165	0.443	0.312	0.18	41.0	63	0.017	0.777	2.038	0.21	0.103	91.6	115	0.021	1.775	3.813	0.209	0.126	99.4
12	0.079	1.402	0.548	0.379	0.266	33.7	64	0.031	4.818	2.05	0.234	0.171	126.6	116	0.033	8.885	3.832	0.251	0.165	96.5
13	0.016	2.445	0.493	0.168	0.124	136.4	65	0.017	5.681	2.016	0.174	0.127	18.5	117	0.027	3.122	3.828	0.229	0.15	31.6
14	0.022	3.632	0.546	0.242	0.117	112.2	66	0.038	7.209	2.275	0.305	0.16	163.6	118	0.023	6.128	3.876	0.214	0.136	92.1
15	0.105	9.553	0.607	0.439	0.305	27.2	67	0.09	2.211	2.349	0.532	0.216	20.2	119	0.066	8.626	3.925	0.298	0.282	41.6
16	0.018	3.35	0.53	0.214	0.109	30.6	68	0.02	3.397	2.341	0.207	0.126	162.3	120	0.045	4.353	3.966	0.287	0.199	94.4
17	0.083	7.716	0.696	0.367	0.288	69.8	69	0.016	5.252	2.44	0.276	0.074	47.5	121	0.032	1.986	3.953	0.242	0.169	130.6
18	0.028	7.324	0.618	0.23	0.157	96.8	70	0.021	3.961	2.471	0.24	0.114	103.4	122	0.016	7.902	3.955	0.153	0.136	159.5
19	0.016	4.63	0.656	0.154	0.128	171.9	71	0.013	1.12	2.453	0.149	0.108	46.6	123	0.027	3.241	4.023	0.277	0.125	35.4
20	0.044	9.085	0.683	0.3	0.188	162.0	72	0.044	9.402	2.503	0.257	0.216	9.6	124	0.043	5.931	4.056	0.311	0.175	7.8
21	0.259	5.696	0.945	0.785	0.421	136.3	73	0.059	1.357	2.589	0.319	0.237	104.7	125	0.015	1.349	4.11	0.197	0.095	82.5
22	0.046	2.512	0.743	0.261	0.224	162.3	74	0.013	7.139	2.609	0.21	0.079	103.0	126	0.027	4.49	4.133	0.285	0.122	38.8
23	0.019	2.83	0.781	0.178	0.137	77.9	75	0.017	8.533	2.583	0.253	0.087	32.4	127	0.025	8.079	4.135	0.245	0.131	71.1
24	0.104	4.579	0.917	0.445	0.297	132.9	76	0.071	2.042	2.753	0.393	0.229	101.3	128	0.133	1.737	4.136	0.505	0.335	76.6
25	0.318	5.115	1.197	0.849	0.477	166.7	77	0.013	4.185	2.635	0.146	0.113	113.9	129	0.06	7.694	4.186	0.321	0.239	127.7
26	0.027	3.209	0.83	0.224	0.151	178.3	78	0.056	6.47	2.761	0.422	0.168	21.0	130	0.075	3.367	4.306	0.401	0.239	58.0

	Area	xm	ym	major	minor	angle		Area	xm	ym	major	minor	angle		Area	xm	ym	major	minor	angle
27	0.018	6.386	0.826	0.164	0.143	50.1	79	0.028	2.299	2.696	0.2	0.179	148.1	131	0.089	3.802	4.412	0.527	0.215	135.2
28	0.03	5.234	0.932	0.259	0.148	154.8	80	0.039	7.544	2.78	0.312	0.16	109.7	132	0.013	4.018	4.272	0.159	0.104	48.6
29	0.081	3.965	1.037	0.384	0.27	115.4	81	0.018	9.563	2.764	0.165	0.135	78.2	133	0.025	7.377	4.352	0.254	0.126	110.1
30	0.016	8.153	0.913	0.162	0.123	177.3	82	0.014	6.835	2.797	0.198	0.088	118.0	134	0.077	4.333	4.407	0.376	0.262	166.7
31	0.02	6.58	0.986	0.183	0.139	142.0	83	0.118	3.838	2.876	0.541	0.277	167.5	135	0.071	2.229	4.517	0.494	0.184	116.9
32	0.056	6.227	1.138	0.466	0.153	67.6	84	0.055	5.917	2.91	0.331	0.213	126.7	136	0.127	5.339	4.573	0.604	0.266	16.6
33	0.013	2.946	0.997	0.173	0.096	45.7	85	0.04	3.065	2.942	0.366	0.14	133.5	137	0.049	4.62	4.568	0.358	0.176	54.8
34	0.041	8.157	1.135	0.285	0.182	71.6	86	0.059	9.293	3.042	0.508	0.147	72.1	138	0.147	2.636	4.763	0.609	0.308	60.0
35	0.039	2.553	1.077	0.353	0.14	0.6	87	0.038	8.474	2.923	0.266	0.184	39.0	139	0.017	8.862	4.582	0.234	0.093	70.6
36	0.058	1.515	1.188	0.367	0.202	122.2	88	0.043	8.157	2.965	0.279	0.198	171.9	140	0.073	7.61	4.721	0.373	0.248	85.0
37	0.013	0.863	1.105	0.182	0.09	177.8	89	0.027	7.245	2.964	0.231	0.146	43.7	141	0.09	3.77	4.781	0.407	0.282	125.2
38	0.043	3.313	1.208	0.265	0.208	166.1	90	0.059	1.022	3.058	0.319	0.237	104.7	142	0.044	6.996	4.74	0.269	0.21	96.5
39	0.017	3.717	1.18	0.179	0.118	165.3	91	0.012	9.65	2.975	0.14	0.113	60.0	143	0.102	4.491	4.937	0.609	0.214	111.2
40	0.152	2.807	1.536	0.682	0.285	117.7	92	0.041	4.657	3.059	0.286	0.182	93.1	144	0.054	1.353	4.852	0.453	0.153	62.3
41	0.022	2.222	1.329	0.206	0.137	175.4	93	0.028	4.47	3.048	0.235	0.15	81.0	145	0.025	3.103	4.769	0.235	0.135	140.1
42	0.056	8.478	1.403	0.371	0.193	178.7	94	0.036	2.631	3.094	0.285	0.16	100.6	146	0.114	5.091	4.927	0.387	0.376	11.3
43	0.101	8.132	1.629	0.543	0.237	107.0	95	0.071	5.118	3.098	0.362	0.249	179.5	147	0.021	0.998	4.902	0.221	0.123	29.7
44	0.047	3.169	1.563	0.31	0.193	79.7	96	0.062	3.425	3.183	0.523	0.152	154.5	148	0.07	0.946	5.326	0.37	0.242	101.4
45	0.02	0.826	1.49	0.221	0.113	155.8	97	0.017	2.348	3.191	0.203	0.105	87.6	149	0.058	5.62	5.179	0.372	0.198	49.6
46	0.031	9.402	1.548	0.221	0.181	111.5	98	0.035	8.649	3.183	0.277	0.163	165.6	150	0.081	6.071	5.181	0.373	0.278	128.9
47	0.024	4.371	1.577	0.224	0.134	116.9	99	0.015	3.024	3.24	0.159	0.118	6.9	151	0.025	7.069	5.139	0.319	0.101	34.8
48	0.078	6.227	1.674	0.443	0.223	137.9	100	0.012	6.913	3.289	0.159	0.097	77.3	152	0.055	4.807	5.193	0.32	0.219	57.8
49	0.078	7.619	1.663	0.332	0.298	115.9	101	0.109	5.038	3.467	0.407	0.339	63.8	153	0.04	7.417	5.179	0.259	0.198	179.1
50	0.101	4.927	1.699	0.454	0.283	168.1	102	0.016	4.457	3.37	0.176	0.115	103.1	154	0.041	9.088	5.238	0.268	0.194	70.9
51	0.015	1.685	1.66	0.167	0.112	167.5	103	0.403	6.87	4.153	1.012	0.508	99.1							
52	0.018	2.316	1.658	0.184	0.128	0.7	104	0.102	2.514	3.478	0.555	0.234	2.4							

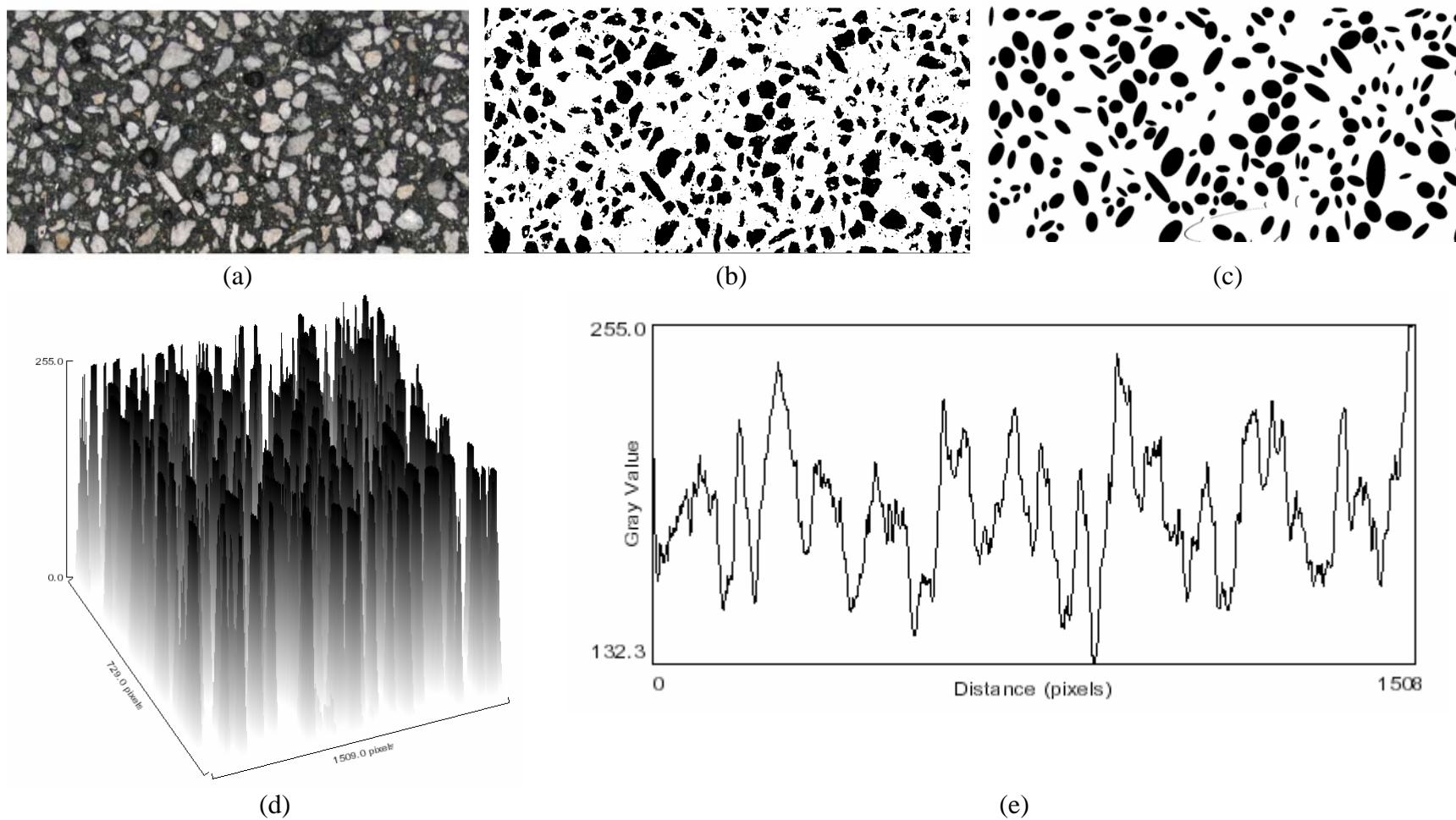


Figure C9. a) Image of MV30L24, b) selected pumices in binary image of MV30L24, c) ellipses mask, d) surface of pumices and (e) plot drawing of MV30L24.

Table C9. Image analysis results for MV30L24 series.

	Area	xm	ym	major	minor	angle		Area	xm	ym	major	minor	angle		Area	xm	ym	major	minor	angle
1	0.02	0.412	0.282	0.362	0.071	86.3	81	0.032	7.49	1.532	0.27	0.15	84.8	161	0.055	9.139	2.986	0.375	0.186	143.5
2	0.053	0.784	0.241	0.303	0.225	13.4	82	0.015	8.178	1.547	0.24	0.081	80.1	162	0.046	2.208	3.049	0.307	0.19	167.1
3	0.022	1.141	0.224	0.19	0.15	15.7	83	0.045	9.245	1.508	0.371	0.153	3.2	163	0.068	4.157	3.115	0.474	0.184	65.3
4	0.014	2.597	0.174	0.18	0.098	11.9	84	0.101	5.572	1.626	0.375	0.342	155.8	164	0.075	5.571	2.99	0.36	0.264	30.3
5	0.049	3.243	0.255	0.3	0.206	107.3	85	0.11	2.938	1.664	0.453	0.31	109.5	165	0.037	6.741	2.987	0.269	0.175	51.0
6	0.021	4.322	0.187	0.232	0.115	159.2	86	0.04	1.317	1.627	0.252	0.201	64.0	166	0.027	4.707	3.084	0.253	0.134	175.1
7	0.032	5.572	0.228	0.217	0.186	158.3	87	0.024	4.636	1.614	0.188	0.164	138.0	167	0.028	1.585	3.157	0.21	0.167	53.1
8	0.036	5.853	0.28	0.244	0.189	67.0	88	0.018	7.667	1.601	0.228	0.103	100.0	168	0.013	2.941	3.112	0.222	0.072	151.7
9	0.017	6.82	0.165	0.288	0.077	177.9	89	0.088	6.442	1.637	0.54	0.207	145.7	169	0.043	2.516	3.314	0.402	0.135	76.5
10	0.034	8.194	0.244	0.364	0.119	16.7	90	0.021	7.237	1.633	0.196	0.136	84.5	170	0.108	3.474	3.417	0.716	0.193	127.2
11	1.053	5.491	3.985	2.442	0.549	8.6	91	0.019	7.92	1.648	0.213	0.117	77.5	171	0.047	9.016	3.334	0.372	0.161	140.1
12	0.058	9.329	0.225	0.344	0.216	77.2	92	0.063	1.586	1.754	0.332	0.242	90.6	172	0.032	4.36	3.276	0.277	0.147	72.7
13	0.057	1.48	0.262	0.43	0.168	15.6	93	0.052	5.156	1.778	0.301	0.218	81.2	173	0.015	8.031	3.217	0.224	0.084	17.9
14	0.036	2.354	0.279	0.268	0.173	8.2	94	0.026	4.096	1.737	0.22	0.152	28.1	174	0.06	4.633	3.369	0.337	0.228	63.2
15	0.051	7.318	0.336	0.269	0.239	34.4	95	0.059	5.883	1.827	0.325	0.233	57.9	175	0.044	7.075	3.372	0.328	0.172	158.6
16	0.012	8.395	0.278	0.181	0.085	43.6	96	0.031	8.39	1.827	0.251	0.155	61.2	176	0.013	6.122	3.231	0.167	0.096	169.7
17	0.036	5.298	0.241	0.328	0.141	138.7	97	0.018	2.458	1.805	0.172	0.133	16.9	177	0.016	5.001	3.306	0.165	0.124	106.3
18	0.027	3.553	0.284	0.232	0.147	54.0	98	0.022	7.144	1.819	0.207	0.137	141.7	178	0.054	6.776	3.399	0.277	0.248	68.6
19	0.058	4.177	0.338	0.46	0.159	142.3	99	0.021	9.497	1.819	0.173	0.157	153.9	179	0.07	5.722	3.472	0.453	0.196	97.3
20	0.067	2.808	0.344	0.386	0.22	0.3	100	0.044	0.9	1.979	0.371	0.153	117.2	180	0.012	0.527	3.298	0.136	0.116	177.8
21	0.023	8.691	0.3	0.193	0.151	168.5	101	0.049	2.704	1.946	0.255	0.243	38.7	181	0.094	1.94	3.371	0.498	0.24	107.8
22	0.019	9.012	0.303	0.165	0.15	139.4	102	0.025	3.868	1.935	0.242	0.131	88.9	182	0.075	8.353	3.442	0.339	0.283	146.0
23	0.019	6.556	0.379	0.199	0.123	32.7	103	0.077	3.15	2.073	0.492	0.2	70.5	183	0.019	1.075	3.436	0.197	0.12	87.2
24	0.06	4.578	0.572	0.336	0.228	89.9	104	0.06	0.475	1.895	0.381	0.2	84.7	184	0.05	5.33	3.407	0.289	0.219	127.9
25	0.025	6.939	0.422	0.21	0.149	1.8	105	0.019	3.563	1.906	0.195	0.121	150.9	185	0.037	3.036	3.44	0.241	0.196	0.7
26	0.081	1.749	0.549	0.407	0.252	32.3	106	0.053	5.61	2.016	0.315	0.216	89.0	186	0.026	8.65	3.541	0.266	0.122	71.3
27	0.018	3.883	0.452	0.175	0.132	149.1	107	0.018	7.593	1.97	0.198	0.117	144.4	187	0.018	0.897	3.412	0.186	0.121	8.3
28	0.023	2.305	0.477	0.209	0.141	137.4	108	0.02	8.141	1.982	0.212	0.121	76.5	188	0.017	2.817	3.508	0.251	0.086	138.7
29	0.022	8.794	0.574	0.31	0.091	62.6	109	0.027	6.893	2.044	0.228	0.148	103.6	189	0.021	6.348	3.525	0.167	0.159	33.1
30	0.018	5.773	0.524	0.229	0.099	112.0	110	0.066	1.229	2.082	0.323	0.258	105.3	190	0.013	0.451	3.57	0.154	0.108	137.5
31	0.041	8.187	0.619	0.322	0.163	90.1	111	0.03	2.134	1.978	0.323	0.117	173.6	191	0.056	4.672	3.616	0.291	0.245	24.6
32	0.031	3.214	0.52	0.36	0.109	173.3	112	0.047	2.467	2.17	0.373	0.159	109.5	192	0.046	4.245	3.574	0.266	0.221	3.5
33	0.021	5.173	0.545	0.204	0.131	102.7	113	0.018	4.522	2.078	0.237	0.097	60.7	193	0.012	3.302	3.6	0.153	0.102	58.1
34	0.089	9.361	0.73	0.49	0.231	65.0	114	0.077	8.732	2.115	0.442	0.221	1.4	194	0.056	1.615	3.677	0.337	0.213	47.6
35	0.021	7.79	0.518	0.276	0.097	170.8	115	0.055	0.603	2.192	0.33	0.211	58.6	195	0.028	7.037	3.644	0.23	0.155	104.6
36	0.067	7.372	0.627	0.323	0.264	56.3	116	0.07	5.892	2.278	0.333	0.266	24.7	196	0.015	0.884	3.619	0.193	0.098	67.6
37	0.109	7.004	0.832	0.446	0.31	34.4	117	0.113	5.174	2.314	0.397	0.363	17.8	197	0.04	6.099	3.716	0.289	0.176	100.7
38	0.035	8.489	0.632	0.258	0.171	20.9	118	0.032	9.048	2.278	0.295	0.138	76.3	198	0.053	6.504	3.769	0.382	0.178	60.4
39	0.082	0.973	0.866	0.378	0.275	117.0	119	0.028	8.328	2.397	0.3	0.119	112.8	199	0.021	6.798	3.689	0.246	0.111	103.5

	Area	xm	ym	major	minor	angle		Area	xm	ym	major	minor	angle		Area	xm	ym	major	minor	angle
40	0.018	4.718	0.658	0.163	0.142	171.2	120	0.026	7.317	2.232	0.244	0.135	123.6	200	0.014	4.55	3.668	0.177	0.099	92.5
41	0.038	2.672	0.688	0.261	0.186	49.5	121	0.031	9.206	2.297	0.33	0.121	82.1	201	0.014	2.525	3.66	0.154	0.113	13.6
42	0.031	9.176	0.707	0.211	0.188	95.2	122	0.017	7.581	2.226	0.188	0.115	78.4	202	0.048	9.428	3.74	0.283	0.216	108.1
43	0.032	3.166	0.866	0.295	0.137	56.6	123	0.044	1.723	2.311	0.352	0.161	138.6	203	0.02	0.722	3.666	0.18	0.139	162.4
44	0.021	7.872	0.709	0.244	0.107	122.8	124	0.06	7.034	2.288	0.311	0.246	152.1	204	0.022	2.793	3.697	0.188	0.147	63.0
45	0.096	2.904	0.941	0.433	0.281	106.8	125	0.014	6.363	2.261	0.234	0.077	38.5	205	0.014	1.391	3.772	0.189	0.097	87.6
46	0.1	1.253	0.959	0.514	0.249	93.6	126	0.014	3.352	2.245	0.211	0.084	165.6	206	0.037	4.025	3.806	0.299	0.159	125.1
47	0.013	7.646	0.793	0.167	0.096	109.7	127	0.052	2.801	2.378	0.298	0.224	94.0	207	0.038	3.774	3.792	0.23	0.209	78.1
48	0.029	8.591	0.772	0.211	0.176	156.7	128	0.019	8.613	2.387	0.287	0.082	130.7	208	0.093	7.43	3.87	0.421	0.28	114.4
49	0.191	3.475	0.963	0.566	0.43	27.2	129	0.071	3.53	2.518	0.495	0.183	61.4	209	0.06	0.495	3.883	0.384	0.198	94.1
50	0.014	7.531	0.901	0.226	0.077	117.8	130	0.04	3.328	2.432	0.265	0.19	47.0	210	0.086	8.61	3.849	0.403	0.272	148.1
51	0.048	5.347	0.803	0.322	0.189	2.4	131	0.012	0.544	2.44	0.214	0.072	129.5	211	0.056	5.731	3.902	0.443	0.16	141.0
52	0.042	8.991	0.961	0.331	0.163	138.0	132	0.031	7.66	2.48	0.302	0.13	52.3	212	0.023	2.599	3.857	0.219	0.132	75.1
53	0.096	6.848	1.08	0.609	0.201	125.6	133	0.024	1.331	2.464	0.27	0.112	148.5	213	0.077	3.041	3.847	0.48	0.203	51.5
54	0.072	2.228	0.934	0.386	0.237	155.0	134	0.121	5.728	2.689	0.53	0.29	41.4	214	0.014	1.243	3.907	0.217	0.082	91.3
55	0.032	9.603	1.016	0.304	0.132	83.3	135	0.077	4.963	2.583	0.374	0.26	151.5	215	0.012	4.5	3.903	0.141	0.111	42.2
56	0.048	1.685	0.975	0.278	0.222	120.0	136	0.088	4.382	2.63	0.408	0.275	90.1	216	0.137	8.058	4.141	0.478	0.364	172.7
57	0.093	0.674	1.12	0.391	0.303	97.4	137	0.04	7.92	2.545	0.256	0.198	81.5	217	0.024	5.103	4.001	0.314	0.097	84.2
58	0.103	4.506	0.878	0.579	0.226	59.3	138	0.045	0.928	2.662	0.259	0.222	45.8	218	0.063	2.262	4.059	0.37	0.216	90.3
59	0.069	9.321	1.205	0.522	0.17	128.6	139	0.023	2.663	2.589	0.28	0.103	122.9	219	0.023	6.971	4.032	0.359	0.083	94.9
60	0.097	8.744	1.153	0.521	0.237	166.4	140	0.036	7.002	2.556	0.226	0.2	28.9	220	0.02	9.606	3.939	0.199	0.127	160.6
61	0.021	6.526	1.022	0.23	0.116	91.4	141	0.096	5.492	2.565	0.417	0.293	73.8	221	0.068	4.466	4.116	0.369	0.235	114.4
62	0.019	2.604	1.055	0.283	0.087	30.0	142	0.028	2.981	2.634	0.244	0.147	37.6	222	0.032	1.519	4.066	0.322	0.128	34.8
63	0.024	5.616	1.084	0.242	0.126	88.0	143	0.133	8.685	2.723	0.443	0.383	122.0	223	0.134	3.773	4.109	0.562	0.303	50.7
64	0.014	1.074	1.091	0.175	0.1	133.3	144	0.054	8.166	2.714	0.317	0.217	143.2	224	0.074	7.239	4.222	0.339	0.277	53.6
65	0.056	4.939	1.218	0.342	0.21	178.9	145	0.056	2.343	2.753	0.365	0.195	142.7	225	0.043	8.338	4.213	0.391	0.14	43.5
66	0.014	0.428	1.097	0.183	0.1	63.7	146	0.084	0.509	2.805	0.456	0.234	63.9	226	0.015	1.678	4.154	0.153	0.123	123.3
67	0.033	2.677	1.219	0.32	0.13	40.3	147	0.034	6.416	2.737	0.27	0.161	164.8	227	0.036	9.258	4.297	0.288	0.161	83.6
68	0.052	5.951	1.21	0.463	0.144	158.4	148	0.022	9.065	2.702	0.211	0.134	27.3	228	0.033	6.378	4.309	0.281	0.149	77.7
69	0.013	7.784	1.144	0.224	0.073	62.7	149	0.023	6.67	2.805	0.222	0.13	79.5	229	0.028	1.145	4.263	0.25	0.141	75.4
70	0.043	2.378	1.307	0.395	0.139	137.9	150	0.161	3.742	2.957	0.588	0.348	60.6	230	0.068	9.042	4.311	0.408	0.213	79.6
71	0.043	6.347	1.241	0.372	0.148	148.5	151	0.013	4.124	2.785	0.164	0.103	41.6	231	0.078	6.731	4.406	0.436	0.229	102.6
72	0.03	9.042	1.257	0.24	0.159	22.4	152	0.037	0.79	2.914	0.351	0.135	78.8	232	0.058	5.76	4.371	0.566	0.13	29.2
73	0.063	1.093	1.449	0.316	0.255	156.7	153	0.233	7.502	3.254	0.879	0.337	85.2	233	0.084	5.364	4.341	0.392	0.273	36.6
74	0.059	0.604	1.466	0.376	0.199	109.3	154	0.075	1.263	2.978	0.413	0.232	101.7	234	0.054	9.572	4.319	0.321	0.212	143.8
75	0.051	3.152	1.388	0.296	0.22	127.5	155	0.034	5.067	3.025	0.36	0.119	85.4	235	0.053	4.935	4.408	0.278	0.241	111.5
76	0.07	3.791	1.451	0.341	0.263	153.5	156	0.017	6.048	2.939	0.293	0.073	88.9	236	0.034	1.453	4.351	0.23	0.187	6.3
77	0.032	1.728	1.366	0.231	0.177	18.9	157	0.019	7.104	2.921	0.239	0.101	67.4	237	0.013	4.335	4.459	0.171	0.099	85.1
78	0.032	3.409	1.431	0.26	0.159	65.0	158	0.026	6.187	2.978	0.251	0.131	80.0	238	0.013	8.284	4.522	0.158	0.106	19.5
79	0.044	5.912	1.433	0.28	0.202	24.5	159	0.019	1.63	2.939	0.174	0.142	156.1	239	0.023	9.336	4.533	0.236	0.124	1.6
80	0.038	8.417	1.523	0.375	0.129	57.8	160	0.03	5.312	2.982	0.281	0.138	148.8							

CIRRICULUM VITAE



Burcu Akçay was born in Kocaeli in 1978. She completed her high school education in Kocaeli Science College in 1994. During her education in high school, she had been awarded by TUBITAK (The Scientific and Technical Research Council of Turkey) as young scientist. She received her Bachelor of Science (Civil Engineering) and Master of Science degrees (with honor) from the University of Kocaeli in 1998 and 2000. She commenced her studies towards the PhD degree at the Institute of Science and Technology, Istanbul Technical University in February 2001. She worked at the University of Kocaeli as a Research Assistance from 1998 to 2001, and since then she has been working at Istanbul Technical University.

The author's publications are listed below.

Papers in refereed journals

Akcay, B., Agar, A.S., Bayramov, F., Atahan, H.N., Sengul, C. and Tasdemir, M.A., Modeling of the size-independent specific fracture energy of concrete, submitted to *ACI Materials Journal*.

Akcay B., "Variation of In-Place Concrete Core Strength from Istanbul Area: A Statistical Analysis of Concrete Core Data", *ASCE Journal of Materials in Civil Engineering*, September/October 2004 , Vol. 16, No. 5, 507-510.

Papers in international conferences

Akcay, B., Haberveren, S., Kocaturk, N., Arslan, G., Yerlikaya, M. and Tasdemir, M.A., 2007. Fracture of Hybrid Steel Fiber Reinforced Self Compacting Concrete, TCMB 3rd International Symposium Sustainability in Cement and Concrete, 21-23 May 2007, Istanbul, Turkey.

Akcay, B. and Tasdemir, M.A., 2006. Influence of lightweight aggregates on internal curing and fracture of concrete, *Proceedings of the International RILEM Conference, Volume Changes of Hardening Concrete: Testing and Mitigation*, Eds. Jensen, Lura, and Kovler, Lyngby, Denmark, PRO 52, 31-40.

Akcay, B. and Tasdemir, M.A., 2006. Effects of Lightweight Aggregates on Autogenous Deformation in Concrete, *plenary lecture in 16th European Conference of Fracture (ECF16), Measuring, Monitoring, and Modeling Concrete Properties: MMMCP in Honor of Surendra P. Shah*, Eds. Konsta-Gdoutos, Greece, 163-170.

Akcay, B. and Tasdemir, M.A., 2005. Utilization of artificial lightweight aggregates in hardened cement paste for internal water curing, *Proc. of fib Keep Concrete Attractive, Budapest*, 23-25 May, Eds., Balazs and Borosnyoi, Vol 1, pp 374-380.

Bayramov, F, **Akcay, B.**, Agar, A.S., Atahan, H.N., Sengül, C., and Tasdemir, M.A., “Determination of the True Specific Fracture Energy of Concrete”, 6th International Congress on Advances in Civil Engineering, 6-8 October 2004, Bogazici University, Istanbul, Turkey, Vol II, pp. 917-926.

Akcay B., “Statistical Analyses of Compressive Strength of Concrete in Istanbul Structures by Core Samples” In Proc.: Structural Engineering World Conference (SEWC), 2002, Yokohama, Japan, October 9-12, 2002.

Abstracts in international conferences

Akcay B., “The extent of damage caused by taking core and strength performance of filling core voids”, ERES 2003: 22 - 24 September 2003, Ancona, Italy

Papers in national conferences

Akcay B., Önen Y.H., Öztekin E., “İstanbul Binalarında Karot Yardımıyla Beton Nitelik Denetimi”, Türkiye İnşaat Mühendisliği XVI. Teknik Kongresi, 1-3 Kasım 2001, Ankara.

Akcay, B. and Tasdemir, M.A., “Prevention of autogenous deformation in high performance concrete”, XIV. National Mechanical Conference, Hatay, Turkey, pp. 45-54 (in Turkish with English Summary).

Mese, O., Sengul, C., **Akcay, B.**, and Tasdemir, M.A., 2005. Meso-mechanical modeling of fracture parameters of cement paste, mortar and concrete, XIV. National Mechanical Conference, Hatay, Turkey, 12-16 September 2005, 631-642 (in Turkish with English Summary).

Aldikacti, K.V., Sengul, C., **Akcay, B.**, and Tasdemir, C., 2005. Meso-mechanical modeling of concrete as a composite material, in 6th National Concrete Congress, High Performance Concrete, Istanbul, Turkey, 16-18 November 2005, pp. 257-271 (in Turkish with English summary)

Invited speaker

M.S. Akman and **B. Akcay**, “Kimyasal Beton Katkılarının Gelişimi ve Çimentolarla Uyumu”, Yapılarda Kimyasal Katkılar Sempozyumu, 24-25 Mart 2005, Ankara, 15-32.